Semiconductors, Vol. 34, No. 3, 2000, pp. 251–254. Translated from Fizika i Tekhnika Poluprovodnikov, Vol. 34, No. 3, 2000, pp. 257–260.
Original Russian Text Copyright © 2000 by Ostrovskiĭ, Steblenko, Nadtochiĭ.

Ultrasound-Induced Surface Hardening of Dislocation-Free Silicon

I. V. Ostrovskiĭ*, L. P. Steblenko, and A. B. Nadtochiĭ

Department of Physics, Kiev State University, Kiev, 252022 Ukraine

**e-mail: iostrov@genphys.ups.kiev.ua*

Submitted April 22, 1999; accepted for publication August 18, 1999

Abstract—The effect of ultrasonic treatment on the microplastic properties of a near-surface layer in dislocation-free silicon single crystals was studied using [111]-oriented *p*-Si samples with artificial dislocation rosettes. The ultrasonic processing resulted in the formation of an approximately 100-μm-thick hardened near-surface layer and the emergence of point-defect pileups of the vacancy and/or vacancy–impurity cluster type on the sample surface. Possible mechanisms of the observed phenomena are discussed. © *2000 MAIK "Nauka/Interperiodica".*

INTRODUCTION

Recent years have testified to the permanent interest of researchers in solving the task of controlling the physical properties of semiconductors by using various surface treatments. This problem has especially important relation to silicon [1–3], a material widely used in the development of novel materials and new technological applications. The possible surface treatments include, in addition to various modes of thermal annealing [1, 2], ultrasonic processing. While earlier investigations primarily employed the ultrasonic waves with frequencies in a kHz range [4, 5], present-day research is mostly concentrated in a MHz frequency range [6–8].

The basic physical principles explaining the effect of ultrasonic waves in the MHz range on the properties of semiconductors are related to interactions of the ultrasound-induced elastic and electric fields with the similar fields of extended, linear, and point defects (including the interaction of mobile defects with each other). This was confirmed by data obtained in various semiconductors [6, 9–12]. The method of acoustic excitation can be effective in the processing of materials with nonideal crystal lattices.

It should be noted that considerable progress has been achieved in the study of optical phenomena related to the motion of dislocations in a high-intensity ultrasonic field [13]. Another well-known effect is the formation of a hard surface layer in dislocated crystalline materials, including semiconductors, upon their surface treatment with ultrasound. This hardening effect is conventionally explained as being due to increasing concentration of dislocations in the near-surface layer [14].

By now, a considerable volume of data has been gained concerning effects of the ultrasonic processing (USP) on the microscopic defect structure in semiconductors [7, 12, 15–17]. The phenomena of USP-stimulated diffusion and association of point defects, as well as dissociation of complex centers [7], may probably account for some anomalous properties of the surface layer of semiconductors upon USP and, hence, for the character of deformation development in these materials.

In this context, it was of interest to study the pattern of USP-induced changes in the surface layer of a dislocation-free silicon. Since it was known that both the shape and the dimensions of the dislocation rosettes in a crystal are sensitive toward the presence of impurities and are correlated with changes in the mechanical properties [18], our experiments were performed on dislocation rosettes artificially introduced into samples. The samples were prepared from the initial dislocation-free silicon–inexpensive and most easily produced material widely used in the modern microelectronics.

EXPERIMENTAL

The experiments were performed on the Czochralski-grown *p*-type silicon single crystals. One sample (see table) was modified by preliminary neutron doping followed by annealing, which allowed the initial point-defect concentration to be changed. The samples had the shape of a parallelepiped with dimensions $0.5 \times 0.5 \times 1.0$ cm. The residual surface roughness and the stressed–strained damaged layer upon cutting were removed by chemical polishing in a HF–HNO_3–CH_3COOH (3:1:1) etching acid mixture. The rate of etching was about 8 μm/min. The measurements were performed on a sample surface with a [111] crystallograhic orientation.

We have monitored the behavior of dislocation rosettes providing information on the variation of the mechanical properties of samples in the course of

1063-7826/00/3403-0251$20.00 © 2000 MAIK "Nauka/Interperiodica"

Arm lengths in dislocation rosettes formed in silicon samples upon ultrasonic processing (USP)

Sample	Initial state	ρ, kΩ cm	USP time, h	Arm length, μm	Experimental conditions
7*N*	*G*	7.5	0	125	Control (no USP)
8*N*	*G*	7.5	0.5	100	Indented before USP
2*N*	*G*	7.5	4	80	Indented before USP
1*N*	*G*	7.5	4	60	Indented after USP
4*N*	*n*, *TA*	20	0.5	60	Annealing (850°C, 2 h)

Note: *G* stands for as-grown (no pretreatment); *n*, for neutron-doped; *TA*, for thermal annealing; and ρ, for resistivity.

microplastic deformation. The dislocations were formed in the sample at room temperature using a PMT-3 microhardness meter operated at an indenter load of $P = 2$ N. About twenty indentations were made on the surface of each sample, after which the samples were exposed to the action of ultrasonic waves.

The USP was effected as follows. A piezoceramic transducer, glued onto the smaller side face of a sample, was excited with a pulsed voltage V supplied from a generator. The ultrasonic waves propagated in the direction perpendicular to the [111] crystallographic direction. Another transducer glued to the opposite face of the sample was used to monitor the acoustic waves passing through the silicon crystal. The effect of USP was studied in the range of frequencies from 0.4 to 4 MHz. The amplitude of USP-induced deformations in a sample was proportional to the voltage V and reached, by our estimates, a level of 10^{-4} for the maximum voltage applied. The USP duration was varied from 30 min to 6 h.

After the USP, the crystals were heat-treated in order to provide for the thermoactivated motion of dislocations. For this purpose, the samples were placed into an electric furnace, heated to 973 K, kept at this temperature for 30 min, and allowed to cool with the furnace. In the course of annealing, the dislocations spread away from the indentation sites to form a rosette.

The distribution of dislocations in the samples upon annealing was studied by the most simple and direct experimental technique based on the selective etching of crystals, which was previously successfully employed for similar investigations [19]. Prior to the selective etching (as well as before USP), the samples were degreased with benzene or ethanol and rinsed in distilled water. The etching was performed in the Sirtle etchant ($Cr_2O_3 : H_2O : HF$, 1 : 2 : 3) at room temperature.

RESULTS AND DISCUSSION

Figure 1 shows the pattern of selective etching for a control silicon sample not subjected to USP. Figures 2 and 3 present the patterns observed upon the selective etching of samples upon USP. As seen from these figures and data presented in the table, the rosette arm lengths L markedly decrease with increasing USP duration, also depending on the sample history. The arm length of a dislocation rosette is a characteristic of the mobility of dislocations. The USP-induced decrease in the rosette dimensions observed in our experiments is evidence of a reduced mobility of dislocations, that is, of the surface hardening.

The surface of the silicon samples etched after USP exhibits characteristic round etch pits (Figs. 2, 3), which are conventionally explained by the presence of diffusing impurity coagulants (e.g., vacancy clusters) in the near-surface layer of the crystal [4].

The repetition frequency of the tension–compression cycles in the surface layers during USP is very high and may stimulate a rapid growth of the vacancy clusters, which serve as sources for the subsequent dislocation loop formation [4]. From this, we may conclude that cyclic loading under the action of ultrasonic oscillations leads to intensification of the process of diffusion microplasticity. This factor may account for the formation of a debris layer responsible for the surface hardening. The appearance of a hardened surface layer upon USP is confirmed by a shortening of the arm length in the dislocation rosettes. A correlation between the degree of surface hardening and the USP duration indicates that the observed effects are related to some diffusion mechanisms.

It was of interest to estimate the thickness of the USP-hardened surface layer. Using the method of layer-by-layer removal by grinding followed by chemical etching, we have established that the USP-induced hardening extends over a rather thick near-surface layer, reaching a depth of up to 100 μm. It should be noted that removal of this layer was also accompanied by a vanishing of the characteristic etch pits related to the vacancy clusters. Moreover, the arm length of the dislocation rosettes at a depth of ~100 μm increased as compared to that observed at the surface of the sample. Indeed, the arm length on the sample surface upon USP was $L \approx 40$–60 μm, while the value at a depth of 100 μm increased to a level ($L \approx 100$–120 μm) typical of the initial silicon samples not subjected to the action of ultrasound.

The effect of surface hardening was observed independently of the order of treatments, that is, both when USP of the silicon surface was followed by indentation and when the indentation of unexposed sample was fol-

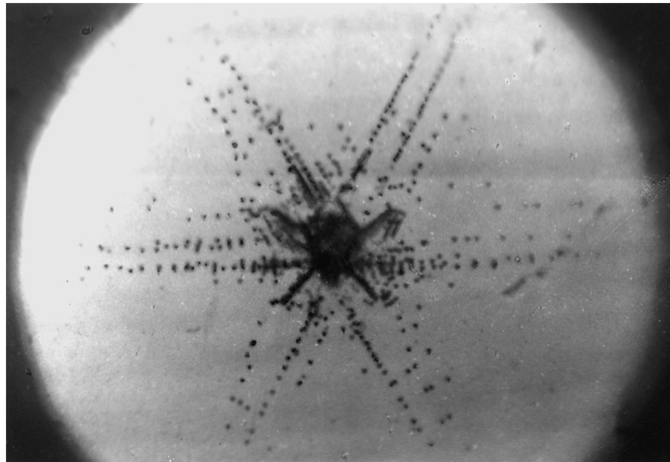

Fig. 1. A dislocation rosette in a control silicon sample (table, sample 7*N*) without USP.

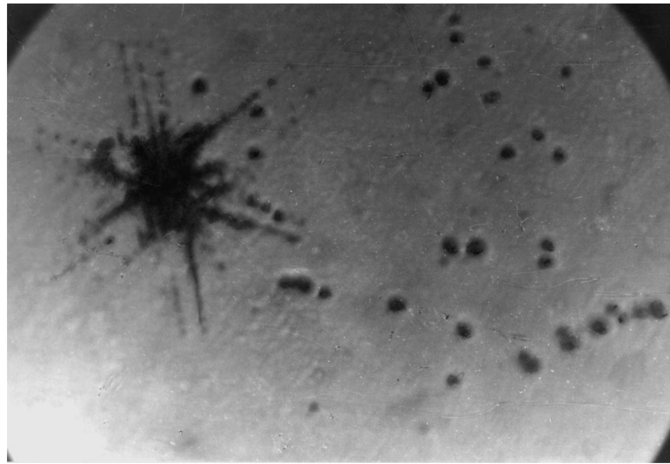

Fig. 2. A dislocation rosette in a silicon crystal upon 4-h USP (table, sample 1*N*). The rosette arm length is about half that in the control sample. The sample surface exhibits traces of vacancy–impurity clusters in the form of dark oval spots.

lowed by USP. However, for equal USP duration, the hardening effect was somewhat more pronounced in the former case as indicated by comparison of the data for samples 2*N* and 1*N* (see table).

It should be emphasized that the USP-induced surface hardening depended not only on the USP duration but on the sample history as well, in particular, on the method of doping and the preliminary high-temperature heat treatment. For example, the preliminary neutron doping and a 2-h anneal at 850°C (sample 4*N*) resulted in that a 30-min subsequent USP decreased the dislocation rosette arm length approximately by half as compared to the value in a sample without pretreatment. In addition, etching of the pretreated surface revealed a large number of etch pits characteristic of the vacancy–impurity clusters (Fig. 3). At the same time, the samples not subjected to preliminary annealing exhibited the surface hardening effect only after a 4-h USP (cf. the data for samples 1*N* and 4*N* in the table). Therefore, the effect of surface hardening in the samples upon preliminary annealing is observed after a shorter USP duration. This phenomenon can be explained by the presence of a greater amount of oxygen and, hence, of a higher concentration of vacancy–oxygen clusters in the samples upon annealing.

It is also possible that the observed effects are related not only to the concentration of clusters but to their charge state as well. The charge state of the clusters may be related, in turn, to the dopant concentration.

Note that the study of the variation of the arm length in the starlike etch pattern formed around the indenter print only qualitatively reflect a change in the mobility of dislocations caused by the USP. It is expected that an analysis of the behavior of dislocation half-loops would allow us to determine some quantitative characteristics related to dislocation mobility. However, this task goes beyond the framework of the present study.

To summarize the above considerations, we conclude the following:

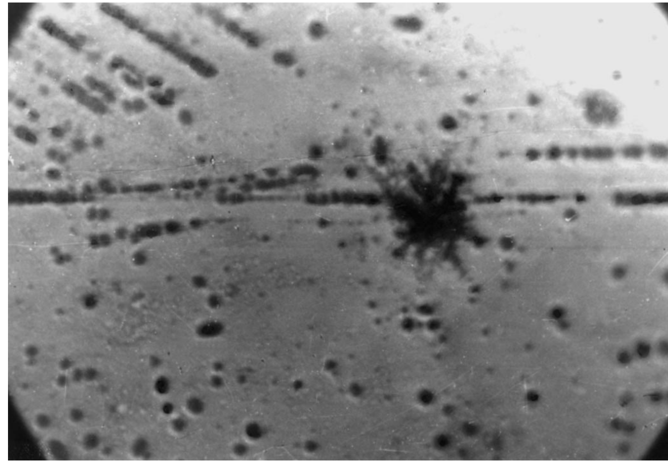

Fig. 3. A dislocation rosette in a preliminarily neutron-doped and annealed silicon crystal upon 30-min USP (table, sample 4 *N*). The emergence of vacancy–impurity clusters at the sample surface is more pronounced as compared to that in samples 8 *N*, 2*N*, and 1*N*.

1. Ultrasonic processing (USP) of a silicon single crystal for a time period exceeding 30 min results in the formation of a hard near-surface region (debris layer) with a thickness of up to 100 μm.

2. The mobility of dislocations in this near-surface crystal layer decreases by a factor of 1.5–2 as compared to the initial level, depending on the USP duration and the preliminary heat treatment (annealing).

3. Room-temperature USP of a Czochralski-grown dislocation-free silicon single crystal in the MHz frequency range results in the formation of point-defects pileups of the type of vacancy and/or vacancy–impurity clusters.

REFERENCES

1. S. A. McHugo, H. Hieslmair, and E. R. Weber, Appl. Phys. A **64**, 127 (1997).
2. T. Mohammed-Brahim, O. Bonnaud, *et al.*, J. Non-Cryst. Solids B **227–230**, 962 (1998).
3. J. Koshka, S. Ostapenko, T. Ruf, *et al.*, Appl. Phys. Lett. **69**, 2537 (1996).
4. V. P. Alekhin, *The Physics of Strength and Plasticity in Surface Layers of Materials* (Nauka, Moscow, 1983).
5. V. P. Grabchak and A. V. Kulemin, Sov. Phys. Acoust. **22**, 475 (1976).
6. Ya. M. Olikh and N. I. Karas', Fiz. Tekh. Poluprovodn. (St. Petersburg) **30**, 1455 (1996) [Semiconductors **30**, 765 (1996)].
7. I. B. Ermolovich, V. V. Milenin, R. V. Konakova, *et al.*, Fiz. Tekh. Poluprovodn. (St. Petersburg) **31**, 503 (1997) [Semiconductors **31**, 427 (1997)].
8. I. V. Ostrovskiĭ, Ju. M. Khalack, A. B. Nadtochiĭ, *et al.*, *Polyse'98, Shwabish-Gmund, Germany, 1998*, p. O43.
9. I. V. Ostrovskiĭ and A. Kh. Rozhko, Fiz. Tverd. Tela (Leningrad) **26**, 3718 (1984) [Sov. Phys. Solid State **26**, 2241 (1984)].
10. V. V. Popov and F. B. Chaplik, Fiz. Tverd. Tela (Leningrad) **18**, 1789 (1976) [Sov. Phys. Solid State **18**, 1043 (1976)].
11. I. V. Ostrovskiĭ and O. A. Korotchenkov, Zh. Prikl. Spektrosk. **45**, 1014 (1986).
12. A. P. Zdebskiĭ, M. K. Sheĭnkman, A. N. Annaniyazov, *et al.*, Fiz. Tverd. Tela (Leningrad) **29**, 1135 (1987) [Sov. Phys. Semiconductors **29**, 648 (1987)].
13. I. V. Ostrovskiĭ, *Acoustoluminescence and Defects in Crystals* (Vyshcha Shkola, Kiev, 1993).
14. *Ultrasound. A Concise Encyclopedia* (Sov. Éntsiklopediya, Moscow, 1979).
15. A. P. Zdebskiĭ, V. L. Korchnaya, T. V. Torchinskaya, *et al.*, Pis'ma Zh. Tekh. Fiz. **12**, 76 (1986) [Sov. Tech. Phys. Lett. **12**, 31 (1986)].
16. A. P. Zdebskiĭ, M. I. Lisyanskiĭ, N. B. Luk'yanchikov, *et al.*, Pis'ma Zh. Tekh. Fiz. **13**, 1009 (1987) [Sov. Tech. Phys. Lett. **13**, 421 (1987)].
17. V. L. Gromashevskiĭ, V. V. Dyakin, and E. A. Sal'kov, Ukr. Fiz. Zh. (Russ. Ed.) **29**, 550 (1984).
18. M. I. Val'kovskaya, B. M. Puginash, and É. E. Maronchuk, *Plasticty and Brittleness of Semiconductor Materials Tested for Microhardess* (Inst. Appl. Phys., Acad. Sci. MoldSSR, 1984).
19. V. I. Trefilov and Yu. V. Mil'man, Dokl. Akad. Nauk SSSR **153**, 824 (1963).

Translated by P. Pozdeev

Semiconductors, Vol. 34, No. 3, 2000, pp. 255–259. Translated from Fizika i Tekhnika Poluprovodnikov, Vol. 34, No. 3, 2000, pp. 261–265.
Original Russian Text Copyright © 2000 by Gnatyuk, Gorodnichenko, Mozol', Vlasenko.

ELECTRONIC AND OPTICAL PROPERTIES OF SEMICONDUCTORS

Photoelectrical and Electrical Properties of Polycrystalline $Cd_xHg_{1-x}Te$ Layers on GaAs Substrates

V. A. Gnatyuk*, E. S. Gorodnichenko, P. E. Mozol', and A. I. Vlasenko

Institute of Semiconductor Physics, National Academy of Science of Ukraine, Kiev, 252028 Ukraine

* *e-mail: gnatyuk@class.semicond.kiev.ua*

Submitted January 11, 1999; accepted for publication September 22, 1999

Abstract—Temperature dependences of electrical conductivity, concentration, and mobility of electrons, as well as photoconductivity spectra and conductivity–illumination characteristics of $Cd_{0.8}Hg_{0.2}Te$ polycrystalline layers grown on GaAs substrates are studied. The features of charge transport and photoconductivity of $Cd_xHg_{1-x}Te$/CdTe/GaAs structures are discussed. It is established that a high photoconductivity at a temperature of 300 K and a jump in conductivity–illumination characteristics at high levels of excitation are caused by the influence of electrically active grain boundaries, which produce the potential barriers for the drift and recombination of charge carriers. It is shown within the framework of the semiconductor barrier model with a random potential relief pattern that, for high levels of excitation by the radiation pulses of ruby or neodymium lasers, the height of potential barriers at the grain boundaries lowers due to screening by nonequilibrium carriers. *© 2000 MAIK "Nauka/Interperiodica".*

This work studies the possibility of the practical use of polycrystalline $Cd_xHg_{1-x}Te$ (MCT) solid solution growth on alternative GaAs substrates. The high-resistivity ($\rho = 1.9 \times 10^3$ Ω cm) polycrystalline $Cd_{0.8}Hg_{0.2}Te$ layers grown by the method of "evaporation–condensation–diffusion" in the isothermal regime on the structures preliminarily fabricated were the objects under study; these structures included a polycrystalline buffer CdTe layer and a substrate of semiinsulating GaAs (100) with a thickness of ~20 μm and a mean grain size of ~30 μm. The layers had the *n*-type conduction with the effective values of concentrations $n_{eff} = 3.2 \times 10^{13}$ cm^{-3} and electron mobility $\mu_{eff} = 1.05 \times 10^2$ cm^2/(V s) at T = 300 K.

Spectral characteristics of photoconductivity (PC) and conductivity–(illumination intensity) characteristics (the $\Delta\sigma(F)$ curves, where F stands for the photon flux) were studied at temperatures T = 77 and 300 K by standard methods under optical excitation from the MCT-layer side. Measurements of the $\Delta\sigma(F)$ curves and the lifetime of nonequilibrium carriers (the latter was calculated from the curves of photocurrent pulse relaxation) were carried out in a linear regime. The multimode ruby (λ = 0.694 μm) and neodymium (λ = 1.06 μm) lasers operating in the Q-switched regime with pulse duration t = 20 ns were used as the radiation sources. Electrical parameters of the polycrystalline MCT layer were determined by the Van der Pauw method. The structure and absolute value of the component composition x of the solid solution were determined with the use of a Superzond-733 X-ray spectral electron-probe microanalyzer. The experimental results can be summarized as follows.

1. In the range of relatively high temperatures (T = 200–300 K), temperature dependences of electrical conductivity $\sigma(T)$ (Fig. 1, curve *1*) and effective electron concentration $n_{eff}(T)$ (Fig. 1, curve *2*) obey the Arrhenius law with the same activation energy E_{a1} = 112 meV that corresponds to an acceptor complex V_{Cd+Cl} [1]. At lower temperatures (T = 77–200 K), the form of dependence $n_{eff}(T)$ is retained but with a lower activation energy E_{a2} = 30 meV that corresponds to the acceptor level and is apparently related to a thermal ionization of the impurity, and the $\ln\sigma$–$T^{-1/4}$ plot yields a straight line. Such a form of the $\sigma(T)$ dependence is satisfactorily described by the Mott relationship $\sigma(T) = \sigma_0 \times \exp[-(T_0/T)^{1/4}]$ (where σ_0 and T_0 are the constants for a given sample) that is inherent in heavily doped and compensated semiconductors and can be indicative of a hopping mechanism of electrical conduction over the localized states near the Fermi level [2]. These states in polycrystalline MCT layers are apparently produced by extended defects (grain boundaries). However, the hopping conduction in the tails of density of states is usually observed at temperatures lower than 77 K [2–4]. Therefore, it is most probable that the $\sigma(T)$ dependence in the range T = 77–200 K corresponds to the model of hops of variable length [5].

The difference in the behavior of temperature dependence $\sigma(T)$ and $n_{eff}(T)$ at low temperatures can be

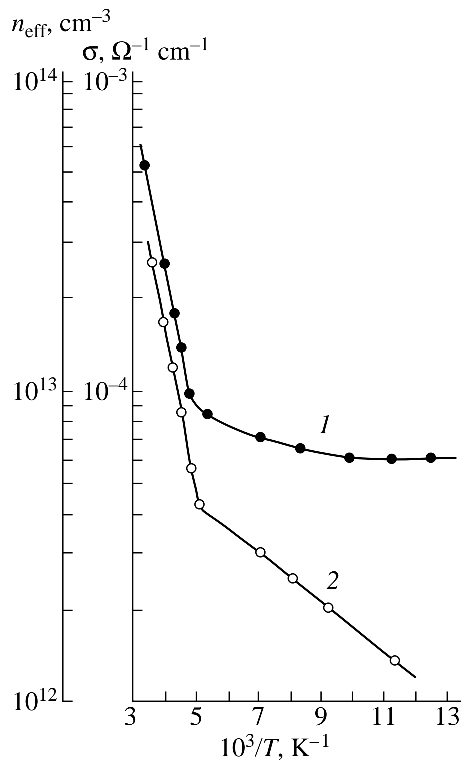

Fig. 1. Temperature dependences of electrical conductivity $\sigma(T)$ (*1*) and effective concentration of electrons $n_{eff}(T)$ (*2*) of polycrystalline $Cd_xHg_{1-x}Te$.

explained by the fact that the effective value of electron concentration determined from the measurements of the Hall coefficient is controlled by the mechanism of current transport throughout the entire volume including a high-resistivity intergrain interface. The electrical conduction is caused by the charge transport over the grains of the polycrystalline MCT layer.

The temperature dependences of mobility $\mu_{eff}(T)$ do not obey the Arrhenius law.

2. Photosensitivity of MCT layers in the spectral range $\lambda = 0.4$–1.6 μm by an order of magnitude compares well in photosensitivity with structurally perfect CdTe and MCT single crystals of the corresponding composition [6–8]. The integrated signal of the PC for the samples at room temperature was larger than that at $T = 77$ K.

3. The $\Delta\sigma(F)$ curves of the layers under study have the slopes of ~1 and ~0.5 (Fig. 2a, curve *1*), which corresponds to the band-to-band generation of nonequilibrium carriers and to the linear recombination (under higher intensities of laser radiation $I > 3 \times 10^{24}$ photon/(cm^2 s), the recombination becomes quadratic). The measurements of PC kinetics showed that, in the entire range of excitation intensities studied, the front of the photocurrent relaxation curves repeats the laser-pulse leading edge, and their decay, the shape of which depended on the sample temperature and radiation intensity, consisted of two regions with characteristic times corresponding to fast and slow recombination channels (Fig. 2a, PC kinetics for curves *1*, *2*). The contribution of the slowly decaying component to the general behavior of photocurrent relaxation decreases with an increase in laser excitation intensity at $T = 77$ K, and, in this case, the relaxation time for this component increases (kinetics of PC for curve *1*). The $\Delta\sigma(F)$ curve for polycrystalline MCT layers at $T = 300$ K has an unusual shape. The slope of the $\Delta\sigma(F)$ curve changes from the value of ~0.5 to ~1 (curve *2*) as the laser pulse intensity increases. In this case, the lifetime of nonequilibrium carriers estimated from the long-term component of the PC pulse decay decreases more than by an order of magnitude. The similar shape of the $\Delta\sigma(F)$ curve is also observed under excitation of PC by nanosecond pulses of the ruby laser radiation. The specificity of the PC kinetics at $T = 300$ K (Fig. 2a, curve *2*), which manifests itself in a sharp increase in the slope of the $\Delta\sigma(F)$ curve for the laser radiation intensities $I = I_\tau \sim 5 \times 10^{23}$ photon/(cm^2 s) and a sharp decrease of nonequilibrium carrier lifetime τ in this case (Fig. 2b) are related to the presence of potential barriers at the grain boundaries of the polycrystalline MCT layer and to their influence on the recombination processes.

The polycrystalline MCT layer that contains macroscopic inhomogeneities (grain boundaries) may be regarded as a semiconductor with a random potential relief pattern $V(r)$ [9]. Such a potential induces a spatial separation of electron–hole pairs generated by light, which results in a sharp increase in the lifetime of nonequilibrium carriers. This fact can explain the presence of slowly decaying components with anomalously large relaxation time constants in the PC kinetics when measuring the $\Delta\sigma(F)$ curve at $T = 77$ K (Fig. 2a, curve *1*) and in the $\Delta\sigma(F)$ curve portion with a slope ~0.5 at $T = 300$ K (curve *2*).

Under illumination of the polycrystalline layer by radiation with energy of quantum $h\nu$ and with intensity I, $\alpha\beta I$ electron–hole pairs are generated in 1 cm^3 for 1 s, where α is the coefficient of interband absorption and β is the quantum efficiency. The pairs are separated by an internal electrical field $E = \nabla V/e$ (e is the elementary charge) and localize in extrema $V(\mathbf{r})$, which are closest to the generation site of the pair. The characteristic time of this process is always shorter than the recombination time τ_r in the absence of spatial separation of electrons and holes.

In the illuminated inhomogeneous semiconductor, the carriers can be regarded as quasi-equilibrium and are characterized by the electron F_e and hole F_h quasi-Fermi levels measured from the edge of corresponding bands. In order for the electron to be at the same point of space with a hole and recombine, it has to overcome the potential barrier with a height $E_\tau = E_g - F_e + F_h$

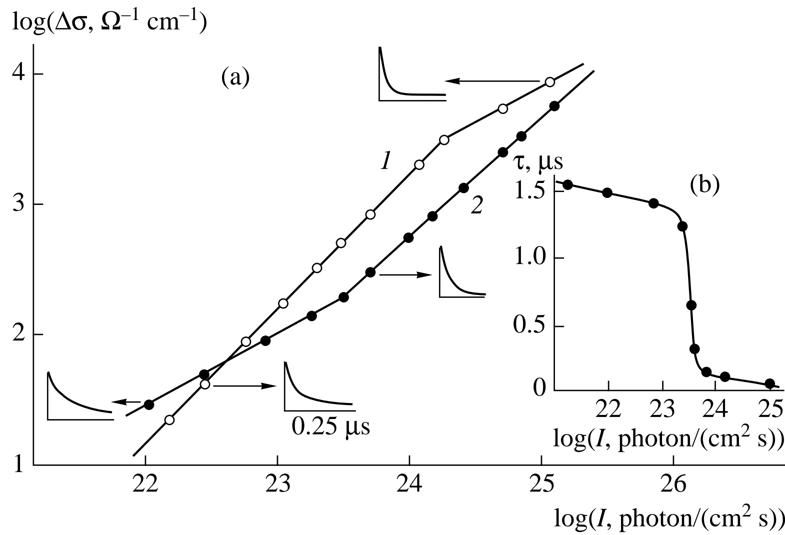

Fig. 2. (a) Lux–ampere characteristics of polycrystalline $Cd_xHg_{1-x}Te$ layers and curves of photoconductivity relaxation under excitation of radiation pulses of a neodymium laser at $T = 77$ (*1*) and 300 K (*2*); (b) dependence of the time-constant of photocurrent relaxation on the intensity of neodymium laser pulses at $T = 300$ K.

(here, E_g is the forbidden band width) [9]. In this case, the nonequilibrium carriers lifetime equals

$$\tau = \tau_r \exp\left(\frac{E_\tau}{kT}\right), \quad (1)$$

and their steady-state concentration is given by

$$\Delta n = \alpha\beta I \tau_r \exp\left(\frac{E_\tau}{kT}\right), \quad (2)$$

where k is the Boltzmann constant.

As follows from (1), the larger the measured lifetime of nonequilibrium charge carriers τ, the higher the potential barrier E_τ at not-too-high temperatures. A slight decrease in the magnitude of the slowly decaying component in the photocurrent relaxation curves with an increase in the laser pulse intensity at $T = 77$ K (Fig. 2a, PC kinetics for curve *1*) observed experimentally is the result of partial lowering of the potential barrier E_τ at high levels of excitation, which is qualitatively consistent with expression (1). At $T = 77$ K, the $\Delta\sigma(F)$ curve of polycrystalline layers has a typical shape for MCT solid solutions of corresponding composition [1]: a linear region transforming under high levels of excitation ($I > 1.3 \times 10^{24}$ photon/(cm^2 s)) into a sublinear one with a slope of ~0.5 (Fig. 2a, curve *1*), which is indicative of the predominant development of recombination processes in the bulk of grains. An inconsistency between the slope of the $\Delta\sigma(F)$ sublinear region (at $T = 77$ K) under a high level of excitation (Fig. 2a, curve *1*) and the above type of recombination indicated (~0.5 instead of the required 0.33 [1]) can be related to the influence of electrically active grain boundaries on the recombination processes due to a lowering of potential barriers owing to their screening by the nonequilibrium carriers.

A different situation is realized under the excitation of the polycrystalline MCT layers under study by laser pulses at $T = 300$ K, when the temperature increase, in contrast to $T = 77$ K, lowers the amplitude of recombination barrier E_τ by 19.2 meV due to thermal activation (which is, however, insufficient to overcome the barrier). The PC dependence on illumination intensity is mainly determined by the nonequilibrium carrier concentration dependence n on the radiation intensity, which in general has the form $\Delta n(I) \sim I^a$, where a depends on the recombination mechanism [1, 2]. Since the quasi-Fermi levels are defined by the carrier concentration, expression (2) specifies the dependence $\Delta n(I)$ in the implicit form. Its characteristics are different under various radiation intensities, and, since

$$\frac{d(F_e - F_h)}{d(\Delta n)} > 0, \quad (3)$$

it is obvious that the dependence $\Delta n(I)$ can have a sublinear ($a < 1$) or, in the limiting case ($d(F_e - F_h)/d(\Delta n) = 0$), a linear ($a = 1$) form. Concentrations of nonequilibrium electrons and holes are assumed to be identical and equal to Δn, and the concentration of equilibrium holes is assumed to be negligibly small as compared to n_0 and Δn, which is usually valid for compensated semiconductors. If, in this case, the condition

$$\alpha\beta I \tau_r \geq \frac{e^6 N^2}{(\varepsilon kT)^3} \quad (4)$$

(where N is the impurity concentration and ε is a dielectric constant) is fulfilled, the screening by nonequilib-

rium carriers lowers the amplitude of recombination potential barrier $V(\mathbf{r})$ to the value of $\sim kT$ [9]. In this case, (2) takes a form characteristic of homogeneous samples:

$$\Delta n = \alpha\beta I\tau_r. \quad (5)$$

In this case, $\alpha = 10^2$ cm^{-1}; $\tau_r = 2 \times 10^{-8}$ s; $N = 3.4 \times 10^{18}$ cm^{-3}; $\varepsilon = 12.52$. In the case of one-photon excitation, β can be assumed as equal to unity, and expression (4) is valid for the laser pulse intensities $I \geq I_\tau$, for which the slope of the $\Delta\sigma(F)$ characteristic (T = 300 K) changes from 0.5 to 1 (Fig. 2a, curve *2*). From expression (5) for $I = I_\tau$, we get $\Delta n = 10^{18}$ cm^{-3}. When calculating expressions (4) and (5), we ignored the change of the sample temperature, which is negligible under the radiation intensities used in experiments. From the condition $F_e + F_h = h\nu - E_g$, which defines the limiting concentration of nonequilibrium carriers (the latter can be attained in a semiconductor under the conditions of one-photon absorption [10] if a neodymium laser $h\nu - E_g = 0.87$ meV is used and the ratio of electron and hole effective masses is $m_e/m_p = 0.2$ [1]), the value of the maximum electron concentration is $\sim 10^{20}$ cm^{-3}. The estimate of Δn from expression (5) shows that the concentration of nonequilibrium carriers attainable under laser excitation intensity $I_\tau < I < 10^{25}$ photon/(cm^2 s) does not exceed the limiting value defined by the Burstein–Moss effect. Therefore, the coefficient of interband absorption α can be assumed to be independent of the concentration of nonequilibrium carriers, and, consequently, of the laser pulse intensity in the range indicated.

The drift potential barriers are low as compared to the recombination barriers, and, consequently, the drift mobility of the nonequilibrium carriers, which determines PC, negligibly changes under illumination [9, 11, 12]. In this case, the quantity that is directly measured experimentally (PC signal J_{PH}) can be considered proportional to the concentration of photogenerated nonequilibrium carriers. In view of (5), the explicit shape of the $\Delta\sigma(F)$ curve is described by a linear dependence on the intensity of the laser pulse radiation

$$J_{PH} \sim \Delta n \sim \Delta\sigma \sim I. \quad (6)$$

Such behavior of the $\Delta\sigma(F)$ curve (with a unit slope $a = 1$) is observed at T = 300 K for intensity $I > I_\tau$ (Fig. 2a, curve *2*). The lowering of the barrier height $V(\mathbf{r})$ to the value of kT for $I \sim I_\tau$ is responsible for the change of the slope of the $\Delta\sigma(F)$ curve from the value of 0.5, caused by bimolecular recombination of nonequilibrium carriers in the grain, to unity, which is characteristic of a homogeneous semiconductor when the recombination proceeds both in the grain and at the grain boundary.

For $I < I_\tau$, the potential barriers significantly affect the PC behavior, with the behavior of the $\Delta\sigma(F)$ curve and the anomalously long lifetime of nonequilibrium carriers verifying the fact mentioned above (Fig. 2a, curve *2*; the PC kinetics, Fig. 2b). It is shown in [9] that, in the case where the condition for the potential barrier

$$E_\tau \sim \frac{e^2 N^{2/3}}{\varepsilon(\Delta n)^{1/3}} \quad (7)$$

is fulfilled and the radiation intensity satisfies the inequality

$$\frac{e^6 N^2}{(\varepsilon kT)^3}\exp\left(-\gamma\frac{E_0}{kT}\right) \leq \alpha\beta I\tau_r \leq \frac{e^6 N^2}{(\varepsilon kT)^3}, \quad (8)$$

expression (2) can be reduced to the form

$$\Delta n \approx N^2\left[\gamma e^2\left(\varepsilon kT\ln\frac{e^6 N^2}{(\varepsilon kT)^3\alpha\beta I\tau_r}\right)^{-1}\right]^3. \quad (9)$$

Here, γ is a numerical factor of the order of unity, and

$$E_0 \sim \frac{e^2 N^{2/3}}{\varepsilon(n_0)^{1/3}}, \quad (10)$$

is the characteristic height of potential barrier $V(\mathbf{r})$ in the absence of illumination, which, for the parameters of the MCT solid solution indicated and the value of the dark electron concentration $n_0 = 3 \times 10^5$ cm^{-3}, is equal to E_0 = 180 meV. Expression (8) is valid for laser radiation intensities 5×10^{20} photon/(cm^2 s) $< I < I_\tau$. Under such an excitation, the concentration of nonequilibrium carriers 10^{15} cm^{-3} $< \Delta n < 10^{18}$ cm^{-3} is produced in the polycrystalline MCT layer; i.e., (8) is valid for the laser-pulse intensity that would produce the concentration of carriers in the above range in the homogeneous sample with the same τ_r values.

Numerical calculation of $\Delta n(I)$ for radiation intensities from the range of values used (5×10^{20} photon/(cm^2 s) $< I < I_\tau$) to satisfy condition (8) shows that the $\Delta\sigma(F)$ curve $J_{PH} \sim \Delta n(I) \sim I^a$, theoretically described by formula (9), is close to the square-root dependence and becomes steeper for intensities close to I_τ. The satisfactory coincidence of the theoretically calculated dependence of PC on the laser pulse intensity and the $\Delta\sigma(F)$ curve measured for $I < I_\tau$ provides evidence in favor of the model of potential barriers at the boundary grains suggested to explain the features of the photoelectrical properties of polycrystalline MCT layers.

REFERENCES

1. A. V. Lubchenko, E. A. Sal'kov, and F. F. Sizov, *Physical Grounds of Semiconductor Infrared Photoelectronics* (Naukova Dumka, Kiev, 1984).
2. V. L. Bonch-Bruevich and S. G. Kalashnikov, *Physics of Semiconductors* (Nauka, Moscow, 1990).

3. B. I. Shklovskiĭ, Fiz. Tekh. Poluprovodn. **7**, 112 (1973) [Sov. Phys. Semicond. **7**, 77 (1973)].

4. E. V. Kuchis, *Galvanomagnetic Effects and Methods of Their Study* (Radio i Svyaz', Moscow, 1990).

5. W. Beyer and H. Overhof, Semicond. Semimet. **21C**, 257 (1984).

6. N. N. Berchenko, V. E. Krevs, and V. G. Shredin, *Semiconducting Solid Solutions and Their Applications* (Voenizdat, Moscow, 1982).

7. C. F. Freeman, J. Vac. Sci. Technol. B **9** (3), 1613 (1991).

8. B. G. Girich and V. M. Lakeenkov, in *News of Sciences and Technics* (Moscow, 1990), No. 3.

9. A. Ya. Shik, Zh. Éksp. Teor. Fiz. **68**, 1859 (1975) [Sov. Phys. JETP **41**, 932 (1975)].

10. G. N. Galkin, Tr. Fiz. Inst. im. P. N. Lebedeva Akad. Nauk SSSR **128** (3) (1981).

11. V. B. Sandomirskiĭ, A. G. Zhdan, M. A. Messerer, *et al.*, Fiz. Tekh. Poluprovodn. **7**, 1314 (1973) [Sov. Phys. Semicond. **7**, 881 (1973)].

12. S. M. Ryvkin, *Photoelectric Effects in Semiconductors* (Fizmatgiz, Moscow, 1963; Consultants Bureau, New York, 1964).

Translated by T. Galkina

Semiconductors, Vol. 34, No. 3, 2000, pp. 260–263. Translated from Fizika i Tekhnika Poluprovodnikov, Vol. 34, No. 3, 2000, pp. 266–269.
Original Russian Text Copyright © 2000 by Gulyamov, Dadamirzaev, Boĭdedaev.

ELECTRONIC AND OPTICAL PROPERTIES OF SEMICONDUCTORS

Kinetics of Attaining the Steady State of Hot Carrier Thermoelectric Power in a *p–n* Junction with Consideration for Lattice Heating

G. Gulyamov, M. G. Dadamirzaev, and S. R. Boĭdedaev
Namangan Engineering-Pedagogical Institute, Namangan, 716003 Uzbekistan
Submitted July 12, 1999; accepted for publication September 22, 1999

Abstract—The lattice heating effect on the kinetics of attaining the steady state of hot carrier thermoelectric power in a *p–n* junction is theoretically studied. It is shown that lattice heating leads to an additional third stage in the process of attaining the steady state in thermal currents and the thermoelectric power of hot carriers with a relaxation time determined by the thermal conductivity and heat capacity of the sample. It is also shown that the relaxation rate of the third stage is lower in comparison with stages I and II observed by Veinger and Sargsyans. © *2000 MAIK "Nauka/Interperiodica".*

The effect of heating an electron–hole gas on the kinetics of attaining the steady state of transient processes in strong microwave fields was studied theoretically and experimentally in [1]. The heating of an electron–hole gas alone leads to two characteristic stages in the relaxation of distribution: a fast stage determined by carrier transit through the *p–n* junction after the removal of the microwave field and a slow stage determined by the redistribution of hot carriers that have passed through a junction. The authors [1] show that the fast stage is independent of the load resistance, while the slow one is not. The heating of the lattice in the experiments [1] was apparently insignificant. However, as is shown in [2], in the steady state, lattice heating can lead to both quantitative and qualitative changes. In particular, a sufficiently high field can reverse the sign of thermoelectric power generated by the *p–n* junction in a strong microwave field. It is known that the application of a heating microwave pulse first heats the electron–hole gas and then, more slowly, heats the lattice [2]. However, the effect of lattice heating on the kinetics of attaining the steady state in thermoelectric power of hot carriers in a *p–n* junction has not been discussed in the literature. The aim of this work is to study the effect of phonon heating on the kinetics of attaining the steady state of hot carrier thermoelectric power in a *p–n* junction in strong microwave fields.

As a result of the action of strongly heating microwave radiation on a sample, the temperature of the carriers reaches its maximum T_e in a time of the order of that for energy relaxation. This value of the electron temperature depends both on the mechanisms of energy and momentum relaxation and on the lattice temperature T_p. Microwave excitation can cause both an increase and decrease in carrier temperature depending on the dissipation and relaxation processes of the energy. The self-consistent change in the temperature of carriers T_e and phonons T_p determines the resulting kinetics of attaining the steady state in hot-carrier thermoelectric power on exposure to strongly heating microwave radiation. An increase in lattice temperature not only has an effect on the temperature of electrons but also strongly affects the generation rate of electron–hole pairs. Thus, a sufficiently long microwave pulse changes the temperature of charge carriers, as well as the charge carrier concentration. As a result, all these processes determine the kinetics of attaining the steady state in the currents and thermoelectric power of hot carriers under the action of a strongly heating microwave pulse. In order to simplify the analysis of the kinetics of attaining an equilibrium state of the currents and voltages, we hereafter assume that the condition for electron temperature approximation is fulfilled [3].

The charge carrier and lattice temperatures are determined by solving the equations of the energy balance of charge carriers and phonons in a microwave field; i.e.,

$$\frac{\partial C_e T_e}{\partial t} + \operatorname{div}\mathbf{Q}_e + \left\langle \frac{dW}{dt} \right\rangle_{ep} = -\mathbf{j}_e \nabla\varphi + P_e, \quad (1)$$

$$\frac{\partial C_h T_h}{\partial t} + \operatorname{div}\mathbf{Q}_h + \left\langle \frac{dW}{dt} \right\rangle_{hp} = -\mathbf{j}_h \nabla\varphi + P_e, \quad (2)$$

$$\frac{\partial C_p T_p}{\partial t} + \operatorname{div}\mathbf{Q}_p + \left\langle \frac{dW}{dt} \right\rangle_{ep} - \left\langle \frac{dW}{dt} \right\rangle_{hp} = 0. \quad (3)$$

Here, $\mathbf{Q}_e$ is the electron energy flux; $\mathbf{Q}_h$ is the hole energy flux; $\mathbf{Q}_p$ is the phonon energy flux; P_e and P_h are the microwave power absorbed by electrons and holes, respectively; $\left\langle \frac{dW}{dt} \right\rangle_{ep,\,hp}$ are the rates of energy losses of electrons or holes scattered by phonons; and $j_{e,\,h}$ are

the electron and hole current densities. The energy fluxes are determined by the following expressions:

$$\mathbf{Q}_e = -\chi_e \nabla T_e + \left(\Pi_e - \frac{\mu_e}{e}\right)\mathbf{j}_e, \quad (4)$$

$$\mathbf{Q}_h = -\chi_h \nabla T_h + \left(\Pi_h - \frac{\mu_h}{e}\right)\mathbf{j}_h, \quad (5)$$

$$\mathbf{Q}_p = -\chi_p \nabla T_p. \quad (6)$$

Here, $\chi_{e,h,p}$ are the electron-, hole-, and phonon-related heat conductivities and $\Pi_{e,h}$ and $\mu_{e,h}$ are the Peltier coefficients and chemical potentials of electrons and holes, respectively. The conditions at the boundaries of the space charge region (see figure) are

$$-\chi_e \frac{dT_e}{dx}\bigg|_{\delta_n} = j_e(\varphi_0 - U). \quad (7)$$

Here, φ_0 is the equilibrium barrier height, and U is the voltage applied to p–n junction. Similar reasoning for a hole gas yields the following boundary condition:

$$-\chi_h \frac{dT_h}{dx}\bigg|_{\delta_n} = j_h(\varphi_0 - U). \quad (8)$$

For a phonon gas, we have

$$-\chi_p \frac{dT_p}{dx}\bigg|_{\delta_n} = \chi_p \frac{dT_p}{dx}\bigg|_{-\delta_p}. \quad (9)$$

If the width of the space charge region is less than the cooling length, the following boundary conditions can be chosen for the carrier and phonon temperatures:

$$T_e(-\delta_p) = T_e(\delta_n), \quad (10)$$

$$T_h(-\delta_p) = T_h(\delta_n), \quad (11)$$

$$T_p(-\delta_p) = T_p(\delta_n). \quad (12)$$

The boundary conditions at the current contacts can be written as

$$-\chi_{e,h} \frac{dT_{e,h}}{dx}\bigg|_{x=\pm a} = \eta_{e,h}(T_{e,h} - T_{1,2})\big|_{x=\pm a}, \quad (13)$$

$$-\chi_p \frac{dT_p}{dx}\bigg|_{x=\pm a} = \eta_p(T_p - T_{1,2})\big|_{x=\pm a}, \quad (14)$$

where $\eta_{e,h}$ is the surface heat conductivity of the electrons or holes [3].

Solving problem (1)–(14) allows one to determine the distribution of the temperatures of charge carriers and phonons under the effect of strongly heating microwave radiation on the p–n junction. The solution to (1)–(14) in the absence of a microwave field was obtained in [4]. In order to study the temperature distribution of carriers and phonons, we have to specify the dissipation mechanisms of the carrier energy at phonons [3].

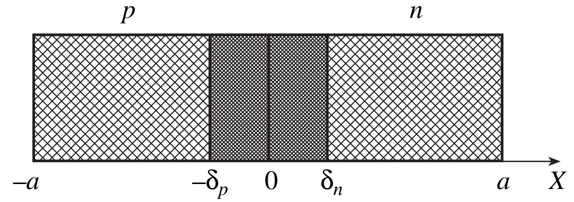

Schematic representation of p–n-junction; $-\delta_p$ and δ_n are the boundaries of the space charge region.

In the case of dissipation of the carrier energy by the deformation mechanism at acoustic phonons, the energy-loss rate $\left\langle \frac{dW}{dt} \right\rangle_{ep}$ can be expressed as [5]

$$\left\langle \frac{dW}{dt} \right\rangle_{ep} = -\frac{\sqrt{2}E_1^2 m^{5/2}}{\pi^{3/2}\hbar^4\rho}(kT_e)^{1/2}\left(1 - \frac{T_p}{T_e}\right), \quad (15)$$

where E_1 is the deformation-potential constant and ρ is the density. If the hot carriers lose their energy in interacting with optical phonons, then

$$\left\langle \frac{dW}{dt} \right\rangle_{ep} = -\frac{\sqrt{2}D^2 m^{5/2}}{\pi^{3/2}\hbar^2\rho}(kT_e)^{1/2} B_0(U_p, U_e), \quad (16)$$

where D is the deformation-potential constant of the optical phonons,

$$B_0(U_p, U_e) = \frac{\exp(U_p - U_e) - 1}{\exp U_p - 1}\exp\left(\frac{U_e}{2}\right)K_1\left(\frac{U_e}{2}\right),$$

$$U_e = \frac{\hbar\omega_0}{kT_e}, \quad U_p = \frac{\hbar\omega_0}{kT_p},$$

ω_0 is the optical-phonon frequency, and $K_1(U_e/2)$ is the second-order Bessel function of the imaginary argument.

To simplify the problem, we assume that the first two terms on the left-hand side of equations (1)–(3) and the first term on the right-hand side may be ignored. Then, equating the power absorbed by the sample and the rate of electron energy loss in interactions with acoustic phonons, we obtain the following expression for the T_e/T_p:

$$\frac{T_e}{T_p} = \begin{cases} \frac{4}{3}\cos^2\left[\frac{1}{3}\arccos\left(\frac{3^{3/2}P}{2a}\right)\right], & \text{if } \frac{P}{a} < \frac{2}{3^{3/2}}, \\ \left[\left(\frac{P}{2a} + \sqrt{\left(\frac{P}{2a}\right)^2 - \frac{1}{27}}\right)^{1/3} + \left(\frac{P}{2a} - \sqrt{\left(\frac{P}{2a}\right)^2 - \frac{1}{27}}\right)^{1/3}\right], & \text{if } \frac{P}{a} > \frac{2}{3^{3/2}}. \end{cases} \quad (17)$$

Here, P is the microwave power, and

$$a = \frac{8\sqrt{2}E_1^2 m^{5/2} n}{\pi^{3/2}\hbar^4\rho}(kT_p)^{3/2} = a_0 T_p^{3/2}. \quad (18)$$

In this solution the lattice temperature T_p varies much more slowly than the carrier temperature T_e. The time dependence of T_p will be determined later from the energy balance equation for phonons.

For the scattering of hot carriers by optical phonons of the deformation potential, when the electron and phonon temperatures satisfy the conditions $h\omega_0 > kT_p$ and $h\omega_0 < kT_e$, we obtain the following expression for the electron temperature:

$$T_e = \frac{\hbar\omega_0}{k}\left(\frac{1}{4}\frac{\mathcal{R}}{1+\frac{1}{4}\ln\frac{4kT}{\hbar\omega_0}}\right)^2, \quad \mathcal{R} = \frac{D^2 m^{3/2}\omega_0 P}{\pi^{3/2}\hbar\rho n}. \quad (19)$$

If $\hbar\omega_0 > kT_p$, the temperature of hot electrons is given by

$$T_e = \frac{\hbar\omega_0}{k\ln\left[\frac{nD^2 m^{3/2}}{2\sqrt{2}P\pi^{3/2}\hbar^2\rho}k^{1/2}(\hbar\omega)^{1/2}\right]}. \quad (20)$$

Hence, it follows that, for the limiting cases considered above, the electron temperature is independent of the lattice temperature and is determined exclusively by the absorbed power. The physical essence of this phenomenon consists in the fact that the probability of phonon emission by electrons at high energies is much higher than the probability of phonon absorption.

The time dependence of the electron temperature is determined by the time dependence of the lattice temperature. In general, the solution to the (1)–(12) system yields this dependence. However, the solution of this system presents some mathematical difficulties. To simplify the problem, let us consider some special cases. We assume that the energy absorbed by the lattice from the system of hot electrons is lost through a lateral surface of the sample. This situation, for example, occurs when a thin plate of the sample is immersed in liquid nitrogen. In this case, the energy balance equation for the lattice takes the form

$$C_p\frac{dT}{dt} = P - \eta_p(T_p - T_0). \quad (21)$$

Here, T_0 is the temperature of the environment; C_p is the lattice heat capacity; and η_p is the surface heat resistance, a phenomenological parameter that accounts for the energy exchange through a lateral surface of the sample.

In the case of absorption of power pulse P with a period of τ and duration t_1, we use equation (21) to obtain the following expression for the lattice temperature:

$$T_p - T_0 = \begin{cases} \frac{P}{\eta_p}\left[1 - \frac{1-\exp\left(\frac{\eta_p}{C_p}(t-\tau)\right)}{1-\exp\left(\frac{\eta_p}{C_p}\tau\right)}\right]\exp\left(-\frac{\eta_p}{C_p}t\right), \\ \text{if} \quad t_0 \le t \le t_0 + t_1, \\ \frac{P}{\eta_p}\left[\frac{1-\exp\left(\frac{\eta_p}{C_p}t\right)}{1-\exp\left(-\frac{\eta_p}{C_p}\tau\right)}\right]\exp\left[\frac{\eta_p}{C_p}(t_1 - t)\right], \\ \text{if} \quad t_0 + t_1 \le t \le t_0 + \tau. \end{cases} \quad (22)$$

It is seen that the process of lattice temperature relaxation occurs with the characteristic time $\tau_T = C_p/\eta_p$; i.e., after the cessation of the microwave pulse, the lattice heating slows down slightly.

Including the explicit form of the temperature dependence of the thermal generation rate $g_{e,h}(T)$ and the recombination rate $R_{e,h}(T)$ of the charge carriers into the continuity equation

$$\frac{dn_{e,h}}{dt} = g_{e,h}(T) - R_{e,h}(T) + e\,\mathrm{div}\,j_{e,h}, \quad (23)$$

we can determine the dependence of the carrier concentration on time t. The most suitable case for the experiment is apparently when the time for increasing the lattice temperature $\tau_T = C_p/\eta_p$ is much longer than the lifetime $\tau_{e,h}$ of the minority carriers. In this case, after completion of the fast and slow stages of relaxation of the thermoelectric power of hot carriers, further change in temperature of the carriers and lattice is determined by the expression

$$U_T = \varphi_0\left(\frac{T_e}{T_0} - 1\right) - \frac{T_e}{T_p}\left(\frac{T_p}{T_0} - 1\right)\frac{E_g}{e}. \quad (24)$$

This expression implies that the ratio T_e/T_p is determined from the simultaneous solutions of the balance equations for electrons and phonons. For example, if the energy and momentum of hot carriers are dissipated at acoustic phonons, then, using (17), one can obtain the following expression for the thermoelectric power of hot carriers:

$$U_T = \varphi_0 \begin{cases} \frac{4}{3}\cos^2\left[\frac{1}{3}\arccos\left(\frac{3^{3/2}P}{2a}\right) - 1\right], \\ \qquad \text{if} \quad \frac{P}{a} > \frac{2}{3^{3/2}}, \\ (A+B)^2, \quad \text{if} \; \frac{P}{a} < \frac{2}{3^{3/2}}, \end{cases} \quad (25)$$

where

$$A = \left(\frac{P}{2a} + \sqrt{\left(\frac{P}{2a}\right)^2 - \frac{1}{27}}\right)^{1/3},$$

$$B = \left(\frac{P}{2a} - \sqrt{\left(\frac{P}{2a}\right)^2 - \frac{1}{27}}\right)^{1/3},$$

with the quantity T_p being determined by expression (22). These formulas imply that the carrier concentration is constant in the bulk of the semiconductor and that they hold when the relaxation time for the energy is longer than the thermal generation time of the carriers. However, if the time constant τ_T of the thermal relaxation is longer than the thermal generation time of the carriers, the increase in lattice temperature alters not only the rate of energy loss of hot electrons but also the concentration of carriers at the diode base. In this case, the variation of thermoelectric power is described by expression (24). The dependence of electron and lattice temperatures are given by (17), (19), and (22).

After the cessation of the heating-power pulse, the relaxation of the current and thermoelectric power of hot carriers occurs. At the onset of this process the *p–n*-junction may be biased in both direct and reverse directions depending on the value of the hot carrier current through the *p–n*-junction. It is clear that the sign of the bias depends on the concentration of minority carriers n_p remaining in the base after cessation of the heating pulse: If n_p is larger than the equilibrium concentration of the minority carriers n_{p0}, the relaxation of thermoelectric power begins with the forward bias, but if $n_p < n_{p0}$, relaxation begins with the reverse bias and the thermoelectric power of hot carriers will relax owing to the temperature change. This relaxation is caused not only by the redistribution of the injected charge carriers but also by the usual thermoelectric power of *p–n* junction due to lattice heating. In the latter case, the thermoelectric power varies according to the same laws as for the lattice temperature. It is noteworthy that the lifetime of minority carriers drastically decreases with lattice heating. This makes the slow stage of thermoelectric-power relaxation faster.

Thus, the pulsed regime the lattice heating causes additional relaxation of the thermoelectric power of hot carriers with a characteristic time determined by the constant of the thermal relaxation of the diode.

REFERENCES

1. A. I. Veĭnger and M. P. Sargsyan, Fiz. Tekh. Poluprovodn. (Leningrad) **14** (12), 2366 (1980) [Sov. Phys. Semicond. **14**, 1402 (1980)].
2. G. Gulyamov and S. Kh. Shamirzaev, Fiz. Tekh. Poluprovodn. (Leningrad) **15** (9), 1858 (1981) [Sov. Phys. Semicond. **15**, 1082 (1981)].
3. F. G. Bass, V. S. Bochkov, and Yu. G. Gurevich, *Electrons and Phonons in Bounded Semiconductors* [in Russian] (Nauka, Moscow, 1989).
4. G. Gulyamov and K. B. Umarov, Fiz. Tekh. Poluprovodn. (St. Petersburg) **29** (1), 33 (1995) [Semiconductors **29**, 17 (1995)].
5. E. M. Conwell, in *Solid State Physics*, Suppl. 9 (Academic, New York, 1967; Mir, Moscow, 1970).

Translated by A. Zalesskiĭ

Semiconductors, Vol. 34, No. 3, 2000, pp. 264–268. Translated from Fizika i Tekhnika Poluprovodnikov, Vol. 34, No. 3, 2000, pp. 270–274.
Original Russian Text Copyright © 2000 by Onopko, Ryskin.

ELECTRONIC AND OPTICAL PROPERTIES OF SEMICONDUCTORS

Structure of the Metastable Centers of the Group-III Atoms in IV–VI Crystals

D. E. Onopko and A. I. Ryskin

Vavilov State Optical Institute, All-Russia Research Center, ul. Babushkina 36/1, St. Petersburg, 194018 Russia

Submitted July 19, 1999; accepted for publication September 23, 1999

Abstract—A comparative analysis of reconstruction of the metastable impurity centers in tetrahedral (III–V and II–VI) and cubic (IV–VI) crystals is performed for the case where the charge of the center changes. The influence of the chemical structure of the crystal matrix on the nature of defect reconstruction is studied on the basis of cluster approximation. For the IV–VI:III centers, the fundamental significance of the three-center crystal bonds and the specific role of the antibonding (weakly bonding) $3a_{1g}$ state, which has the properties of both the impurity and perturbed crystal states simultaneously, are emphasized. © *2000 MAIK "Nauka/Interperiodica".*

Among the metastable impurity centers in semiconductor crystals, defects whose structure is modified while the charge of the center is varied, occupy a special place. The nature of this reconstruction in III–V and II–VI tetrahedral crystals with the sphalerite structure [1–3] differs from IV–VI cubic crystals with the NaCl structure doped with elements of Group III [4, 5]. The problem of impurity centers in III–V and II–VI compounds [6–12] was investigated in detail, but data are almost absent for IV–VI:III crystals. In this work, we analyze the aforementioned problem by the example of PbTe.

We used the cluster approximation. Boundary conditions were taken into account according to a method [13] which has proved to be effective in studying the electron structure of different crystals, both intrinsic and extrinsic [14]. All calculations have been performed using the self-consistent scattered-wave technique [15] within the context of the smallest AB_n^{Q-} cluster approximation ($n = 6$ is the number of the nearest neighbors). The total charge Q of a cluster is determined by the iteration method in the self-consistent solution procedure. It is assumed that the value of the charge does not change significantly in the course of doping.

In the scattered-wave method, the space occupied by a cluster (molecule) is divided into three types of regions: atomic spheres with centers at the cluster atoms; an external region, i.e., the region outside of a large sphere, including all atomic spheres; and an interatomic region located between the large and atomic spheres. All selected spheres touch each other. In each region, the specific model potential and the appropriate molecular-orbital expansion method are used. The existence of the orbital charge in the atomic spheres of the different cluster atoms and in the interatomic region is indicative of the covalent character of the bond realized in the molecular orbital between these atoms. If one of the conditions is not fulfilled, the orbital has an ionic (atomic) nature.

In intrinsic tetrahedral crystals, each atom is linked by four sp^3-hybridized bonds to its nearest neighbors. These bonds are two-center; in other words, the electron density is mostly localized between the interacting atoms. The bonding orbitals determine the valence band, and the antibonding orbitals determine the conduction band. Ionic–covalent interaction between the cation and anion in these crystals is quite strong; and, as a consequence, the bond energy and the energy gap are usually rather large.

If a cation or an anion in III–V and II–VI crystals are replaced by atoms from the neighboring Groups, shallow delocalized donor or acceptor states appear in the energy gap. The behavior of the impurity is determined by the relative position of the dopant and substituted atoms in the periodic system, that is, by the variation in the valence electron number when the defect is formed.

The results of electron-structure calculations for intrinsic PbTe and doped PbTe:M (M = Ga and In) crystals (clusters AB_6^{Q-}) are presented in the table. The chemical bonding in PbTe [the electron structure of the valence shells of Pb ($6s^26p^2$) and Te ($5s^25p^4$)] is mostly covalent: The magnitude of the charge of the relevant ions is about $0.05e$ ($Q = 0.25$e). The main contribution to the bond energy is determined by the interaction of the Pb and Te p electrons ($2t_{1u}$ orbital); the $5d$ ($6d$) functions of Pb ($3e_g$) also give a small contribution. The contribution of the deep valence s shells of Pb and Te is insignificant. This conclusion for $2e_g$ and $1t_{1u}$ states is based on the character of the charge-distribution: These orbitals are nearly completely determined by the $5s$ functions of Te. Three $1a_{1g}$, $2a_{1g}$ and $3a_{1g}$ orbitals appear as a result of interaction of three atomic func-

tions (6*s* Pb, 5*s* and 5*p* Te); therefore, only the addition of the excited states (7*s* Pb, 6*s* and 5*d* Te) can neutralize the antibonding influence of the last occupied $3a_{1g}$ state and provide an insignificant summary bonding effect to these orbitals. The $3a_{1g}$ state is localized mostly inside the $PbTe_6^{Q-}$ cluster; therefore, the influence of farther coordination shells does not change the situation. Thus, the antibonding (or weakly bonding) $3a_{1g}$ state can be regarded as a typical state near the valence-band maximum of a IV–VI crystal. This agrees with the narrow-band nature of these types of crystals. It is noteworthy that, in the III–V and II–VI compounds, similar states are bonding.

The results of the electron-band calculations [16] confirm the passive role of *s* shells in the chemical bond formation of these compounds. The valence *p* band is separated by the energy gap from the underlying cation and anion *s* bands (1.5–5 eV for PbTe).

Therefore, in the IV–VI crystals, there are only six electrons that participate in forming six atomic bonds with the nearest neighbors; that is, there is a deficit of electrons in these compounds. As a result, two-electron bonds have a three-center character in these crystals. The electron density of these bonds is equally distributed between three atoms and causes a decrease in the bonding energy and in the energy gap.

Replacement of Pb by the Group III (Al, Ga, In and Tl) atoms [the electron structure of the valence shells is $ns^2(n+1)p^1$] does not affect the PbTe chemical bond (see table); i.e., the three-center character of the interatomic bonds is maintained. However, because of an increase in the energy gap between the *p*-electron states of the impurities and ligands, the bonding role of the central-atom *p* states is diminished. At the same time, due to partial filling of the antibonding $3a_{1g}$ state, the influence of the impurity atom *s* shell increases significantly in contrast to the intrinsic PbTe crystal.

The wave function of the $3a_{1g}$ state is rather strongly localized at the impurity atom (see table). As a result, one may regard the impurity level as a deep level [4, 5]. The existence of only one electron in the $3a_{1g}$ state determines its double role in the formation of the impurity-center chemical bond. Due to the weak bonding energy, this level can easily accept and also easily give away electrons; that is, it acts as both acceptor and donor. The impurity states in the III–V and II–VI crystals do not have these properties.

Due to the strong localization of the $3a_{1g}$ level at the impurity in the narrow-gap IV–VI crystals, this level, depending on the specific III Group impurity, may occur in both the bandgap and the bands (conduction and valence) of the crystal [4, 5]. When this level is located in an allowed band, the cases where the chemical potential is determined by this level are of the most interest; that is, pinning of the Fermi level takes place. Different charged states of the center are probable only in this case. In [17], the authors attempted to relate the impurity-level position to the ionization potential of the free atoms and the interaction of the impurity with the crystal. Variation of the impurity-level position with respect to the band edges is realized in solid solutions (such as $Pb_{1-x}Sn_xTe$) due to the variation of the energy-band edges at a fixed impurity level position in the energy spectrum.

In III–V and II–VI crystals and solid solutions of these compounds, the donor impurities may form negatively charged *DX* centers, which causes self-compensation of the sample according to the reaction

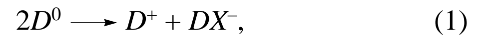

$$2D^0 \longrightarrow D^+ + DX^-, \quad (1)$$

where *D* is a tetrahedrally symmetric defect. Reaction (1) is exothermic if *DX*-center formation is accompanied by a large lattice relaxation, which can compensate for energetically unfavorable localization of two electrons at the same orbital; i.e., the relaxation determines the negative correlation energy of the defect. If a tetrahedral center with two-center chemical bonds has two additional electrons, lattice relaxation leads to the breaking of one or two bonds. As a result, the defect symmetry is reduced to the C_{3v} trigonal or C_{2v} orthorhombic [6, 7, 9–12] symmetries. Such center reconstruction occurs if the *DX* level becomes much deeper than the original hydrogen-like state.

In acceptor centers in III–V and II–VI crystals, the additional electron, in contrast, stabilizes the tetrahedral defect symmetry, restoring the electron structure of the crystal matrix.

If the donor impurity center in III–V and II–VI crystals loses the antibonding electron, the electron structure of the defect becomes quite stable and preserves the lattice site symmetry. In contrast, in an acceptor center, the additional loss of the bonding electron causes an increase in the deviation from the electron structure of the intrinsic crystal. As a result, the probability of defect reconstruction increases. In particular, for $ZnSe:P^+$ and $ZnSe:As^+$, defect symmetry is reduced to the C_{3v} trigonal one [8].

As noted above, the weakly bonding impurity state $3a_{1g}$ in IV–VI:III crystals is determined by the wave functions of the dopant atom. Therefore, reconstruction processes where an additional electron is attached [in accordance with reaction (1)] would develop regardless of the level position in the energy spectrum of the crystal.

If we consider the IV–VI:III impurity center to be a donor and, correspondingly, the $3a_{1g}$ state to be the impurity state, then the attachment of an additional electron to the center, that is, the appearance of two excess electrons to form a chemical bond, will very likely lead to significant reconstruction of the defect, by analogy with the donor centers in III–V and II–VI compounds. At the same time, the additional electron to a large extent restores the electron structure of the crystal matrix; to put it differently, the occupied $3a_{1g}$ state may be considered a perturbed state of the intrinsic crystal.

Charge distribution at the valence orbitals in PbTe, PbTe:Ga, and PbTe:In crystals (AB_6^{Q-} clusters)

Crystal	Γ	–ε(Ry)	q_A	q_B	q_{II}	q_{III}
PbTe	$4t_{1u}$	0.133				
	$3a_{1g}$	0.359	0.177	0.650	0.155	0.018
	$3e_g$	0.431	0.031	0.770	0.157	0.042
	$1t_{1g}$	0.432	0.004	0.752	0.242	0.002
	$3t_{1u}$	0.446	0.023	0.703	0.251	0.023
	$1t_{2u}$	0.449	0.002	0.710	0.270	0.018
	$2t_{2g}$	0.485	0.005	0.640	0.336	0.019
	$2t_{1u}$	0.541	0.191	0.522	0.260	0.027
	$2a_{1g}$	0.827	0.613	0.242	0.140	0.005
	$2e_g$ (5*s* Te)	1.050	0.005	0.885	0.102	0.008
	$1t_{1u}$ (5*s* Te)	1.061	0.013	0.864	0.114	0.009
	$1a_{1g}$ (5s Te)	1.095	0.103	0.746	0.147	0.004
	$1t_{2g}$ (5*d* Pb)	1.912	0.995	0.0	0.005	0.0
	$1e_g$ (5*d* Pb)	1.913	0.995	0.001	0.004	0.0
PbTe:Ga	$4a_{1g}$	0.094				
	$3a_{1g}$	0.358	0.194	0.636	0.151	0.019
	$1t_{1g}$	0.413	0.003	0.757	0.239	0.001
	$3e_g$	0.414	0.030	0.770	0.156	0.044
	$3t_{1u}$	0.425	0.028	0.712	0.235	0.025
	$1t_{2u}$	0.430	0.001	0.714	0.267	0.018
	$2t_{2g}$	0.466	0.005	0.643	0.333	0.019
	$2t_{1u}$	0.501	0.142	0.566	0.263	0.029
	$2a_{1g}$	0.764	0.677	0.191	0.128	0.004
	$2e_g$ (5*s* Te)	1.035	0.005	0.886	0.101	0.008
	$1t_{1u}$ (5*s* Te)	1.043	0.010	0.870	0.111	0.009
	$1a_{1g}$ (5s Te)	1.067	0.061	0.799	0.136	0.004
	$1t_{2g}$ (3*d* Ga)	1.553	0.999	0.0	0.001	0.0
	$1e_g$ (3*d* Ga)	0.554	0.998	0.001	0.001	0.0
PbTe:In	$4a_{1g}$	0.102				
	$3a_{1g}$	0.325	0.275	0.572	0.137	0.016
	$3e_g$	0.426	0.029	0.773	0.156	0.042
	$1t_{1g}$	0.428	0.004	0.755	0.240	0.001
	$3t_{1u}$	0.439	0.024	0.715	0.236	0.025
	$1t_{2u}$	0.445	0.001	0.713	0.268	0.018
	$2t_{2g}$	0.480	0.005	0.643	0.333	0.019
	$2t_{1u}$	0.515	0.125	0.577	0.268	0.029
	$2a_{1g}$	0.723	0.563	0.254	0.177	0.006
	$2e_g$ (5*s* Te)	1.047	0.006	0.885	0.101	0.008
	$1t_{1u}$ (5*s* Te)	1.057	0.010	0.869	0.112	0.009
	$1a_{1g}$ (5s Te)	1.080	0.049	0.809	0.138	0.004
	$1t_{2g}$ (4*d* In)	1.575	0.995	0.0	0.005	0.0
	$1e_g$ (4*d* In)	1.576	0.993	0.003	0.004	0.0

Note: Γ is the irreducible representation according to which the orbital is transformed; ε is the orbital energy; and q_A, q_B, q_{II}, and q_{III} are parts of the orbital charge in the central atomic sphere, ligand spheres, and interatomic and outer regions, respectively. In the PbTe crystal, the $4t_{1u}$ level is not occupied; in the PbTe:M (M = Ga or In) crystal, the $4a_{1g}$ level is not occupied.

Such variations are typical of negatively charged acceptor centers, and, again by analogy with similar defects in III–V and II–VI compounds, they promote stabilization of the center and preservation of its cubic symmetry. The inconsistency of the above situation is determined by the double role of the antibonding $3a_{1g}$ state as both the impurity and the perturbed state of the crystal matrix. The three-center character of the chemical bonds in the IV–VI compounds, that is, the possibility of significant electron-charge redistribution over these bonds (high lattice polarizability), brings about both donor and acceptor types of reconstruction, although in a modified form. The additional electron at the $3a_{1g}$ orbital leads to displacement of the valence p electrons of the impurity center into the regions of the bonds belonging to the first and second neighbors of the dopant atom. This break in the symmetric charge distribution between atoms with three-center bonds leads to an increase in the distances between the central atom and ligands and a decrease in these distances between the first and second neighbors. Similar alternating variations of the interatomic distances will also take place, although to a lesser extent, for succeeding coordination shells. The direct consequence of such reconstruction of the IV–VI:III center is preservation of its cubic symmetry.

However, the above consideration gives no way of deducing whether the capture of the additional electron by the IV–VI:III center is energetically favorable; i.e., it is not clear whether this center has negative correlation energy. The gain in energy as a result of the reconstruction described above makes the assumption that the defect under consideration has negative correlation energy quite credible. For IV–VI:III crystals, realization of reaction (1) is indicative of impurity-center self-compensation only if the corresponding impurity level is located in the energy gap.

We have a twofold situation in IV–VI crystals both for the positively charged IV–VI:III$^+$ centers and for the negatively charged centers described above. The loss of the impurity-level $3a_{1g}$ electron by the donor center, similar to the defects in III–V and II–VI compounds, should stabilize the center. However, in this case, the $3a_{1g}$ state is empty, and the distinction from the electron structure of a IV–VI crystal is sharpest if we regard this state as crystalline. This structure corresponds to an ionized acceptor center; therefore, conversely, there is a high probability that this defect is reconstructed. As in the case of the negatively charged IV–VI:III$^-$ center, this phenomenon is related to the twofold character of the $3a_{1g}$ state. The three-center character of the chemical bonds in IV–VI compounds allows us to reconcile the conflicting tendencies. The positive charge of the impurity atom (with respect to the substituted lattice ion) is conducive to displacement of the electron charge of the chemical bonds into the region between the impurity atom and ligands and to a decrease in this charge between the atoms of the first and second coordination spheres. As a result, the distances between the center atom and ligands decrease but increase between the first and second neighbors. The alternating character of the interatomic-distance variation is retained (although damped) for succeeding coordination shells. Thus, atom displacements in the vicinity of the positively charged center are opposite to the displacement of the negatively charged defect. The cubic symmetry of the impurity center, as in the case of IV–VI:III$^-$ compounds, is not distorted.

At present, it is established that the correlation energy of the IV–VI:III impurity centers is negative [5, 18, 19]. The experimental verification of this is the absence of paramagnetism in the ground state of these centers. Paramagnetism is observed only during the transition of the IV–VI:III center into the metastable state with one electron at the impurity level [4, 5].

The authors [5] conclude that the charged (positively or negatively) IV–VI:III impurity center has cubic symmetry. On the basis of infrared reflection spectra [20, 21] and Raman spectra [22], they conclude that the structure of the defect in the neutral state is distorted: The impurity atom is displaced from the center of symmetry. This distortion seems to be quite natural in the context of the above model: The existence of one excess electron at the neutral center, which is not sufficient for totally symmetric pushing apart the ligands, should displace the impurity. The existence of potential barriers between the various charged states of the impurity center now becomes clear. It is significant variations of the chemical bond character during reconstruction that gives rise to the barriers. The existence of the barriers in particular explains the persistent-photoconductivity phenomenon in IV–VI:III crystals [4, 5].

As a result of this analysis, we conclude that the structure of metastable cation centers in IV–VI:III crystals is determined by the three-center character of the chemical bonds in the crystal matrix and by the twofold role of the $3a_{1g}$ antibonding state, which represents impurity and distorted crystal states simultaneously. These factors are responsible for the significant distinction between the properties of the above defects and those of classical metastable centers in III–V and II–VI crystals.

REFERENCES

1. P. M. Mooney, J. Appl. Phys. **67**, R1 (1990).
2. R. K. Watts, W. C. Holton, and M. de Wit, Phys. Rev. B: Condens. Matter **3**, 404 (1971).
3. A. R. Reinberg, W. C. Holton, M. de Wit, *et al.*, Phys. Rev. B: Condens. Matter **3**, 4 (1971).
4. V. I. Kaĭdanov and Yu. I. Ravich, Usp. Fiz. Nauk **145**, 51 (1985).
5. D. R. Khokhlov and B. A. Volkov, in *The Physics of Semiconductors*, Ed. by M. Scheffler and R. Zimmermann (World Scientific, Singapore, 1996), Vol. 4, pp. 2941–2948.

6. J. Dabrowdsi and M. Scheffler, Mater. Sci. Forum **83–87**, 735 (1992).
7. D. J. Chadi and K. J. Chang, Phys. Rev. B: Condens. Matter **39**, 10063 (1989).
8. D. J. Chadi and K. J. Chang, Appl. Phys. Lett. **55**, 575 (1989).
9. D. J. Chadi, Phys. Rev. Lett. **72**, 534 (1994).
10. D. J. Chadi and C. H. Park, Mater. Sci. Forum **196–201**, 285 (1995).
11. D. E. Onopko and A. I. Ryskin, Phys. Lett. A **208**, 244 (1995).
12. D. E. Onopko, N. T. Bagraev, and A. I. Ryskin, Fiz. Tekh. Poluprovodn. (St. Petersburg) **31**, 1310 (1997) [Semicond. **31**, 1128 (1997)].
13. D. E. Onopko and L. M. Mogileva, Fiz. Tverd. Tela (Leningrad) **26**, 3483 (1984) [Sov. Phys. Solid State **26**, 2097 (1984)].
14. D. E. Onopko, N. T. Bagraev, and A. I. Ryskin, Fiz. Tverd. Tela (St. Petersburg) **37**, 2376 (1995) [Phys. Solid State **37**, 1299 (1995)].
15. K. H. Johnson, Adv. Quantum Chem. **7**, 143 (1973).
16. G. Martínez, M. Schlüter, and M. L. Cohen, Phys. Rev. B: Condens. Matter **11**, 651 (1975).
17. K. Weiser, Phys. Rev. B: Condens. Matter **23**, 2741 (1981).
18. I. A. Drabkin and B. Ya. Moĭzhes, Fiz. Tekh. Poluprovodn. (Leningrad) **15**, 625 (1981) [Sov. Phys. Semicond. **15**, 357 (1981)].
19. I. A. Drabkin and B. Ya. Moĭzhes, Fiz. Tekh. Poluprovodn. (Leningrad) **17**, 969 (1983) [Sov. Phys. Semicond. **17**, 611 (1983)].
20. N. Romcevic, Z. V. Popovic, D. R. Khokhlov, *et al.*, Phys. Rev. B: Condens. Matter **43**, 6712 (1991).
21. A. I. Belogorokhov, S. A. Belokon’, I. I. Ivanchik, *et al.*, Fiz. Tverd. Tela (St. Petersburg) **34**, 2966 (1992) [Sov. Phys. Solid State **34**, 1592 (1992)].
22. N. Romcevic, Z. V. Popovic, and D. R. Khokhlov, J. Phys.: Condens. Matter **7**, 5105 (1995).

Translated by I. Kucherenko

Semiconductors, Vol. 34, No. 3, 2000, pp. 269–271. Translated from Fizika i Tekhnika Poluprovodnikov, Vol. 34, No. 3, 2000, pp. 275–277.
Original Russian Text Copyright © 2000 by Nasredinov, N. Seregin, P. Seregin, Bondarevskiĭ.

ELECTRONIC AND OPTICAL PROPERTIES OF SEMICONDUCTORS

A Mössbauer Study of a Two-Electron Acceptor Impurity of Zinc in Silicon

F. S. Nasredinov, N. P. Seregin, P. P. Seregin, and S. I. Bondarevskiĭ

St. Petersburg State Technical University, ul. Politekhnicheskaya 29, St. Petersburg, 195251 Russia

Submitted September 20, 1999; accepted for publication October 12, 1999

Abstract—Mössbauer emission spectroscopy of the $^{67}Ga(^{67}Zn)$ isotope was used to show that the two-electron acceptor impurity of Zn is present in silicon only in the form of neutral (Zn^0) or doubly ionized (Zn^{2-}) centers, depending on the Fermi-level position. Broadening of the spectra corresponding to the above centers indicates that the local symmetry of these centers is not cubic. The absence of the line corresponding to the singly ionized state (Zn^{2-}) of zinc in the Mössbauer spectra of partially compensated samples is regarded as evidence that the correlation energy is negative. © *2000 MAIK "Nauka/Interperiodica".*

Impurity atoms of zinc act as acceptors in silicon and form two deep acceptor levels in the forbidden band [1, 2]. It is assumed that zinc diffuses over interstitial sites at high temperatures and that, if the sample is cooled, predominantly occupies lattice sites, with the concentration of electrically active zinc virtually coinciding with the overall zinc concentration [1]. It is presumed that impurity atoms of zinc in silicon give rise to two-electron acceptor centers with ionization energies of $E_1 \sim 0.31$ eV [the process (0 / –) and $E_2 \sim 0.55$ eV [the process (– / – –)] [2]; thus, depending on the Fermi-level position, zinc can be found in the following three charge states: neutral (Zn^0), singly charged (Zn^-), and doubly charged (Zn^{2-}).

The first attempts to detect the electron paramagnetic resonance (EPR) of Zn^- paramagnetic centers in silicon were unsuccessful [3]. In [4], these centers were assigned the EPR spectrum measured in silicon samples doped with zinc and subjected to uniaxial compression. However, the spectra were not completely identified. Subsequently, two EPR spectra were detected in silicon doped with zinc [5]; these spectra were measured only in high-resistivity *p*-type samples exposed to illumination with white light. One of these spectra was related to Zn^- centers with orthorhombic symmetry [6]. In connection with this behavior of the EPR spectra, it was assumed that the two-electron acceptor Zn center had a negative correlation energy U: The sequence of levels of these centers is inverted [for the processes (0 / –) and (– / – –), and the thermal-ionization energies are equal to $E_1 = 0.316$ eV and $E_2 = 0.167$ eV, respectively]. The Zn^{2-}, Zn^-, and Zn^0 centers occupy different sites in the silicon lattice (they are substitutional centers that are somewhat displaced with respect to the unperturbed lattice site; as a result, the symmetries of these centers correspond to C_{3V}, C_{2V}, and D_{2d}, respectively); and due to the negative sign of U, the Zn^- center is unstable and decomposes spontaneously according to the reaction $2Zn^- \longrightarrow Zn^0 + Zn^{2-}$ [6, 7].

It is obvious that, in order to choose between two possible models of acceptor zinc impurity in silicon (i.e., between $U > 0$ [2] and $U < 0$ [6, 7]), we have to identify the Zn^0 and Zn^{2-} centers, determine the symmetry of their local surroundings, and experimentally determine the ratios of concentrations of these centers in relation to the position of the Fermi level. In this connection, it is considered highly desirable to study the behavior of zinc impurity atoms by emission Mössbauer spectroscopy using the $^{67}Ga(^{67}Zn)$ isotope. Diffusion introduction of ^{67}Ga isotope into silicon ensures that both the parent (^{67}Ga) and daughter (^{67}Zn) atoms occupy the substitutional sites; variation of the charge-carrier concentration in the original samples makes it possible to control the Fermi-level position and thus obtain a material with the desired ratios of charge states of zinc; and the parameters of Mössbauer spectra of ^{67}Zn allow one to reliably determine the charge (electron) state of zinc atoms, the symmetry of their local surroundings, and the ratio of concentrations of different charge states of zinc.

The radioactive ^{67}Ga isotope was obtained by the reactions $^{67}Zn(p, n)^{67}Ga$ and $^{66}Zn(d, n)^{67}Ga$ with subsequent chromatographic separation of noncarrying agents. Silicon was doped with ^{67}Ga by gas-phase diffusion in evacuated quartz ampules for 5 h at 1320°C, unless otherwise specified (the penetration depth was ~1.5 μm, and the near-surface gallium concentration was no higher than 5×10^{14} cm^{-3}). The following three samples (A, B, and C) were obtained:

Sample A: The starting silicon crystal was *p*-type (the background impurity was boron, with $p = 2 \times 10^{16}$ cm^{-3}); diffusion doping with gallium did not affect either the type of electrical conductivity or the concentration of charge carriers; and according to [2, 7], the

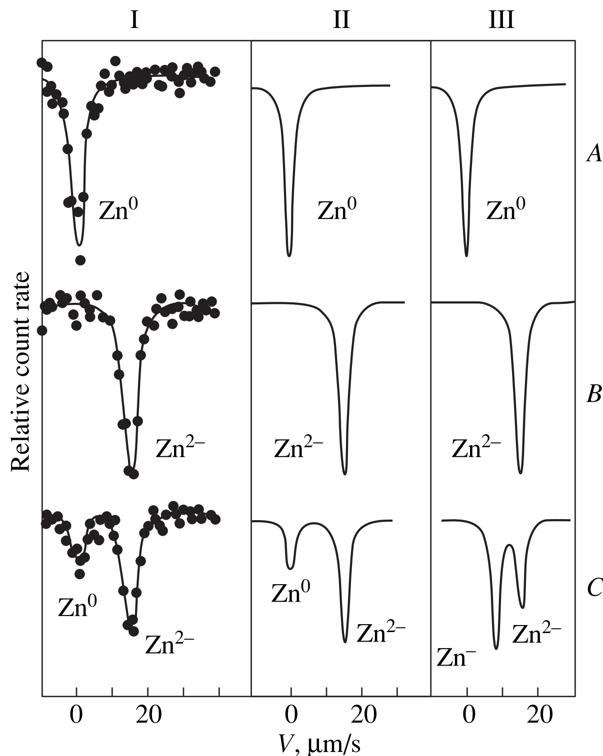

I. Emission Mössbauer spectra of $^{67}Ga(^{67}Zn)$ impurity atoms in silicon at 4.2 K for sample *A* (the spectrum corresponds to Zn^0 centers), sample *B* (the spectrum corresponds to Zn^{2-} centers), and sample *C* (the spectrum corresponds to the presence of both Zn^0 and Zn^{2-} centers). II. Calculated Mössbauer spectra of ^{67}Zn for samples *A*, *B*, and *C* for $U < 0$. The spectral lines corresponding to the Zn^0 and Zn^{2-} centers are indicated. III. Calculated Mössbauer spectra of ^{67}Zn for samples *A*, *B*, and *C* for $U > 0$. The spectral lines corresponding to the Zn^0, Zn^-, and Zn^{2-} centers are indicated. The velocity scale for all spectra is adjusted to that of the spectrum of sample *A*.

Fermi level was located near the top of the valence band and all the zinc centers were in the Zn^0 state.

Sample *B*: The starting silicon crystal was *n*-type (the background impurity was phosphorus, with $n = 2 \times 10^{16}$ cm^{-3}); diffusion doping with gallium did not affect either the type of electrical conductivity or the concentration of charge carriers; and according to [2, 7], the Fermi level was located near the bottom of the conduction band and all the zinc centers were in the Zn^{2-} state.

Sample *C*: The starting silicon crystal was *n*-type (the background impurity was phosphorus, with $n = 2 \times 10^{16}$ cm^{-3}). The sample was initially doped with zinc (by gas-phase diffusion in evacuated quartz ampules for 60 h at 1080°C with subsequent removal of a near-surface layer about 0.1 mm thick, so that the zinc concentration in the sample was 1.5×10^{16} cm^{-3} [2]); as a result, the low-resistivity (~0.3 Ω cm) starting sample acquired high resistivity (~10^4 Ω cm) without changing the type of conductivity. The sample was then doped with gallium, which did not affect either the type of conductivity or the concentration of charge carriers, and according to [2], the Fermi level was located near the level $E_1 = 0.55$ eV, so that the zinc centers were predominantly in the Zn^- state, whereas, according to [7], the Fermi level was located between the levels $E_1 = 0.316$ eV and $E_2 = 0.167$ eV and the zinc centers were in the Zn^0 and Zn^{2-} states.

The Mössbauer spectra of $^{67}Ga(^{67}Zn)$ were measured at 4.2 K using a ^{67}ZnS absorber with a surface density of 1000 mg cm^{-2} with respect to the ^{67}Zn isotope. The spectra of samples *A* (spectrum *A*) and *B* (spectrum *B*) consisted of single lines, with the transition from the *p*- to *n*-type sample resulting in a shift of the spectrum's centroid *S* to higher velocities (see figure, column I). Obviously, spectrum *A* corresponds to neutral centers ($^{67}Zn^0$), whereas spectrum *B* corresponds to doubly ionized centers ($^{67}Zn^{2-}$). For identical measurement temperatures, the quantity *S* is given by

$$S = -(9/16)(k\Delta\theta/Mc^2) + \alpha\Delta\rho(0),$$

where *k* is the Boltzmann constant, *M* is the mass of the probe nucleus, *c* is the speed of light in vacuum, $\Delta\theta$ is the difference in the Debye temperatures of the two samples, α is the calibration constant, and $\Delta\rho(0)$ is the difference in relativistic electron-charge densities at ^{67}Zn nuclei in the two samples.

The first term in the above expression describes the effect of the second-order Doppler shift and, since both spectra are related to Zn impurity atoms in the Si matrix, can be ignored. The second term accounts for the isomer shift that emerges as a result of the difference in electron density at ^{67}Zn nuclei in the two samples. An increase in *S* during the transition from Zn^0 to Zn^{2-} indicates an increase in electron density at ^{67}Zn nuclei and, consequently, of localization of two electrons at a Mössbauer center.

The spectrum of sample *C* (spectrum *C*) is a superposition of spectra *A* and *B* (see figure, column I). Columns II and III in the figure show the expected shapes of the Mössbauer spectra for ^{67}Zn for $U < 0$ and $U > 0$. The method for constructing these spectra was described in [8], and the results of calculations of electron densities for different electron configurations of zinc [9, 10] were used. A comparison of experimental (see figure, column I) and calculated (see figure, columns II and III) Mössbauer spectra unambiguously indicates that $U < 0$ for two-electron zinc centers in silicon.

It is noteworthy that the spectra corresponding to the Zn^0 and Zn^{2-} centers are broadened [for the spectrum of $Cu(^{67}Ga)$ with a ZnS absorber, the width of the spectral line at half-height $\Gamma = 2.6(3)$ µm s^{-1} [11], whereas $\Gamma = 5.0(5)$ µm s^{-1} for the experimental spectra shown in column I of the figure]. Such significant broadening of the

spectra indicates that the local symmetry of zinc impurity atoms is not cubic and may be interpreted as evidence for a noncentral position of zinc centers at the silicon lattice sites.

Thus, we showed that zinc impurity atoms in silicon constitute two-electron acceptor centers with negative correlation energy and that the local symmetry of the Zn^0 and Zn^{2-} centers is noncubic.

REFERENCES

1. C. S. Fuller and F. J. Morin, Phys. Rev. **103**, 379 (1957).
2. R. O. Carlson, Phys. Rev. **108**, 1390 (1957).
3. G. W. Ludwig and H. H. Woodbury, Solid State Phys. **13**, 223 (1962).
4. V. B. Ginodman, P. S. Gladkov, B. G. Zhurkin, *et al.*, Fiz. Tekh. Poluprovodn. (Leningrad) **5**, 2214 (1971) [Sov. Phys. Semicond. **5**, 1930 (1971)].
5. H. E. Altnik, T. Gregorkiewicz, and C. A. Ammerlaan, Solid State Commun. **75**, 115 (1990).
6. N. T. Bagraev, Semicond. Sci. Technol. **9**, 61 (1994).
7. N. T. Bagraev, Solid State Commun. **95**, 365 (1995).
8. V. F. Masterov, F. S. Nasredinov, S. A. Nemov, *et al.*, Fiz. Tekh. Poluprovodn. (St. Petersburg) **31**, 291 (1997) [Semiconductors **31**, 237 (1997)].
9. A. Svane and E. Antoncik, Phys. Rev. B: Condens. Matter **34**, 1944 (1986).
10. D. W. Mitchell, T. P. Das, W. Potzel, *et al.*, Phys. Rev. B: Condens. Matter **48**, 16 449 (1993).
11. A. Forster, W. Potzel, and G. M. Kalvius, Z. Phys. B: Condens. Matter **37**, 209 (1980).

Translated by A. Spitsyn

Semiconductors, Vol. 34, No. 3, 2000, pp. 272–276. Translated from Fizika i Tekhnika Poluprovodnikov, Vol. 34, No. 3, 2000, pp. 278–282.
Original Russian Text Copyright © 2000 by Zubkova, Izyumov, Rusina, Smelyanskaya.

ELECTRONIC AND OPTICAL PROPERTIES OF SEMICONDUCTORS

Multivalley Splitting of the Shallow Donor Energy Spectrum in Semiconductors with Diamond and Sphalerite Structures

S. M. Zubkova*, V. A. Izyumov*, L. N. Rusina*, and E. V. Smelyanskaya**

** Frantsevich Institute of Materials Science Problems, National Academy of Sciences of Ukraine, ul. Krzhizhanovskogo 3, Kiev, 252680 Ukraine;*

e-mail: ludm@rus.semicond.kiev.ua

*** Polytechnical Institute, pr. Permogi 37, Kiev, 252056 Ukraine*

Submitted April 27, 1999; accepted for publication November 13, 1999

Abstract—The consistent application of the perturbation theory to the solution of the Schrödinger equation describing the shallow-donor state in multivalley semiconductors has allowed us to obtain a secular equation of an order equal to the number of valleys. The solution of this equation yields both the characteristics and the magnitudes of the splitting of the donor-center ground state. Intervalley interaction-matrix elements entering the secular determinant were constructed in the Bloch pseudofunction representation. The pseudowave functions were computed as the eigenvectors of a system of equations in the method of the empirical pseudopotential with a basis set of 65 plane waves. These matrix elements differ considerably from those constructed in a plane wave approximation. The impurity-center perturbing potential is approximated by a screened point Coulomb potential. The numerical calculations are illustrated by the examples of shallow isochoric donors of Group V in Ge and Si. Our results are in excellent agreement with experimental data for the lowest level A_1 (1) and differ by 14–15% for the levels T_1 (3) and E (2). *© 2000 MAIK "Nauka/Interperiodica".*

1. INTRODUCTION

The problem of the energy spectrum of the shallow donor of Group V in diamond- and sphalerite-type semiconductors has been studied for at least 40 years. Despite the numerous fundamental studies, there is still a great interest in this problem. This interest is motivated by the various approaches to generalization of the equations in the effective mass method (EMM) for multivalley semiconductors, by the discrepancies in estimation of the contribution of intervalley terms to the bonding energy of the donor center, by the method of their account, and by the method of choosing the potential and the wave function of the donor center. In addition, interest in this problem has been revived in connection with the successful development of numerical pseudopotential calculations and the possibility of correctly constructing the crystal and impurity pseudopotentials.

The EMM approximation developed by Kohn and Luttinger [1, 2] has been used for many years to describe the shallow impurity states in semiconductors. The Schrödinger equation for the donor electron in Si was reduced to six independent equations for each valley and yielded the sixfold degenerate ground-state energy level of the donor center. Ten years later, the IR absorption experiments [3] showed that the degeneracy is partially removed and the sixfold degenerate level splits into levels A_1 (1), E (2), and T_1 (3).

In [4], the first consistent multivalley approach to EMM was developed. The model impurity potential with two adjustable parameters V_{imp} tends to a constant value for $r \longrightarrow 0$ and becomes a Coulomb potential for $r \longrightarrow \infty$. The ground state energy was calculated by the variational method.

In [5], for the calculation of a shallow donor in Si, a model impurity pseudopotential without adjustable parameters (*ab initio*) was used for the first time. In [6–8], the theory of pseudoimpurity was developed taking into account intervalley mixing. This theory is applicable to the calculations of both shallow and deep levels of substitutional and interstitial donors in semiconductors of the Si type and in GaP. In [9], the generalized equation in EMM with the renormalized type of the external field potential was derived. The renormalization is caused by the interference of Bloch functions from different valleys. The equation is solved numerically using a model impurity potential for donors in Si and the pseudopotential Bloch functions. The results are very sensitive to the behavior of the potential at short distances and exhibit an instability of the shallow–deep-impurity type. The model consideration of spatial dispersion leads to the occurrence of a deep level of the ground state of a donor, which qualitatively agrees with the experimental data for hydrogen and muonium impurities. In [10], the effective mass approximation for the donor center in GaAs was generalized to the case of intervalley interaction. The Schrödinger equation involves the renormalized Coulomb potential with the renormalized factor essentially

different from unity inside a sphere of small radius r_0 around the impurity ion. The solution yields the position of the ground state of the impurity center corresponding to the points Γ, X, and L of the Brillouin zone. For valley L, the donor center is found to have a deep level due to the intervalley interaction. In [11, 12], the IR absorption spectra were used to obtain the magnitudes of the valley–orbit splitting of the N donor in hexagonal positions (h): 7.6 and 12.6 meV for 4H-SiC and 6H-SiC, respectively.

This work is devoted to the theoretical study and numerical calculation of a shallow donor energy spectrum in the semiconductors of diamond structure with consideration of the actual band structure of these crystals. Similar to [13], where the multivalley splitting of Wannier–Mott excitons in cubic semiconductors is considered, the matrix elements of intervalley interaction (mixing) are considered here in the context of the perturbation theory [10]; the electron wave function of the impurity center is chosen as the linear combination of Bloch pseudopotential functions, which are the eigenvectors of the system of equations of the empirical pseudopotential for various $\mathbf{k}_i$, $i = 1, \ldots, p$, where p is the number of equivalent energy minimums.

2. DERIVATION OF THE SECULAR EQUATION FOR OBTAINING CORRECTIONS TO THE ENERGY OF THE SHALLOW-DONOR GROUND STATE

The Schrödinger equation for an ideal crystal is written as

$$H^0\Psi^0_{n\mathbf{k}}(\mathbf{r}) = E^0_n(\mathbf{k})\Psi^0_{n\mathbf{k}}(\mathbf{r}), \tag{1}$$

where n is the number of energy band, $\mathbf{k}$ is the wave vector, and

$$\Psi^0_{n\mathbf{k}}(\mathbf{r}) = (1\sqrt{v})U^0_{n\mathbf{k}}(\mathbf{r})e^{i\mathbf{kr}} \tag{2}$$

are the Bloch functions representing the total orthonormalized system of wave functions of an ideal crystal.

For a crystal containing impurities, the Schrödinger equation is given by

$$[H^0 + V(\mathbf{r})]\psi(\mathbf{r}) = E\psi(\mathbf{r}), \tag{3}$$

where $V(\mathbf{r})$ is the perturbing potential of the impurity center. The wave function of an impurity electron can be written in Bloch's representations as

$$\psi(\mathbf{r}) = \sum_n\sum_{\mathbf{k}} B_n(\mathbf{k})\psi^0_{n\mathbf{k}}(\mathbf{r}). \tag{4}$$

For shallow donors, we may restrict ourselves to the lowest conduction band in expansion (4). Then, (3) can be rewritten as

$$[E^0_C(\mathbf{k}) - E]B_C(\mathbf{k}) + \sum_{\mathbf{k}'} V_{\mathbf{kk}'}B_C(\mathbf{k}') = 0, \tag{5}$$

where

$$\begin{aligned} V_{\mathbf{kk}'} &= \int(\psi^0_{\mathbf{k}'})^*(\mathbf{r})V(\mathbf{r})\psi^0_{\mathbf{k}}(\mathbf{r})d\tau \\ &= \frac{1}{\nu}\int(U^0_{C\mathbf{k}'})^*(\mathbf{r})V(\mathbf{r})U^0_{C\mathbf{k}}(\mathbf{r})e^{i(\mathbf{k}-\mathbf{k}')\mathbf{r}}d\tau, \end{aligned} \tag{5'}$$

and $U^0_{C\mathbf{k}}(\mathbf{r})$ is the periodic part of the Bloch function.

In order to solve system (5)–(5'), we can use the perturbation theory method assuming that the matrix elements $V_{\mathbf{kk}'}$ are of the zero order of smallness if $\mathbf{k}$ and $\mathbf{k}'$ are close to the same minimum $\mathbf{k}_i$ and are of the first order of smallness if the vector $\mathbf{k}$ is close to minimum $\mathbf{k}_i$ and if $\mathbf{k}'$ is close to minimum $\mathbf{k}_j$. Let us expand $E^0_C(\mathbf{k})$ into a series up to the terms quadratic with respect to $(\mathbf{k} - \mathbf{k}_i)$ near the minimum of $E(\mathbf{k}_i)$ as

$$E^0_C(\mathbf{k}) = E(\mathbf{k}_i) + \sum_{\alpha,\beta}(1/2m^i_{\alpha,\beta})(k_\alpha - k_{i\alpha})(k_\beta - k_{i\beta}), \tag{6}$$

where α and β are x, y, and z; and $1/m^i_{\alpha,\beta}$ is the tensor of reciprocal reduced effective mass for the ith minimum. Then, system (5) in zero approximation decomposes into several independent systems according to the number of minimums k; i.e.,

$$\begin{aligned} &\left[E(\mathbf{k}_i) + \sum_{\alpha,\beta}\frac{1}{2m^i_{\alpha,\beta}}(k_\alpha - k_{i\alpha})(k_\beta - k_{i\beta})\right]B^0(\mathbf{k}) \\ &\qquad + \sum_{\mathbf{k}'} V^0_{\substack{\mathbf{kk}'\\ \mathbf{k}\approx\mathbf{k}'\approx\mathbf{k}_i}}, \\ &B^0(\mathbf{k}') = E^0_{\text{imp}}B^0(\mathbf{k}). \end{aligned} \tag{7}$$

The solution of these equations yields the system of the coefficients $B_i(\mathbf{k})$ decreasing rapidly with an increase in distance from $\mathbf{k}$ to $\mathbf{k}_i$. Then, in order to solve the equations to the first approximation, we can take, as the zero approximation, the linear combination:

$$B^0(\mathbf{k}) = \sum_j C_jB^0_j(\mathbf{k}). \tag{8}$$

The equations of the first approximation for minimum $\mathbf{k}_i$ take the form

$$\begin{aligned} &\left[E(\mathbf{k}_i) + \frac{1}{2}\sum_{\alpha,\beta}\frac{1}{2m^i_{\alpha,\beta}}(k_\alpha - k_{i\alpha})(k_\beta - k_{i\beta})\right]B^1(\mathbf{k}) \\ &\qquad + \sum_{\mathbf{k}'} V^0_{\substack{\mathbf{kk}'\\ \mathbf{k}\approx\mathbf{k}'\approx\mathbf{k}_i}}B^1(\mathbf{k}') - E^0_{\text{imp}}B^1(\mathbf{k}) \\ &\qquad = -\sum_{\mathbf{k}'} V^0_{\substack{\mathbf{kk}'\\ \mathbf{k}\approx\mathbf{k}_i;\ \mathbf{k}'=\mathbf{k}_j}}B^0(\mathbf{k}') + E^1B^0(\mathbf{k}). \end{aligned} \tag{9}$$

From the condition for solvability of (9), i.e., from the orthogonality of the right-hand side to any solution of $B_i^0(\mathbf{k}')$ in the left-hand side, we have

$$E^1 C_i \sum_{\mathbf{k}\approx\mathbf{k}_i} \left|B_i^0(\mathbf{k})\right|^2 - \sum_{j\neq i}\sum_{\mathbf{k}\approx\mathbf{k}_i}\sum_{\mathbf{k}'\approx\mathbf{k}_j} C_j B_i^{*0}(\mathbf{k}) V^1_{\mathbf{k}\mathbf{k}'} B_j^0(\mathbf{k}') = 0. \tag{10}$$

Here

$$\sum_j^p B_j^0(\mathbf{k}) B_j^0(\mathbf{k}) = \delta_{j,j}$$

and p is the number of equivalent energy minimums. After the introduction of a smoothed function

$$\varphi_i^0(\mathbf{r}) = \sum_{\mathbf{k}\approx\mathbf{k}_i} B_i^0(\mathbf{k}) e^{i\mathbf{kr}}, \tag{11}$$

the system of the linear algebraic homogeneous equations in C_i takes the form

$$\frac{1}{\nu} C_i E^1 - \sum_{j\neq 1}^p C_j \varphi_i^*(0) V^1_{\mathbf{k}_i\mathbf{k}_j} \varphi_j(0) = 0. \tag{12}$$

From the condition for solvability of system (12), we obtain the p-degree equation in the energy correction to the bonding energy of the impurity center:

$$\left|\frac{1}{\nu} E^1 \delta_{ij} - \sum_{j\neq 1}^p \varphi_i^*(0) V^1_{ij} \varphi_j(0)\right| = 0. \tag{13}$$

Thus, the degeneracy of the ground state of the donor level related to the multivalley mixing is at least partially removed, and the energy level splits into p levels according to the number of equivalent minimums.

3. CALCULATION OF THE MATRIX ELEMENTS OF INTERVALLEY MIXING

From equation (5'), it follows that

$$V'_{ij} \equiv V'_{\mathbf{k}_i\mathbf{k}_j}(\mathbf{r}) = \frac{1}{\nu}\int (U^0_{c\mathbf{k}j})^*(\mathbf{r}) V(\mathbf{r}) U^0_{c\mathbf{k}j}(\mathbf{r}) e^{-i(\mathbf{k}_i-\mathbf{k}_j)\mathbf{r}} d\tau. \tag{14}$$

The perturbing potential for a shallow donor is written as

$$V(r) = -1/\varepsilon_0\tau, \tag{15}$$

where ε_0 is the static dielectric constant.

Let us use the known expansion of the product of periodic components of Bloch functions into a series in plane waves with wave vectors equal to the reciprocal lattice vectors $\mathbf{G}$:

$$(U^0_{c\mathbf{k}i})^*(\mathbf{r}) U^0_{c\mathbf{k}j}(\mathbf{r}) = \sum_{\mathbf{G}} b_{\mathbf{G}}(\mathbf{k}_i, \mathbf{k}_j) e^{i\mathbf{Gr}}, \tag{16}$$

where the functions

$$(U^0_{c\mathbf{k}i})^*(\mathbf{r}) = \sum_{\mathbf{g}} a^c_{\mathbf{g}}(\mathbf{k}_i) e^{-i\mathbf{gr}}, \qquad U^0_{c\mathbf{k}j}(\mathbf{r}) = \sum_{\mathbf{g}'} a^c_{\mathbf{g}'}(\mathbf{k}_j) e^{-i\mathbf{g}'\mathbf{r}} \tag{17}$$

can be found as the eigenvectors of the system of equations of the empirical pseudopotential method. From (16)–(17), we have

$$b_{\mathbf{G}}(\mathbf{k}_i, \mathbf{k}_j) = \sum_{\mathbf{g}} (a^c_{\mathbf{g}})^*(\mathbf{k}_i) a^c_{\mathbf{g}+\mathbf{G}}(\mathbf{k}_j). \tag{18}$$

Substituting (15)–(18) into (14) and performing a number of transformations, we obtain

$$V'_{ij} = -\frac{4\pi e^2}{\varepsilon_0 \nu} \sum_{\mathbf{G}} \frac{b_{\mathbf{G}}(\mathbf{k}_i - \mathbf{k}_j)}{\left|\mathbf{G}+\mathbf{k}_j-\mathbf{k}_i\right|^2} = -\frac{4\pi e^2}{\varepsilon \nu} \sum_{\mathbf{G}}\sum_{\mathbf{g}} \frac{(a^c_{\mathbf{g}})^*(\mathbf{k}_i) a^c_{\mathbf{g}+\mathbf{G}}(\mathbf{k}_j)}{\left|\mathbf{G}+\mathbf{k}_j-\mathbf{k}_i\right|^2}. \tag{19}$$

4. CALCULATION OF THE GROUND-STATE ENERGY AND THE SMOOTHED WAVE FUNCTION OF THE IMPURITY CENTER IN THE CONTEXT OF A SINGLE-VALLEY APPROACH

In order to calculate $\varphi_i^0(\mathbf{r})$ (11) and E^0_{imp} (7) of the impurity center, we employ the equation of the effective mass method, which can be represented in dimensionless variables as

$$\left[-\frac{m_0}{2m^*_{1,2}}\left(\frac{\partial^2}{\partial x^2} + \frac{\partial^2}{\partial y^2}\right) - \frac{m_0}{2m^*_3}\frac{\partial^2}{\partial z^2} - \frac{1}{\varepsilon_0 \rho}\right]\varphi_0(\rho) = \varepsilon\varphi_0(\rho), \tag{20}$$

$$\rho = r m_0 e^2/\hbar^2, \quad \varepsilon = E\hbar^2/m_0 e^4.$$

Here, $m^*_{1,2}$ and m^*_3 are the transverse and longitudinal effective masses of the constant-energy ellipsoid of the electron at the bottom of the lowest conduction band. Equation (20) can be solved by the direct variational method. The test function is chosen in the form

$$\varphi_i^0(\rho) = A\exp(-\sqrt{\alpha(x^2+y^2)+\beta z^2}),$$

where α and β are the variational parameters, and $A^2 = \alpha\sqrt{\beta}/\pi$ is the normalizing coefficient.

The variational procedure yields the following system of equations for the determination of variational parameters:

$$\begin{cases} \frac{x}{3m_{1,2}^*} + \frac{1}{6m_3^*} - \frac{1}{2\varepsilon_0}\sqrt{\frac{x}{(1-x)\beta}}\arctan\sqrt{\frac{1-x}{x}} = 0, \\ \frac{\sqrt{\beta}}{3m_{1,2}^*} + \frac{1}{2\varepsilon_0(1-x)} \\ -\frac{1}{2\varepsilon_0}\sqrt{\frac{1}{x(1-x)^3}}\arctan\sqrt{\frac{1-x}{x}} = 0. \end{cases} \quad (21)$$

Here, $x = \alpha/\beta$ ($\alpha < \beta$). If $\alpha > \beta$, we obtain the value corresponding to the excited energy level of the impurity center inside the conduction band.

5. ILLUSTRATION OF THE NUMERICAL CALCULATIONS FOR Ge AND Si

In this section, we present the results of calculations that allow us to obtain qualitative and quantitative information about the character of the splitting, the relative position, and the values of the energy levels of a shallow-donor ground state of a Group-V element (P, N, and As) in Si and Ge. The numerical solution of the system (21) for Ge and Si yields the results listed in Table 1.

The calculation of the matrix elements of the impurity potential V_{ij}' (19) was reduced to the calculation of the eigenvectors $a_{\mathbf{g}}^c(\mathbf{k}_i)$ and $a_{\mathbf{g}+\mathbf{G}}^c(\mathbf{k}_j)$ at the points of equivalent lowest energy minimums in the conduction band for the system of equations in the empirical pseudopotential method (65 plane waves) and the subsequent double summation over the vectors of the reciprocal lattice. In Ge, there are four such minimums at the points $\mathbf{k}_i = \frac{\pi}{a}(\bar{1}\bar{1}\bar{1}, \bar{1}11, 1\bar{1}1, 11\bar{1})$, and six minimums in Si at the points $\mathbf{k}_i = 0.85\frac{\pi}{a}(100, 010, 001, \bar{1}00, 0\bar{1}0, 00\bar{1})$. The values of the form factors of the pseudopotential for these crystals were taken from [15].

The solution of the secular equation (12) for the determination of correction E' partially removes the degeneracy of the impurity level. Thus, for Ge, we obtain

$$E_1' = -1.97 \text{ meV}, \quad E_{2,3,4}' = 0.66 \text{ meV}.$$

For Si, we have

$$E_1' = -4.30 \text{ meV}, \quad E_{2,3,4}' = 1.73 \text{ meV},$$

$$E_{5,6}' = 3.83 \text{ meV}.$$

Table 1. Variational parameters (α, β), normalizing coefficient squared (A^2), and bonding energy of the impurity E_{imp}^0

Semiconductor	X	β, 10^{-4} a_B^2	α, 10^{-5} a_B^2	A^2, 10^{-7} a_B^3	E_{imp}^0, meV
Ge	0.126	5.82	7.36	5.65	–12.33
Si	0.330	15.06	49.61	61.31	–41.21

Table 2. Bonding energy (in meV) of the components of the ground state of Group-V donors in Si and Ge

Data source	Si			Ge	
	A_1	T_1	E	A_1	T_1
This work	45.5	39.5	37.4	14.3	11.7
Baldereschi [14]	40.5	29.5	28.8	10.1	9.5
Ning, Sah [4]	45.5	33.7	32.4		
Altarelli, Hsu, *et al.* [16]	47.5	31.4	30.6	12.5	9.7
Experimental results [3]	45.3	33.7	32.3	14.2	10.0

Table 3. Comparison of matrix elements V_{ij}'

Semiconductor	Plane wave approximation	The Bloch function approximation
Ge	1.44	1.47
Si	1.85, 0.924	2.27, 1.31

Table 2 lists the bonding energies obtained here for the ground state levels of an isochoric Group-V donor in Si and Ge, the theoretical results from [4, 14, 16], and the experimental data from [3]. As can be seen from Table 2, the lowest level A_1 in Si and Ge is in excellent agreement with the experimental data. The values for the T_1 and E levels differ by 14–15% from the experimental data.

According to [14], the experimental values of the splitting energy $\Delta = E(T_1) - E(A_1)$ in Ge are equal to 2.83, 4.23, and 0.32 meV for P, As, and Sb impurities, respectively. The experimental splitting energies for P, As, and Sb impurities in Si are equal respectively to 11.85, 21.15, and 9.94 meV for $\Delta_1 = E(A_1) - E(T_1)$, and to 1.35, 1.42, and 2.50 meV for $\Delta_2 = E(T_1) - E(E)$.

6. DISCUSSION

The problem of the application of Bloch pseudofunctions to the calculation of intervalley interaction has been discussed, for example, in [16, 17]. Our data for the factor $b_{\mathbf{G}} = (\mathbf{k}_i, \mathbf{k}_j)$ calculated for $\mathbf{G} = 0$ in Si for the cases where the minimums of the conduction band are located on the same axis ($\mathbf{k}_i = -\mathbf{k}_j$) and on the mutually perpendicular axes (65 plane waves) are equal to

$b = 0.17$ and to $b = -0.44$, respectively. These data are in good agreement with the results obtained in [17]: b is equal to 0.18 and to 0.41 (59 plane waves). The layer-by-layer contributions to $b_{\mathbf{G}}(\mathbf{k}_i, \mathbf{k}_j)$ in summation over $\mathbf{g}$ in (18) turned out to be quite different from unity and are in good agreement with the data obtained in [16] for Si and Ge.

As one would expect, the matrix elements of the intervalley interaction V'_{ij} (19) calculated from the pseudopotential Bloch functions, which are better suited for a description of an ideal crystal than a solitary plane wave, essentially differ from the matrix elements based on plane waves. In the latter case, $V'_{ij} \propto 1/|\mathbf{k}_i - \mathbf{k}_j|^2$ (see Table 3).

7. CONCLUSION

The analysis of matrix elements of intervalley interaction V'_{ij} with respect to the order of the system of equations in the method of electron plane waves and to the number of the vectors $\mathbf{G}$ of the reciprocal lattice in expansion (16) has shown that the further refinement of the results and the improvement in agreement with the experiment for the chosen impurity potential can be attained by increasing the number of plane waves in the method of electron plane waves and the number of the vectors of reciprocal lattice in the expansion of the product of periodical components of the Bloch functions.

REFERENCES

1. W. Kohn and J. M. Luttinger, Phys. Rev. **98**, 915 (1955); in *Problems of Semiconductor Physics*, Ed. by V. A. Bonch-Bruevich (Inostrannaya Literatura, Moscow, 1957), p. 551.
2. J. M. Luttinger and W. Kohn, Phys. Rev. **97**, 869 (1955); in *Problems of Semiconductor Physics*, Ed. by V. A. Bonch-Bruevich (Inostrannaya Literatura, Moscow, 1957), p. 515.
3. R. L. Aggarwal and A. K. Ramdas, Phys. Rev. A: Gen. Phys. **140**, 1246 (1965); J. H. Reuszer and P. Fisher, Phys. Rev. A: Gen. Phys. **135**, 1125 (1964).
4. T. H. Ning and C. T. Sah, Phys. Rev. B: Solid State **4**, 3468 (1971).
5. S. T. Pantelides and C. T. Sah, Solid State Commun. **11**, 1713 (1972).
6. S. T. Pantelides and C. T. Sah, Phys. Rev. B: Condens. Matter **10**, 621 (1974).
7. S. T. Pantelides, Solid State Commun. **14**, 1255 (1974).
8. S. T. Pantelides, Solid State Commun. **30**, 65 (1979).
9. L. Resca and R. Resta, Solid State Commun. **29**, 265 (1979).
10. J. C. Bourgoin and A. Mauger, Appl. Phys. Lett. **53**, 749 (1988).
11. W. Suttrop, W. J. Choyke, W. Gotz, *et al.*, J. Appl. Phys. **73**, 3332 (1993).
12. W. Suttrop, G. Pensl, W. J. Choyke, *et al.*, J. Appl. Phys. **72**, 3708 (1992).
13. S. M. Zubkova, L. N. Rusina, and K. B. Tolpygo, Fiz. Tekh. Poluprovodn. (Leningrad) **21**, 1429 (1987) [Sov. Phys. Semicond. **21**, 867 (1987)].
14. A. Baldereschi, Phys. Rev. B: Condens. Matter **1**, 4673 (1970).
15. M. L. Cohen and T. K. Bergstresser, Phys. Rev. **141**, 789 (1966).
16. M. Altarelli, W. Y. Hsu, and R. A. Sabatini, J. Phys. C: Solid-State Phys. **10**, L605 (1977).
17. R. Resta, J. Phys. C: Solid-State Phys. **10**, L179 (1977).

Translated by A. Zalesskiĭ

Semiconductors, Vol. 34, No. 3, 2000, pp. 277–283. Translated from Fizika i Tekhnika Poluprovodnikov, Vol. 34, No. 3, 2000, pp. 283–289.
Original Russian Text Copyright © 2000 by Gol'dman, Zhdan, Kukharskaya, Chucheva.

Generation of Minority Charge Carriers at the Semiconductor Surface during Thermally Activated Ionic Depolarization of Metal–Insulator–Semiconductor Structures

E. I. Gol'dman, A. G. Zhdan, N. F. Kukharskaya, and G. V. Chucheva

Institute of Radio Engineering and Electronics (Fryazino Branch), Russian Academy of Sciences, pl. Vvedenskogo 1, Fryazino, Moscow oblast, 141120 Russia

Submitted April 22, 1999; accepted for publication July 12, 1999

Abstract—Relaxation signals represented by the temperature dependences of current $J(T)$ and high-frequency capacitance $C(T)$ and generated in the course of the thermally stimulated depolarization of a metal–insulator–semiconductor structure were analyzed numerically. Both the depletion of ionic traps located at the insulator–semiconductor interface and the generation of minority charge carriers from a bulk center with the activation energy E_D were taken into account. *© 2000 MAIK "Nauka/Interperiodica".*

Variation of the width of the space-charge region at the semiconductor surface in the course of thermally stimulated ionic depolarization of a metal–insulator–semiconductor (MIS) structure affects appreciably both the pulse shapes of current flowing in the circuit external to this structure and, correspondingly, the approach to the interpretation of experimental data [1]. The situation considered in [1] corresponded to the case where the shift of surface potential in a semiconductor (from the state of accumulation to the state of inversion) as induced by thermally stimulated displacement of positive ions in the insulator did not violate the thermal equilibrium in the space-charge region. Thus, no consideration in [1] was given to a wide range of phenomena defining the dynamics of electronic–ionic processes at the insulator–semiconductor phase boundary; in particular, these processes involve the electron–ion interaction manifesting itself, for example, in a strong influence of ions pushed by a polarizing field to the SiO_2/Si interface on the kinetics of thermally stimulated generation of minority charge carriers at the Si surface [2]. The formation rate for the surface inversion channel depends critically on the physicochemical properties of the interphase boundary (electrical inhomogeneity, the density of localized electron states at the surface and in the space-charge region of semiconductor, and so on [3–6]); therefore, it is the observations of the kinetics of generation of minority charge carriers in thermally stimulated depolarization (TSD) that are most sensitive to variations in electron properties of the boundary, whether these variations are caused by direct influence of ions or by electron–ion reactions occurring at this boundary [2, 7–11]. The above offers new possibilities of developing effective methods for studying the ion transport in dielectric layers at the surface of semiconductors, for assessing the quality of semiconductor–insulator interfaces, and for determining the amount of ionic contaminations in the insulator and their influence on the generation of minority charge carriers.

Qualitative and quantitative manifestations of electron–ion reactions (the effects of ion neutralization) and ionic traps in the characteristics of TSD in MIS structures were considered in [12]. Although the generation of minority charge carriers was taken into account in [12], the influence of ions on this generation was not specially studied. In connection with this, we use the system of equations derived in [12] to analyze numerically the relaxation signals; the latter are represented by the temperature dependences of current $J(T)$ and high-frequency capacitance $C(T)$ of a MIS structure on the conditions where neutralization of ions is unimportant and the peak of thermally stimulated generation of minority charge carriers is preceded by the current peak in TSD. Interest in such a problem is caused by a number of circumstances. First, a fraction of neutralized ions at the interface is smaller than 100%: According to the data reported in [10, 11], a fraction of unbound ions amounts to 5–20% of the total number of particles (ions and neutral complexes consisting of an ion and electron). Second, neutralization is basically impossible if the localized states formed by ions of a given type and by their dielectric surroundings are found above the Fermi level of a semiconductor (i.e., if electron affinity is inherent in positive ions of only a limited type [13]). Third, the probability of tunneling electron transitions from the above neutral complexes to the valence band may be very low; in this case, the generation of minority charge carriers occurs after thermal dissociation of neutral complexes and after positive ions appearing at the interface can influence the generation of electron–hole pairs. Finally, the opposite situation (the peak of current corresponding to TSD current precedes the peak of generation of minority charge carriers)

excludes the possibility of studying the influence of ions on the generation process.

Following [12], we assume that mobile (for the sake of definiteness, positive and singly charged) ions are present at the surface of an electron semiconductor; we also assume that, in the polarizing fields and under the conditions of equilibrium, all of these ions are concentrated at the insulator–semiconductor interface and are trapped by initially neutral monoenergetic ion traps having the activation energy E_i. If the initial surface density of ions is fairly high, it is then obvious that the semiconductor surface is in a state of pronounced equilibrium accumulation. If a depolarizing field is applied, the equilibrium in the system is violated and it becomes possible that minority charge carriers are generated thermally and the ions leave the interface. Let the initial temperature of the sample T_0 be low (i.e., kT_0 is much smaller than both E_i and E_D, where k is the Boltzmann constant and E_D is the activation energy for generation of holes via a bulk center present in a semiconductor with concentration N_D); let the surface density of trapped ions N_i be much lower than the ion-trap density; let the depolarizing field induce the depletion of the semiconductor surface of electrons; and let the time of ion transit through the dielectric layer be small as compared to ion lifetime in traps and the corresponding capture time (the latter assumptions are certainly valid for comparatively high depolarizing fields). In this situation, the state of nonequilibrium depletion and the ion charge localized at the traps can be retained for a very long time; relaxation of the nonequilibrium state of the MIS structure is limited by the rates of both the generation of minority charge carriers (holes) and the release of ions from the traps. Under these conditions, the system of equations [12] describing the relaxation kinetics is simplified and can be written as

$$\frac{dN_i}{dt} = -\frac{N_i}{\tau_i}e^{-\frac{E_i}{kT}}, \tag{1}$$

$$\frac{dp_s}{dt} = \frac{N_D(z_2 - z_1)}{\tau_{DC}}e^{-\frac{E_i}{kT}}\left[1 - \frac{N_d p}{N_C N_V}e^{\frac{E_g - U}{kT}}\right], \tag{2}$$

where p_s is the surface density of holes; N_D and p are the bulk concentrations of donors and holes in the semiconductor in the immediate vicinity of interface with insulator; t is time; E_g is the bandgap of the semiconductor; U is the surface band-bending in the semiconductor in the state of depletion (inversion); τ_i^{-1} and τ_{DC}^{-1} are the frequency factors of probabilities for emptying the ion traps and for electron transitions from the bulk center of hole generation to the conduction band of the semiconductor; and z_1 and z_2 are the coordinates of the region of bulk generation of holes in the semiconductor near-surface depletion region of width W. According to [14, 15], the coordinates z_1 and z_2 are determined from the following relationships:

$$\frac{U}{kT} = \frac{(W - z_1)^2}{2L_d^2} + \ln\left(\frac{pe^{\frac{E_g - E_D}{kT}}}{N_V} + 1\right),$$
$$\frac{(W - z_2)^2}{2L_d^2} = \left(\frac{E_g - E_D - F}{kT}\right) + \ln\theta. \tag{3}$$

Here, $L_d = (\kappa_s kT/4\pi q^2 N_d)^{1/2}$ is the Debye length; κ_s is the permittivity of the semiconductor; q is the elementary charge; $F = kT\ln(N_C/N_d)$ is the Fermi energy in the bulk of the semiconductor; and $\theta = \tau_{DV}/\tau_{DC}$, with τ_{DV}^{-1} being the frequency constant of probability for electron transitions from the valence band to the bulk center of the hole generation. The relation between p, p_s, W, and U can be derived by approximating empirically the result of integration of the Poisson equation [14, 15]; i.e.,

$$p = 2\pi q^2/(\kappa_s kT)(p_s^2 + 2p_s N_d W),$$
$$\frac{U}{kT} = \frac{W^2}{2L_d^2} + 2\ln\left(\frac{p_s}{N_d W} + 1\right). \tag{4}$$

System (1)–(4) is closed by the electroneutrality equation

$$qV_g = U + 4\pi q^2 h/\kappa_i(N_i + p_s + N_d W), \tag{5}$$

in which V_g = const is the field-electrode potential and h and κ_i are the thickness and permittivity of the insulating layer. The condition V_g = const is fundamentally important for generation of minority charge carriers in the state of profound nonequilibrium depletion because, if the high-frequency capacitance of the MIS structure is maintained constant (i.e., for W = const), it is impossible to attain the equilibrium state of the system [14–16].

The relaxation signals J and C are defined as

$$J = \frac{qN_i e^{-\frac{E_i}{kT}}}{\tau_i} + q\frac{d}{dt}(N_i + p_s + N_d W); \tag{6}$$
$$C^{-1} = C_i^{-1} + C_s^{-1}, \quad C_i = \kappa_i/(4\pi h), \quad C_s = \kappa_s/(4\pi W).$$

We now analyze the dependences of the current density $J(T, U)$ and the specific high-frequency capacitance of the MIS structure $C(T, U)$ in the mode of linear temperature scanning (the mode of TSD: $T = T_0 + \beta t$ and $d/dt \longrightarrow \beta d/dt$, with β = const denoting the heating rate); these dependences were obtained by solving numerically equations (1)–(6) for a Si MIS structure with the following typical parameters (used previously in [12]): $h = 1 \times 10^{-5}$ cm, $\kappa_i = 3.9$, $N_d = 10^{15}$ cm^{-3}, κ_s = 11.9 eV, E_g = 1.12 eV, E_i = 0.98 eV, E_D = 0.79 eV, N_D =

$2.8 \times 10^{19}(T/300)^{3/2}$ cm^{-3}, $N_V = 1.04 \times 10^{19}(T/300)^{3/2}$ cm^{-3}, $N_D = 10^{15}$ cm^{-3} and $T_0 = 100$ K. The system of dimensionless variables $-t/\tau_i$, N_i/N_0, p_s/N_0, $W/N_0 N_d^{-1}$, $z_1/N_0 N_d^{-1}$, and $z_2/N_0 N_d^{-1}$ was used; here, N_0 is the initial ($t = 0$) surface density of ions. The values of J and C were normalized as $\tilde{J} \Rightarrow J/(qN_0\tau_i^{-1})$ and $\tilde{C}_s \Rightarrow C_s/(\kappa_s/4\pi N_0 N_d^{-1})$. Assuming that the lifetimes of ions captured by the traps and the rate of bulk generation of holes are largely defined by the activation energies E_i and E_D, we set $\tau_i = \tau_{DC} = \tau_{DV}$. The quantity $\beta = 4.46 \times 10^{-10}/\tau_i$ (in degrees per second) corresponds to the thermal stimulation for the values of E_i and E_D involved in calculations; this can be easily verified by using the condition for the existence of a maximum for the current $E/kT_m = \ln(kT_m^2/\beta\tau_i E)$ [17] for $T_m > T_0$ ($E = E_i$; $E = E_D$; and T_m is the temperature corresponding to the maximum) if this condition is represented as $E/kT_0 \gg \ln(kT_m^2/\beta\tau_i E)$.

For the case of $N_0 = 10^{11}$ cm^{-2}, Fig. 1 shows the families of curves $\tilde{J}(T)$ and $\tilde{C}_s^{-1}(T) \sim W(T)$ in relation to the quantity U_0 and also the curves $p_s(T)$ and $N_i(T)$ for $\tilde{U}_0 = U_0/300k = \text{const} = 50$. The current $\tilde{J}(T)$ exhibits two peaks; one of them, referred to as peak α, is located at lower temperatures and is highly asymmetrical, whereas the other peak (γ) is located at higher temperatures and is almost symmetrical. As the value of U_0 increases, the magnitude of peak α increases and it shifts to higher temperatures, whereas the magnitude of peak γ and its position virtually do not change; in view of the latter observation and the normalization condition $\tilde{J} \Rightarrow J/(qN_0\tau_i^{-1})$, we then have $J \sim N_0$ for the current observed actually at the peak γ.

The peak α is largely caused by thermal generation of minority charge carriers (holes), whereas peak γ is due to an emptying of ion traps; this is evidenced by the behavior of the dependences $p_s(T)$ and $N_i(T)$ shown in Fig. 1b. Generation (and accumulation at the interface) of holes begins at peak α and continues at higher temperatures, including in peak γ, under the conditions of quasi-equilibrium because $E_i - E_D \gg kT$. The emptying of ion traps is an independent process, whereas the generation of holes and the narrowing of the space-charge region are self-consistent processes: The band bending at the surface increases with decreasing N_i and decreases as the holes are accumulated at the interface. For these reasons, the peak γ acquires an almost symmetrical shape, which is unusual for the assumed monomolecular kinetics of the emptying of the ion traps. Ignorance of these circumstances can lead to the erroneous treatment of peak γ as a manifestation of the ion traps distributed in energy [8, 18]. In the vicinity of peak α, the dependences $\tilde{C}_s^{-1}(T)$ exhibit sharp steplike changes caused by rapid narrowing of the space-charge region as a result of accumulation of holes at the interface. As a result, the contribution of temperature variation of W to this peak is larger than that to peak γ; in the latter case, the slope of the function $\tilde{C}_s^{-1}(T)$ is smaller because an increase in depletion accompanied by the escape of positive ions from the interface is compensated by the simultaneously generated holes. At higher temperatures, all the curves $\tilde{C}_s^{-1}(T)$ gradually merge into a common line that describes the temperature dependence of the equilibrium value of W [14]. An

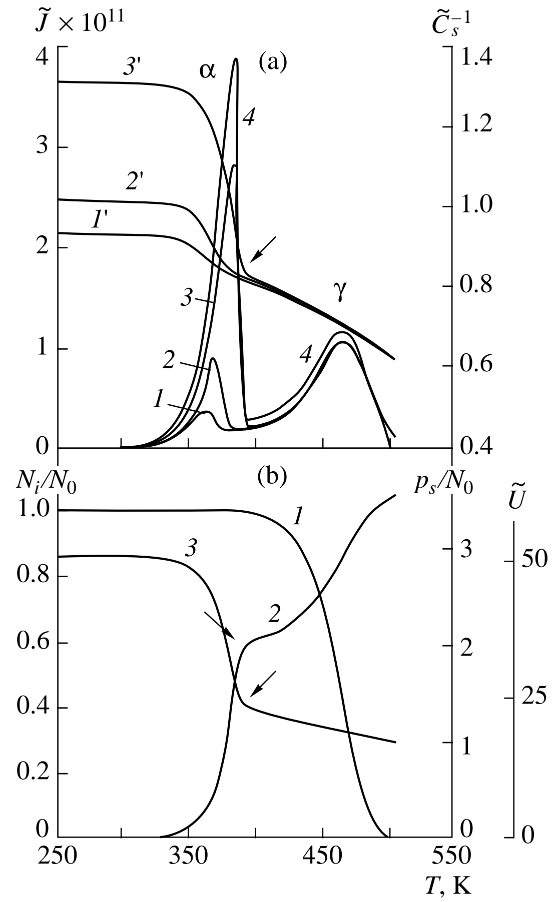

Fig. 1. Temperature dependences of (a) the current $\tilde{J}(T)$ and the reciprocal capacitance $C_s^{-1}(T)$ in relation to the initial band bending U_0 (curves *1*–*4* and *1'*–*3'*, respectively), with $U_0/300k$ = (*1*, *1'*) 25, (*2*, *2'*) 30, and (*3*, *3'*) 50; curve *4* corresponds to $\tilde{J}(T)$ without the component of current caused by a temperature-related decrease in width W of the depletion layer ($U_0/300k = 50$); the values of the parameters used in calculations were $N_0 = 1 \times 10^{11}$ cm^{-2}, $E_i/300k = 38$ (0.98 eV), and $E_D/300k = 30.3$ (0.78 eV). (b) Temperature dependences of (*1*) ion density $N_i(T)$, (*2*) hole density $p_s(T)$, and (*3*) band bending $\tilde{U} = U/300k$ for $U_0/300k = 50$.

increase in the height and steepness of the steps in $\tilde{C}_s^{-1}(T)$ and also in the amplitude of peak α is caused by an increase in the amount of potential "capacity" for holes and in the generation rate of holes as a result of expansion of the generation zone $(z_1, z_2)|_{U = U_0}$. The pattern in the behavior of the functions $\tilde{J}(T, U_0)$ and $\tilde{C}_s^{-1}(T)$ in the peak α is completely consistent with experimentally verified physical concepts of thermal generation of minority charge carriers via a bulk center in the semiconductor [14]. Variation of W with T prevents the dependence $J(T)$ from being used to determine p_s and N_0 by the conventional method of integrating the curves of thermally stimulated current [17]. In order to create the possibility of using this method to calculate p_s and N_0, we have to either stabilize the MIS-structure high-frequency capacitance $C(T)$ in the course of measuring the curves $J(T)$ [19] or measure $C(T)$ synchronously with $J(T)$; the latter makes it possible to exclude the component of current caused by a variation in $W(T)$. The regime $C(T) = \text{const}$ (and, correspondingly, $C_s(T) = \text{const}$ and $W(T) = \text{const}$) imposes certain constraints on the smallest value of the capacitance $C_s(T_0, V_{g0})$ to be stabilized and thus on the initial depletion voltage V_{g0} [14–16]. The role of the above component of current is illustrated by curve *4* in Fig. 1a (to be compared with curve *3*); the parameters of curve *4* are defined by the fact that, under the conditions of quasi-equilibrium of the hole system, the escape of positive ions from the interface is compensated by an increase in the density of holes, with this increase being somewhat larger than a decrease in the density of ions, because the ions are assumed to be concentrated in the immediate vicinity of the interface, whereas holes are distributed in the semiconductor within the corresponding Debye length. The activation energy of an increase in current in the peak γ is defined by E_i rather than by E_D, because $E_i - E_D \gg kT$. Consequently, integrating the "purified" current between T_0 and a given temperature $\tilde{T}$, we can determine the number of holes accumulated at the interface in the range of temperatures from T_0 to $\tilde{T}$. Finally, curve *3* in Fig. 1b illustrates the behavior of the surface potential $U(T)$ of the semiconductor in the course of the thermally stimulated relaxation of the MIS structure.

In order to use the above tools to study the generation of minority charge carriers and the TSD, we have to independently determine the following seven parameters: N_0, N_D, τ_i, τ_{DC}, τ_{DV}, E_D, and E_i. The procedure for determining the quantities N_{DC}, τ_{DC}, and E_D was developed in [14]: E_D and the ratio N_D/τ_{DC} are determined from the region of the initial slope of peak α "freed," according to [16], from the component of current caused by the relaxation of the width of space-charge region, and the concentration N_D is estimated from the quasi-equilibrium value W_∞ corresponding to kinks in the dependences $W(T)$, $p_s(T)$, or $U(T)$ (these points are indicated by arrows in Fig. 1). The accuracy of estimation of N_D increases if the experiments are performed with a nonpolarized MIS structure ($N_0 \sim 0$ and the peak γ is absent). A conceptually similar procedure can be easily implemented to determine N_0, τ_i, and E_i. However, in this case, it is necessary to exclude the possibility that both the variation in $W(T)$ and the "tails" of the current peak α contribute to the peak γ. The latter contribution is eliminated by thermal "purification" of the current peaks obtained for small band bendings ($p_s \ll N_0$ and $U_0 < E_D - F$), in which case there is practically no accumulation of minority charge carriers at the interface; this "purification" is accomplished by heating the sample from the temperature T_0 to the point corresponding to quasi-equilibrium of the minority charge carriers with subsequent cooling to T_0 and a repeat heating, for example, to the temperature corresponding to the peak. Current in the region of initial build-up of the peak $\gamma(T \sim T_0)$: $J \cong qN_0\tau_i^{-1}\exp(-E_i/kT)$; the slope of the straight line $\ln J = f(T^{-1})$ determines the value of E_i, and the intersection of this line with the axis $T^{-1} = 0$ defines the value of $N_0\tau_i^{-1}$ [1]; and N_0 is determined by integrating the TSD current. The frequency factor τ_{DV}^{-1} can be determined from independent experiments alone, for example, from observations of the kinetics of recombination of minority charge carriers. In the first approximation, we may assume that $\tau_{DV} = \tau_{DC}$.

We now compare the results of calculations with experimental data. The experiments were conducted using the conventional technique of thermally stimulated discharge of a MIS capacitor under the conditions of generation of minority charge carriers [14] and ionic depolarization [1]; MOS (100) structures consisted of a KEF-4.5 silicon (n-Si:P with $\rho = 4.5\ \Omega$ cm and the donor concentration of $N_d = 6.7 \times 10^{14}$ cm^{-3}), a thermal oxide with a thickness of $h = 1180$ Å, and an Al gate with an area of $S = 5.6 \times 10^{-3}$ cm^2. The sample was polarized at 473 K (for 30 min under a voltage of 10 V under the positive potential applied to the gate), was cooled to $T_0 \cong 100$ K, a depolarizing voltage $V_{g0} < 0$ was then applied to the gate, and the MOS structure was finally heated with a constant rate of $\beta \cong 0.17$ K/s. The method reported in [16] was used to measure the current $J(T)$ and the high-frequency capacitance $C(T)$ in the course of heating.

Figure 2 shows the results of experiments and the dependence $C_s^{-1}(T) = C^{-1}(T) - C_i^{-1}$. General qualitative correlation between the results of calculations (Fig. 1a) and experimental data is evident. The curves $J(T)$ exhibit two peaks of current, a low-temperature one (α) and a high-temperature peak (γ). The amplitude of the former peak increases as the degree of initial

depletion (i.e., the quantity U_0) increases, whereas the magnitude and the position of the latter peak remain virtually unchanged. In the temperature region of the peaks in the plot $C(T)$, the dependence $C_s^{-1}(T)$ exhibits steps, as in Fig. 1. For $|V_{g0}| < 15$ V, we have $U_0 < 0$, $C(|V_{g0}|) = C_i = \text{const} = 164$ pF, and the peak α of TSD is not seen; this indicates that there is an accumulation layer at the Si surface. Initial bendings of the bands $U_0(V_{g0}) = 2\pi q N_d W_0^2/\kappa_s$ (see the caption to Fig. 2) were calculated from the values of $C_s(T_0, W_0)$ according to conventional capacitance relationships (6). Thus, the peaks α in Fig. 2 should be related to thermal generation of holes, whereas the peaks γ should be attributed to thermally stimulated ionic depolarization.

Differences between the results of calculations and experimental data are also evident. Experimentally, the peaks α shift to lower temperatures, rather than to higher temperatures, as $U_0(V_{g0})$ increases; furthermore, the peaks become appreciably narrower, mainly due to a steeper build-up of current; in addition, the temperatures corresponding to the peaks are much lower than those obtained by calculations (cf. Figs. 1a and 2a). Therefore, the approach we developed cannot be used to quantitatively describe the general rules in generation of minority charge carriers. These discrepancies between theory and experiment stem from the inadequacy of the model used to describe the generation of minority charge carriers and are caused by a radical influence of ions on electronic properties of the Si surface, which manifests itself in an increased generation rate of holes and in its strong dependence on V_{g0}. An analysis of such an influence requires consideration of additional physical concepts that may involve the Franz–Keldysh effect in edge fields of ion spots at the interface [6, 20], the near-surface generation of minority charge carriers at the periphery of an MIS structure [21], and so on.

Deviations of experimental peaks γ (Fig. 2) from calculated peaks (Fig. 1) manifest themselves in a broadening of the regions near the extrema; in addition, gently sloping tails are evident. TSD curves of this type are described by an analytical model developed in [10, 11]. This model is based on the concepts of tunneling ionization of neutral complexes in the case where there exists a spread in the characteristic times of such ionization; this spread is caused by spatial distribution of neutral complexes over the insulator layer adjoining the semiconductor. The stage of depolarization related to the tunneling dissociation of neutral complexes sets in after the unbound ions have left the interface (in Fig. 2, this process is obscured by the tails of peaks α). The rate of tunneling ionization decreases with the observation time, because the neutral complexes more and more distant from the interface are consecutively ionized. In this stage of TSD, the current $J(T)$ is limited by the dissociation rate of neutral complexes alone, because the time of thermally activated transit of ions

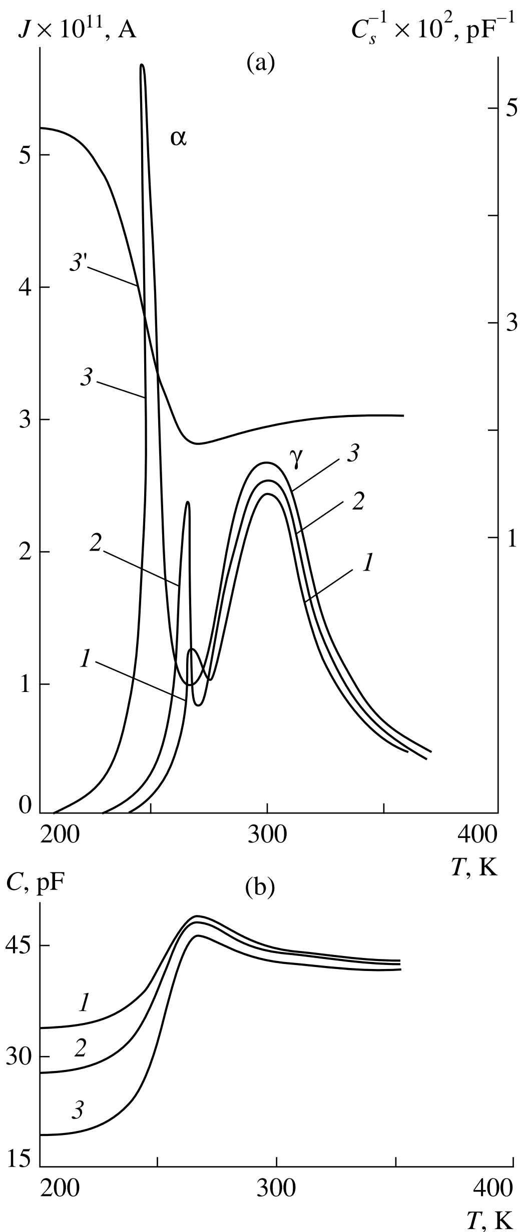

Fig. 2. (a) The thermally stimulated currents $J(T)$ (*1–3*) and the reciprocal capacitance of Si depletion layer $C_s^{-1}(T)$ (*3'*) in relation to the initial band bending U_0 = (*1*) 1.02, (*2*) 1.58, and (*3*, *3'*) 3.65 eV. (b) Temperature dependences of total high-frequency (1 MHz) capacitance of the sample for U_0 = (*1*) 1.02, (*2*) 1.58, and (*3*) 3.65 eV. The parameters of the studied Si-MOS structure were $S = 5.6 \times 10^{-3}$ cm^2, h = 118.0 nm, $N_d = 6.7 \times 10^{14}$ cm^{-3}, $N_D = 6.5 \times 10^{15}$ cm^{-3}, E_D = 0.79 eV [14], and β = 0.17 K/s.

through the dielectric gap becomes rather short in the temperature range under consideration [11]. As a result, the TSD peaks broaden and there appear the "tails" of the current that is independent of the depolarizing field, temperature, and the scanning rate β and is a single-val-

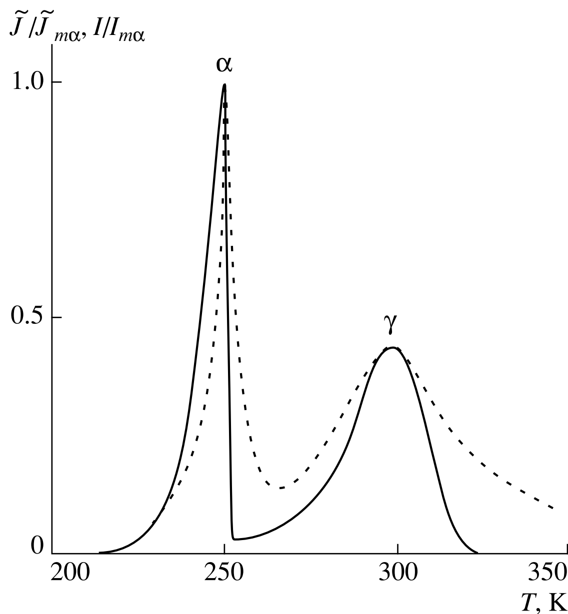

Fig. 3. Comparison of temperature dependence of the TSD current $\tilde{J}(T)/\tilde{J}(T_{m\alpha})$ calculated from equations (1)–(6) with experimental dependence $I(T)/I(T_{m\alpha})$ for $N_0 = 2 \times 10^{11}$ cm^{-2} and $E_i = 0.67$ eV (see the caption to Fig. 2 and curve *3* in Fig. 2a). The temperatures corresponding to the peaks and the ratios of the magnitudes of the peaks α and γ for calculated (continuous line) and experimental (dashed line) curves are fitted by adjusting the values of τ_D and τ_i ($\tau_D \longrightarrow 2.5 \times 10^{-13}$ s and $\tau_i \longrightarrow 3.4 \times 10^{-10}$ s) and the value of initial bending of the bands U_0 ($U_0/300k = 60$). The normalization factors $\tilde{J}(T_{m\alpha})$ and $I(T_{m\alpha})$ are the amplitudes of the peaks α in the calculated and experimental peaks, respectively.

ued function of the time $t = (T - T_m)/\beta$, where T_m is the temperature corresponding to the maximum of current. The behavior of the function $C_s^{-1}(T)$ in the vicinity of the peaks γ (Fig. 2) is consistent with this model: For moderately high U_0, the initial and final (equilibrium) states of the interface are close to each other; consequently, the initial and final values of C_s are also almost the same. In the transient process, there is an accumulation of positive ions at the interface (due to dissociation of neutral complexes); these ions subsequently leave the surface. This is why, in the course of transition from initial depletion to final equilibrium, the function $C_s^{-1}(T) \propto W(T)$ at first decreases, then attains a minimum, and finally increases. Such behavior is directly indicative of neutralization of ions and clearly manifests itself in the results of numerical simulation of the dependences $C_s^{-1}(T, U_0)$ under the conditions where positive ions localized at the interface are neutralized by electrons from the accumulation layer in the semiconductor ([12]; Fig. 2, curves *1*, *2*). Consequently, rigorous quantitative description of the peaks γ (Fig. 2) is also impossible without invoking the above model of dissociation of neutral complexes; in general, this model can be easily included in the scheme of calculations. Nevertheless, by following the above-considered algorithms for processing the experimental data, we can still gain a certain insight into the characteristics of the structures under investigation. Thus, considering the initial region of the current build-up in the peak γ, which is thermally decontaminated from the tail of the peak α, and introducing, in accordance with [16], the correction for relaxation of the space-charge region, we obtain $E_i = 0.67$ eV, $N_0\tau_i^{-1} = 8.7 \times 10^{21}$ cm^{-2} s^{-1};[1] for the value $N_0 \cong 2 \times 10^{11}$ cm^{-2} determined by integrating the thermal-polarization current; the above yields $\tau_i \cong 2.3 \times 10^{-11}$ s. The temperature $T_{m\gamma}$ corresponding to the calculated peak γ for the given values of τ_i and E_i is found to be appreciably lower (by more than 20 K) than the experimental value of temperature ($T_{m\gamma} \cong 298$ K); on the other hand, the characteristic generation time of holes should be shorter than the lifetimes of ions captured by traps because the peak α precedes the peak γ (Fig. 2). The samples under investigation were prepared from a KEF-4.5 Si (n-Si:P, $\rho = 4.5\ \Omega$ cm) that is identical to the Si samples employed in [14], which makes it possible to use the data reported in [14] ($N_d = 6.7 \times 10^{14}$ cm^{-3}, $N_D = 6.5 \times 10^{15}$ cm^{-3}, $E_D = 0.79$ eV, and $\tau_D = 4 \times 10^{-12}$ s) in estimation. However, for these parameters, the temperature $T_{m\alpha}$ corresponding to the maximum of the hole-generation current is in the vicinity of 300 K [14] even for relatively small values of U_0, whereas the actual values of $T_{m\alpha}$ are in the range of 250–260 K (Fig. 2). Consequently, fitting the calculated values of $T_{m\alpha}$ and $T_{m\gamma}$ to the experimental values necessitates a significant decrease in E_D or τ_D or an increase in E_i or τ_i. The outcome of this fit, which results in an enhanced clarity of qualitative and quantitative discrepancies, between theory and experiment and in refining the understanding of these discrepancies is important for the development of models of actual TSD mechanisms that define the characteristics of the MIS structures. In Fig. 3, the results of the above fitting are shown for curve *3* in Fig. 2; this fitting is accomplished by a decrease in τ_D ($4 \times 10^{-12} \longrightarrow 2.5 \times 10^{-13}$ s) and an increase in τ_i ($2.3 \times 10^{-11} \longrightarrow 3.4 \times 10^{-10}$ s). Needless to say, the equivalent result could be also obtained by correspondingly varying the quantities E_D and E_i; however, the data on the value of E_i are fairly reliable, and the increasing portions of peaks α (Fig. 2) are not necessarily defined by a discrete activation energy [6, 20]. The need for quantitative correction of the values of τ_D and τ_i estimated experimentally and radical differences of the observed peaks α and γ from

[1] This procedure is correct because the peak γ (Fig. 1a) is controlled only by the rate of escape of ions from the interface; this rate governs the accumulation rate for holes.

the calculated peaks (narrowing of the first peak and broadening of the second peak) are clearly indicative of (i) an unconventional mechanism of generation of minority charge carriers and (ii) a manifestation of the effects of neutralization of ions at the SiO_2/Si interface in the course of ionic thermal depolarization.

Thus, the developed system of modeling physical tests (see also [12]) makes it possible to identify the contributions of the generation of minority charge carriers, the dissociation of neutral complexes, the ionic thermal depolarization of the insulator, and the variation in the width of the depletion layer in the semiconductor to the relaxation signals $J(U_0, T, t)$ and $C(U_0, T, t)$. Qualitative agreement between the theory and the experiment indicates that experimental data can be quantitatively analyzed practically without the use of any adjustable parameters; on the other hand, a discrepancy between calculated and experimental results indicates that the mechanisms of a generation of minority charge carriers and of ionic thermal depolarization are unconventional. This reasoning made it possible to gain insight into the decisive role of neutral complexes in the formation of TSD curves of Si-MOS structures and to elucidate the origin of the radical influence of ions concentrated near the SiO_2/Si interface on the generation of electron–hole pairs. This fact, on the one hand, makes urgent studies of the mechanism of minority charge carrier generation at anomalously low temperatures and, on the other hand, opens up new opportunities in the search for methods aimed at monitoring the composition of the medium surrounding an MIS structure and based on the pronounced effect of agents (e.g., ions) penetrating into the interface region on the generation of minority charge carriers. The above-formulated tests for realizing specific relaxation modes in MIS structures and the considered schemes for modification of experiments make it possible to both study the origin of discrepancies between theory and experiment and to determine (even when there are discrepancies) certain important parameters characterizing the relaxation of an MIS structure from a state of nonequilibrium depletion to a state of inversion.

REFERENCES

1. A. G. Zhdan and Yu. V. Markin, Fiz. Tekh. Poluprovodn. (St. Petersburg) **28**, 756 (1994) [Semicond. **28**, 444 (1994)].
2. A. G. Zhdan, Yu. V. Markin, and A. M. Sumaroka, Mikroélektronika **22**, 66 (1993).
3. E. R. Nicollian and J. R. Brews, *MOS (Metal–Oxide–Semiconductor) Physics and Technology* (Wiley, New York, 1982).
4. *Charge-Coupled Devices and Systems*, Ed. by M. J. Howes and D. V. Morgan (Wiley, Chichester, 1979; Énergoizdat, Moscow, 1981).
5. S. M. Sze, *Physics of Semiconductor Devices* (Wiley, New York, 1981; Mir, Moscow, 1984).
6. E. I. Gol'dman, A. G. Zhdan, and A. M. Sumaroka, Pis'ma Zh. Éksp. Teor. Fiz. **57**, 783 (1993) [JETP Lett. **57** (12), 797 (1993)].
7. K. Yamashita, M. Iwamoto, and T. Hino, Jpn. J. Appl. Phys. **20**, 1429 (1981).
8. M. R. Boudry and J. P. Stagg, J. Appl. Phys. **52**, 885 (1981).
9. M. L. Reed, Semicond. Sci. Technol. **4**, 980 (1989).
10. E. I. Gol'dman, A. G. Zhdan, and G. V. Chucheva, Fiz. Tekh. Poluprovodn. (St. Petersburg) **33** (1999) (in press).
11. E. I. Gol'dman, A. G. Zhdan, and G. V. Chucheva, Fiz. Tekh. Poluprovodn. (St. Petersburg) **33** (1999) (in press).
12. E. I. Gol'dman, A. G. Zhdan, and N. F. Kukharskaya, Fiz. Tekh. Poluprovodn. (St. Petersburg) **33** (3) (1999) (in press).
13. V. N. Vertoprakhov, B. M. Kuchumov, and E. G. Sal'man, *Composition and Properties of Si–SiO_2–M Structures* (Nauka, Novosibirsk, 1981).
14. E. I. Gol'dman, A. N. Zhdan, and A. M. Sumaroka, Fiz. Tekh. Poluprovodn. (St. Petersburg) **26**, 2048 (1992) [Sov. Phys. Semicond. **26**, 1152 (1992)].
15. E. I. Gol'dman and A. G. Zhdan, Mikroélektronika **23**, 3 (1994).
16. A. G. Zhdan, A. M. Klochkova, and Yu. V. Markin, Prib. Tekh. Éksp., No. 4, 140 (1994).
17. A. G. Zhdan, V. B. Sandomirskiĭ, and A. D. Ozheredov, Fiz. Tekh. Poluprovodn. (Leningrad) **2**, 11 (1968) [Sov. Phys. Semicond. **2**, 7 (1968)].
18. M. K. Bondry and J. P. Stagg, J. Appl. Phys. **50**, 942 (1979).
19. V. I. Antonenko, A. G. Zhdan, A. I. Minchenko, *et al.*, Fiz. Tekh. Poluprovodn. (Leningrad) **20**, 208 (1986) [Sov. Phys. Semicond. **20**, 131 (1986)].
20. E. I. Gol'dman, Fiz. Tekh. Poluprovodn. (St. Petersburg) **27** (2), 269 (1993) [Semiconductors **27**, 150 (1993)].
21. V. A. Gerdel', V. A. Zimoglyad, N. V. Zykov, *et al.*, Mikroélektronika **17**, 496 (1988).

Translated by A. Spitsyn

Semiconductors, Vol. 34, No. 3, 2000, pp. 284–290. Translated from Fizika i Tekhnika Poluprovodnikov, Vol. 34, No. 3, 2000, pp. 290–296.
Original Russian Text Copyright © 2000 by Slobodchikov, Salikhov.

Influence of Humidity and Hydrogen on the Charge Transport in *p*-InP Diode Structures with a Palladium Contact

S. V. Slobodchikov and Kh. M. Salikhov

Ioffe Physicotechnical Institute, Russian Academy of Sciences, ul. Politekhnicheskaya 26, St. Petersburg, 194021 Russia

Submitted August 23, 1999; accepted for publication August 23, 1999

Abstract—The *p*-InP–*n*-In_2O_3–P_2O_5–Pd diode structure was fabricated using a two-stage technological procedure, which involved cold etching, polishing, and electrochemical deposition of palladium. The charge transport is investigated in the temperature range of 110–300 K, and the current–voltage characteristics are explained in terms of tunneling through a barrier, over deep trapping centers, and band-to-band tunneling. It is found that the open-circuit photovoltage increases in a water vapor atmosphere. It is demonstrated that this effect is defined by the variation of the recombination kinetics via bound states on the *n*-In_2O_3–P_2O_5 heteroboundary because of the absorption of H_2O molecules in P_2O_5 oxide. The open-circuit photovoltage increases linearly with the water vapor concentration, and the relaxation of the photovoltage pulse takes ~1–2 s. Photovoltage relaxation for the forward and reverse currents after the action of H_2 is investigated. The data obtained revealed the possibility of devising a detector of threefold application, namely, for detecting near-infrared radiation, humidity, and hydrogen. © *2000 MAIK "Nauka/Interperiodica".*

Previously, we experimentally investigated the electrical and photoelectical properties of *p*-InP structures with a palladium contact. It was shown that these structures could be used as efficient detectors (sensors) of hydrogen [1–3]. It is characteristic that the variation of the open-circuit photovoltage in a hydrogen atmosphere can be appreciably larger than the variation in the electrical characteristics, namely, in forward or reverse currents. This was clearly demonstrated for the *p*(*n*)-Si structures [4]. It turned out that the method of obtaining the Pd–*p*(*n*)–InP structures both affects the charge-transport mechanism and brings about strong dependence on other external factors, in particular, on the humidity [2]. It was found that the open-circuit photovoltage varies most strongly in this case, whereas the forward and reverse currents vary only slightly. Humidity affects the structures grown by electrochemical deposition of palladium but has no effect on the structures grown by vacuum deposition of palladium. The data on the humidity dependence of the open-circuit photovoltage were first obtained in [2] in the case of Pd–*n*-InP structures. This paper is devoted to the results of investigations of charge transport in Pd–*p*-InP structures obtained by electrochemical deposition of Pd and to the effects of humidity and hydrogen on charge transport.

1. EXPERIMENTAL

(a) Technology

Czochralski-grown *p*-InP(100) crystals with the hole concentration $p = 5 \times 10^{18}$ cm^{-3} were used to fabricate the diode structures. A substrate with a high charge carrier concentration was chosen in order to reduce the relaxation times after the action of the water vapor pulse on *n*-InP-based structures as was observed in [2]. Since the decrease in the absolute value of the open-circuit photovoltage is apparent in this connection, the structures we fabricated were kept in air for a long time (about 0.5 year) in order to compensate it to some extent. The required photoresponse level was obtained as a result of structural rearrangement processes, which were considered in [4]. Before palladium deposition, the crystals were thoroughly etched and polished in order to remove the mechanically damaged layer and then were cleaned and degreased. Two procedures were tested, and chemical etching in a cold etchant was found to be the optimum one. At first, the surface was sequentially cleaned with acetone, sulfuric acid, and a $H_2SO_4 + H_2O_2 + H_2O$ solution (for 1 min). After that, the surface was polished in the polishing etchant Br (5%) + CH_3COOH (95%) and was repeatedly subjected to the above cleaning operations. Subsequently, palladium was electrochemically deposited through a mask of chemically resistant lacquer. The electrolyte included $PdCl_2$, $Na_2PO_4 \cdot 12H_2O$, and C_6H_5COOH. Deposition was carried out at 50–60°C at a current density of 1 mA/cm^2. The palladium layer thickness was ~400 Å, and the active area was 7×10^{-2} cm^2. The nonrectifying contacts for the rear surface of the substrate were deposited by evaporation of the Ag/Zn alloy.

(b) Measurements and Their Results

The current–voltage characteristics were measured at $T = 110$ K and $T = 300$ K. The temperature depen-

dence of the forward and reverse currents in the range T = 110–300 K was also measured. The steady-state open-circuit photovoltage of the structures was measured at T = 300 K, as well as its dependence on the pulse effect of water vapor and hydrogen. The relaxation process of the forward and reverse currents and the open-circuit photovoltage under the effect of water vapor and hydrogen were investigated. The measurements were carried out under steady-state conditions using mainly conventional measuring devices and units.

The typical current–voltage characteristics of the structures recorded at T = 110 K and T = 300 K are shown in Fig. 1. Their characteristic features are the following. The forward portion for T = 300 K can be described by the dependence

$$I \sim \exp\frac{qV}{n_1 kT} \tag{1}$$

in the voltage range of ≤0.2 V. In this case, the coefficient n_1 = 1.3 (curve *1*). As the temperature is lowered to T = 110 K, the dependence remains exponential, but with n_1 = 3.4 (curve *2*). The reverse portion, excluding the bias range ≤0.1 V, shows a power dependence (curves *3*, *4*)

$$I \sim V^{n_2} \tag{2}$$

with n_2 = 3.3–3.5. This dependence is observed with an identical slope at both temperatures, and only a moderate difference in currents is found. The form of the temperature dependence of the forward and reverse currents is also somewhat similar (Fig. 2). A narrow range of constant currents is observed at low temperatures. As the temperature increases, the dependence transforms into the linear function $\log I = f(T)$. The reverse current becomes almost independent of temperature with increasing bias (curve *3* for V = 0.42 V).

An increase in the open-circuit photovoltage depending on the humidity is of special interest (Figs. 3–5). The dependence of the open-circuit photovoltage on the wavelength of the exciting radiation for constant water vapor pulse is presented in Fig. 3. The largest increase in open-circuit photovoltage is observed on both the short- and long-wavelength sides of the spectral range of indium phosphide sensitivity. The photovoltage dependence on the water vapor concentration is nonlinear (Fig. 4). The photovoltage relaxation under the effect of the water vapor pulses takes ≤2 s for both the ascending and descending portions of the curve (Fig. 5).

The relaxation curves for open-circuit photovoltage for the forward and reverse currents under the pulse effect of hydrogen are shown in Figs. 6 and 7. As can be seen, the relaxation times are approximately equal for the open-circuit photovoltage and the reverse current. The relaxation time for the forward current is three times greater.

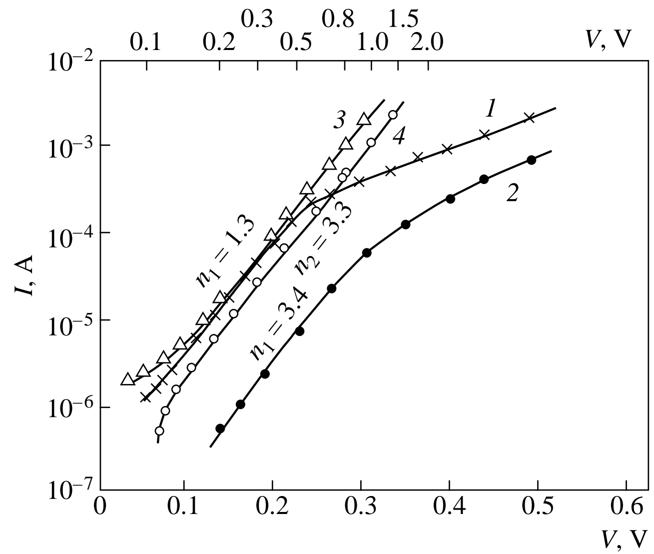

Fig. 1. Current–voltage characteristics of the p-InP–n-In_2O_3–P_2O_5–Pd structures. Forward portions (positive voltage is applied to p-InP) $\log I = f(V)$: curves *1* and *2*. Reverse portions $\log I = f(\log V)$ the upper horizontal scale: curves *3* and *4*. T = (curves *1*, *3*) 300 and (curves *2*, *4*) 110 K.

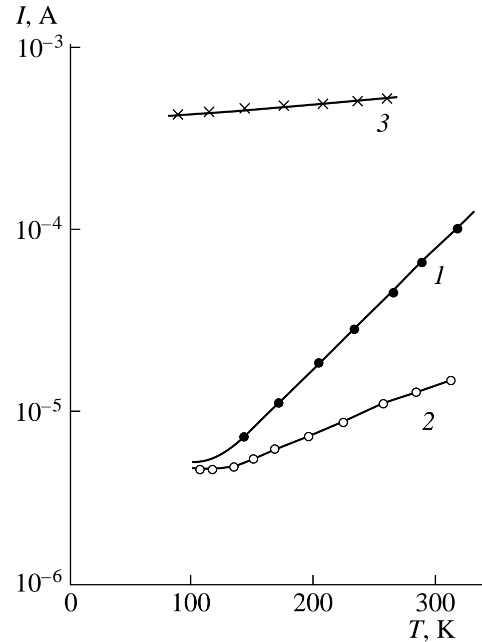

Fig. 2. Temperature dependences of the forward and reverse currents. V = (*1*) 0.2, (*2*) 0.2, and (*3*) 0.42 V.

2. DISCUSSION OF RESULTS

2.1. A Model of the Structure and the Charge Transport Mechanism

When analyzing the overall set of data obtained, we can conclude that the object of our investigations is not a simple Pd–p-InP Schottky diode. Both the shape of the current–voltage characteristics and their tempera-

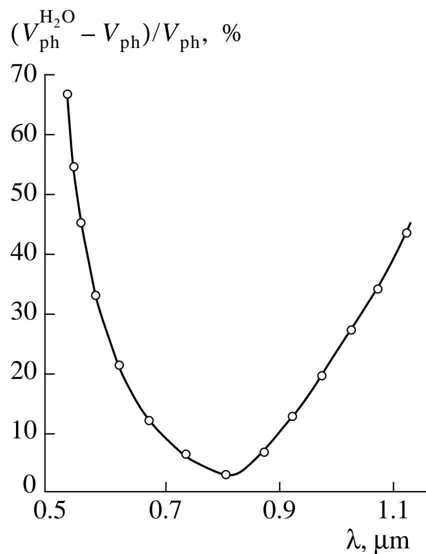

Fig. 3. Open-circuit photovoltage rise (%) on the water vapor pulse effect as a function of the wavelength of the exciting light.

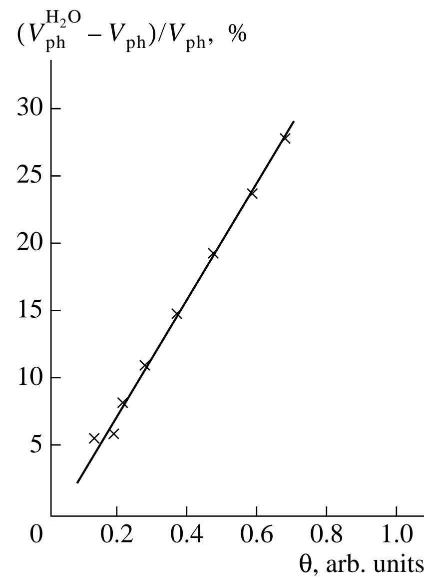

Fig. 4. Photovoltage change (%) as a function of the water vapor concentration.

ture dependence differ from those for a conventional metal–semiconductor structure. The phenomena related to the humidity effect on the open-circuit photovoltage seem to be inexplicable. The photovoltage variation under the effect of the hydrogen pulse and its relaxation also differ from those measured previously.

We analyzed the published data on the physicochemical processes of oxidation of the InP surface [5–7]. In terms of the results of [8], the totality of experimental results can be explained on the basis of a model of the structure and its possible energy diagram, which are presented in Fig. 8. It is our opinion that the complex diode structure Pd–P_2O_5–n-In_2O_3–p-InP was formed by the action of three main factors. These are (i) the cold etching and polishing, (ii) the electrochemical deposition of palladium, and (iii) the relatively prolonged holding period in air. It is possible that one of the first two factors is the main one while the third is of secondary importance. We did not have the opportunity to perform the corresponding physicochemical analysis. In connection with this, it should be mentioned that the structure with n-In_2O_3 and P_2O_5 layers was successfully obtained by electrochemical deposition using a solution of H_3PO_4 in propylene glycol [7].

Possible mechanisms of charge transport should be considered in terms of the model of the structure, which is presented in Fig. 8. The P_2O_5 oxide is assumed to be an insulator with a proposed band-gap width of $E_G \approx$ 8 eV, n-In_2O_3 is a partially degenerate semiconductor with $E_G \approx 3.6$ eV. The voltage applied to this structure can be written as

$$V = \Delta V_1 + \Delta V_2 + \Delta V_3, \quad (3)$$

where ΔV_1 is the voltage drop at the p-InP–n-In_2O_3 heterojunction, ΔV_2 is the voltage drop on the n-In_2O_3–P_2O_5 heteroboundary, and ΔV_3 is the voltage drop across the P_2O_5 dielectric layer. The current passing through the structure is defined by the contributions of the corresponding resistances R_1, R_2, and R_3. In the first approximation, two main regions restrict the current passing through the structure. The first region is the p-InP–n-In_2O_3 heteroboundary (R_1), and the second

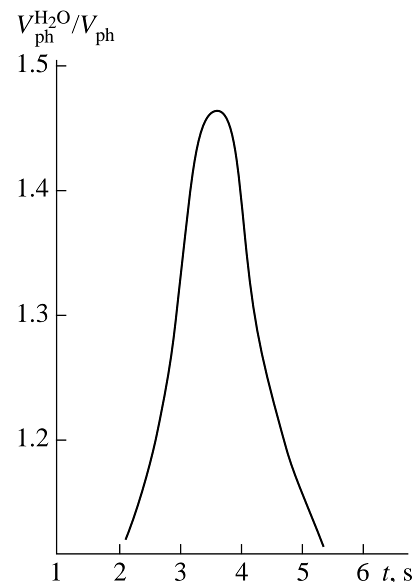

Fig. 5. Photovoltage pulse responding to the water vapor "pulse."

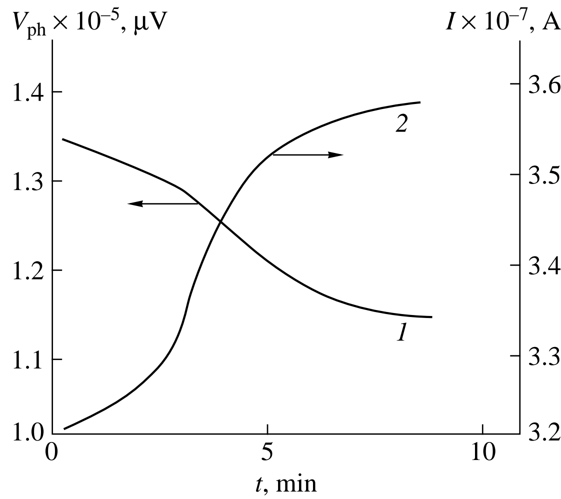

Fig. 6. Relaxation of (*1*) the open-circuit photovoltage and (*2*) reverse current under the hydrogen pulse effect.

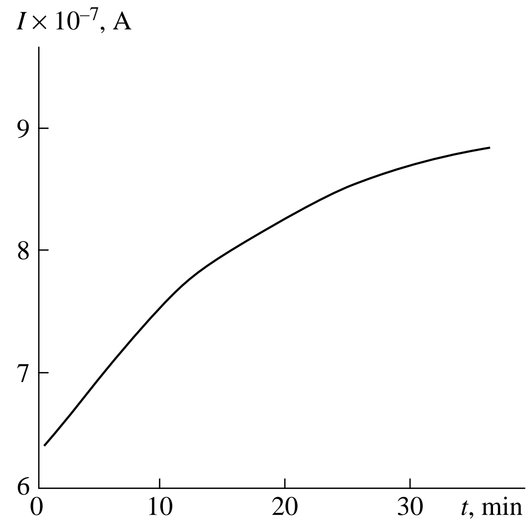

Fig. 7. Relaxation of the forward current after hydrogen pulse cessation.

one is related to the presence of the P_2O_5 insulator layer and Schottky barrier ($R_2 + R_3$). The current magnitude is defined as

$$I = \frac{V}{R_1(V) + R_2(V) + R_3(V)}. \quad (4)$$

The dependences of current on the voltage and temperature are defined by the relative contribution of the R_1 and $R_2 + R_3$ regions to the resistance. Let us consider the charge transport mechanism in the low-temperature region of the measured temperature range. The overall independence of the current on temperature at the forward and reverse biases can be regarded as a consequence of the field emission. In this case, the tunneling current for the second region can be represented as [9]

$$I \sim \exp\frac{V}{E_{00}}, \quad (5)$$

where E_{00} is an almost constant quantity. Such a dependence in the forward portion of the current–voltage characteristic is observed for a Schottky diode based on a degenerate semiconductor. At T = 110 K, E_{00} = 0.29 V. Taking into account that, for n-In_2O_3 with $m_r^* = 0.55m_0$ [10], $\varepsilon = 7$, and assuming that the concentration $N_d \le 10^{20}$ cm^{-3}, we use

$$E_{00} = 18.5 \times 10^{-15}\left(\frac{N_d}{m_r^*\varepsilon}\right)^{1/2} \quad (6)$$

to obtain $E_{00} \ge 0.1$ V. Since $E_{00}/kT > 3$ even at room temperature, one would expect dependence (5) to be valid for the entire temperature range. However, as can be seen from Fig. 2, this is not observed. The charge transport in the major part of the temperature range up to $T = 300$ K can be explained in terms of the main contribution of R_1 in (4). The latter resistance is defined by the region of the p-InP–n-In_2O_3 heteroboundary. In this connection, the model that was used for this heterojunction in [8] can be applied. The main channel of charge transport in this model is tunneling through the trapping centers in n-In_2O_3 (Fig. 8b). The hole concentration in p-InP is below the critical degeneracy concentration, which exceeds 10^{19} cm^{-3}. As a result, the second step of the (B–C) transition is apparently defined by the transition into the tail of the density of states of the valence band in p-InP. The tunneling current through trapping centers of density D is given by

$$I \simeq A_1 D\exp[-\alpha(E_G - qV - qV_n)], \quad (7)$$

where A_1 and α are constants, and V_n is the Fermi level shift in relation to the conduction band bottom for n-In_2O_3. Then, since $E_G = E_G(0) - \beta T$, where β is the temperature coefficient of the E_G variation, we have

$$I \simeq A_1 D\exp\{-\alpha[E_G(0) - qV] + \alpha\beta T\}. \quad (8)$$

It follows from (8) that the temperature dependence $\log I = f(T)$ is linear for a constant V and is exponential as a function of V. The slope of the straight line for the tunneling current (Fig. 2, curve *1*) is ~0.007. The order of magnitude for the relative effective mass of the tunneling electron can be estimated from the relationship

$$\frac{8\pi(m_r^*)^{1/2}Wq^{3/2}\beta}{6qh} \sim 0.007.$$

The width of the space charge layer is estimated from the relationship for an abrupt heterojunction with $N_a = 5 \times 10^{18}$ cm^{-3}, $N_d \sim 10^{20}$ cm^{-3}, $\varepsilon = 11$ (for InP), and

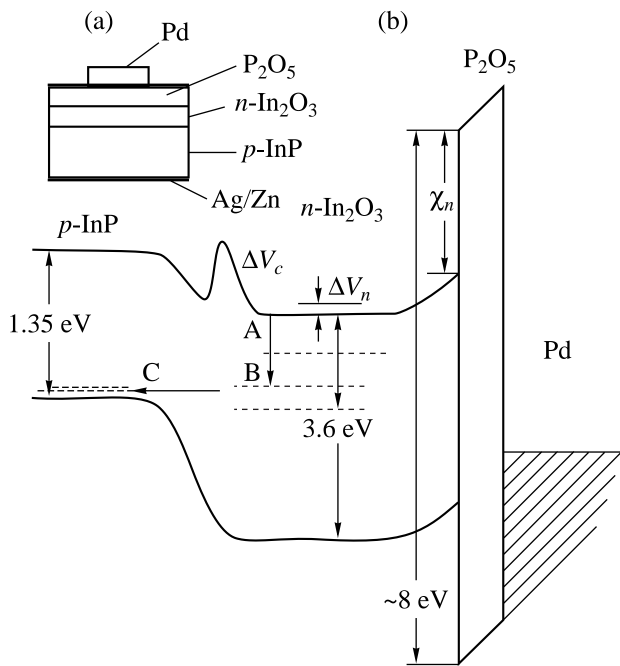

Fig. 8. (a) Schematical representation of the structure and (b) energy-band diagram.

$W = \left[\frac{\varepsilon(V_k - V)}{2\pi q N_a}\right]^{1/2}$, with $V_k \leq 0.6$ eV [8]. In this case, $W = 10^{-6}$ cm; and for $\beta = 2.9 \times 10^{-4}$ eV/K, the reduced effective mass $\approx 0.04m_0$. This value is close to that calculated for InP from the density states.

The reverse portion of *I–V* curve of the structure has a characteristic dependence with a slope of $n_2 = 3.3$ at both $T = 110$ and 300 K, with a slight difference in absolute values of the current. Similarly to [8], such a power dependence for this structure can be accounted for by band-to-band tunneling. In this case, the exponential dependence

$$I \sim \exp[-4(2m_r^*)^{1/2}(E_{G1} + \Delta V_c)^{3/2}/3qh(V_d - V)^{1/2}] \quad (9)$$

can be expressed as a power one. Band-to-band tunneling should be observed for a limited voltage range. For this reason, the straight line *3* in Fig. 2, which was measured at $V = 0.42$ V, can be defined by tunneling through the second region ($R_2 + R_3$). This line corresponds to the field-enhanced thermal emission at the forward (for this region) bias.

2.2. Open-Circuit Photovoltage of the Structure and Its Dependence on Humidity

One of the most interesting properties of the structure we investigated is a considerable increase in photosensitivity (photovoltage) in the presence of water vapor. We were the first to observe this phenomenon [2] in n-InP-based structures. It is evident that the second region of n-In_2O_3–P_2O_5–Pd plays the main role in this phenomenon. For this reason, the presence of the intermediate P_2O_5 layer, which acts as an adsorber of H_2O, is of basic importance. It is noteworthy that we had never observed this phenomenon in our previous investigations [11, 12] of diode structures with a palladium contact.

For low signal levels, which are related to the limiting sensitivity of the structure, the open-circuit photovoltage can be represented as

$$V_{ph} \simeq I_{ph}R_0, \quad (10)$$

where I_{ph} is the short-circuit current, and R_0 is the resistance at the zero bias. Hence, the photovoltage variation should be defined either by the variation of one or the other parameter or by the preferential variation of one of them. Water vapor adsorption by the P_2O_5 oxide should considerably vary the properties of the oxide layer and very significantly affect the characteristics of the n-In_2O_3–P_2O_5 and P_2O_5–Pd heteroboundary. The experiments demonstrated that both the forward and reverse currents of the structure as a whole undergo practically no variation under the water vapor effect. The behavior of n-InP-based structures is almost the same [2]. A slight rise in the reverse current was observed for only some of these samples. For this reason, we should assume that the photovoltage rise is caused mainly by an increase in I_{ph}, i.e., eventually by the variation of the characteristics of nonequilibrium minority carriers.

Taking into account the intermediate P_2O_5 layer, the photocurrent can be expressed as

$$I_{ph} \simeq \frac{I_{ph0}}{1 + D_1\sigma_n f_s \exp(bn\chi_n^{1/2}\delta)}, \quad (11)$$

where I_{ph0} is the Schottky diode photocurrent without an intermediate layer, D_1 is the density of bound states at the n-In_2O_3–P_2O_5 heteroboundary, σ_n is the electron capture cross section, f_s is the occupation probability for bound states, b_n is the tunneling factor, χ_n is the height of the semiconductor–insulator barrier, and δ is the thickness of the P_2O_5 insulator layer. It is highly improbable that appreciable variation of the oxide transparency factor $bn\chi_n^{1/2}\delta$ would be observed on water vapor adsorption. On the contrary, a drastic variation of the preexponential multiplier $D_1\sigma_n f_s$, which reflects the recombination characteristics of minority carriers, should be expected. One can suppose that the recombination flux of minority carriers to the bound states of D_1 density, which are located at the n-In_2O_3–P_2O_5 interface, is large in the absence of the water vapor pulse. In this case, in (11), $D_1\sigma_n f_s \exp(bn\chi_n^{1/2}\delta) > 1$. The quantity D_1 should decrease considerably under the effect of the water vapor pulse. This would bring about an increase in the minority carrier lifetime τ_n. A possible

mechanism for this variation is defined by the interaction between H_2O molecules and bound states at the heteroboundary. According to the data from [13], no significant dissociation of H_2O molecules is observed during their interaction with the surface of the semiconductor, although a slight partial dissociation cannot be excluded. It is known that orthophosphoric acid H_3PO_4 is formed by the water effect on P_2O_5. We believe that this process does not play a significant role during a short-width pulse. It is found that adsorption of H_2O impairs the insulating characteristics of P_2O_5; in particular, its conductivity increases. Taking into account all these factors, we can assume that molecular adsorption of H_2O leads to oxide lattice "expansion" and formation of new "defect" bound states at the heteroboundary and in the bulk P_2O_5. These new states suppress the influence of the initial states by lowering their concentration D_1. Since we may consider that $D_1 \sim 1/N_0$ for this process, where N_0 is the concentration of adsorbed water molecules on the heterointerface, then

$$I_{ph} \sim \frac{I_{ph0} N_0}{\sigma_n f_s \exp(bn\chi_n^{1/2}\delta)}, \tag{12}$$

i.e., the open-circuit photovoltage V_{ph} should be proportional to the water vapor concentration. The corresponding linear characteristic is presented in Fig. 4. It can be seen from Fig. 3 that the maximum rise in the absolute values of the open-circuit photovoltage are observed in the short- and long-wavelength regions of the spectral range of 0.5–1.1 μm. We believe that this dependence is related to occupancy of the D_1 centers by excess minority carriers. A high excitation level near the fundamental-absorption edge for *p*-InP yields a high concentration of electron–hole pairs; in this case, the quantities Δn and Δp can be comparable to D_1. In these conditions, the recombination characteristics are varied because of minority carrier capture by the D_1 bound states and the water vapor pulse hardly affects the recombination kinetics. The suppression of recombination activity for D_1 centers is practically absent in this case. It is characteristic that the photovoltage rise is nearly absent for $\lambda = 0.8$ μm, which corresponds to the maximum of the spectral curve of the open-circuit photovoltage. A decrease in photocurrent is observed in the short-wavelength region because of surface recombination at the *p*-InP–*n*-In_2O_3 heteroboundary, and in the long-wavelength region, this decrease is due to the weak absorption in the *p*-InP substrate. In both cases, the number of excess carriers at the *n*-In_2O_3–P_2O_5 heteroboundary is small and the effect of suppression of bound states D_1 is pronounced.

The relaxation time of the photovoltage pulse (Fig. 5) is small (about 1–2 s) for both ascending and descending slopes. This fact may also confirm that no dissociation of H_2O molecules is observed during adsorption in the P_2O_5 oxide under our experimental conditions.

2.3. Influence of Hydrogen on the Electrical Characteristics and Open-Circuit Photovoltage

The relaxation curves for the forward and reverse currents, as well as for open-circuit photovoltage (Figs. 6, 7) after the hydrogen pulse, should reflect the features of the charge transport mechanism with and without illumination. The symmetrically opposite run of curves *1* and *2* (Fig. 6), which define the relaxation of open-circuit photovoltage and reverse current, is characteristic. Since, for a structure with an intermediate layer

$$V_{ph} \sim \frac{kT}{q}\ln\left[\frac{I_{ph}}{I_{p0}\exp(bp\chi_p^{1/2}\delta)} + 1\right], \tag{13}$$

it follows from (13) that the variation of the dark current determined from $I_{p0}\exp{-(bp\chi^{1/2}\delta)}$ brings about the opposite variation of V_{ph}.

It was already noted [4] that a dipole layer can form on the dissociation of H_2 at the heteroboundary. This brings about an increase in the barrier height and a decrease in the transparency factor of the intermediate layer. Since both processes are related to each other, the relaxation times for the reverse current and open-circuit photovoltage are identical and equal ~9 min. The relaxation time for the forward current is more than three times longer, exceeding 30 min (Fig. 7). This phenomenon may have various causes. One of the most probable is that "temporary" deep levels, which are formed during hydrogen adsorption, serve as effective trapping levels for the majority carriers. The relaxation time for these levels after cessation of the H_2 pulses is large. Since the variation of the forward current is not large, it is difficult to estimate the energy of these levels analytically.

In conclusion, we note that the results obtained for the investigated structure *p*-InP–*n*-In_2O_3–P_2O_5–Pd are of interest, on the one hand, as hybrid structures with several types of tunneling current transport mechanisms. On the other hand, they are of interest as structures with potential for use in triple detection, namely, of near-infrared radiation, humidity, and hydrogen.

ACKNOWLEDGMENTS

We are grateful to A.M. Marinina for help in the sample preparation technology.

REFERENCES

1. G. G. Kovalevskaya, L. Kratepa, M. M. Meredov, *et al.*, Pis'ma Zh. Tekh. Fiz. **15** (12), 55 (1989) [Sov. Tech. Phys. Lett. **15**, 478 (1989)].
2. G. G. Kovalevskaya, A. M. Marinova, and S. V. Slobodchikov, Zh. Tekh. Fiz. **59** (11), 155 (1989) [Sov. Phys. Tech. Phys. **34**, 1327 (1989)].
3. S. V. Slobodchikov, G. G. Kovalevskaya, M. M. Meredov, *et al.*, Pis'ma Zh. Tekh. Fiz. **17** (15), 1 (1991) [Sov. Tech. Phys. Lett. **17**, 535 (1991)].

4. G. G. Kovalevskaya, M. M. Meredov, E. V. Russu, *et al.*, Zh. Tekh. Fiz. **63** (2), 185 (1993) [Tech. Phys. **38**, 149 (1993)].
5. K. M. Geib and C. M. Wilmsen, J. Vac. Sci. Technol. **17**, 952 (1980).
6. J. F. Wager, D. L. Ellsworth, S. M. Goodnick, *et al.*, J. Vac. Sci. Technol. **19**, 513 (1981).
7. D. H. Laughlin and C. M. Wilmsen, Appl. Phys. Lett. **37** (10), 915 (1980).
8. M. M. Meredov, G. G. Kovalevskaya, E. V. Russu, *et al.*, Fiz. Tekh. Poluprovodn. (Leningrad) **26** (9), 1590 (1992) [Sov. Phys. Semicond. **26**, 893 (1992)].
9. F. A. Padovani and R. Stratton, Solid-State Electron. **9**, 695 (1966).
10. R. L. Weiher, J. Appl. Phys. **33**, 2834 (1962).
11. G. G. Kovalevskaya, M. M. Meredov, E. V. Russu, *et al.*, Fiz. Tekh. Poluprovodn. (Leningrad) **26** (10), 1750 (1992) [Sov. Phys. Semicond. **26**, 978 (1992)].
12. S. V. Slobodchikov, E. V. Russu, Kh. M. Salikhov, *et al.*, Pis'ma Zh. Tekh. Fiz. **21** (10), 50 (1995) [Tech. Phys. Lett. **21**, 791 (1995)].
13. G. J. Hughes, T. P. Humphreys, V. Montgomery, *et al.*, Vacuum **31** (10–12), 539 (1981).

Translated by N. Korovin

Semiconductors, Vol. 34, No. 3, 2000, pp. 291–295. Translated from Fizika i Tekhnika Poluprovodnikov, Vol. 34, No. 3, 2000, pp. 297–301.
Original Russian Text Copyright © 2000 by Aleksandrov, Gavrikova, Zykov.

SEMICONDUCTOR STRUCTURES, INTERFACES, AND SURFACES

Study of GaN:O Films and Related Heterostructures

S. E. Aleksandrov, T. A. Gavrikova, and V. A. Zykov

St. Petersburg State Technical University, ul. Politekhnicheskaya 29, St. Petersburg, 195251 Russia

Submitted January 11, 1999; accepted for publication, September 23, 1999

Abstract—GaN:O solid solution films with various content of oxygen were obtained by the vapor phase deposition method using pyrolytic decomposition of gallium monoammine chloride in the presence of water vapors on substrates of crystalline quartz and silicon. Structure and optical properties of the films were studied to find that, as the oxygen content in the films increased, the energy gap at 300 K increased from 3.4 to 3.9 eV. Photoelectric properties of Si/GaN:O heterojunctions were studied. In a temperature range of 80–290 K, all heterojunctions are photosensitive; the photoresponse and the spectral characteristics depend on the oxygen content in the GaN:O film. The specific features of the "metallurgical" boundary of the heterojunction are discussed.
© 2000 MAIK "Nauka/Interperiodica".

INTRODUCTION

Introduction of oxygen into gallium nitride is accompanied by the formation of oxynitride solid solutions GaN:O. The maximum solubility of oxygen in gallium nitride, corresponding to the quasibinary section GaN–Ga_2O_3, is ~30 at. % at $T = 700–900°C$ [1, 2]. Oxygen is assumed to occupy positions in the anion sublattice of the crystal structure of GaN, substituting for nitrogen. One of the manifestations of this substitution is a decrease in the concentration of donor-type nitrogen vacancies, which can be judged from a decrease in the conductivity of samples containing oxygen [3]. The effect of oxygen on the electronic properties of GaN are not fully understood, since formally the substitution of a group VI element for a group V element should give a donor effect, which contradicts the experimentally observed decrease in the conductivity upon doping GaN with oxygen. Apparently, the electron effects of oxygen are not so simple as follows from formal analysis, which can be judged from its behavior in gallium nitride analogues such as gallium phosphide and gallium arsenide [4]. No information on the physical properties of oxynitride solid solutions exists in the literature. Nevertheless, the high solubility of oxygen in GaN, along with the marked difference in the physical parameters of gallium nitride and gallium oxide, gives hope that by doping gallium nitride with oxygen, we will be able to change physical characteristics of the nitride material in sufficiently wide limits.

In this paper, we present the results of our investigation of optical and photoelectric properties of GaN:O films (with various contents of oxygen) and of Si/GaN:O heterostructures.

EXPERIMENTAL

GaN:O films were prepared by the chemical vapor deposition method in a chloride–hydride system [2, 3] using pyrolytic decomposition of gallium monoammine chloride (GMAC). To dope the growing film with oxygen, we introduced water vapors into the reaction space. The amount of oxygen in the material was controlled by varying the relationship between the concentrations of the oxidizing and nitriding elements in the vapor–gaseous mixture. The films were grown on substrates of optical quartz. The temperature in the deposition zone in all experiments was identical, equal to 750°C; the GMAC pressure was $P_{GMAC} = 160$ Pa; and the partial pressure of water vapors (P_{H_2O}) varied from 0 to 100 Pa.

RESULTS AND DISCUSSION

In order to determine the band parameters of GaN:O solid solutions, we experimentally studied spectral

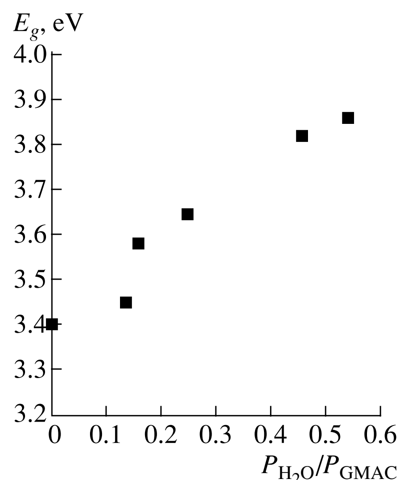

Fig. 1. Energy gap of GaN:O films grown on quartz substrates as a function of oxygen content in the gaseous mixture.

1063-7826/00/3403-0291$20.00 © 2000 MAIK "Nauka/Interperiodica"

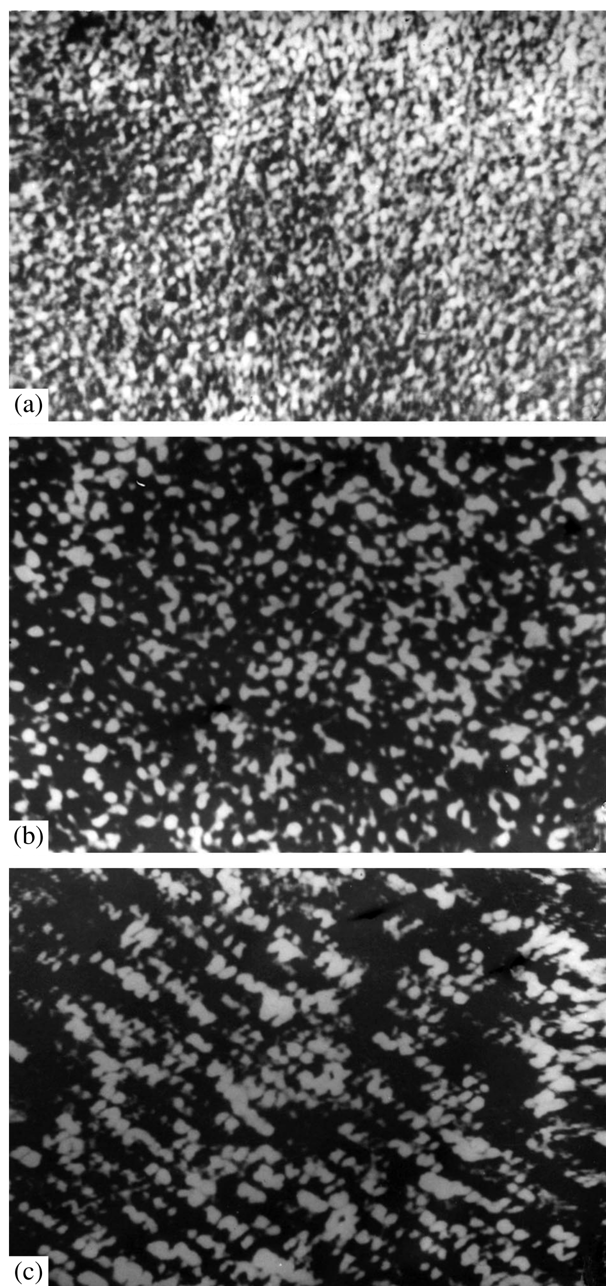

Fig. 2. Structure of the surface of GaN⟨O⟩ films grown on silicon substrates using various partial pressures of water vapors P_{H_2O}/P_{GMAC}: (a) 0, (b) 0.267, and (c) 0.725. Magnification ×5000.

characteristics of light absorption coefficient on a series of film samples of oxynitrides obtained using the chloride–hydride technology at various partial pressures of water vapors in the reaction mixture. The investigations showed that as the P_{H_2O}/P_{GMAC} ratio increased from 0 to ~0.6, the optical energy gap E_g increased from 3.4 to ~3.9 eV (Fig. 1). Along with an increase in E_g, a significant (by several orders of magnitude) growth in resistivity was detected in doped films. This growth is related to a significant decrease in the concentration of electrons in the film, whose presence in gallium nitride is caused by nitrogen vacancies. Structural investigations show that, while the P_{H_2O}/P_{GMAC} ratio does not exceed 0.35, the oxynitride films consist of homogeneous solid solutions of oxygen in gallium nitride with a structure inherent in the GaN. At higher concentrations of water vapors in the reaction mixture, X-ray diffraction patterns contain β-Ga_2O_3 lines, whose intensity increases with increasing P_{H_2O}. The second phase appears as discrete oxide inclusions in electron-microscopic micrographs of the film surface; first, these inclusions are isolated (Figs. 2a, 2b); at higher P_{H_2O}/P_{GMAC} ratios, they form a virtually continuous layer, which covers the whole surface of the oxynitride film (Fig. 2c).

At the same time, in spite of the appearance of the second phase inclusions, the lattice parameters of gallium oxynitrides continue to change monotonically (the c parameter increases, while the a parameter decreases) even at $P_{H_2O}/P_{GMAC} > 0.35$ (up to $P_{H_2O}/P_{GMAC} \simeq 0.6$). This indicates that the appearance of the oxide phase at small P_{H_2O}/P_{GMAC} ratios is not the consequence of saturation of the oxynitride film with oxygen. It is reasonable to suppose that the formation of the oxide phase is not related to the decomposition of supersaturated oxynitride solid solutions but occurs as a result of chemical interaction in the vapor phase, so that the oxide product arrives into the growing film in the form of ready β-Ga_2O_3 particles.

Thus, the gallium oxynitride films obtained in our work in reality represent a set of solid solutions of oxygen in gallium nitride which have greater energy gaps E_g in comparison with GaN and significantly smaller concentrations of charge carriers, supposedly because of the less perfect structure of the anion sublattice. Such a combination of the material parameters is favorable for photoelectric applications, in particular for the production of radiation detectors for visible and near ultraviolet ranges on the basis of Si/GaN:O heterojunctions.

Silicon–gallium oxynitride heterojunctions (HJs) were obtained by depositing gallium oxynitride films (with various oxygen content) onto n- and p-type silicon substrates with charge-carrier concentrations of 1.5×10^{15} cm^{-3}. The films were grown by the technique described above under conditions of a controlled humidity.

The heterojunctions obtained were used for studying photoelectric properties, including measuring photoresponse signal (in the photoemf regime) from a black body heated to 900 K, as well as measuring spectral distribution of sensitivity. Measurements of the photoresponse were carried out at temperatures T = 80–290 K; spectral characteristics were studied at room temperature. Spectral characteristics were recorded

Photoelectric parameters of Si/GaN:O heterojunctions

Sample	P_{H_2O}/P_{GMAC}	P_{H_2O}, Pa	Conductivity type of Si	U_s, mV	τ, μs	Phase composition of the film
1	0	0	*n*	13	80	GaN
			p	0.09	35	
2	0.137	20	*n*	30	–	GaN:O
			p	0.06	60	
3	0.150	30	*n*	54	45	GaN:O
			p	0.03	6	
4	0.267	40	*n*	70	50	GaN:O
			p	0.26	20	
5	0.464	77	*n*	32	60	GaN:O,
			p	0.02	5	β-Ga_2O_3
6	0.550	88	*n*	30	–	GaN:O,
			p	0.06	9	β-Ga_2O_3
7	0.725	100	*n*	0.12	7	GaN:O,
			p	0.02	5	β-Ga_2O_3

using an MDR-23 monochromator. In all the experiments, the radiation was incident perpendicular to the heterojunction plane through a wide-bandgap material (through the GaN:O film). The area of the receiving region of the samples was 5 × 5 mm^2. For the contact material, a two-layer Ti/Al coating was used whose components were successively applied (using the magnetron sputtering method) onto the wide-gap material in the form of stripes 0.7 × 5 mm^2 in size. The thickness of each layer of metallization was ~1 μm. The ohmic contacts to *p*-type silicon was prepared in the form of a continuous aluminum layer on the opposite side of the heterojunction. As the contacts to *n*-type silicon, electrochemically deposited nickel was used. The linearity of the current–voltage characteristics of the contacts permits us to consider them to be nearly ohmic.

All heterojunctions studied in our work are photosensitive to the black-body radiation in the temperature range of $T = 80$–290 K (see table). The absolute photosensitivity is higher by three orders of magnitude for the heterojunctions prepared on *n* silicon than on *p* silicon. For this reason, all data that are given below refer to heterojunctions produced on *n* silicon. At each temperature, the magnitude of the photoresponse signal (U_s) depends on the concentration of oxygen in the nitride film. This dependence is clearly seen for heterojunctions on *n*-Si at $T = 290$ K (see table). In the pressure range $P_{H_2O} = 0$–40 Pa, the photoemf of the heterojunctions grows with increasing oxygen content. The greatest photoemf was detected for an *n*-Si/GaN:O heterojunction with a gallium oxynitride film grown at $P_{H_2O} = 40$ Pa (sample 4). For this sample, the specific detectivity was $D^* = 2.1 \times 10^{12}$ Hz$^{1/2}$ W^{-1} cm. At higher oxygen concentrations in the oxynitride film, the photosensitivity decreases and at $P_{H_2O} = 100$ Pa the photoresponse signal falls off by about two orders of magnitude (sample 7). If we take into account that, as the oxygen content increases, the film becomes inhomogeneous, it is reasonable to suppose that the observed decrease in photoresponse is related to the appearance of a second phase in the oxynitride films.

Temperature dependences of the photoresponse signal are nonmonotonic. As the temperature decreases from 290 K, the photoresponse increases for all heterojunctions, reaching a maximum at 200–250 K, after which it decreases. For some heterojunctions, the sensitivity in the maximum of the temperature dependence is higher by an order of magnitude than at 290 K.

The investigation of the photoresponse kinetics shows that the time constant of the photoresponse of heterojunctions τ behaves in a complex manner. Upon illumination of a heterojunction, the photoresponse rapidly reaches a maximum ($\tau \sim 5 \times 10^{-5}$ s), after which it falls off slowly ($\tau \sim 10^{-3}$ s) but at the instant at which the light pulse ceases an inverse peak is observed, and again a slow relaxation of the photoresponse to the zero value occurs. The differential form of the photoresponse is most likely related to the recharging of boundary states. The dependence of the fast component of the photoresponse time on the film composition is shown in the table.

All heterojunctions obtained on *n*-Si possess rectifying properties. Typical current–voltage curves $I(U)$ of heterojunctions with various oxygen contents in the gallium oxynitride film are shown in Fig. 3.

Spectral characteristics of heterojunctions on *n*-Si measured at $T = 290$ K are typical of all heterojunctions (see Fig. 4). Two bands of photosensitivity can be distinguished in the spectral characteristics. One extends

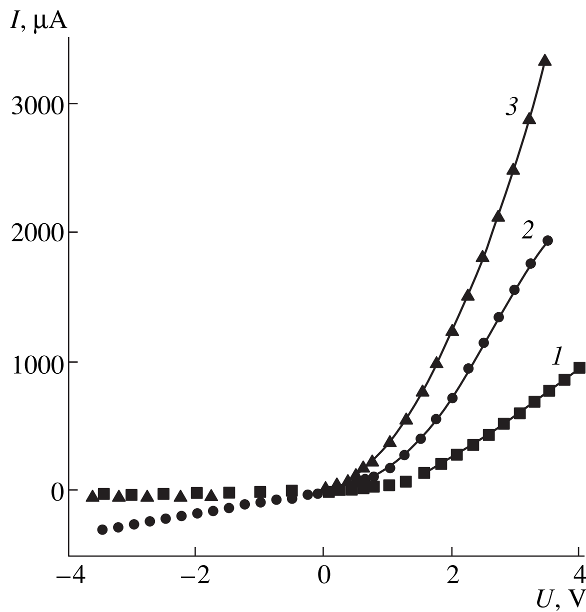

Fig. 3. Current–voltage characteristics of *n*-Si/GaN:O heterojunctions prepared using various partial pressures of water vapors P_{H_2O}/P_{GMAC}: (*1*) 0, (*2*) 0.464, and (*3*) 0.725.

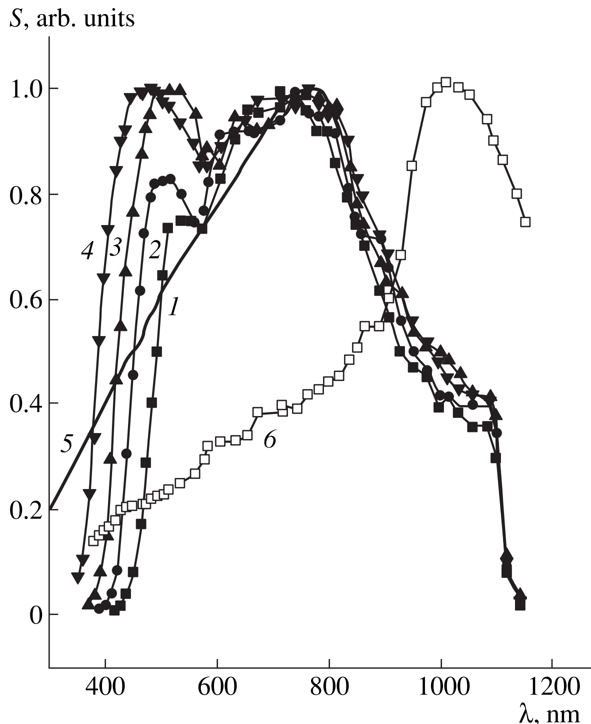

Fig. 4. Spectral characteristics of the photoresponse $S(\lambda)$ of *n*-Si/GaN:O heterojunctions prepared using various partial pressures of water vapors P_{H_2O}/P_{GMAC}: (*1*) 0; (*2*) 0.150; (*3*) 0.464; (*4*) 0.725; (*5*), (*6*) spectral characteristics of commercial silicon photodiodes (for explanations, see text).

in a wavelength range of $\lambda = 600$–1000 nm with a maximum at 800–900 nm, which corresponds to the photosensitivity in a range of λ less than ~500 nm. The levels of the photoresponse signal (S) in the long-wavelength and short-wavelength portions of the spectrum are comparable. The red boundary of the long-wavelength portion of the spectral characteristic is determined by the width of the forbidden band of the narrower-band semiconductor, i.e., Si. The second peak in the spectral characteristic is related to the photosensitivity in the wide-gap component of the heterojunction. A comparison of the spectral distribution of photosensitivity of the obtained heterojunctions with the characteristic (obtained under the same conditions) of a silicon commercial photodiode (Fig. 4, curve *6*) shows that the photosensitivity in the short-wavelength portion of the spectrum of the *n*-Si/GaN:O heterojunction is undoubtedly related to absorption in the gallium oxynitride film. It should also be noted that the absolute signals of photoresponse of the *n*-Si/GaN:O heterojunction significantly exceed the signals of the silicon photodiode: by a factor of 25 in the long-wavelength region and by a factor of 50–100 in the short-wavelength region. The short-wavelength band of photosensitivity of the *n*-Si/GaN:O heterojunction is clearly revealed also upon a comparison of the spectral characteristics of the heterojunction studied with the spectral distribution of the sensitivity of a commercial silicon photodiode with a shallow *p*–*n* junction [5] (Fig. 4, curve *5*).

The extension of the spectral characteristic of the *n*-Si/GaN:O heterojunction toward the short-wavelength side depends on the oxygen content in the oxynitride film: As the oxygen content in the film grows, the short-wavelength boundary is shifted to shorter wavelengths. The red boundary of photosensitivity in the short-wavelength portion is pronounced indistinctly. However, even if the short-wavelength limit of photosensitivity is not revealed, a certain disagreement between the position of the short-wavelength peak of photosensitivity and the width of the forbidden gap of the GaN:O film is observed. This disagreement is characteristic of all heterojunctions that were studied, with any oxygen content in the GaN:O film. Comparison of the E_g values for films grown on quartz with energies corresponding to the photosensitivity limit of a heterojunction in the short-wavelength range of spectrum shows that the E_g values in films grown on Si are smaller than in films on quartz. In other words, the observed spectral characteristics correspond to Si/GaN:O heterojunctions for which the E_g in the oxynitride film, at least in the region of the metallurgical boundary of the heterojunction, is smaller than the value which follows from the dependence of the forbidden band on the oxygen content in the solid solution.

The cause for this disagreement was not established in this work. We may only suppose that this can be related to both the structure of the oxynitride films and the state of the boundary. Scanning electron microscopy of the surface structure of GaN and GaN:O films

grown on Si shows that all the films, irrespective of the oxygen content, are finely dispersed (with grain size of about 0.01 μm). Taking into account that the Hall mobility in these films does not exceed 2–3 $cm^2/(V\ s)$, we may assume that the films grown on Si are amorphized. The amorphization of the layer can lead to a shift of the fundamental absorption edge to the long-wavelength range [6]. This factor apparently should be taken into account, but it is unlikely that it gives the main contribution to the observed effect. The more likely cause of the change in spectral characteristics are the specific features of the structure and composition of the GaN:O film in the region of the metallurgical boundary.

We can suppose that the chemical composition of the film region adjacent to silicon differs from that at a distance from the metallurgical boundary. The difference can be due to the interaction of GaN:O with the products of silicon oxidation at the surface, which is accompanied by the formation of Ga–Si–N–O solid solutions. Similar solid solutions (sialons) are known to be formed in the quaternary Al–Si–N–O system [7]; we cannot exclude them to form in the system at hand as well. A shift of the spectral characteristic in the photosensitivity region of GaN:O toward the long-wavelength range can be related to a decrease in the energy gap due to the introduction of Si into GaN:O. In this case, the extension of the solid solution region should be sufficiently large, at least exceeding the extension of the space-charge region in the film. In terms of this assumption, the heterojunction studied is a structure more complex than Si/GaN:O. It rather should be considered as a variable-gap structure of the $Si/Ga_xSi_{1-x}N_yO_{1-y}$ type. In this connection, the problem of studying physical characteristics of solid solutions in the Ga–Si–N–O system arises.

CONCLUSION

Thus, the investigations performed in this work show that doping gallium nitride with oxygen permits uniform solid solutions with an energy gap monotonically increasing up to 3.9 eV to be formed in the GaN:O system. Gallium oxynitride films with various oxygen content can be grown by chemical vapor deposition in a chloride system with the addition of water vapors into the reaction mixture. Using an oxynitride layer as a component of Si/GaN:O heterojunctions, structures that are photosensitive in virtually the entire visible range can be produced, which also are promising for detecting radiation in the near ultraviolet region. The main problem in the expansion of the spectral characteristic to the short-wavelength range is related to the monitoring of chemical processes at the initial stage of growth of an oxynitride film on the surface of a silicon substrate that reveal tendency to the formation of $Ga_xSi_{1-x}N_yO_{1-y}$ solid solutions with a probable decrease in the energy gap.

REFERENCES

1. S. E. Aleksandrov, A. M. Zykov, and V. A. Kryakin, in *Seventh Conf. on the Processes of Growth and Synthesis of Semiconductor Crystals and Films, Abstracts of Papers* [in Russian] (Novosibirsk, 1986).
2. F. F. Grekov, D. M. Demidov, and A. M. Zykov, Zh. Prikl. Khim. **52**, 1394 (1979).
3. S. E. Alexandrov and V. A. Criakin, in *Abstracts of the Proc. 14th Int. Conf. and EuroCVD-11 (Paris, 1997)*, p. 2115 [J. Electrochem. Soc. **97**, 22 (1997)].
4. V. I. Fistul', L. Ya. Pervova, and É. M. Omel'yanovskiĭ, in *Proc. All-Union Conf. on the Technology and Electrical Properties of III–V Semiconductor Compounds* [in Russian] (Leningrad, 1981) p. 3.
5. I. D. Anisimova, I. M. Vikulin, F. A. Zaitov, *et al.*, *Semiconductor Photodetectors: Visible and Near Infrared Ranges* [in Russian], Ed. by V. I. Stafeev (Moscow, 1984).
6. N. Mott and É. Davis, *Electronic Processes in Non-Crystalline Materials* (Oxford Univ. Press, Oxford, 1971; Mir, Moscow, 1974), Vol. 1.
7. M. F. Lisov and I. Ya. Guzman, in *Nitrides: Preparation, Properties, and Application* [in Russian] (Riga, 1984), Abstracts of Papers, Vol. 2, p. 88.

Translated by S. Gorin

Semiconductors, Vol. 34, No. 3, 2000, pp. 296–299. Translated from Fizika i Tekhnika Poluprovodnikov, Vol. 34, No. 3, 2000, pp. 302–305.
Original Russian Text Copyright © 2000 by Zavodinskiĭ.

SEMICONDUCTOR STRUCTURES, INTERFACES, AND SURFACES

Computer Study of Phosphorus Segregation Mechanisms at a SiO_2/Si(100) Interface

V. G. Zavodinskiĭ

Institute of Automation and Control, Far East Division, Russian Academy of Sciences, Vladivostok, 690041 Russia

Fax: 7(4232) 310452; e-mail: zavodins@iapu2.marine.su

Submitted September 16, 1999; accepted for publication, September 23, 1999

Abstract—Phosphorus is shown to segregate both at a perfect SiO_2/Si(100) interface and at an interface with defects. Depending on the particular mechanism of segregation (substitution for isolated silicon atoms near the interface, attraction to vacancies and self-interstitial silicon atoms accumulated near the interface, etc.), the segregation energy can vary from 0.5 to 1.0 eV. At high concentrations of defects (comparable with that of silicon atoms), the segregation energy decreases to 0.15–0.7 eV. The segregation energy for ideal boundary is less than that for a boundary with defects. *© 2000 MAIK "Nauka/Interperiodica".*

1. INTRODUCTION

The SiO_2/Si(100) interface plays an important role in the operation of many semiconductor devices (first of all, field transistors), and phosphorus is one of the main doping elements used in silicon semiconductor technology. Phosphorus atoms are known to be accumulated near this interface up to very high concentrations (of about 1/3 of a monolayer [1, 2]), which changes device characteristics, since phosphorus becomes electrically inactive in this case. This effect should be pronounced most strongly in thin oxide layers and can serve as a serious obstacle for the further development of the technology.

Experimental data based on the investigations by the Auger electron spectroscopy method [3] indicate that phosphorus at the SiO_2/Si interface does not form P–O bonds, but other details of the segregation process have not been studied. In particular, neither concrete atomic configurations in which phosphorus atoms can exist nor their energy characteristics are known. The situation is additionally complicated by the fact that silicon dioxide used in silicon technology is not crystalline; therefore, the SiO_2/Si interfaces exhibit a variety of morphological features and contain various structural defects.

The aim of this work is to study energy characteristics of phosphorus in various atomic configurations that can arise at SiO_2/Si(100) interfaces. The (100) orientation is chosen for the reason that this is the most frequently used one in the technology of silicon field-effect devices.

2. INVESTIGATION TECHNIQUE AND ATOMIC MODELS

Equilibrium atomic configurations and their energies were calculated by the cluster version of the semiempirical AM1 method [4, 5], which is a development of the quantum-mechanical MINDO method. Previously, this method was successfully applied for studying the energies of bonding of phosphorus and boron near the silicon surface [6, 7] and the formation of silicon oxide on various substrates, including the Si(100) surface [8, 9].

In this work, we consider models of the SiO_2/Si(100) interface represented as both an "ideal" heterointerface and real boundary containing (generating) structural defects. By the ideal interface, we mean such a boundary at which all silicon and oxygen bonds are closed; i.e., each silicon atom is connected with four neighbors (these may be both silicon and oxygen atoms) and each oxygen atom is bound with two silicon atoms. At a real boundary, part of interatomic bonds may be broken. We also consider various defects (vacancies, interstitial silicon atoms, isolated oxygen atoms) that can exist near the boundary.

The ideal SiO_2/Si(100) boundary was simulated as follows.

1. We constructed a cluster of silicon atoms that had a (100) free surface. The broken bonds on other surfaces were terminated with hydrogen atoms. At each surface silicon bond, we placed an oxygen atom which terminated with hydrogen atoms (forming OH groups). The geometry of the system thus obtained was optimized. The hydrogen atoms that terminate the boundaries of the silicon cluster were kept at a rest; the hydrogen atoms that entered into the OH groups could move.

2. Hydrogen atoms entering into the OH groups were replaced by SiH_3 groups. The geometry of the system again was optimized using boundary conditions similar to those specified in point 1.

3. Isolated hydrogen atoms in the oxide portion of the system were replaced by oxygen atoms to ensure that Si–O–Si bonds to be formed and the geometry obtained again was optimized.

The SiO_2/Si(100) boundary simulated in such a way does not contain broken silicon or oxygen bonds and stresses are minimum in it, due to optimization performed at each step. Its atomic scheme is shown in Fig. 1. The method we used to construct the ideal SiO_2/Si(100) boundary is not the only possible, of course, but its main features, i.e., the saturation of all the bonds and the minimization of stresses, should be present, in our opinion, in any model.

When studying the behavior of phosphorus near a real boundary with defects, we used the ideal boundary as the basic one and simulated these or those defects in it. The detailed structure of such boundaries will be discussed below along with the results of calculations.

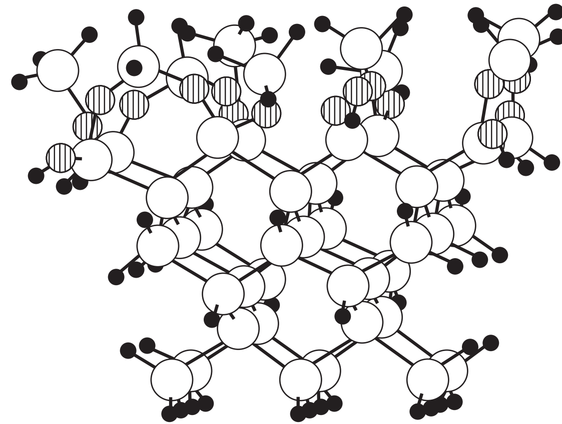

Fig. 1. Atomic structure (schematic) of an ideal SiO_2/Si(100) boundary. Empty circles show silicon atoms; hatched circles, oxygen atoms; and solid circles, hydrogen atoms.

3. CALCULATION RESULTS AND DISCUSSION

3.1. General Results

First of all, we had to clarify whether the approach we selected could describe the effect of removal of phosphorus from the oxide (upon oxidation of silicon) and explain the absence of P–O bonds in the boundary. To this end, we calculated the energies of our cluster system for two cases: (1) A phosphorus atom substitutes for a silicon atom located far from the boundaries (in particular, it was located in the fourth layer from the boundary), and (2) a phosphorus atom replaces a silicon atom in the oxide portion of the system. The energy of one P–O bond proved to be 0.7 eV less than that of one P–2Si bond.

Since phosphorus is a pentavalent element, we could expect that, being located in the lattice of a four-coordinated silicon atoms in a substitutional position, it would readily form bonds with a fifth atom (e.g., with an interstitial oxygen atom). We checked this possibility and found that such a configuration is unstable: The oxygen atom spontaneously moves away from the phosphorus atom, breaks one of the nearest silicon bonds, and becomes introduced in it to form a Si–O–Si "bridge"; i.e., indeed, phosphorus avoids direct contacts with oxygen.

3.2. Ideal Boundary

The position right at the boundary (in contact with oxygen atoms) is energetically unfavorable for a phosphorus atom; therefore, we placed a phosphorus atom into the second layer from the boundary and compared with the case where it was in the fourth layer. We found an 0.5-eV gain in energy per phosphorus atom. In the third layer, the gain was 0.1 eV; i.e., the energetical advantageousness of such positions is evident, at least for isolated atoms.

Since experimental data indicate that the phosphorus concentration at the boundary can be comparable with the concentration of silicon atoms, it was necessary to study if it is advantageous for phosphorus atoms to be located (segregate) near one another. Preliminarily, we studied the "energetics" of phosphorus atom pairing far from the boundary. The direct P–P bonds (nearest neighbors) were shown to be disadvantageous in silicon: The energy loss was 0.2 eV per phosphorus atom. The disposition of phosphorus atoms as next nearest atoms to one another also proved to be unfavorable; the energy loss was 0.5 eV in this case.

When two phosphorus atoms were placed as nearest neighbors in the positions immediately under the boundary (one atom in the second layer and the other atom in the third layer), this gave an energy gain of 0.35 eV as compared to their disposition as isolated atoms far from the boundary. However, when comparing with their location as isolated atoms in the second layer, this yields a loss of 0.15 eV per atom; i.e., it is more favorable for the phosphorus atoms to be apart in the second layer than to be paired, because one of the atoms on a pair should in this case to be located in the third layer, where its energy is higher.

Approximately the same is the energetics of two phosphorus atoms that are next-nearest atoms to one another: Their pairing in the second layer is unfavorable (giving an energy loss of by 0.3 eV/atom) in comparison with their location as isolated atoms in the same layer but is favorable (giving an energy gain of 15 eV/atom) in comparison with the location in the form of isolated atoms in the bulk of silicon.

Thus, phosphorus can accumulate near an ideal SiO_2/Si(100) boundary first in the form of isolated separated atoms, and then as close atomic pairs.

3.3. Real Boundary

At a real SiO_2/Si(100) boundary, various structural defects, both point and extended, can exist. We considered only some of these. On the oxide side, these are primarily unsaturated silicon or oxygen bonds; on the

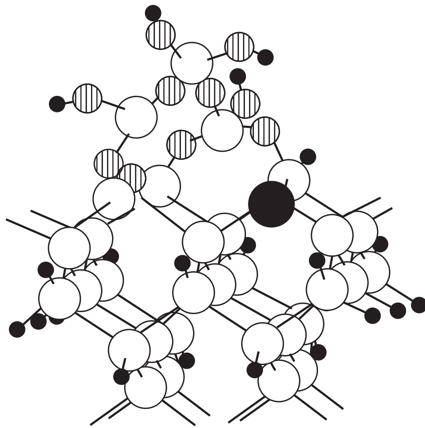

Fig. 2. Phosphorus atom (large solid circle) substitutes for a silicon atom in a dimer at the SiO_2/Si(100) boundary.

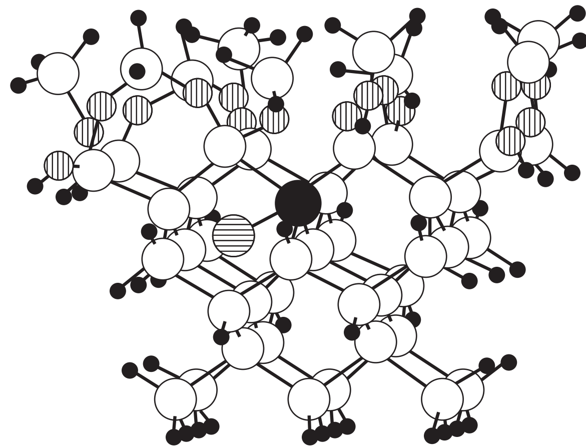

Fig. 3. 1P + Si(*i*) complex near the SiO_2/Si(100) boundary. Large solid circle shows the phosphorus atom; large hatched circle indicates the silicon atom.

silicon side, these are vacancies, self-interstitial silicon atoms, and oxygen atoms penetrated from the oxide side and located in various positions. In addition, Si–Si dimers can exist at the SiO_2/Si(100) boundary, which are similar to dimers characteristic of the Si(100) surface with a reconstruction of the (2×1) type.

Calculations show that at a real boundary, as on an ideal one, phosphorus can be located in the second layer and be characterized by a segregation energy of 0.5–0.6 eV. However, phosphorus atoms can also reside in the first silicon layer if they do not contact directly with oxygens, i.e., if a phosphorus atom substitutes for one of the atoms forming a Si–Si dimer, namely, that atom that has an unsaturated bond. A fragment of such a boundary is shown in Fig. 2. The energy gain here is 0.7–0.9 eV, depending on the disposition of the dimer in the boundary. Interestingly, the study of phosphorus segregation on the Si(100)–(2×1) surface [7] also shows that the surface dimers (whose atoms have unsaturated bonds) are suitable sites for accumulation of phosphorus atoms (with a segregation energy of the process of about 1 eV).

A configuration similar to the substitution for a silicon atom in a surface dimer is also realized upon phosphorus substitution for a silicon atom adjoining a vacancy. In this case, the energy gain is also about 1 eV per atom. However, near the boundary with the oxide oxygen atoms penetrate into silicon and tend to saturate broken bonds existing in vacancies, forming specific defects called *A* centers; apart from a vacancy, such a center contains an oxygen atom which forms a bridge between two silicon atoms bordering a vacancy. If the other two silicon atoms of the *A* center are replaced by phosphorus atoms, then the energy gain is 0.6 eV per phosphorus atom.

Definitely, vacancies can play a significant role in the process of impurity segregation only if their concentration is comparable with the concentration of impurity atoms. Usually, the amount of vacancies in silicon is small; however, if they are accumulated at a boundary, their contribution to phosphorus segregation can be noticeable. Calculations show that the energy of vacancy formation near the SiO_2/Si(100) boundary (in the second atomic layer) is smaller by 1.2 eV than the corresponding value in bulk silicon; i.e., vacancies indeed should be accumulated near a boundary and favor the accumulation of phosphorus. The self-interstitial silicon atoms behave similarly. They are generated in the process of silicon oxidation (or ion implantation) and can affect phosphorus segregation. Calculations show that the energy of an interstitial silicon atom located directly under a boundary (Fig. 3) is less by 0.75 eV than in the bulk of silicon and less by 0.3 eV than in SiO_2.

When being located near a pentavalent phosphorus atom, a self-interstitial silicon atom Si(*i*) becomes bound with it, which leads to a decrease in the energy of the system. Calculations show that the energy gain from the formation of one P–Si(*i*) pair in the bulk of silicon is about 1 eV. If this pair approaches the oxide boundary, the total energy of the system decreases. The maximum additional gain in energy (1.25 eV) is reached when Si(*i*) is under the first layer and the phosphorus atom substitutes for a silicon atom located in the second layer. Thus, the total energy gain from the formation of a P–Si(*i*) pair and its migration to the oxide boundary is 2.25 eV. From this value, we should subtract the sum of segregation energies of P and Si(*i*) atoms near the ideal boundary (0.5 + 0.75 = 1.25 eV). The residue (1.0 eV) is equal to the energy gain from the segregation of the P–Si(*i*) complex in comparison with the separate segregation of P and Si(*i*) atoms; i.e., in the presence of interstitial silicon atoms Si(*i*), phosphorus atoms should be attracted to them and be accumulated along with them near the oxide boundary.

Segregation energy of phosphorus (eV/atom) at the SiO_2/Si(100) boundary for various atomic configurations

Ideal boundary	Real boundary					
1P in the second layer	1P in the first layer (in a dimer)	1P in the second layer	Complexes			
			1P–vacancy	2P–*A* center	1P–Si(*i*)	2P–Si(*i*)
0.5	0.7–0.9	0.5	1.0	0.6	1.0	0.5

Note: 1P and 2P stand for one and two phosphorus atoms, respectively.

Analogous investigation performed for complexes of composition 2P–Si(*i*) show that these complexes are stable in the bulk of silicon and the energy gain is 0.7 eV per phosphorus atom, which is 0.3 eV less than for the P–Si(*i*) pair; the reason is the P–P repulsion, which was discussed above. At the boundary with the oxide, the aggregation of two phosphorus atoms and an interstitial silicon atom into a 2P–Si(*i*) complex gives an energy gain of 0. 5 eV.

The above results refer to the so-called tetrahedral (*T*) configuration of an interstitial silicon atom. Unfortunately, the technical features of that version of the AM1 method we used in this work prevented the investigation of other configurations, such as the hexagonal (*H*) or dumbbell (*X*) ones. However, the main mechanism of energy lowering (as a result of binding of an interstitial silicon atom with the fifth valence electron of phosphorus atom) will work for these configuration as well.

4. CONCLUSION

Our calculations indicate that phosphorus is accumulated near both an ideal and real (containing defects) SiO_2/Si(100) boundary. Various mechanisms of segregation can act simultaneously in this case. The segregation energies characteristic of various mechanisms are given in the table.

All the mechanisms work according to approximately the same scenario: First, phosphorus atoms move to the oxide boundary separately, as isolated atoms; their gradual accumulation is accompanied by a decrease in the segregation energy and proceeds to concentrations at which the phosphorus atoms can become next-nearest and even nearest neighbors to one another. Near an ideal boundary, the segregation energy is smaller; the presence of defects (especially, vacancies and self-interstitial atoms) favors its increase.

As to the electron activity, the first-principle calculations (performed by the method of the electron density functional [10]) show that in all configurations we considered in this work phosphorus is inactive. Depending on the concrete mechanism of segregation, phosphorus either gives no donor states at all or they are located quite far (several tenths of an electron volt) from the Fermi level.

ACKNOWLEDGMENTS

I am very grateful to J. Dąbrowski for his fruitful participation in discussions of the results and Prof. E.F. Shek and V.D. Khavryuchenko, who kindly supplied me with the computer program for the realization of the AM1 method.

This work was supported in part by the Russian Research Program "Physics of Solid State Nanostructures."

REFERENCES

1. L. P. Hunter, in *Handbook of Semiconductor Electronics*, Ed. by L. P. Hunter (McGraw-Hill, New York, 1976).
2. P. B. Griffin, S. W. Crowder, and J. M. Knight, Appl. Phys. Lett. **67**, 482 (1995).
3. J. Dąbrowski and H.-J. Müssig, *Abstracts of the Spring Meeting of the Germ. Phys. Soc.* (Münster, 1999).
4. M. J. S. Dewar, E. G. Zoebisch, E. F. Healy, *et al.*, J. Am. Chem. Soc. **107**, 3902 (1985); N. C. Baird and M. J. S. Dewar, J. Chem. Soc. **50**, 1262 (1969); R. C. Bingham, M. J. S. Dewar, and D. H. Lo, J. Am. Chem. Soc. **97**, 1285 (1975).
5. V. A. Zayetz, *CLUSTER-Z1: Quantum Chemical Software* [in Russian] (Inst. Surf. Chem., Acad. Sci. UkrSSR, Kiev, 1990); V. D. Khavryutchenko and A. V. Khavryutchenko, *DYQUAMOD: Dynamical Quantum Modeling Software for Personal Computers* [in Russian] (Joint Inst. Nucl. Res., Dubna and Inst. Surf. Chem., Nat. Acad. Sci., Kiev, 1993).
6. V. G. Zavodinskiĭ, I. A. Kuyanov, and E. N. Chukurov, Eur. Phys. J. B **6**, 273 (1998).
7. V. G. Zavodinskiĭ and I. A. Kuyanov, Appl. Surf. Sci. **141**, 193 (1999).
8. V. G. Zavodinskiĭ, I. A. Kuyanov, and O. M. Zavodinskaya, J. Non-Cryst. Solids **243**, 123 (1999).
9. V. G. Zavodinskiĭ, Phys. Low-Dimens. Struct. **3/4**, 43 (1999).
10. R. Bairle, M. J. Caldas, J. Dąbrowski, *et al.*, *Abstracts of ICDS Symposium* (Berkeley, 1999).

Translated by N. Korovin

Semiconductors, Vol. 34, No. 3, 2000, pp. 300–304. Translated from Fizika i Tekhnika Poluprovodnikov, Vol. 34, No. 3, 2000, pp. 306–310.
Original Russian Text Copyright © 2000 by Krylov.

SEMICONDUCTOR STRUCTURES, INTERFACES, AND SURFACES

Influence of Electric-Field-Assisted Thermal Ionization on the Formation of the Schottky Barrier between Metal and Amorphous Silicon

P. N. Krylov
Udmurt State University, Izhevsk, 426034 Russia
Submitted September 27, 1999; accepted for publication October 6, 1999

Abstract—The expression for a distribution function of charge carriers over deep levels in terms of the Poole–Frenkel effect in the space charge region is obtained. The inclusion of this effect permitted us to calculate the influence of the electric-field-assisted thermal ionization effect on a space charge density, a distribution of potential in the space charge region, and quasistatic capacitance–voltage characteristics of the metal–⟨amorphous silicon⟩ contact. © *2000 MAIK "Nauka/Interperiodica".*

INTRODUCTION

The properties of the Schottky barrier on the amorphous silicon (a-Si) substantially differ from the properties of the barrier in crystals. In the former case, the total space charge in the barrier region is defined by both ionized impurities and localized states related to dangling covalent bonds. A large density of localized states define the electrophysical properties of a-Si, namely, a weak sensitivity to doping, a hopping conductivity, etc. The electrical conductivity for amorphous silicon that was obtained from a suspension [1] and by silane decomposition [2] is substantially nonlinear at the electric field strength $E > 10^4$ V/cm and can be described by the Poole–Frenkel theory. The Poole–Frenkel effect is related to a thermal escape of captured electrons or holes from traps, which is enhanced by an electric field. In other words, this is so-called electric-field-assisted thermal ionization. The applied electric field E causes a lowering of the potential barrier, which prevents the captured carrier from escaping from the neutral local center, and increases the probability of escape from the trap for a one-dimensional case by the multiplier [3]

$$F = \exp(\beta E^{1/2}/kT), \quad (1)$$

and for a three-dimensional case by the multiplier [4]

$$F = (kT/\beta E^{1/2})\sinh(\beta E^{1/2}/kT), \quad (2)$$

where $\beta = (e^3/4\pi\varepsilon\varepsilon)^{1/2}$ is the Poole–Frenkel constant.

The electric field in a space charge region of the Schottky barrier, as a rule, is strong. However, the influence of the electric-field-assisted thermal ionization effect on the formation and properties of the contact metal–⟨amorphous silicon⟩ is not considered in the literature. Since the probability of carrier escape from the neutral trap is affected by a strong electric field, the generation–recombination kinetics should be considered in terms of the field influence.

INFLUENCE OF THE ELECTRIC-FIELD-ASSISTED THERMAL IONIZATION OF THE DEEP CENTER ON THE ELECTRON DISTRIBUTION OVER THE DONOR AND ACCEPTOR TRAPS

We assume that the donor trap concentration is equal to N_t and their energy level is E_t. In this case, the rate of electron trapping from the conduction band by the traps is $r_n = \alpha_n N_t(1 - f_t)n$, where α_n is the coefficient of trapping of the nonequilibrium electrons by the traps.

The rate of electron emission from the donorlike traps into the conduction band, which is accelerated by the electric field, can be expressed as $g_n = g_{nt}F$, where $g_{nt} = \beta_n N_t f_t$ is a thermal emission rate. Here, β_n is the liberation coefficient for trapped electrons. The correlation between α_n and β_n can be found from the principle of detailed balancing $\beta_n = \alpha_n n_1$, where

$$n_1 = g^{-1}N_c\exp[-(E_c - E_t)/kT]$$

is the equilibrium electron concentration in the conduction band when the Fermi level coincides with the trap level. The total rate of the electron generation from the donorlike traps into the conduction band equals

$$U^c_{nd} = g_n - r_n = \alpha_n N_d[n_1 f_t F - n(1 - f_t)]. \quad (3)$$

Similarly, the total rate of hole generation into the valence band from the acceptor-like traps can be expressed as

$$U^v_{pa} = g_p - r_p = \beta_p N_a(1 - f_t)F - \alpha_p N_a f_t. \quad (4)$$

Here, the first term defines the amount of holes generated by the acceptor-like traps under the field action,

1063-7826/00/3403-0300$20.00 © 2000 MAIK "Nauka/Interperiodica"

and the second term defines the amount of holes captured by traps from the valence band. The quantities α_p and β_p are the capture and liberation coefficients for holes. By equating r_p and g_p for the equilibrium case, we derive the relation between β_p and α_p as $\beta_p = \alpha_p p_t$, where $p_1 = gN_v\exp[-(E_t - E_v)/kT]$ is the equilibrium hole concentration when the Fermi level coincides with the trap level. In this case, expression (4) can be rewritten as

$$U^v_{pa} = \alpha_p N_a[p_1(1-f_t)F - pf_t]. \quad (5)$$

Let us now consider the balance between the transitions ⟨donor level⟩–⟨valence band⟩ and ⟨acceptor level⟩–⟨conduction band⟩. Here, the recombination rate is F-fold increased. A reason, for example, can be that the electron recombination from the conduction band to the acceptor level is equivalent to hole generation from the level with the E_a energy into the conduction band. By analogy with (3) and (5), we have

$$U^v_{pd} = \alpha_p N_d[p_1(1-f_t) - pf_tF], \quad (6)$$

$$U^c_{na} = \alpha_n N_a[n_1 f_t - n(1-f_t)F]. \quad (7)$$

The overall rate of electron generation from traps of both types into the conduction band and the holes into the valence band are correspondingly equal:

$$U_n = U^c_{nd} + U^c_{na}, \quad U_p = U^v_{pa} + U^v_{pd}.$$

We will now dwell on the steady but nonequilibrium states in more detail. Let us consider the condition for the zero current through the system. We have

$$U^c_{nd} = U^v_{pd} = U^c_{na} = U^v_{pa} = U_n = U_p = 0,$$
$$j_n = j_p = 0,$$

and we can derive the electron distribution function over the donorlike traps as

$$f^n_d = [1 + g^{-1}_{dn}F\exp(E_d - \xi_0/kT)]^{-1} \quad (8)$$

and over the acceptor-like traps as

$$f^n_a = [1 + g^{-1}_{an}F^{-1}\exp(E_d - \xi_0/kT)]^{-1}, \quad (9)$$

where $E_d = E^0_d - e\varphi$, $E_a = E^0_a - e\varphi$, and ξ_0 is a chemical potential.

Let us consider the balance between the transition processes donor–acceptor ($d \rightleftarrows a$). The rate for transitions $d \longrightarrow a$ equals

$$g_{d\to a} = \alpha N_d f_d N_a(1-f_a)F^2,$$

since this process can be conceived as follows: The electron escapes from the donor, the hole escapes from the acceptor, and in both cases field ionization takes place. After that, the electron and hole recombine. The rate of the inverse transitions $a \longrightarrow d$ equals

$$g_{a\to d} = \beta N_a f_a N_d(1-f_d).$$

From the condition for the thermal equilibrium $g^0_{d\to a} = g^0_{a\to d}$, we derive the relation between the coefficient of capture β and the coefficient of ionization α:

$$\beta = \alpha(g_{dn}/g_{an})\exp[(E_a - E_d)/kT],$$

Substituting this relation into the balance equation $g_{d\to a} = g_{a\to d}$, we derive the equation

$$\frac{f_d}{1-f_d}F^2 = \frac{g_{dn}}{g_{an}}\frac{f_a}{1-f_a}\exp\left(\frac{E_a - E_d}{kT}\right).$$

Substituting (8) and (9) into this equation, we obtain the identity. Hence, the distribution functions of charge carriers over the local states (8) and (9) ensure the balance between each pair of processes:

$$d \rightleftarrows E_c,\ d \rightleftarrows E_v,\ a \rightleftarrows E_c,\ d \rightleftarrows E_v,\ d \rightleftarrows a.$$

As can be seen from (8) and (9), the electric-field effect is reduced to an increase in the number of charged (ionized) traps in the semiconductor without regard for the trap type.

SPACE CHARGE DENSITY IN AMORPHOUS SILICON AT THE ELECTRIC-FIELD-ASSISTED THERMAL EMISSION

For amorphous semiconductors, the density of states inside the mobility gap can be presented as an overlapping of donorlike and acceptor-like states. Let us accept the following partial densities of states as the model ones:

$$g(E) = g_d(E) + g_a(E),$$
$$g_d(E) = g_d(E_v)\exp[(E_v - E)/E_{0d}], \quad (10)$$
$$g_a(E) = g_a(E_c)\exp[(E - E_c)/E_{0a}].$$

Henceforth, E is the charge carrier energy. The space charge density ρ can be written as

$$\rho = e(N^+_d - N^-_a), \quad (11)$$

where

$$N^+_d = \int_{E_v}^{\infty} g_d(E)[1 - f^n_d(E)]dE \quad (12)$$

is the concentration of the ionized donorlike centers, and

$$N^-_a = \int_{-\infty}^{E_c} g_a(E)f^n_a(E)dE \quad (13)$$

is the concentration of acceptor-like centers.

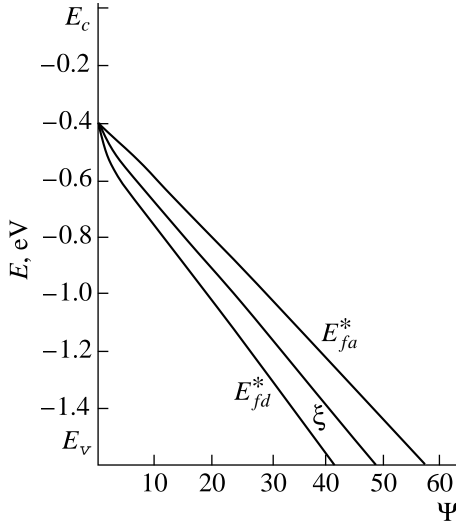

Fig. 1. Fermi level ξ and quasi-Fermi levels E^*_{fd}, E^*_{fa} in relation to a reduced potential of electric field inside the barrier $\Psi = e\varphi/kT$.

Substituting (8)–(10) in (12) and (13), we express the charged trap concentrations in terms of hypergeometric functions:

$$N_d^+ = g_d(E_v)kT\frac{F(1, \alpha, \alpha+1, A)}{\alpha}, \tag{14}$$

$$N_a^- = g_a(E_c)kT\frac{F(1, \beta, \beta+1, B)}{\beta}, \tag{15}$$

where

$$A = \exp[(E^*_{fd} - E_v)/kT],$$
$$B = \exp[(E_c - E^*_{fd})/kT],$$

$$E^*_{fd} = \xi_0 + e\varphi + kT\ln(g_{dn}F),$$
$$E^*_{fa} = \xi_0 + e\varphi - kT\ln(g_{an}^{-1}F),$$
$$\alpha = kT/E_{0d}, \quad \beta = kT/E_{0a}.$$

Here, E^*_{fa} and E^*_{fd} are the quasi-Fermi levels for electrons localized at acceptor-like and donorlike centers, respectively. Substituting (14) and (15) in (11) and taking into account the electroneutrality condition for a bulk, we derive

$$\frac{F(1, \alpha, \alpha+1, -A^*)}{\alpha} = \frac{F(1, \beta, \beta+1, -B^*)}{\beta} = C, \tag{16}$$

where

$$A^* = \exp[(\xi_0 - E_v)/kT], \quad B^* = \exp[(E_c - \xi_0)/kT];$$

the space-charge density can be written as

$$\rho = eg_d(E_v)kTC\left[\frac{F(1, \alpha, \alpha+1, -A)}{F(1, \alpha, \alpha+1, -A^*)} - \frac{F(1, \beta, \beta+1, -B)}{F(1, \beta, \beta+1, -B^*)}\right]. \tag{17}$$

The shape of the space-charge distribution defines the form of the potential φ inside the space charge region according to the Poisson equation:

$$\frac{d^2\varphi}{dx^2} = -\frac{\rho}{\varepsilon\varepsilon_0}. \tag{18}$$

Using the dimensionless variables

$$e\varphi/kT = \psi, \quad x/L = y, \quad L^2 = 2\varepsilon\varepsilon_0/e^2gd(E_v),$$
$$\alpha = (e/\pi\varepsilon\varepsilon_0 LkT)^{1/2}$$

we can rewrite the Poisson equation as

$$\frac{d^2\psi}{dy^2} = \frac{1}{C}\left[\frac{F(1, \beta, \beta+1, -B)}{\beta} - \frac{F(1, \alpha, \alpha+1, -A)}{\alpha}\right] \tag{19}$$

with boundary conditions

$$y \longrightarrow \infty, \quad \psi, d\psi/dy \longrightarrow 0;$$
$$y \longrightarrow 0, \quad \psi \longrightarrow \psi_c + eV/kT, \tag{20}$$

where ψ_c is the contact potential difference, and V is the external bias. However, the first boundary condition could not be used in a numerical analysis. Using the new variable $z = (d\psi/dy)^2$, we can rewrite equation (19) as

$$\frac{dz}{d\psi} = \frac{2}{C}\left[\frac{F(1, \beta, \beta+1, -B)}{\beta} - \frac{F(1, \alpha, \alpha+1, -A)}{\alpha}\right], \tag{21}$$

where

$$A = \exp(\Delta + \eta_0 + \psi - az^{1/4}),$$
$$B = \exp(\eta_0 - \psi - az^{1/4}),$$
$$\Delta = E_g/kT, \quad \eta_0 = (\xi_0 - E_c)/kT$$

with the boundary conditions

$$\psi \longrightarrow 0, \quad z \longrightarrow 0;$$
$$\psi \longrightarrow \psi_k + eV/kT, \quad z \longrightarrow z_k. \tag{22}$$

It is known [5] that the hypergeometric Gaussian series $F(a, b, c, z)$ converges for $|z| < 1$. Using the Gaussian relationship for contiguous functions, we derive the for-

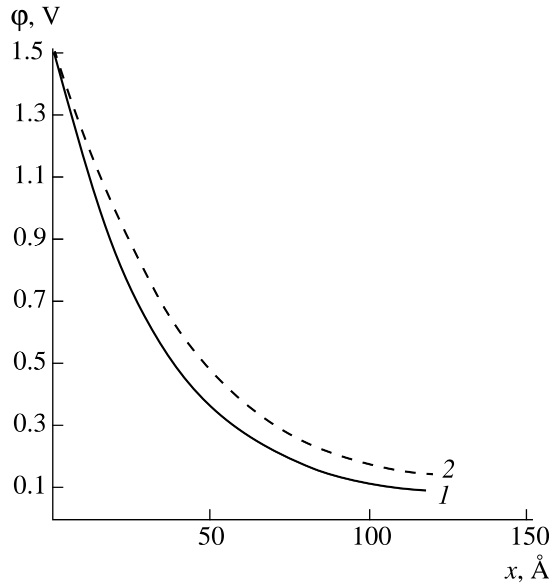

Fig. 2. Distribution of potential in the space charge region of the metal–⟨amorphous silicon⟩ Schottky barrier (*1*) with and (*2*) without consideration of the electric-field-assisted thermal ionization.

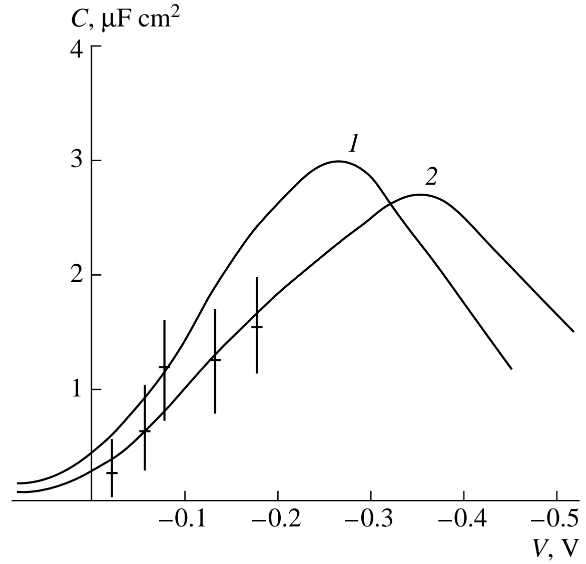

Fig. 3. Reverse bias (*V*) dependence of capacitance (*C*) for the metal–⟨amorphous silicon⟩ Schottky barrier. The dependences are computed for $E_c - \xi = 0.65$ eV (*1*) with and (*2*) without consideration of the electric-field-assisted thermal ionization.

mula for calculating the function $F(1, \alpha, \alpha + 1, -A)$ for $|A| < 1$:

$$F(1, \alpha, \alpha+1, -A) = \frac{1}{1+A} + \frac{A}{1+A}\left(\frac{\alpha+1}{\alpha}\right) \times \sum_{n=0}^{\infty} \frac{(-A)^n}{(\alpha+n)(\alpha+n+1)}. \tag{23}$$

For $|A| > 1$, we use the relationship

$$F(1, \alpha, \alpha+1, -A) = \frac{\pi\alpha}{\sin\pi\alpha}\frac{1}{A^{\alpha}} + \left(\frac{\alpha}{\alpha+1}\right) \times \frac{1}{A}F(1, 1-\alpha, 2-\alpha, -A^{-1}), \tag{24}$$

where the function $F(1, 1 - \alpha, 2 - \alpha, -A^{-1})$ can be calculated from formula (23).

Poisson equation (21) with conditions (22)–(24) was solved numerically by the method of trapezoids. The $\psi'(\psi)$ dependence was derived and was also integrated by the method of trapezoids. As a result, the coordinate dependence of potential was derived. The differential capacitance as a function of the voltage can be calculated simultaneously with the solution of the Poisson equation. Actually, the voltage dependence of capacitance is defined by the expression $C(V) = \psi''/\psi'$. In view of the $\psi'(\psi)$ dependence derived, this expression takes an explicit form, which is appropriate for a numerical analysis:

$$C = \psi''[\psi, \psi'(\psi)]/\psi'(\psi). \tag{25}$$

RESULTS OF NUMERICAL COMPUTATIONS AND THEIR DISCUSSION

The typical voltage dependence of the Fermi level ξ in relation to the mobility thresholds as well as the quasi-Fermi levels for electrons localized at the donor-like (E_{fd}^*) and acceptor-like (E_{fa}^*) levels are shown in Fig. 1. The distinction of E_{fd}^* and E_{fa}^* from ξ is defined by the influence of the Poole–Frenkel effect. This effect causes a decrease in E_{fd}^* and an increase in E_{fa}^* because of the ionizing action of the electric field. Furthermore, this leads to a more abrupt potential drop in the space charge region (Fig. 2), which reduces the thickness of this region. The dependence of the barrier capacitance C on the applied voltage is shown in Fig. 3. As can be seen from Fig. 3, the capacitance behavior significantly differs from that predicted by the classical theory of a Schottky barrier:

$$C^{-2} \propto V_k - V. \tag{26}$$

The onset of this type of dependence is observed only at sufficiently large negative biases, for example, in the case of $\eta_0 = -32$ for $\psi > 35$ without considering electric-field-assisted thermal ionization, and for $\psi > 45$ taking into account electric-field-assisted thermal ionization. This behavior can be explained qualitatively by considering the position of the quasi-Fermi level in relation to mobility thresholds. The onset of the appearance of the dependence of type (26) is observed only

for bias voltages V, at which no variation in the charged state of local levels is observed. This means that we construct the Schottky barrier model, in which the charge state density is constant. The electric-field-assisted thermal effect somewhat flattens the initial portion of the curve for the voltage V dependence of capacitance C. The experimental data on the reverse bias dependence of capacitance for the interface barrier between undoped hydrogenated amorphous silicon and gold [6] are known from the literature. We compared these data with our computations. The calculated curves for $E_c - \xi = 0.65$ eV and $g(\xi_0) = 10^{17}$ eV^{-1} cm^{-3} both with and without consideration of the electric-field-assisted thermal ionization are shown in Fig. 3. As can be seen from Fig. 3, the experimental and theoretical curves fit each other more precisely when the electric-field-assisted thermal ionization is taken into account.

REFERENCES

1. A. A. Andreev, O. A. Golikova, M. M. Kazanin, *et al.*, Fiz. Tekh. Poluprovodn. (Leningrad) **14** (9), 1859 (1980) [Sov. Phys. Semicond. **14**, 1110 (1980)].
2. A. K. Jonscher and R. M. Hill, in *Physics of Thin Films: Advances in Research and Development, Vol. 8*, Ed. by G. Haas, M. H. Francombe, and R. W. Hoffman (Academic, New York, 1974; Mir, Moscow, 1978).
3. J. L. Harkle, J. Appl. Phys. **39**, 4871 (1968).
4. M. Ieda, G. Sawa, and S. Kato, J. Appl. Phys. **42**, 3727 (1971).
5. *Handbook of Mathematical Functions*, Ed. by M. Abramowitz and I. A. Stegun (Dover, New York, 1965; Nauka, Moscow, 1979).
6. *Amorphous Semiconductors*, Ed. by M. H. Brodsky (Springer-Verlag, Berlin, 1979; Mir, Moscow, 1982).

Translated by N. Korovin

Semiconductors, Vol. 34, No. 3, 2000, pp. 305–307. Translated from Fizika i Tekhnika Poluprovodnikov, Vol. 34, No. 3, 2000, pp. 311–313.
Original Russian Text Copyright © 2000 by Krylov.

SEMICONDUCTOR STRUCTURES, INTERFACES, AND SURFACES

The Generation–Recombination Current through a Contact of Metal with Amorphous Silicon under the Conditions of Thermal Field Ionization in a Space-Charge Region

P. N. Krylov

Udmurt State University, Krasnoarmeiskaya ul. 71, Izhevsk, 426034 Russia

Submitted September 27, 1999; accepted for publication October 6, 1999

INTRODUCTION

The mechanism of current passage through a metal–(amorphous silicon) Schottky barrier was studied in [1–3]. In [3], assumption analytic formulas for current were derived; the current–voltage (*I–V*) characteristic of the metal–*a*-Si:H contact was then numerically calculated taking into consideration physical features of formation of the space charge region (SCR) in *a*-Si. It was shown that, in the case of the above-barrier and tunnel mechanisms of current passage, the *I–V* characteristic of the contact is exponential. An increase in the density of states in the mobility gap results in a noticeable increase in the absolute value of the reverse current. This leads to degradation of rectifying characteristics of the contact. The *I–V* characteristic can be almost symmetrical; however, they remain exponential under forward and reverse biases. The generation–recombination current (GRC) in contacts was calculated in [4] under the assumption that Shockley–Read's statistics for exponential distribution of localized-state density in the mobility gap is valid. The GRC dependence at reverse biases is determined by the voltage V dependence of the SCR thickness L. Using the relation reported in [3] for J, one can obtain the expression

$$J_{\mathrm{gr}} = J_{\mathrm{gr}0}\arccos\left[\exp\left(-\frac{\varphi_0 - eV}{2}\beta_1\right)\right], \tag{1}$$

where β_1 is the exponential factor in local state distribution and φ_0 is the barrier height. It can be seen from (1) that rapid saturation of GRC under the reverse bias takes place with an increase in bias voltage V.

The *I–V* characteristics of amorphous silicon produced by deposition from a suspension state [5] and by decomposition of monosilane [6] at electric-field strength of $E_{\mathrm{cr}} > 10^4$ V/cm are described within the context of the Frenkel–Poole theory. In the SCR of the Schottky barrier, electric fields frequently exceed the E_{cr} value; however, the effect of the Frenkel thermal–field ionization (TFI) on the generation–recombination current of the metal–(amorphous silicon) contact was not taken into consideration in [2, 4].

THE GENERATION–RECOMBINATION CURRENT UNDER THERMAL–FIELD IONIZATION IN THE SPACE CHARGE REGION

Let us examine the thermal–field ionization effect in SCR on the generation–recombination current J_{gr} in the metal-(amorphous silicon) contact using Shockley–Read's statistics with continuous distribution of localized-state density in the mobility gap. Allowing for TFI, the electron recombination rates are given by [7]

$$U_{nd} = \alpha_n N_d[n_1 f_{nd} F - n(1 - f_{nd})], \tag{2}$$

$$U_{pd} = \alpha_p N_d[p_1(1 - f_{nd}) - p f_{nd} F)], \tag{3}$$

$$U_{na} = \alpha_n N_a[n_1 f_{na} F - n(1 - f_{na})F], \tag{4}$$

$$U_{pa} = \alpha_p N_a[p_1(1 - f_{na})F - p f_{na}], \tag{5}$$

where $F = \exp(\beta_0 E^{1/2}/kT)$ is a factor that accounts for amplification of thermal excitation of captured electrons or holes from traps by electric field E;

$$\beta_0 = (e^3/4\pi\varepsilon\varepsilon_0)^{1/2}$$

is the Frenkel–Poole constant; $\alpha_{n(p)}$ are coefficients of electron (hole) capture by traps;

$$n_1 = g^{-1}N_c\exp[-(E_c - E_t)/kT],$$

$$p_1 = gN_v\exp[-(E_t - E_v)/kT];$$

and E_t is the energy level of traps. Electron- and hole-recombination rates in the steady state are equal to one another:

$$U_{nd} = U_{pd}, \quad U_{na} = U_{pa}. \tag{6}$$

Equating (2) and (3), (4) and (5), one can obtain expressions for stationary functions of electron distribution over donor and acceptor levels:

$$f_{nd} = \frac{\alpha_n n + \alpha_p p_1}{\alpha_n n + \alpha_p p_1 + (\alpha_n n_1 + \alpha_p p)F}, \tag{7}$$

$$f_{na} = \frac{F(\alpha_n n + \alpha_p p_1)}{\alpha_n n_1 + \alpha_p p_1 + (\alpha_n n_1 + \alpha_p p_1)F}, \tag{8}$$

where α_n, α_p are coefficients of electron and hole capture, respectively. Substituting (7) into (2) and (8) into (5), the generation rate for the donor level can be written as

$$U_d = N_d\alpha_n\alpha_p\frac{F(np-n_i^2)}{\alpha_n(n+n_1F)+\alpha_p(p_1+pF)}, \quad (9)$$

and for the acceptor level as

$$U_a = N_a\alpha_n\alpha_p\frac{F(np-n_i^2)}{\alpha_n(n_1+nF)+\alpha_p(p+p_1F)}, \quad (10)$$

where n_i is the concentration of the intrinsic charge carriers.

If the only mechanism of charge carrier transport through the barrier is the generation–recombination mechanism, the expression for current is

$$J_{\mathrm{gr}} = e\int_0^L U dx, \quad (11)$$

where L is the SCR layer thickness.

Using the simplifying assumption that quasi-Fermi levels of free electrons F_n and free holes F_p in SCR are constant, one can find that $F_n - F_p = eV$, where V is the external bias voltage. Then,

$$np - n_i^2 = n_i^2[\exp(eV/kT)-1].$$

The spectrum of recombination centers in amorphous semiconductors is quasi-continuous in the entire mobility gap in contrast to crystalline semiconductors. To calculate generation–recombination rates for levels that are characterized by quasi-continuous distribution, expressions (9) or (10) should be integrated over the forbidden band from E_v to E_c. Then,

$$U_d = \int_{E_v}^{E_c} g_d(E)\frac{\alpha_n\alpha_p(np-n_i^2)FdE}{\alpha_n(n+n_1F)+\alpha_p(pF+p_1)}, \quad (12)$$

$$U_a = \int_{E_v}^{E_c} g_a(E)\frac{\alpha_n\alpha_p(np-n_i^2)FdE}{\alpha_n(nF+n_1)+\alpha_p(p+p_1F)}, \quad (13)$$

where

$$g_d(E) = g_d(E_v)\exp[(E_v-E)/E_{0d}],$$

$$g_a(E) = g_a(E_c)\exp[(E-E_c)/E_{0a}].$$

Unlike study [4], the electric field effect on charge-carrier generation–recombination rates is taken into consideration here. In this connection, it is necessary to treat recombination at donor and acceptor centers separately.

Let us first examine processes of generation–recombination at donorlike levels. In this case, virtually all the levels are lower than the mobility midgap. Then, $\alpha_n n_1 F$ in (12) can be disregarded, since $\alpha_n \approx \alpha_p$, $n_1 \ll p_1$, and $n_1 \ll n, p$. Integrating (12), one can obtain an expression for the rate of generation–recombination at donorlike levels

$$U_d = \alpha_n\alpha_p n_i^2[\exp(eV/kT)-1]F(\varphi)\frac{g_d(E_v)}{a} \times {}_2F_1(1, \beta, \beta+1, -b/a), \quad (14)$$

where

$$a = \alpha_n n + \alpha_p pF, \quad b = \alpha_p N_v, \quad \beta = kT/E_{0d},$$

$$n = n_0\exp(-e\varphi/kT),$$

$$n_0 = N_c\exp[(E_{\mathrm{F}0}-E_c)/kT],$$

$$p = p_0\exp(e\varphi/kT),$$

$$p_0 = N_v\exp[(E_v-E_{\mathrm{F}0})/kT],$$

and φ is the potential in the SCR. Substituting (14) into (11) and integrating with respect to the potential, rather than the coordinate, one can obtain expressions for the generation–recombination current over donorlike levels of an amorphous semiconductor with consideration of the thermal–field ionization according to Frenkel:

$$J_{grd} = e\alpha_n\alpha_p n_i^2[\exp(eV/kT)-1]g_d(E_v)kTL\beta^{-1} \times \int_{-V_k+V}^{0}\frac{\exp\left(\frac{\beta_0\sqrt{\dot\varphi}}{kT}\right){}_2F_1\left(1, \beta, \beta+1, -\frac{b}{a}\right)}{a\dot\varphi}d\varphi. \quad (15)$$

Dependence of $\dot\varphi = \dot\varphi(\varphi)$ is determined by expression [7]

$$\ddot\varphi = \frac{eg_d(E_v)kT}{\varepsilon\varepsilon_0}C\left[\frac{F(1, \beta, \beta+1, -B)}{F(1, \beta, \beta+1, -B^*)} - \frac{F(1, \alpha, \alpha+1, -A)}{F(1, \alpha, \alpha+1, -A^*)}\right], \quad (16)$$

where

$$C = F(1, \alpha, \alpha+1, -A^*)\alpha^{-1} = \beta^{-1}F(1, \beta, \beta+1, -B^*),$$

$$A = \exp[(E_{fd}^* - E_v)/kT],$$

$$B = \exp[(E_c - E_{fa}^*)/kT],$$

$$A^* = \exp[(E_{f0}-E_v)/kT],$$

$$B^* = \exp[(E_c-E_{f0})/kT],$$

$$E_{fd}^* = E_{f0} + e\varphi + kT\ln(gF),$$

$$E_{fa}^* = E_{f0} + e\varphi - kT\ln(g^{-1}F),$$

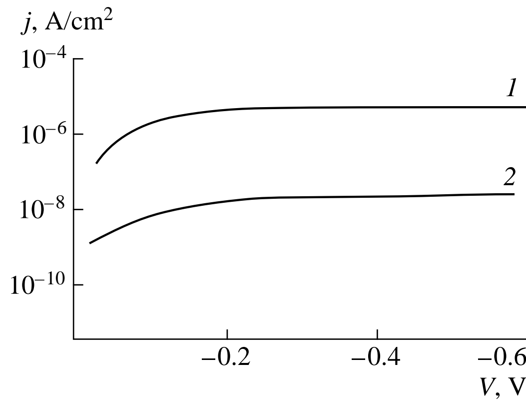

Current–voltage characteristics of the metal–(amorphous silicon) contact with the generation–recombination mechanism of transport over the space charge region: (*1*) with consideration of the thermal–field ionization effect; (*2*) without consideration of the thermal–field ionization effect. The values of $g(E_F) = 10^{19}$ eV^{-1} cm^{-3} and $E_c - E_F = 0.6$ eV were used in calculations.

and E^*_{fd} and E^*_{fa} are the quasi-Fermi levels for electrons localized on acceptor-like and donorlike levels, respectively.

In the case of charge transport by the generation–recombination mechanism over acceptor-like centers in the mobility gap of an amorphous semiconductor, virtually all the levels are above the mobility midgap. Then, $\alpha_p p_1 F$ in equation (13) can be disregarded, since $\alpha_n \approx \alpha_p$, $p_1 \ll n_1$, and $p_1 \ll n, p$. Integrating (13) with respect to energy within the mobility gap, the expression for the generation–recombination rate is

$$U_a = \alpha^{-1} d^{-1} e \alpha_n \alpha_p n_i^2 [\exp(eV/kT) - 1] \times F(\dot{\varphi}) g_a(E_c) kT {}_2F_1(1, \alpha, \alpha+1, -c/d), \tag{17}$$

where $c = \alpha_n N_c$, $d = \alpha_p p + \alpha_n nF$.

Substituting (17) into (11) and integrating with respect to the potential, rather than the coordinate, in the same manner as in case of generation at donorlike levels, one can obtain an expression for the generation–recombination current over acceptor-like levels, taking into consideration thermal-field ionization according to Frenkel:

$$J_{\text{gra}} = e \alpha_n \alpha_p n_i^2 [\exp(eV/kT) - 1] g_a(E_c) kTL \alpha^{-1} \times \int_{-V_k+V}^{0} \frac{\exp(\beta_0 \dot{\varphi}^{1/2}/kT) d {}_2F_1(1, \alpha, \alpha+1, -c/d) d\varphi}{\dot{\varphi}(\varphi)}. \tag{18}$$

The total generation current J_{gr} is equal to $J_{\text{grd}} + J_{\text{gra}}$. The figure shows the results of numerical integration of (15), (16), and (18) with and without consideration of TFI in the SCR. It can be seen that the generation–recombination current for reverse biases becomes saturated more rapidly under effect of the Frenkel thermal–field ionization, and, in this case, the current increases by several orders of magnitude.

REFERENCES

1. V. V. Il'chenko and V. I. Strikha, J. Non-Cryst. Solids **90**, 335 (1987).
2. V. V. Il'chenko, V. G. Levandovskiĭ, and V. I. Strikha, Ukr. Fiz. Zh. (Russ. Ed.) **2**, 290 (1987).
3. V. I. Strikha and V. V. Il'chenko, Fiz. Tekh. Poluprovodn. (Leningrad) **18** (5), 873 (1984) [Sov. Phys. Semicond. **18**, 544 (1984)].
4. A. Ya. Leiderman, Phys. Status Solidi A **87** (1), 363 (1985).
5. A. A. Andreev, O. A. Golikova, M. M. Kazanin, *et al.*, Fiz. Tekh. Poluprovodn. (Leningrad) **14** (9), 1859 (1980) [Sov. Phys. Semicond. **14**, 1110 (1980)].
6. A. K. Jonscher and R. M. Hill, in *Physics of Thin Films: Advances in Research and Development*, Ed. by G. Haas, M. H. Francombe, and R. W. Hoffman (Academic, New York, 1975; Mir, Moscow, 1978), Vol. 8, p. 180.
7. P. N. Krylov, Fiz. Tekh. Poluprovodn. (St. Petersburg) **34** (3), 306 (2000).

Translated by N. Vtorova

Semiconductors, Vol. 34, No. 3, 2000, pp. 308–311. Translated from Fizika i Tekhnika Poluprovodnikov, Vol. 34, No. 3, 2000, pp. 314–317.
Original Russian Text Copyright © 2000 by Kissine, Sysoev, Voroshilov, Simakov.

Effect of Oxygen Adsorption on the Conductivity of Thin SnO_2 Films

V. V. Kissine[1]*, V. V. Sysoev[1], S. A. Voroshilov[2], and V. V. Simakov[1]

[1] Saratov State Technical University, Saratov, 410054 Russia
[2] Saratov State University, Saratov, 410026 Russia
**e-mail: vkissine@star.sstu.runnet.ru*
Submitted April 23, 1999; accepted for publication October 4, 1999

Abstract—The effect of oxygen adsorption on the conductivity of a thin homogeneous film of tin dioxide was studied. The concentration of free electrons in the film as a function of the partial oxygen pressure in the atmosphere is described using a model formulated within the framework of a flat band approximation. The results of calculations are compared to experimental data. *© 2000 MAIK "Nauka/Interperiodica".*

INTRODUCTION

As is known, the presence of oxygen ions on the surface of a polycrystalline metal oxide layer affects the electric conductivity of this structure [1]. Adsorbed oxygen atoms are capable of trapping electrons from the bulk, which results in the bulk being depleted of the free charge carriers. Parameters of the near-surface space charge region are determined by the surface charge density and may vary depending on the partial oxygen pressure in the ambient atmosphere or upon exposure of the oxide layer to a medium containing reducing agents (H_2, CO, etc.). The adsorption-related processes are the underlying operation of the resistive gas sensors [2], which accounts for the necessity of studying features of these effects.

From the standpoint of practice, of most interest is a still unsolved task of providing mathematical description for the effect of partial oxygen pressure on the conductivity of oxide layers depleted of charge carriers throughout the layer thickness. Indeed, the maximum sensitivity of a polycrystalline oxide layer to ambient gases is observed in the case of ultimately depleted grains, whereby the Debye screening length L_D exceeds the average crystallite size L_C [3]. In this case, theoretical analysis of the situation is considerably simplified due to the fact that the transport of charge carriers in a strongly depleted layer can be described within the framework of a flat band approximation with neglect of both the inhomogeneity of charge carrier distribution in the bulk of grains and a jumplike change of the carrier mobility at the grain boundaries [4].

The purpose of this work was to study the effect of oxygen adsorption on the conductivity of polycrystalline *n*-type tin dioxide films with the average grain size L_C smaller than L_D. In particular, we aimed at establishing a relationship between the major carrier concentration in the grain and the partial oxygen pressure.

EXPERIMENTAL

The experiments were performed on polycrystalline SnO_2:Cu films. The electrical properties and gas sensitivity of similar tin dioxide layers were studied by various researchers (see, e.g. [5–9]). The films were prepared by RF magnetron sputtering of targets made of a SnO_2 powder with various amounts of CuO. The conditions for the film deposition are described in more detail elsewhere [9, 10]. The film preparation was completed by a 2-h anneal at 700°C in a flow of oxygen.

The crystal structure and surface morphology of the films were studied by X-ray diffraction on a DRON-2.0 diffractometer (Russia) using CuK_α radiation and an EVM-100BR electron microscope (Russia). The film thickness was measured with the aid of an SF-4A profilometer (Kosaka Laboratory Company, Japan) or an MII-10 interference microscope (Russia).

The electrical characteristics of the films were studied in a measuring microthermostat [11] mounted in a vacuum chamber of an UVP-2M setup (Russia). The sample temperature was 350°C and the partial pressure of oxygen in the chamber was varied using an SNA-2 controlled gas admit system (Russia). In order to increase stability of the residual gas pressure in the vacuum chamber, the pumping stage was provided with a ballast volume. Data of the X-ray diffraction analysis and electron micrographs showed that the tin dioxide films studied had a single-phase (SnO_2) polycrystalline structure and a texture oriented in the [110] direction perpendicular to the substrate surface. The films had a thickness of 1 μm and an average grain size of 100 nm.

RESULTS AND DISCUSSION

Figure 1 presents data on the conductivity G of tin dioxide films sputter-deposited using targets with different content of copper oxide, plotted as a function of the partial oxygen pressure P in the chamber. In the

range of $P = 0.1$–10 mtorr, the conductivity is a power function of the oxygen pressure with an exponent of 0.6–0.8. As the pressure increases further, the curves exhibit saturation. The samples with greater copper content showed a tendency to saturation in the region of low pressures as well. Increase in the CuO concentration in the target was accompanied by a growth in the film conductivity in the entire range of oxygen pressures.

We have used the conductivity value in the region of saturation at small oxygen pressures in the chamber (Fig. 1, curve *1*, $P = 0.1$ mtorr) to evaluate the concentration of free charge carriers n_0 in a nondepleted grain and the screening length L_D in the samples studied. The latter quantity was calculated by the formula [12]

$$L_D = \sqrt{\frac{\varepsilon\varepsilon_0 kT_c}{e^2 n_0}},$$

where $\varepsilon \approx 15$ [13] and ε_0 are the dielectric permittivities of the material and vacuum, respectively, k is the Boltzmann constant, e is the electron charge, and T_c is the critical temperature of the semiconductor. For a carrier mobility of $\mu \approx 10$ cm^2 V^{-1} s^{-1}, which is typically observed in polycrystalline SnO_2 films, the calculated values are $n_0 \approx 10^{14}$ cm^{-3} and $L_D \approx 500$ nm in agreement with the estimates reported by other researchers [14]. Our estimates were obtained with neglect of the possible influence of deep energy levels.

Since the average grain size in the films studied was about 100 nm, which is markedly lower compared to the above estimate for L_D, a relationship between the film conductivity and the partial oxygen pressure was described using the flat band approximation.

The mathematical model was formulated proceeding from the following major assumptions:

1. The semiconductor layer is continuous and is uniformly depleted throughout the thickness. The film surface is in equilibrium with the gas phase, which is maintained due to the neutral form of adsorption. The charge carrier mobility in the layer is constant and the electron gas is nondegenerate.

2. The experimental working temperature of the semiconductor layer is such that the shallow donor levels are fully ionized, while the intrinsic transitions can still be ignored.

3. There is a single type of adsorbed oxygen species on the semiconductor surface, which may occur in either charged or neutral form (O_2^- or O_2^0, respectively). The adsorbed species are arranged within a monolayer and do not interact with each other. The bound oxygen forms surface acceptor levels, which are filled with electrons in accordance with the Fermi level position in the system.

Within the framework of the flat band model with the above assumptions, the condition of electroneutrality for the film as a whole can be written as follows:

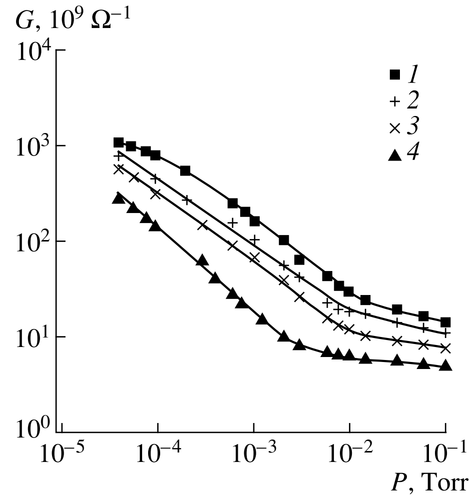

Fig. 1. Logarithmic plots of the conductivity G versus partial oxygen pressure P in the chamber for SnO_2:Cu films sputter-deposited using targets with different content of CuO (wt %): (*1*) 4; (*2*) 2; (*3*) 1; (*4*) 0.5.

$$\left(N_d - n + \frac{n_i^2}{n}\right)V = N_a^- S, \qquad (1)$$

where N_d is the concentration of shallow (fully ionized) donors; n and n_i are the electron concentrations in the film and in the intrinsic semiconductor, respectively; S and V are the sample surface area and volume, respectively ($V = SL_c$, L_c is the layer thickness); and N_a^- is the surface number density of ionized acceptor centers. The left and right parts of equation (1) refer to the charge in the bulk and on the surface of the film, respectively.

The surface charge is determined by the number density N_a of adsorbed species and the Fermi level position (i.e., the electron concentration) in the bulk, $E_F = E_c + kT_c\ln(n/N_c)$, where E_c is the conduction band bottom energy and N_c is the effective density of states at the conduction band edge. Taking into account that oxygen adsorbed on the SnO_2 surface creates energy levels of the acceptor type, the number density of charged species on the surface can be written as [12]

$$N_a^- = \frac{N_a}{1 + 2\exp\left(\frac{E_a - E_F}{kT_c}\right)}, \qquad (2)$$

where E_a is the acceptor energy level.

Denoting by n_a the doubled electron concentration in the conduction band for the Fermi level coinciding with E_a,

$$n_a = 2N_c\exp\left(-\frac{E_c - E_a}{kT_c}\right) \qquad (3)$$

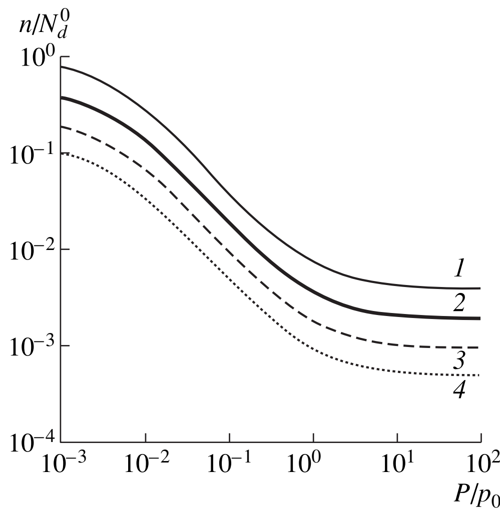

Fig. 2. Logarithimic plots of oxygen pressure P versus free electron concentration n calculated for depleted semiconductor films with $N_d^0 = 10^{14}$ cm^{-3}, $n_a = 10^{13}$ cm^{-3}, $n_s = 10^{15}$ cm^{-3}, $n_i = 0$, and various relative concentrations of ionized donor centers: $N_d/N_d^0 = 1$ (*1*); 0.5 (*2*); 0.25 (*3*); 0.125 (*4*).

and excluding E_F from equation (2), we arrive at a relationship between the number density of species adsorbed on the film surface and the concentration of free electrons in the bulk:

$$N_a = \left(N_d - n + \frac{n_i^2}{n}\right)\left(1 + \frac{n_a}{n}\right)L_c. \quad (4)$$

At the same time, the number density of adsorbed species can be expressed using an equation of balance for the fluxes of molecules at the film surface [15]:

$$\alpha P(N_s - N_a) = \nu N_a^0 \exp\left(-\frac{Q}{kT_c}\right), \quad (5)$$

where α is the kinetic coefficient of the Langmuir adsorption isotherm, N_s is the number of adsorption centers per unit surface area of the film, $\nu \approx 10^{13}$ s^{-1} is the characteristic phonon frequency, $N_a^0 = N_a - N_a^-$ is the surface number density of oxygen species adsorbed in the neutral form, and Q is the heat of desorption for these species. The left part of equation (5) describes the probability (frequency) of the oxygen atom sticking to vacant adsorption centers for the charged particles. Note that equation (5) ignores the desorption of charged particles, which is markedly lower compared to the probability of desorption of the electrically neutral molecules.

Equation (5) leads to the Vol'kenshteĭn isotherm described by the following expression:

$$N_a = \frac{N_s}{1 + \frac{p_0 n_a}{P(n + n_a)}}, \quad (6)$$

where

$$p_0 = \frac{\nu}{\alpha}\exp\left(-\frac{Q}{kT_c}\right).$$

Excluding the parameter N_a from equations (4) and (6) and introducing the notation $n_s = N_s/L_c$, we obtain a relationship between the concentration of free charge carriers in the bulk of the film and the oxygen pressure in the gas phase

$$\frac{P}{p_0} = \frac{n_a(n_i^2 + N_d n - n^2)}{n^3 + (n_s + n_a - N_D)n^2 - (n_i^2 + N_d n_a)n - n_i^2 n_a}. \quad (7)$$

Using equation (7) and the expression relating the electric conductivity to the concentration of free charge carriers, we may readily derive a relationship between conductivity and the partial oxygen pressure in the ambient atmosphere. Should the concentration of free electrons markedly exceed the concentration of holes, the layer conductivity would be merely proportional to the electron concentration.

Figure 2 shows a family of curves calculated using equation (7) with the concentration of donor centers N_d in the film considered as a parameter. The shape of the curves agrees with the results of our experiments characterizing conductivity as a function of the oxygen pressure (Fig. 1). Note that the relative change in conductivity and the ratio of pressure limits for the interval featuring this change quantitatively agree with the experimental data.

According to the model under consideration, a qualitative pattern of the gas sensitivity behavior of a thin tin dioxide film is as follows. At a constant oxygen pressure in the ambient atmosphere, the flux of molecules supplied per unit time from the gas phase to the surface is constant as well. The proportion of sticking molecules is determined by the incident flux and the number of vacant adsorption centers. Desorption of the electrically neutral species proceeds in accordance with the degree of filling of the adsorption centers, the temperature, and the corresponding activation energy. The working temperature of the semiconductor layer has to be selected so as to provide that only species occurring in a charged state would be retained on the surface.

As the adsorption centers are filled with charged species, the free electron concentration in the bulk decreases and the Fermi level shifts deeper into the forbidden band, thus decreasing the proportion of charged acceptor centers and stimulating desorption. When the Fermi level position reaches that of the acceptor energy levels created at the film surface due to the adsorbed

species, the latter levels are no longer occupied by electrons. An interplay between the fluxes of adsorbing and desorbing molecules determines stationary values of the occupancy of adsorption centers and the concentration of free charge carriers established in the semiconductor layer. This state corresponds to a stable conductivity value of the semiconductor film.

Thus, the equilibrium conductivity value of the film is directly related to the oxygen pressure in the ambient atmosphere. The conductivity ceases to depend on the pressure in two cases: (i) at a very low oxygen pressure in the gas phase, whereby the amount of adsorbed species is markedly smaller than the total number of free electrons in the layer; (ii) at a sufficiently high oxygen pressure, when the layer is depleted so strongly that the Fermi level approaches the energy levels created by the adsorbed species.

CONCLUSION

The results of our investigation show that the proposed flat band model with certain assumptions provides satisfactory description of a relationship between the conductivity of a tin dioxide layer and the oxygen pressure in the ambient atmosphere. This relationship can be used for monitoring the partial oxygen pressure in a residual vacuum or in an inert gas, for example, in manometric transducers for vacuum reactive sputtering setups where the process is carried out in a mixture of Ar and O_2.

REFERENCES

1. M. J. Madou and S. R. Morrison, *Chemical Sensing with Solid State Devices* (Academic, London, 1991), p. 67.
2. *Semiconductor Sensors in Physicochemical Studies*, Ed. by L. Yu. Kupriyanov (Elsevier, Amsterdam, 1996).
3. N. Yamazoe and N. Miura, in *Chemical Sensor Technology*, Ed. by S. Yamauchi (Elsevier, Amsterdam, 1992), Vol. 4, p. 4.
4. V. Demarne and R. Sanjines, in *Gas Sensors: Principles, Operation and Development*, Ed. by G. Sberveglieri (Dordrecht, Kluwer, 1992), Chap. 3, p. 89.
5. N. Yamazoe, Sens. Actuat. B **5**, 7 (1991).
6. R. M. Vashchilova, D. P. Dimitrov, N. I. Dolgov, *et al.*, Fiz. Tekh. Poluprovodn. (St. Petersburg) **29** (11), 1987 (1995) [Semiconductors **29**, 1036 (1995)].
7. B. A. Akimov, A. V. Albul, A. M. Gas'kov, *et al.*, Fiz. Tekh. Poluprovodn. (St. Petersburg) **31** (4), 400 (1997) [Semiconductors **31**, 335 (1997)].
8. A. Gadikas, A. Mironas, D. Senulienc, *et al.*, Thin Solid Films **323**, 275 (1998).
9. V. V. Kissine, S. A. Voroshilov, and V. V. Sysoev, Thin Solid Films **348**, 307 (1999).
10. V. V. Kissine, S. A. Voroshilov, and V. V. Sysoev, Sens. Actuat. B **55**, 55 (1999).
11. V. V. Kissine, V. A. Elistratov, and B. M. Gur'ev, Prib. Tekh. Éksp., No. 5, 244 (1993).
12. P. S. Kireev, *The Physics of Semiconductors* (Vysshaya Shkola, Moscow, 1975).
13. Z. M. Jarzebski and J. P. Marton, J. Electrochem. Soc. **123** (10), 333C (1976).
14. E. J. Gutierrez, L. Ares, J. I. Robla, *et al.*, Sens. Actuat. B **15–16**, 98 (1993).
15. F. F. Vol'kenshteĭn, *Electronic Processes during Chemisorption on the Surface of Semiconductors* (Nauka, Moscow, 1987).

Translated by P. Pozdeev

Semiconductors, Vol. 34, No. 3, 2000, pp. 312–318. Translated from Fizika i Tekhnika Poluprovodnikov, Vol. 34, No. 3, 2000, pp. 318–324.
Original Russian Text Copyright © 2000 by Taskin, Zaĭtsev, Obodnikov, Tishkovskiĭ.

SEMICONDUCTOR STRUCTURES, INTERFACES, AND SURFACES

Special Features of Spatial Redistribution of Selenium Atoms Implanted in Silicon

A. A. Taskin, B. A. Zaĭtsev, V. I. Obodnikov, and E. G. Tishkovskiĭ*

Institute of Semiconductor Physics, Siberian Division, Russian Academy of Sciences, pr. akademika Lavrent'eva 13, Novosibirsk, 630090 Russia

**e-mail: tish@thermo.isp.nsc.ru*

Submitted January 19, 1999; accepted for publication July 14, 1999

Abstract—The spatial distribution of selenium atoms implanted in silicon was studied by secondary-ion mass spectrometry after annealing in the temperature range of 600–1200°C. For implantation doses exceeding the amorphization dose for silicon, formation of a peak of selenium concentration was detected beyond the mean projected range of selenium ions. The spatial position of the peak correlates well with the spatial position of the plane in which the calculated value of the specific energy losses of selenium ions in elastic collisions (according to the TRIM code) corresponds to the critical value for amorphization of silicon. Accumulation of impurities at the peak occurs at temperatures of 700°C and higher after recrystallization of the amorphized layer. Redistribution of selenium atoms to deeper layers of the sample due to diffusion is controlled by the temperature dependence of the solubility of selenium in silicon. © *2000 MAIK "Nauka/Interperiodica".*

INTRODUCTION

By now, chalcogen impurities have been well studied in silicon and, in a number of cases, can serve as a model system for investigating impurity rearrangements in a crystal [1, 2]. These impurities are distinguished by a fairly low ultimate concentration at substitutional sites; as a result, it is possible to attain a high level of supersaturation in the lattice after even a low-dose implantation. For example, the limiting concentration of selenium atoms at the lattice sites in silicon does not exceed 10^{17} cm^{-3} [3].

Another distinctive feature of chalcogens is their ability to form impurity complexes as long as the heat-treatment temperature is sufficiently high to ensure significant mobility of the atoms and, thus, to stimulate decomposition of the solid solution. For oxygen, thermodonors act as complexes preceding the formation of precipitates; for selenium and probably sulfur and tellurium, these complexes are quasimolecules consisting of two or more atoms [4–7].

Studying the redistribution of chalcogen atoms implanted in silicon to a concentration exceeding the limiting concentration for these atoms at the lattice sites by 3–4 orders of magnitude makes it possible to analyze the process of formation of a new phase consisting, first, of the simplest molecules and, finally, of macroscopic inclusions. However, a number of processes inherent in any ion implantation accompany the implantation of selenium atoms and can also induce the redistribution of impurities, especially at doses exceeding the dose of amorphization. It is also important that, in ion-implantation doping, the proximity of the outer boundary of the crystal (the surface) has to be taken into account.

The objective of this work was to study the spatial redistribution of selenium atoms implanted in silicon during postimplantation heat treatments.

EXPERIMENTAL

Selenium ^{80}Se ions with energies of 50 and 125 keV and doses from 2×10^{14} to 4×10^{15} cm^{-2} were implanted in wafers of KDB-20 silicon (*p*-Si:B, $\rho = 20\ \Omega$ cm) with (100) orientation; the implantations were performed through an oxide layer 3–50 nm thick. The wafers were then annealed in a temperature range of 600–1200°C. The duration of heat treatment ranged from several minutes to several hours.

The spatial distribution of impurity atoms (Se, O, N, and C) in the near-surface layer (up to 1000 nm thick) of the wafer was measured by secondary-ion mass spectrometry (SIMS) using an MIQ-256 system (CAMERA-RIBER). The constancy of the etching rate was checked by measuring the yield of secondary Si ions. The primary Cs-ion beam had an energy of 10 keV. The area scanned by the focused ion beam was $500 \times 700\ \mu$m^2. In order to eliminate the contribution of secondary ions emitted from the crater walls, we measured the desired secondary-ion signal coming from the central area, amounting to 10% of the total scanned area.

The concentration profiles of selenium at depths from 200 nm to several tens of micrometers where the selenium concentration was lower than 10^{17} cm^{-3} were determined by measuring the temperature dependences of the Hall emf and electrical conductivity and using successive etching of the silicon layers. An HF : HNO_3 (1 : 40) solution was used as the etchant. The back surface of the sample was coated with a chemically resistant varnish, and the thickness of the etched-off layer was determined by measuring the sample's thickness to an accuracy of ±0.5 μm. The spatial distribution of selenium concentration was calculated from the measured concentrations of electrically active centers related to selenium on the basis of previously obtained data on the composition of these centers [7].

The crystallinity of the implanted and annealed samples was checked by electron diffraction.

RESULTS

Figure 1 shows the concentration profiles of the analyzed impurities obtained from SIMS measurements; these profiles most clearly demonstrate the effects of heat treatments in the range of 600–1200°C on the spatial distribution of concentrations of impurity atoms $N(x)$. A characteristic feature of redistribution of impurities illustrated in Fig. 1 is the appearance of an inflection point in the profile after annealing for 4 h at 600°C (Fig. 1, curve *2*). Following additional annealing for 50 min at 1100°C, a concentration peak emerges at the same depth (Fig. 1, curve *3*); this peak is located farther from the surface than the peak in the original distribution of implanted atoms. Furthermore, the concentration of implanted ions at the annealing-induced peak is much larger than the corresponding concentration at the same depth before annealing. In the same curve, a peak of selenium concentration is observed, which is located near the mean projected range R_p of selenium ions. This peak is not related to the accumulation of selenium atoms at this depth; rather, it was formed by a fraction of the Se atoms that were not involved in diffusive redistribution of the impurity in the course of annealing.

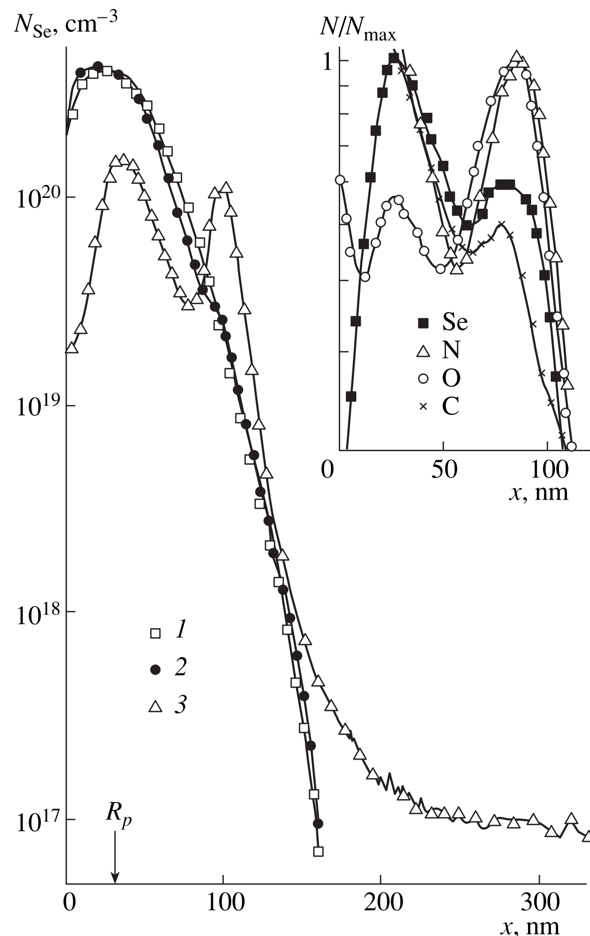

Fig. 1. Distributions of selenium concentration $N_{Se}(x)$ with depth (*1*) after ^{80}Se ions with an energy of 125 keV and dose $\Phi = 2.5 \times 10^{15}$ cm^{-2} were implanted into the sample through a SiO_2 layer 50 nm thick; (*2*) after postimplantation annealing for 4 h at $T = 600$°C; and (*3*) after additional annealing for 50 min at $T = 1100$°C. The concentration profiles for Se, O, N, and C in the sample implanted with 3.7×10^{15} cm^{-2} of Se and annealed for 50 min at $T = 1100$°C are shown in the insert in relative units.

The observed formation of the peaks is not a special feature of selenium concentration profiles alone. As can be seen from the insert in Fig. 1, oxygen, nitrogen, and carbon atoms are accumulated at approximately the same depth where the selenium peak is observed. It is noteworthy that the ratio of the concentrations of O, N, and C to the Se concentration are different for the two peaks. This was especially evident for oxygen atoms, for which we were able to observe the formation of a local concentration peak at a depth corresponding to the mean projected range R_p of Se ions. The distinction between the ratios of the concentrations of O, N, and C to the Se concentration in the vicinity of the peaks is apparently related to the distinction between the mechanisms of interaction of impurities in the corresponding regions of the sample. However, the data available are not adequate to judge the manner in which the formation of the peaks is related to the specific chemical nature of the atoms.

Transformation of the inflection point into a peak located at a depth greater than the mean projected range of ions is observed after annealing at temperatures of 700°C and higher. Accumulation of atoms at the peak at 700°C continues for several hours. The steady state is established in less than 10 min during annealing at 800°C (Fig. 2); in this case, the concentration of Se atoms at the peak does not change during further annealing at the same temperature for at least another 20 h.

The significance of the depth corresponding to the additional peak increases with both an increase in the

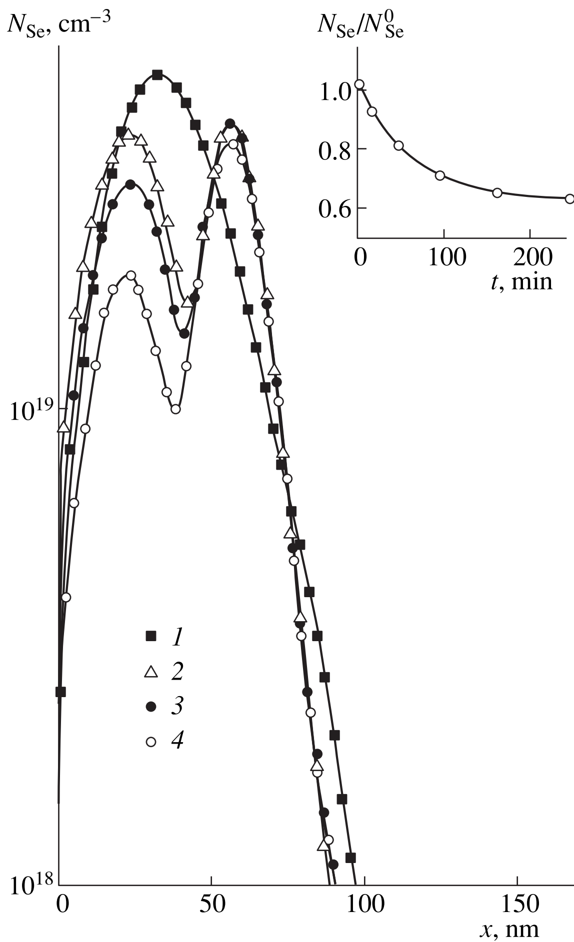

Fig. 2. Concentration profiles of selenium $N_{Se}(x)$ (*1*) after ^{80}Se ions with an energy of 50 keV and dose $\Phi = 2.3 \times 10^{14}$ cm^{-2} were implanted into the sample through oxide $d \simeq 3$ nm thick; and (*2*)–(*4*) after subsequent annealing at 800°C for t = (*2*) 10, (*3*) 40, and (*4*) 250 min. The dependence of the total amount of selenium N_{Se} on the duration of annealing at T = 800°C (the results are represented as the ratio N_{Se}/N_{Se}^0, where N_{Se}^0 is the total amount of selenium in the as-implanted sample) is shown in the insert.

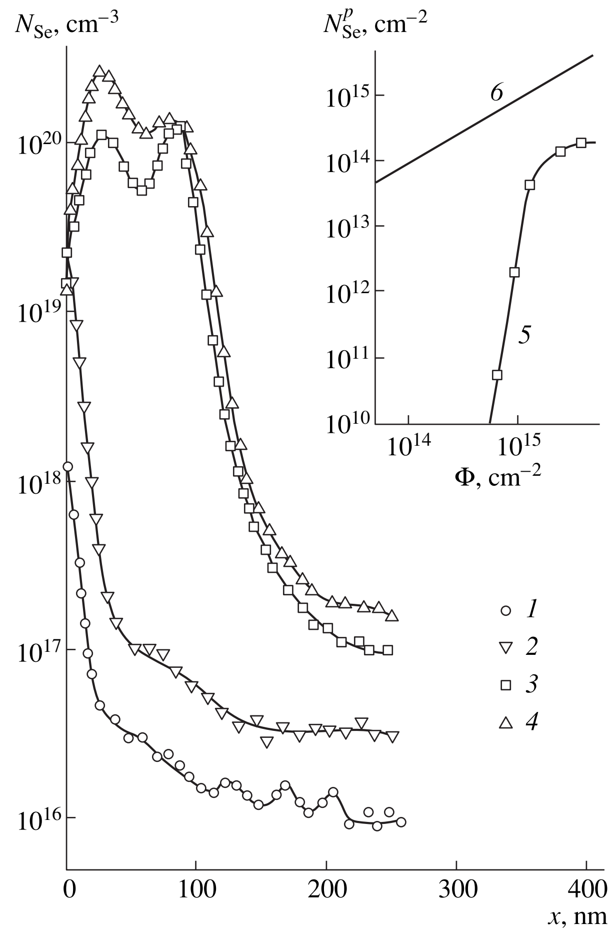

Fig. 3. The concentration profiles of selenium $N_{Se}(x)$ after postimplantation annealing for 50 min at T = 1100°C of the samples implanted with ^{80}Se ions with an energy of 125 keV through a layer of SiO_2 50 nm thick. The ion doses Φ were (*1*) 1.9×10^{14}, (*2*) 6.2×10^{14}, (*3*) 2.5×10^{15}, and (*4*) 3.7×10^{15} cm^{-2}. In the insert: (*5*) the total amount of selenium in the peak N_{Se}^p after annealing for 50 min at T = 1100°C as a function of the ion dose Φ; and (*6*) the unit-slope straight line.

energy of the ions from 50 to 125 keV and an increase in the ion dose from 2×10^{14} to 4×10^{15} cm^{-2}. Furthermore, the relative shift of the peak virtually coincides with the shift of the plane in which the ion-energy losses due to elastic collisions amount to 6×10^{20} keV cm^{-3} (according to the TRIM-code simulation).

Concentration of Se atoms at the peak N_{Se}^p depends on the ion dose Φ, as can be seen from Fig. 3, where the Se concentration profiles for samples implanted with various doses and annealed in the same manner (for 50 min at 1100°C) are shown. The dose dependence of the peak concentration is characterized by a drastic decrease in concentration at the peak as the implantation dose decreases. On the other hand, the tendency towards saturation of the peak concentration is observed for doses larger than 2×10^{15} cm^{-2}.

The impurity-concentration peak that is formed remains unchanged in virtually the entire range of the annealing temperatures used; furthermore, the time needed to significantly change this peak is longer by 2–3 orders of magnitude than the time required for its formation. Significant transformation of the peak is observed only after annealing for several hours at the highest temperature (1200°C) (Fig. 4, curve *3*). In this case, the isolated deep peak in the distribution $N_{Se}(x)$ vanishes, the concentration profile is leveled off and broadened, and the total amount of impurity in the near-

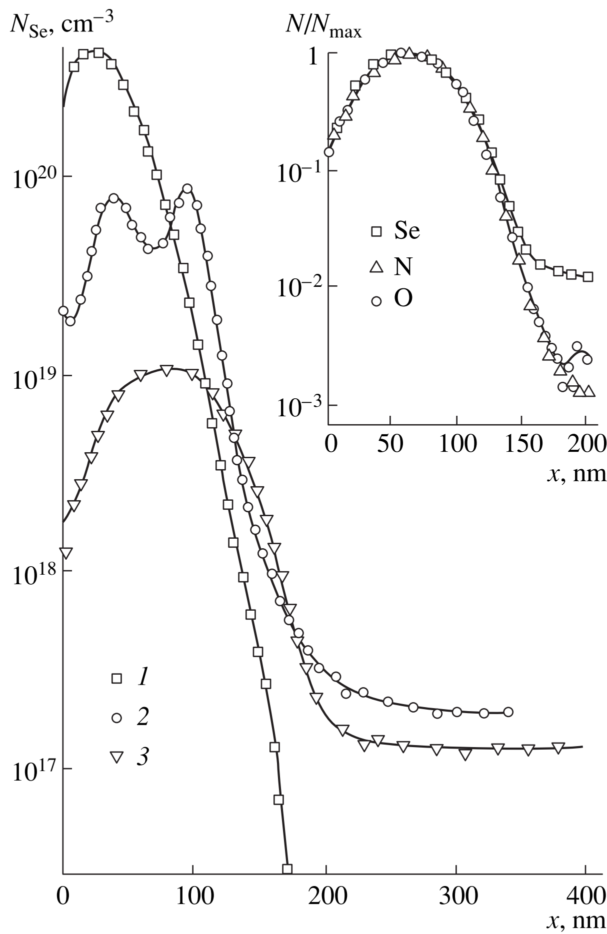

Fig. 4. Concentration profiles of selenium (*1*) after ^{80}Se ions with an energy of 125 keV and dose $\Phi = 2.5 \times 10^{15}$ cm^{-2} were implanted into the sample through a SiO_2 layer 50 nm thick; (*2*) after postimplantation annealing for 10 min at 1200°C; and (*3*) after postimplantation annealing for 160 min at 1200°C. The concentration profiles $N(x)$ for Se, N, and O normalized to unity for $N = N_{max}$, where N_{max} is the corresponding peak concentration, for the sample implanted with selenium with the dose $\Phi = 2.5 \times 10^{15}$ cm^{-2} and then annealed for 160 min at $T = 1200$°C are shown in the insert.

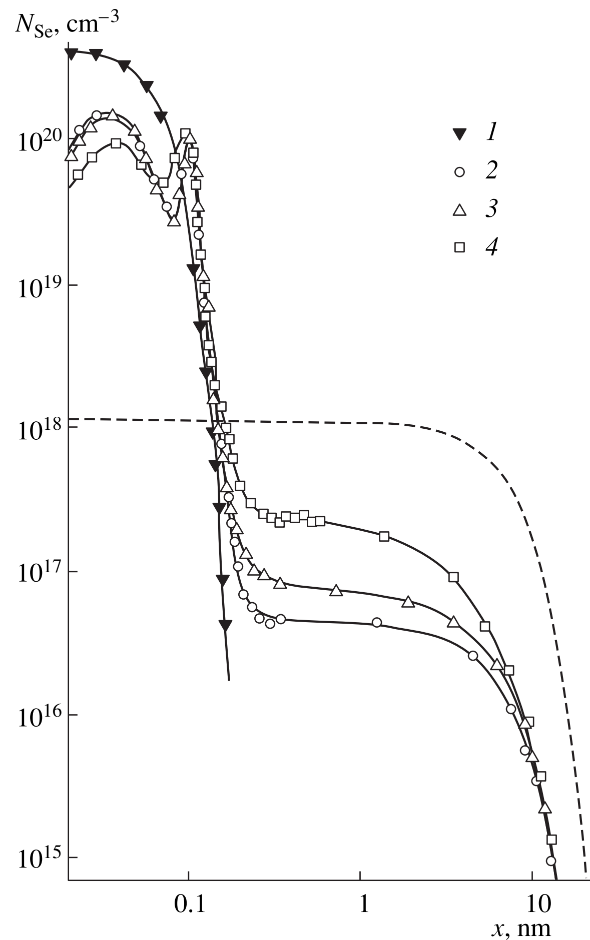

Fig. 5. Concentration profiles of selenium $N_{Se}(x)$ (*1*) after ^{80}Se ions with an energy of 125 keV and dose $\Phi = 2.5 \times 10^{15}$ cm^{-2} were implanted into the sample through a SiO_2 layer 50 nm thick; (*2*) after postimplantation annealing for 120 min at $T = 1050$°C; (*3*) after annealing for 50 min at 1100°C; and (*4*) after annealing for 10 min at $T = 1200$°C.

surface region decreases. Selenium atoms remaining in this region are not involved in diffusive redistribution owing to the fact that the concentration of mobile atoms is limited by their ultimate solubility at a given temperature. Simultaneously, the concentration profiles of oxygen and nitrogen are also modified and become completely similar to the selenium concentration profiles (see the insert in Fig. 4).

A decrease in the total amount of impurity in the near-surface region of the sample in the course of annealing occurs in the entire range of annealing temperatures used. An appreciable fraction of selenium leaves the sample through the Si–SiO_2 interface. This is most evident if annealing is performed at 800°C (Fig. 2), in which case the fraction of selenium that penetrates into deeper layers as a result of diffusion is negligibly small (see below) and almost all the changes in the concentration of atoms in the region under consideration are related to their escape into SiO_2. It is noteworthy that variations in the concentration of selenium in the diffusion source due to the escape of selenium through the Si–SiO_2 interface do not affect the region in the Se concentration profile where the characteristic peak is formed. The peak formed in less than 10 min at the above temperature remains virtually unchanged during subsequent heat treatments.

During heat treatments, selenium atoms also penetrate to a depth of more than 0.2 μm. In the concentration profiles obtained by SIMS, this deep penetration manifests itself in the fact that a concentration plateau at a depth greater than 0.2 μm is observed; this plateau corresponds to a region with an almost constant Se con-

centration, which is very low compared to the Se concentration in the near-surface region. Figure 5 shows the concentration profiles of Se in the samples implanted with the same dose of Se ions but annealed at 1050, 1100, and 1200°C with durations such that the resulting diffusion lengths were the same. The concentration profiles obtained by SIMS and those obtained by measuring the temperature dependences of the Hall emf and electrical conductivity combined with layer-by-layer etching of silicon are in good agreement with respect to the concentration level at the plateau; it should be noted that the scale on the horizontal (spatial coordinate) axis is logarithmic in Fig. 5. The concentration level at the plateau depends on the annealing temperature: the lower the temperature, the lower the concentration. For annealing at 1050, 1100, and 1200°C, these concentration levels are 5×10^{16}, 9×10^{16}, and 2.5×10^{17} cm^{-3}, respectively.

DISCUSSION

In our opinion, the transformations of the concentration profiles of implanted selenium observed during heat treatments can be explained if we assume that selenium atoms are distributed over several possible types of sites in the silicon lattice. Selenium atoms residing at at least one of these sites are mobile in the range of temperatures used in the heat treatments; as a result, we observe the diffusive transport of selenium to distances of about 100 nm (this is the scale of the observed spatial redistributions of Se impurity). The times required to establish steady-state concentrations at the peaks during heat treatments at 700 and 800°C are in good agreement with the times required for diffusive transport of Se atoms to such distances [3].

It should be noted that the time needed to attain steady-state concentration values at the peak is not the same for different impurities. Accumulation of oxygen, carbon, and nitrogen atoms at the additional peak is slowed down compared to that of selenium atoms, which is consistent with the smaller values of the diffusion coefficients for O, N, and C in Si.

Since the data obtained by electron diffraction indicate that, in the entire dose range of ions, implantation results in complete amorphization of the damaged layer, one of the possible processes occurring during subsequent heat treatments of the sample is (along with diffusion) recrystallization in the solid phase. The motion of the recrystallization front from the boundary of the damaged layer to the surface can in principle induce the redistribution of impurities due to the effects of segregation.

According to electron diffraction data, annealing for 4 h at $T = 600$°C leads to complete recrystallization of the amorphous layer. In this case, the changes in spatial distribution of selenium (Fig. 1, curve *2*) manifest themselves in the appearance of an insignificant inflection at the depth where the concentration peak is formed as a result of subsequent heat treatments at higher temperatures. A single additional annealing (for example, for 50 min at $T = 1100$°C; see Fig. 1, curve *3*) gives rise to an accumulation of selenium in this region. In our opinion, this indicates that the mechanism for redistribution of selenium by the recrystallization front is of little importance in the case under consideration and that the accumulation of selenium is caused by diffusive transport to a specific region after recrystallization of the amorphous layer.

For an impurity to be accumulated with subsequent formation of a peak in the concentration profile, mobile atoms must be trapped and immobilized. As follows from the data obtained, it is relaxation of a system of defects during annealing that gives rise to a region where impurity atoms are effectively trapped. In fact, the dependence of the relative shift of the region where the impurity is fixed and accumulated during heat treatments on the energy and dose of the implanted ions correlates well with a similar shift of the plane in which the specific energy losses by ions due to elastic collisions (as calculated with the TRIM code) amount to 6×10^{20} keV cm^{-3}.

On the one hand, using model concepts of the amorphization process [8–10], we can relate the value of 6×10^{20} keV cm^{-3} to the critical density of energy losses due to elastic collisions; at this critical density, the damaged silicon layer becomes completely amorphized. In general, since the distribution of elastic energy losses over the depth is bell-shaped, two critical-density planes can correspond to the above value. However, in this work, a single plane located deeper than the mean projected range R_p of selenium ions corresponds to this critical value for all implantation conditions used (with allowance made for the fact that the ions were implanted through the masking oxide).

On the other hand, the region where the impurity-concentration peak is formed is located deeper than R_p for selenium ions and is separated from R_p by a distance comparable to the half-width of the initial profile. This is exactly the region where the formation of so-called end-of-range defects is observed [8].

The spatial positions of these regions is completely defined by the implantation conditions for selenium ions. In both cases, a subsystem of defects in the crystal can form a relatively thin region in the depth space where the impurity atoms can become trapped.

The existence of a rather wide range of temperatures and time spans of heat treatments where impurity-transport processes beyond the boundary of the near-surface region do not affect the profile shape in the vicinity of the peak makes it possible to estimate the total amount of impurity fixed in this vicinity. A fraction of the impurity atoms present in the region of the peak are not fixed but are involved in diffusive trans-

port; therefore, we can estimate the total amount of impurity immobilized in the region of the peak by subtracting the value obtained by linear interpolation of the values of impurity concentration outside the peak region from the total amount of impurity in this region (from the point of local minimum to the point corresponding to the beginning of the concentration plateau at the sample depth). It is noteworthy that the contribution of this interpolated value is most important for the samples implanted with low doses of ions, in which case either the peak is not formed at all (Fig. 3, curve *1*) or it has very small magnitude (Fig. 3, curve *2*).

The total calculated steady-state amount of selenium contained in the additional peak depends only slightly on the annealing temperature in the entire temperature range. The largest spread of this value for similar samples differing only in the conditions of heat treatment does not exceed 50%.

At the same time, the amount of selenium in the additional peak depends substantially on the ion dose (see the insert in Fig. 3, curve *5*). For the samples annealed for 50 min at 1100°C, an increase in the ion dose by approximately a factor of 3 (from 6×10^{14} to 2×10^{15} cm^{-2}) brings about an increase in the total amount of selenium in the peak of more than three orders of magnitude. Compared to the unit-slope straight line (see the insert in Fig. 3, curve *6*), the dose dependence of the amount of impurity accumulated in the peak is of the threshold type. Under the experimental conditions of this work, we were able to observe the formation of the peak if the doses exceeded $\Phi = 1.9 \times 10^{14}$ cm^{-2}, which is related to the existence of a plateau at the level of concentration corresponding to the onset of diffusion of selenium atoms into the bulk of the sample. Continuation of the dose dependence of the amount of impurity in the peak (see the insert in Fig. 3, curve *5*) to the low-dose range leads to dose values corresponding to those of amorphization for ions similar in mass to selenium. In particular, for arsenic ions with an energy of 100 keV, a value of ~(2–5) $\times 10^{13}$ cm^{-2} was reported [10].

Examining the concentration profile of selenium atoms (Fig. 5), we can recognize two regions differing appreciably in the scale of depths and in the concentration of atoms: a diffusion-source region and a region of diffusive distribution of selenium in the depth of the sample. The amount of impurity penetrating to deeper layers is significantly less than that stored in the diffusion source even if the fact that selenium atoms are immobile in the vicinity of the peak is taken into account. In the case of diffusion from a source of this strength, the concentration profile of diffusing impurities would have the shape shown by the dashed curve in Fig. 5. However, the observed diffusive redistribution of selenium atoms has the form characteristic of diffusion of impurities whose concentration is bounded above (Fig. 5, experimental points and solid lines). The concentration level of selenium atoms diffusing into the bulk to depths greater than 0.2 μm is found to be appreciably lower than the mean concentration in the diffusion source and depends on the temperature of heat treatment of the sample. In the entire range of annealing temperatures, the value of this concentration is in satisfactory agreement with the published data on selenium solubility in silicon [3] and is most likely consistent with the temperature dependence of the solubility.

CONCLUSION

Thus, we report the following results:

(i) Annealing in the temperature range of 600–1200°C leads to the formation of special features in the form of inflection points and additional peaks in the concentration profile of selenium; the selenium concentration at the peak can exceed the as-implanted selenium concentration in this region of the sample.

(ii) The spatial position of the peak correlates well with the position of the plane where the specific energy losses of ions due to elastic collisions amount to 6×10^{20} keV cm^{-3}. This value is close to the critical specific energy loss corresponding to the formation of a continuous amorphous layer. Consequently, the spatial position of the peak can correspond to either the region of the end-of-range defects or the region where the boundary between the continuous amorphous layer and the crystalline matrix is located.

(iii) The aforementioned special features in the concentration profiles are formed only at doses exceeding that for amorphization, while accumulation of selenium is caused by diffusive transport to the specified region after the amorphous layer is recrystallized. In the sample region containing the selenium concentration peak, the atoms of impurities such as oxygen, carbon, and nitrogen can also be trapped.

(iv) The concentration of selenium atoms penetrating by diffusion to a depth greater than 0.2 μm is considerably lower than the mean concentration of implanted impurity in the diffusion source and depends on the temperature during heat treatment of the sample. In the entire range of annealing temperatures, the value of the mobile-selenium concentration is in satisfactory agreement with the published data on the solubility of selenium in silicon.

ACKNOWLEDGMENTS

We are grateful to S.I. Romanov for electron diffraction analysis of the samples.

This work was supported by the Russian Foundation for Basic Research, project no. 96-15-97272.

REFERENCES

1. E. Sörman, W. M. Chen, A. Henry, *et al.*, Phys. Rev. B: Condens. Matter **51**, 2132 (1995).
2. M. Thiagarajan, K. Iyakutti, and E. Palaniyandi, Phys. Status Solidi B **205**, 553 (1998).
3. H. R. Vydyanath, J. S. Lorenzo, and F. A. Kröger, J. Appl. Phys. **49**, 5928 (1978).
4. E. Janzén, R. Stedman, G. Grossmann, *et al.*, Phys. Rev. B: Condens. Matter **29**, 1907 (1984).
5. R. W. Jansen and O. F. Sankey, Phys. Rev. B: Condens. Matter **33**, 3994 (1986).
6. H. Overhof, M. Scheffler, and C. M. Weinert, Phys. Rev. B: Condens. Matter **43**, 12494 (1991).
7. A. A. Taskin and E. G. Tishkovskiĭ, Fiz. Tekh. Poluprovodn. (St. Petersburg) **32**, 1306 (1998) [Semiconductors **32**, 1162 (1998)].
8. K. S. Jones, S. Prussin, and E. R. Weber, Appl. Phys. A **45**, 1 (1988).
9. J. F. Gibbons, Proc. IEEE **60**, 1962 (1972).
10. S. Prussin, D. L. Margolese, and R. N. Tauber, J. Appl. Phys. **57**, 180 (1985).

Translated by A. Spitsyn

Semiconductors, Vol. 34, No. 3, 2000, pp. 319–322. Translated from Fizika i Tekhnika Poluprovodnikov, Vol. 34, No. 3, 2000, pp. 325–329.
Original Russian Text Copyright © 2000 by Vavilova, Kapitonov, Livshits, Lyutetskiĭ, Murashova, Pikhtin, Skrynnikov, Tarasov.

LOW-DIMENSIONAL SYSTEMS

Photoluminescent and Electroluminescent Properties of Spontaneously Forming Periodic InGaAsP Structures

L. S. Vavilova, V. A. Kapitonov, D. A. Livshits, A. V. Lyutetskiĭ, A. V. Murashova, N. A. Pikhtin, G. V. Skrynnikov, and I. S. Tarasov*

Ioffe Physicotechnical Institute, Russian Academy of Sciences, Politekhnicheskaya ul. 26, St. Petersburg, 194021 Russia

** e-mail: tarasov@hpld.ioffe.rssi.ru*

Submitted September 16, 1999; accepted for publication September 22, 1999

Abstract—Photoluminescence and electroluminescence techniques were used to study spontaneously forming periodic InGaAsP structures that consisted of two types of alternating solid-solution domains differing in composition and lattice constant. It was found experimentally that the volume of the narrow-gap material domains is smaller than that of the wide-gap domains. Existence of the inelastic strain caused by the large (2–3%) lattice constant mismatch between the adjacent domains was inferred. Laser diodes with the spontaneously forming periodic InGaAsP structures in the active region were fabricated, and lasing in the long-wavelength electroluminescence spectral band that originated from the radiative recombination in the narrow-gap domains was obtained. Lasing at the threshold current densities of 70 A/cm^2 at 77 K and 700 A/cm^2 at 300 K was observed in the highest-quality samples. © *2000 MAIK "Nauka/Interperiodica".*

1. INTRODUCTION

A technique for fabricating spontaneously forming periodic InGaAsP structures was proposed by us previously [1, 2]. The technique is based on the phenomenon of the spinodal decomposition of the multicomponent III–V semiconductor solid solutions [3–14]. Theoretical and experimental studies [15, 16] of the InGaAsP structures spontaneously formed due to the solid-solution spinodal decomposition indicate that they consist of two types of domains differing in composition and, hence, in the bandgap widths E_{g1} and E_{g2} and that they periodically alternate in the directions [100] and [010], which are the easiest compression directions of the crystal. The domain size can be determined by the transmission electron microscopy and, in the different structures investigated, ranges from 200 to 600 Å [2, 15].

In this work, photoluminescent and electroluminescent properties of spontaneously forming periodic InGaAsP structures are studied.

2. SAMPLES

To study the photoluminescent and electroluminescent properties of the spontaneously forming periodic InGaAsP structures, isotypic and anisotypic double heterostructures with such a layer in the active region were grown by liquid-phase epitaxy on the GaAs(001) substrates. The active region thickness was 0.2–0.3 µm. The sample layout is shown in Fig. 1.

To study the electroluminescencent properties, four-faceted laser diodes were cleaved from the anisotypic heterostructures. Conventional techniques were employed for the photoluminescence and electroluminescence measurements.

3. EXPERIMENTAL RESULTS

3.1. Photoluminescence of the Spontaneously Forming Periodic InGaAsP Structures

The photoluminescence (PL) spectra of the spontaneously forming periodic InGaAsP structures at liquid-nitrogen and room temperatures typically exhibit a short-wavelength (λ_1) and a long-wavelength (λ_2) band related to the radiative recombination in the domains of different solid-phase compositions with bandgap widths of E_{g1} and E_{g2}, respectively [1, 15]. This can be seen in Figs. 2a and 2b, where the PL spectra of one of the structures under study are shown. For the samples considered in this paper (all grown under identical con-

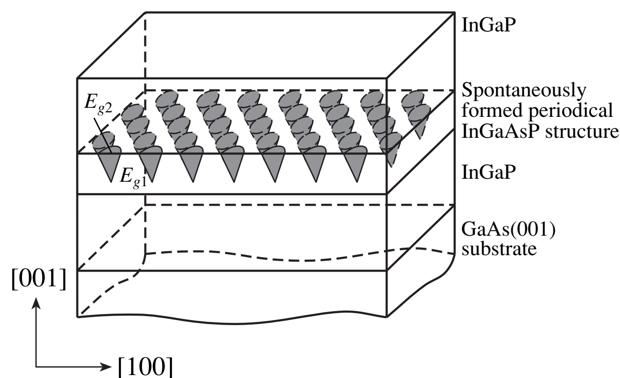

Fig. 1. Configuration of the structure under study.

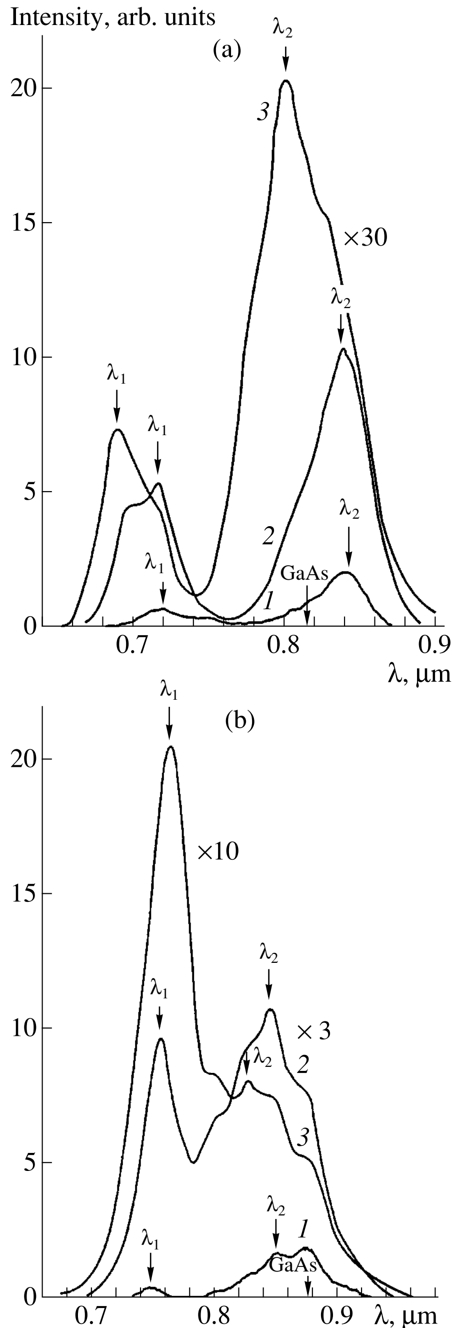

Fig. 2. Photoluminescence spectra of the spontaneously formed periodic InGaAsP structures: (a) $T = 77$ K, excitation intensity equals (*1*) 0.06, (*2*) 0.14, and (*3*) 3.7 kW/cm^2; (b) $T = 300$ K, excitation intensity equals (*1*) 0.17, (*2*) 1.4, and (*3*) 8.0 kW/cm^2.

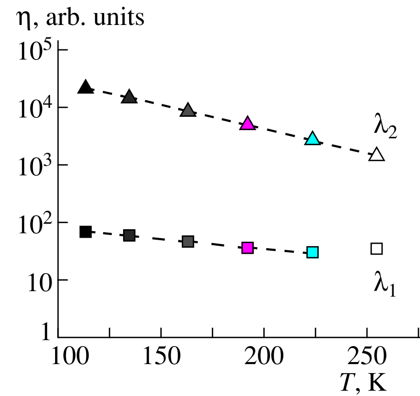

Fig. 3. Temperature dependence of the quantum efficiency η of the spontaneously formed periodic InGaAsP structure photoluminescence for the short- and long-wavelength spectral bands (λ_1 and λ_2, respectively).

ditions), the peaks of the radiative recombination bands at 77 K under low excitation levels appear approximately at $\lambda_1 \approx 0.72$ μm ($E_{g1} \approx 1.72$ eV) and $\lambda_2 \approx 0.85$ μm ($E_{g2} \approx 1.46$ eV). At 300 K, the band peaks are shifted slightly to longer wavelengths. The band corresponding to the InGaP emission is not shown in Figs. 2a and 2b. Additional peaks observed approximately at $\lambda = 0.816$ μm (at $T = 77$ K) and $\lambda = 0.877$ μm (at $T = 300$ K) are due to the radiative recombination in the GaAs substrate.

The dependence of the PL spectra of the spontaneously forming periodic InGaAsP structures on the excitation level both at liquid-nitrogen and room temperatures in the intensity range from 60 W/cm^2 to 8 kW/cm^2 was investigated.

At $T = 77$ K, the relative intensities of the long-wavelength and short-wavelength bands do not change as the excitation level increases (Fig. 2a). A broadening of the long-wavelength band was observed, apparently related to the spread in the composition of the corresponding domains.

At $T = 300$ K, the long-wavelength band intensity saturates with an increase in the excitation level (Fig. 2b). We believe that this is related to the smaller volume of the domains responsible for the long-wavelength emission, as compared to the volume of the domains responsible for the short-wavelength emission.

Analysis of the temperature dependence of the PL spectra revealed that the decrease in the quantum yield of the long-wavelength luminescence with temperature is more pronounced than that of the luminescence in the short-wavelength band (Fig. 3). The simplest explanation for this observation is based on the existence of the defects due to inelastic strain in the bordering heterogeneous domains [15]. The inelastic strain appears because of the lattice mismatch between the solid solutions of different composition forming the domains. Indeed, the theoretically estimated mismatch $(a_2 - a_1)/a_1$ of the domain lattice constants in the structures under investigation is 2–3% [8]; in the case of bulk epitaxial films of the semiconductor solid solutions, such a mismatch is known to result in the inelastic deformation of the crystal lattice [17].

The results presented here were obtained for one specific type of spontaneously formed periodic InGaAsP structures. However, for the growth temperature chosen (T_G = 750°C), the quaternary InGaAsP material cannot be grown as a homogeneous solid solution in a range of compositions [8, 15]. Epitaxial layers of these solid solutions also appear as spontaneously formed periodic InGaAsP structures with different domain solid phase composition and, consequently, different spectral positions of the luminescence bands. In this connection, it should be noted that the PL properties described above are characteristic of all of these spontaneously formed periodic InGaAsP structures.

3.2. Electroluminescence of the Spontaneously Formed Periodic InGaAsP Structures

Electroluminescence (EL) spectra of the four-faceted laser diodes with the active region containing a spontaneously formed periodic InGaAsP structure described in the previous section were investigated at liquid-nitrogen and room temperatures (see Figs. 4a, 4b). Both spectra exhibit the long- and short-wavelength spontaneous emission bands. In Fig. 4, we present the EL spectra of the laser diode at a fairly low pump level, so that the short-wavelength spontaneous emission band is not clearly resolved. This corresponds to the PL spectra of the isotypic structure (Figs. 2a, 2b). With an increase in the pumping level, lasing in the long-wavelength EL band was attained. The threshold current densities for the four-faceted laser diodes were J_{th} = 70–250 A/cm^2 at T = 77 K and J_{th} = 0.7–1.3 kA/cm^2 at T = 300 K.

Stripe lasers with the stripe width W = 20, 50, and 100 μm and cavity length L = 510 μm were also fabricated from the anisotypic double heterostructures. The long-wavelength spontaneous emission band in the EL spectra of such laser diodes was observed only at low pump levels (for current densities lower than 300 A/cm^2 at T = 77 K and 1 kA/cm^2 at T = 300 K). The long-wavelength band intensity saturated rapidly with the pump level and the short-wavelength band appeared. With a further increase in the pump level, lasing sets in the short-wavelength band of the EL spectrum. The threshold current densities for the stripe laser diodes were J_{th} = 2.9–6.3 kA/cm^2 at T = 300 K. The differential quantum efficiency of these lasers was low (10–20%).

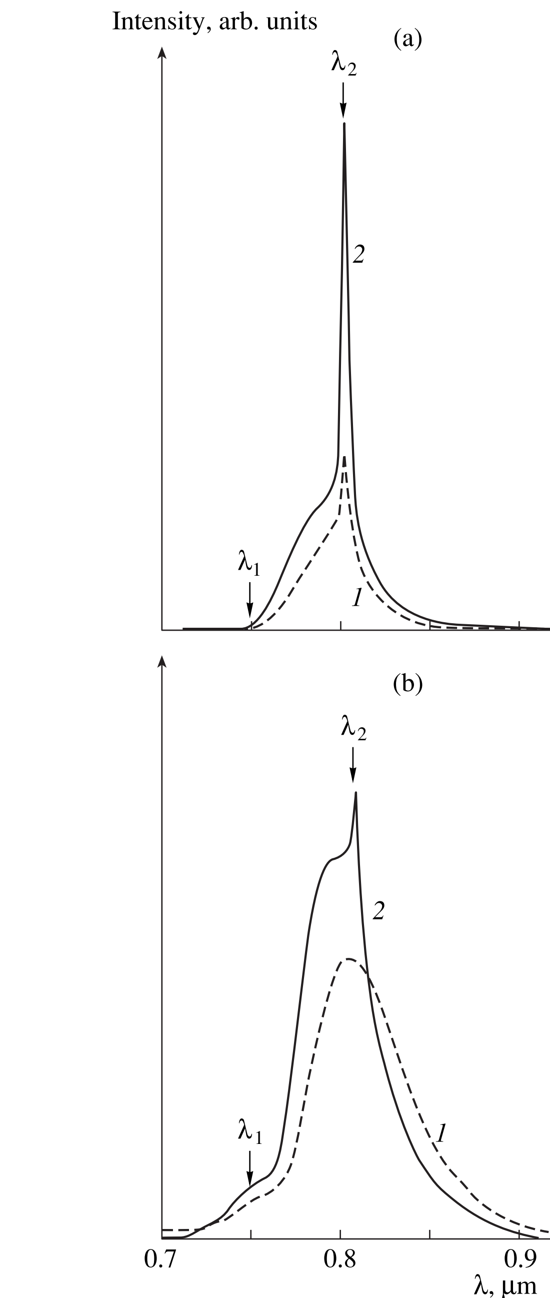

Fig. 4. Electroluminescence spectra of the four-faceted laser diode with the spontaneously formed periodic InGaAsP structure in the active region: (a) T = 77 K, (*1*) $J = J_{th}$ = 75 A/cm^2 and (*2*) J = 110 A/cm^2; (b) T = 300 K, (*1*) J = 375 A/cm^2 and (*2*) $J = J_{th}$ = 1100 A/cm^2.

4. DISCUSSION

1. Investigations of the PL and EL properties of the spontaneously formed periodic InGaAsP structures consisting of alternating domains of different composition demonstrated that (i) the volume of the narrow-gap material domains is smaller than that of the wide-gap material domains and (ii) inelastic strain exists in the structures, apparently due to the poor matching of the domains of different compositions and lattice constants (this implies a large (2–3%) mismatch in the lattice constants of adjacent domains).

2. Lasing was obtained in the long-wavelength band of the EL spectrum of the four-faceted laser diodes fabricated from the anisotypic double heterostructures with a spontaneously formed periodic InGaAsP structure in the active region. The best samples available are

characterized by the threshold current density of J_{th} = 70 A/cm^2 at $T = 77$ K ($\lambda = 0.81$ μm) and J_{th} = 700 A/cm^2 at 300 K ($\lambda = 0.82$ μm). These values correspond to the experimentally observed threshold currents in the anisotypic double heterostructures with an active region composed of homogeneous solid solution with $E_g = 1.51$ eV ($\lambda = 0.82$ μm).

Thus, no significant reduction of the threshold current densities in the four-faceted laser diodes with the spontaneously formed periodic InGaAsP structures in the active region was observed, in contrast to the expectations based on the existence of the wide-gap solid-solution domains surrounding the narrow-gap material in the active region. One can model such a laser structure by the asymmetric double heterostructure with the active region characterized by the bandgap E_{g2} of the narrow-gap material and asymmetric waveguide characterized by the bandgap E_{g1} of the wide-gap material. The threshold current densities calculated in the context of this model are J_{th} = 20 A/cm^2 at $T = 77$ K and J_{th} = 90 A/cm^2 at $T = 300$ K. However, nonradiative recombination is not taken into account in this estimate. In the actual laser structures, defects associated with inelastic strain in the active region provide the nonradiative recombination channels, which cause an increase in the threshold current, as compared to the calculated values.

5. CONCLUSION

We should note in conclusion that, despite the potential advantages of the spontaneously formed periodic InGaAsP structures, their present quality is inadequate for effective employment in light-emitting devices. We believe that the problem can be solved by growing the structures with a domain size of 50–150 Å. Then, the defect formation at the domain boundaries will be avoided, notwithstanding the large (2–3%) domain lattice-constant mismatch. This enables one to lower the nonradiative recombination rate in such layers and preserve high quantum efficiency in the laser diodes with an active region of the spontaneously formed periodic InGaAsP structure.

ACKNOWLEDGMENTS

We are grateful to I. P. Ipatova for her helpful participation in discussions during preparation of the manuscript.

This work was supported by the Russian Foundation for Basic Research (project no. 97-02-18105) and the State Program "Physics of the Solid-State Nanostructures."

REFERENCES

1. I. S. Tarasov, L. S. Vavilova, I. P. Ipatova, *et al.*, in *Proceedings of 23rd International Symposium on Compound Semiconductors, ISCS-23, St. Petersburg, Russia, 1997*, p. 117.
2. L. S. Vavilova, A. V. Ivanova, V. A. Kapitonov, *et al.*, Fiz. Tekh. Poluprovodn. (St. Petersburg) **32**, 658 (1998) [Semiconductors **32**, 590 (1998)].
3. J. W. Cahn, Trans. Met. Soc. **242**, 166 (1967).
4. B. de Cremoux, J. Phys. (Paris) **43**, C5-19 (1982).
5. K. Onabe, Jpn. J. Appl. Phys. **21**, L323 (1982).
6. G. B. Stringfellow, J. Cryst. Growth **58**, 194 (1982).
7. A. G. Khachaturyan, *Theory of Structural Transformations in Solids* (Wiley, New York, 1983).
8. I. P. Ipatova, V. G. Malyshkin, A. Yu. Maslov, *et al.*, Fiz. Tekh. Poluprovodn. (St. Petersburg) **27**, 285 (1993) [Semiconductors **27**, 158 (1993)].
9. I. P. Ipatova, V. G. Malyshkin, and V. A. Shchukin, Philos. Mag. **70**, 557 (1994).
10. D. Bimberg, I. P. Ipatova, P. S. Kop'ev, *et al.*, Usp. Fiz. Nauk **167**, 552 (1997) [Physics–Uspekhi **40**, 529 (1997)].
11. A. Zunger and S. Mahajan, in *Handbook on Semiconductors*, Ed. by T. S. Moss (Elsevier, 1994), Vol. 3, p. 1399.
12. S. Mukai, J. Appl. Phys. **54**, 2635 (1983).
13. A. Behres, M. Heuken, C. Mendorf, *et al.*, in *EW MOVPE VII, Berlin, 1997*, p. A13.
14. C. Mendorf, G. Brockt, Q. Liu, *et al.*, in *Microsc. Semicond. Mater. Conf. Ser. No. 157*, Oxford (1997), p. 25.
15. N. A. Bert, L. S. Vavilova, I. P. Ipatova, *et al.*, Fiz. Tekh. Poluprovodn. (St. Petersburg) **33**, 544 (1999) [Semiconductors **33**, 510 (1999)].
16. A. A. Sitnikova, N. A. Bert, A. V. Murashova, *et al.*, in *Proceedings of International Symposium on Electron Microscopy ICEM 14, Cancun, Mexico, 1998*, p. 199.
17. N. A. Bert, A. T. Gorelenok, A. G. Dzigasov, *et al.*, Fiz. Tekh. Poluprovodn. (Leningrad) **16**, 60 (1982) [Sov. Phys. Semicond. **16**, 35 (1982)].

Translated by M. Skorikov

Semiconductors, Vol. 34, No. 3, 2000, pp. 323–326. Translated from Fizika i Tekhnika Poluprovodnikov, Vol. 34, No. 3, 2000, pp. 330–333.
Original Russian Text Copyright © 2000 by Tsatsul'nikov, Volovik, Bedarev, Zhukov, Kovsh, Ledentsov, Maksimov, Maleev, Musikhin, Ustinov, Bert, Kop'ev, Bimberg, Alferov.

LOW-DIMENSIONAL SYSTEMS

Mechanisms of InGaAlAs Solid Solution Decomposition Stimulated by InAs Quantum Dots

A. F. Tsatsul'nikov*, B. V. Volovik*, D. A. Bedarev*, A. E. Zhukov*, A. R. Kovsh*, N. N. Ledentsov*, M. V. Maksimov*, N. A. Maleev*, Yu. G. Musikhin*, V. M. Ustinov*, N. A. Bert*, P. S. Kop'ev*, D. Bimberg, and Zh. I. Alferov***

** Ioffe Physicotechnical Institute, Russian Academy of Sciences, Politekhnicheskaya ul. 26, St. Petersburg, 194021 Russia*

*** Institut für Festkörperphysik, Technische Universität Berlin, D-10623 Berlin, Germany*

Submitted September 21, 1999; accepted for publication September 23, 1999

Abstract—Mechanisms of InGaAlAs solid solution decomposition stimulated by a purposely deposited layer of InAs quantum dots are studied. Decomposition of the solid solution results in an increase in the effective quantum dot size and the shift of the photoluminescence line to as far as 1.3 μm. When aluminum atoms are added to the solid solution, the effect of In atom "conservation" within the dots is observed, which also causes an increase in the effective dot size. *© 2000 MAIK "Nauka/Interperiodica".*

Studies of structures with (In,Ga)As quantum dots (QDs) in a GaAs matrix are currently [1–4] attracting considerable attention. This is related to the possibility of extending the wavelength range of the optical emission from structures grown on the GaAs substrates up to 1.3 μm. Creation of an injection laser operating at 1.3 μm with an active region based on such QDs has recently been reported [5]. However, there exists the problem of reducing the density of dislocations in these structures, because an InGaAs layer of large effective thickness is to be deposited. It was shown in [6, 7] that the emission wavelength can also reach 1.3 μm in structures where InAs QDs are covered by a thin layer of InGaAs. Due to the stimulated decomposition of the solid solution, which takes place in such systems, localized regions enriched in In are formed in the vicinity of the QDs, which results in the long-wavelength shift of the photoluminescence (PL) line. With this technique, 1.3-μm emission can be achieved in structures with a smaller effective thickness of the InGaAs layer. In this work, the mechanisms of InGaAlAs solid solution decomposition stimulated by a purposely deposited layer of InAs QDs are investigated in detail.

The structures used in the study were grown on semi-insulating GaAs(100) substrates by molecular-beam epitaxy in a Riber 32P system. The effective thickness d_{QD} of the deposited InAs layer, the thickness W of the InGaAlAs layer, and its composition are given in the table. Transmission electron microscopy (TEM) studies were carried out on a Philips EM-420 microscope at an accelerating voltage of 100 kV. PL was excited by an Ar^+ laser (λ = 514.5 nm and excitation power density $P_{ex} \simeq 100$ W/cm^2) and was detected by a cooled Ge photodiode.

TEM studies in the cross-sectional geometry were made in the dark-field mode with the use of the (200) reflection, which is highly sensitive to the chemical composition of III–V materials. No features in the image contrast are observed in the micrograph of structure 1 (Fig. 1a), where only the InGaAlAs layer, which forms a quantum well (QW) in the plane of the heterostructure (hereinafter we refer to this layer as the QW), is deposited; this indicates that QDs are not formed. In the case of sequential deposition of the InAs QD layer and InGaAlAs QW (Fig. 1b), dark contrast is observed in the regions above the QDs; it differs from the usual strain contrast stemming from the lattice-constant mismatch between the QDs and the matrix. A simple analysis of the (200) reflection intensity for a quaternary InGaAlAs solid solution demonstrates that its decrease (i.e., the appearance of dark contrast) can be related to a decreased Al and/or increased In content. We suggest

Table

Sample	d_{QD}, nm	Layer composition	W, nm	L_{QD}, nm	ρ_{QD}, 10^{10} cm^{-2}
1	–	$In_{0.15}Al_{0.15}Ga_{0.70}As$	8	–	–
2	0.65	$In_{0.15}Al_{0.15}Ga_{0.70}As$	8	19	2.8
3	0.65	GaAs			
4	0.65	$In_{0.18}Ga_{0.82}As$	2.5	15	3.4
5	0.8	$In_{0.18}Ga_{0.82}As$	2.5	18	4.3
6	0.8	$In_{0.18}Ga_{0.82}As$	3.0	28	4.5
7	0.65	$Al_{0.20}Ga_{0.80}As$	4.0		
8	0.65	$In_{0.05}Al_{0.20}Ga_{0.75}As$	4.0		
9	0.65	$In_{0.10}Al_{0.20}Ga_{0.70}As$	4.0		
10	0.65	$In_{0.15}Al_{0.15}Ga_{0.70}As$	4.0	17	1.8

Note: L_{QD} and ρ_{QD} are the lateral size and areal density of the quantum dots, respectively.

1063-7826/00/3403-0323$20.00 © 2000 MAIK "Nauka/Interperiodica"

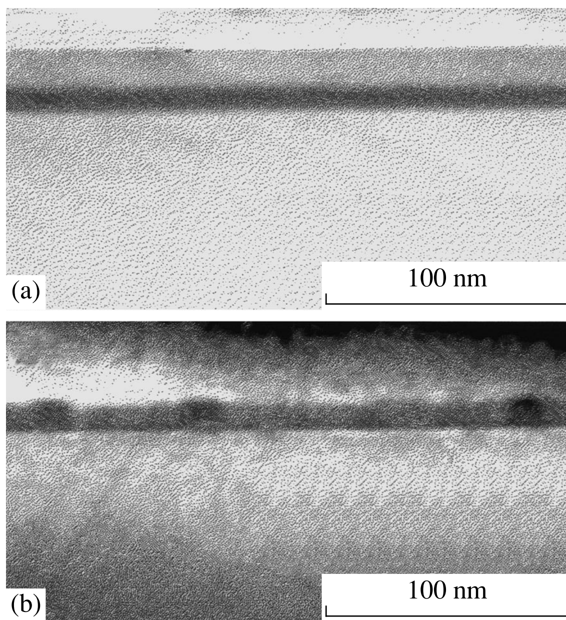

Fig. 1. Cross-sectional TEM images of structures (a) 1 and (b) 2.

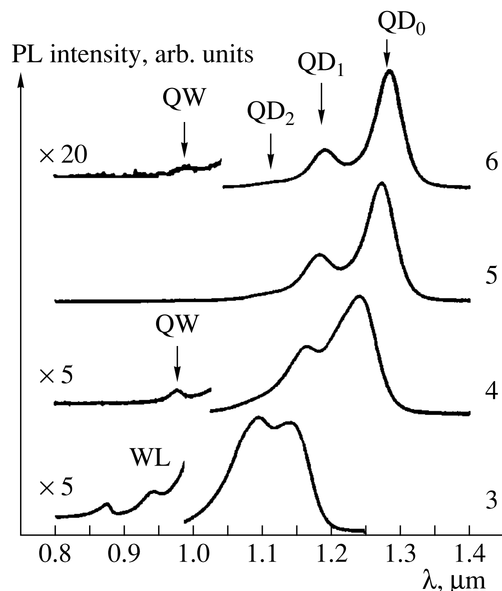

Fig. 2. Photoluminescence spectra of structures 3–6 at T = 300 K. The line WL originates from charge carrier recombination via the states in the wetting layer.

that the local strain induced by a QD in the matrix stimulates the redistribution of In and/or Al in such a way that the region near and above the dot becomes enriched in In and/or depleted of Al. This redistribution should lead to an increase in the effective QD size. In addition, the spread in the QD size is noticeably reduced with an increase in the QW layer thickness; this can be seen from an analysis of TEM images in the planar geometry. We believe that this effect also results from the redistribution of In and/or Al in the QW regions adjacent to the QDs, which evidently results in the growth of the effective QD size and a decrease in the size spread.

The PL spectra of samples 3–6 with different effective thicknesses of the InAs and $In_xGa_{1-x}As$ layers are shown in Fig. 2. Along with the lines QD_0–QD_2 related to recombination in the QDs, a short-wavelength band QW, originating from the recombination in the $In_xGa_{1-x}As$ QW, is observed in the spectra of the samples containing the QW layer. The growth of the QD size is accompanied by a pronounced long-wavelength shift and narrowing of the corresponding PL lines. It has been found in previous studies of the spectral position of the PL peak related to InAs QDs in a GaAs matrix [8] that the maximum emission wavelength from those dots (attained with an average deposition thickness of about four or more monolayers and/or long growth interruptions) equals ~1.24 μm. Coating the QDs obtained by depositing a significantly smaller amount of InAs with a thin InGaAs layer with a low (15–20%) In content results in a shift of the PL maximum up to 1.28 μm. Let us consider the reasons for such strong variation of the optical transition energy.

The reduction in the bandgap of the material surrounding the QDs might be the cause of the decrease in the optical transition energy after coating the QDs with an InGaAs layer. However, we demonstrate below that the transition energy does not increase after coating the QDs with an InAlGaAs layer, whose bandgap is wider than that of GaAs. Moreover, the transition energy is even reduced in the case of QDs obtained after submonolayer deposition.

Another reason for this long-wavelength shift of the PL line is an increase in the In atom concentration in the vicinity of QDs coated with a solid-solution layer, which is evidenced by the TEM data and results from the strain induced around the dots. The QW line position in the spectrum of sample 6 corresponds to the one calculated for recombination in a 3.3-nm-wide $In_{0.25}Ga_{0.75}As$ QW. This is consistent with the configuration of an active region (where recombination takes place) consisting of a 0.3-nm-thick wetting layer, which is formed during QD deposition [3, 4], and a 3-nm-thick $In_{0.18}Ga_{0.82}As$ layer. Hence, an increase in the In concentration near a QD can only occur owing to the atoms deposited in the adjacent region. Thus, the effective thickness of the InAs layer in the vicinity of a QD can increase by ~0.5 nm, which yields a total of ~1.3 nm for structure 6. According to the data obtained for pyramid-shaped QDs coated with GaAs [8, 9], consideration of this increase alone is insufficient to explain the observed PL line shift. This is consistent with our TEM data, which indicates additionally that the QD shape changes in the case of consecutive deposition of the QD and QW layers, which results in a still-larger shift of the optical transition energy compared to QDs embedded in the GaAs matrix.

In order to study the influence of the solid solution composition in the QW layer on the size and optical properties of the QDs, we investigated samples 7–9, where the dots are coated with $In_xAl_yGa_{1-x-y}As$ layers with different x and y. One can see from Fig. 3 that deposition of a wide-gap $Al_{0.20}Ga_{0.80}As$ layer also results in a large long-wavelength shift of the PL line, while an increase in the bandgap of the barrier material around the QD should result in the enhancement of the size quantization and a decrease in the localization energy of the carriers in the QD. Such nontrivial behavior of the PL spectra may be due to inhibition of In atom diffusion out of the dots coated with AlGaAs (the "conservation" effect). This leads to an increase in the QD size and, consequently, to the long-wavelength shift of the PL line. An increase in InAs molar fraction x in the $In_xAl_yGa_{1-x-y}As$ layer results in an additional long-wavelength shift of the PL line; this may be related to the decomposition effect, which results in an increase in the In atom concentration in the vicinity of the QDs, and to narrowing of the bandgap of the $In_xAl_yGa_{1-x-y}As$ material.

Along with the QD_0 line related to ground-state recombination, the short-wavelength bands QD_1 and QD_2 are observed in the spectra of all the structures we studied. It should be noted that, in structures with the InAlGaAs solid-solution layer, unlike those with the InGaAs layer, an increase in the InAs mole fraction leads to an increase in the QD_0 line intensity relative to the high-energy bands. To determine the origin of these lines, the dependences of their intensity on temperature and excitation level were examined. In structure 10, the ratio of the total intensity of the QD_1 and QD_2 lines to the intensity of the QD_0 line decreases with temperature (Fig. 4), which is not typical of QD excited-state recombination. Next, a 200-fold increase in the excitation level at $T = 15$ K results in only a slight (by about a factor of 1.5) increase in the QD_1 and QD_2 line intensities relative to the QD_0 line (Fig. 5). This behavior of the PL spectra indicates that the QD_1 and QD_2 lines might be a superposition of the PL bands originating from excited-state recombination and recombination through groups of QDs differing in their size. We prepared two samples with the same layer sequence as in structure 10 but grown on substrates misoriented by 3° and 5° from the [100] direction; the corresponding PL spectra are shown in Fig. 6. One can see that, for a misorientation angle of 3°, the QD_0 line intensity is reduced, while the intensities of the QD_1 and QD_2 lines remain unchanged. When the misorientation angle is increased to 5°, a single broad band is observed in the spectrum in place of the QD_1 and QD_2 lines. It was shown in [10–12] that misorientation of the substrate results in the suppression of large-size QD formation; thus, the results we obtained support our conclusion that there exist groups of QDs with different sizes. These groups may be due to the strong dependence of the extent of solid-solution decomposition on the size of the deposited InAs QDs. This is confirmed by the

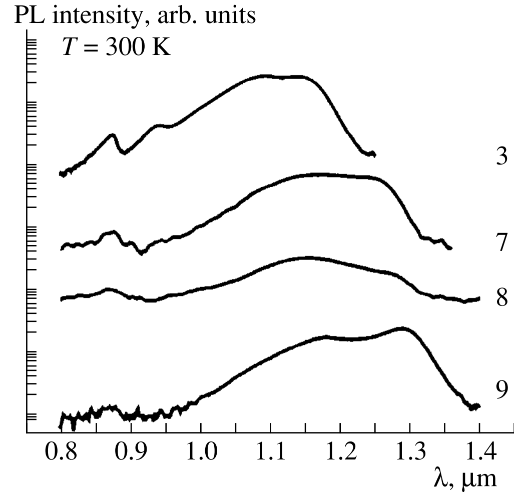

Fig. 3. Photoluminescence spectra of structures 3 and 7–9 at $T = 300$ K.

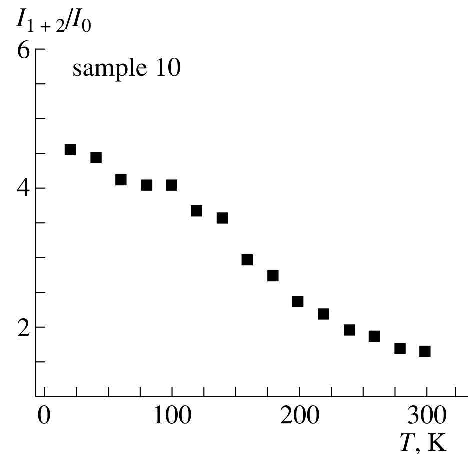

Fig. 4. Temperature dependence of the ratio of the total QD_1 and QD_2 band intensity I_{1+2} to the QD_0 band intensity I_0 for sample 10.

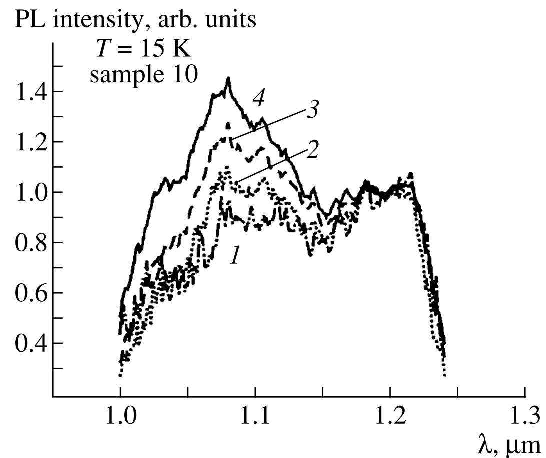

Fig. 5. Photoluminescence spectra of structure 10 taken at excitation power density P_{ex} of (*1*) 1, (*2*) 4, (*3*) 30, and (*4*) 100 W/cm^2. The curves are normalized to the spectrum taken at $P_{ex} = 0.5$ W/cm^2.

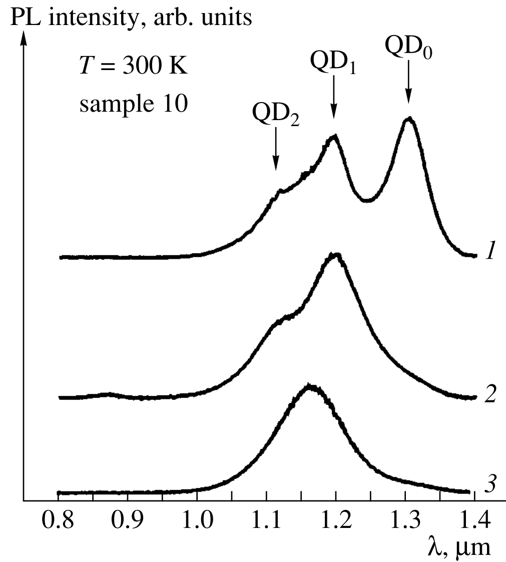

Fig. 6. Photoluminescence spectra of (*1*) structure 10 and structures with the same layer sequence grown on the substrates misoriented by (*2*) 3° and (*3*) 5°.

fact that, as the QD size increases with effective thickness of the deposited InAs layer, the PL linewidth is reduced and the intensities of the QD_1 and QD_2 lines decrease with respect to that of the QD_0 line (Fig. 2). This could be related to the formation of equilibrium QDs, which are characterized by high uniformity in size and shape in the case of thicker InAs layers.

In summary, the results obtained in this work demonstrate that the large long-wavelength shift of the PL line, observed after coating InAs QDs with a thin InGaAlAs layer, occurs due to solid-solution decomposition with the formation of In-rich regions in the vicinity of the QDs and the effect of In atom "conservation" in the QDs. Depending on the thickness of the deposited InAs layer, dots of different sizes can be formed, which results in the existence of several lines in the PL spectra.

ACKNOWLEDGMENTS

This work was supported by the Russian Foundation for Basic Research (project no. 96-0467), INTAS (grant no. 94-1028-YSF-41), the Russian Ministry of Science and Technology under the Program "Physics of the Solid-State Nanostructures," and the Volkswagen Foundation.

REFERENCES

1. L. Goldstein, F. Glass, J. Y. Marzin, *et al.*, Appl. Phys. Lett. **47**, 1099 (1985).
2. S. Guha, A. Madhukar, and K. C. Rajkumar, Appl. Phys. Lett. **57**, 2110 (1990).
3. M. Moison, F. Houzay, F. Barthe, *et al.*, Appl. Phys. Lett. **64**, 196 (1994).
4. P. M. Petroff and S. P. DenBaars, Superlattices Microstruct. **15**, 15 (1994).
5. D. L. Huffaker, G. Park, Z. Zou, *et al.*, Appl. Phys. Lett. **73**, 2564 (1998).
6. A. E. Zhukov, A. R. Kovsh, A. Yu. Egorov, *et al.*, Fiz. Tekh. Poluprovodn. (St. Petersburg) **33**, 180 (1999) [Semiconductors **33**, 153 (1999)].
7. K. Nishi, H. Saito, S. Sugou, *et al.*, Appl. Phys. Lett. **74**, 1111 (1999).
8. A. Yu. Egorov, A. E. Zhukov, P. S. Kop'ev, *et al.*, Fiz. Tekh. Poluprovodn. (St. Petersburg) **30**, 1345 (1996) [Semiconductors **30**, 707 (1996)].
9. S. S. Ruvimov, P. Werner, K. Scheerschmidt, *et al.*, Phys. Rev. B: Condens. Matter **51**, 14766 (1995).
10. A. Sasaki, Thin Solid Films **267**, 24 (1995).
11. A. F. Tsatsul'nikov, B. V. Volovik, N. N. Ledentsov, *et al.*, Fiz. Tekh. Poluprovodn. (St. Petersburg) **32**, 95 (1998) [Semiconductors **32**, 84 (1998)].
12. V. P. Evtikhiev, V. E. Tokranov, A. K. Kryzhanovskiĭ, *et al.*, Fiz. Tekh. Poluprovodn. (St. Petersburg) **32**, 860 (1998) [Semiconductors **32**, 765 (1998)].

Translated by M. Skorikov

Semiconductors, Vol. 34, No. 3, 2000, pp. 327–333. Translated from Fizika i Tekhnika Poluprovodnikov, Vol. 34, No. 3, 2000, pp. 334–339.
Original Russian Text Copyright © 2000 by Golant, Pashkovskiĭ.

Two-Level Wave Functions of Electrons in Double-Barrier Quantum-Size Structures in an Electric Field with Finite Amplitude

E. I. Golant and A. B. Pashkovskiĭ
GNPO ISTOK, Fryazino, Moscow oblast, 141120 Russia
Submitted September 8, 1999; accepted for publication September 27, 1999

Abstract—The applicability of various two-level approximations to calculation of electron transitions in a double-barrier structure with current pumping in a resonance electric field with finite amplitude was analyzed. It is shown that the solution obtained by applying a simple iterative procedure to the perturbation method of first order in the field amplitude can be appreciably extended beyond the convergence domain of the iteration method. On the other hand, it is demonstrated that the two-level approximation itself becomes inapplicable for field amplitudes much smaller than those generally assumed. This limitation is due to the influence of satellites represented by nonresonance components of the wave function. A model of double-barrier structures with electron pumping is suggested; this model is valid in the entire domain of applicability of the two-level approximation and makes it possible to take into account arbitrary forms of barriers and perturbations. *© 2000 MAIK "Nauka/Interperiodica".*

1. INTRODUCTION

The great interest recently expressed in the development of infrared lasers based on coherent transport of electrons in quantum-size semiconductor heterostructures [1–4] makes the elaboration of methods for calculating the interaction of coherently tunneling electrons with a high-frequency field very topical. Even if the problem is simplified as much as possible and reduced to a single-particle Schrödinger equation (with the potential harmonically dependent on time) for an electron in a quantum well with walls in the form of infinitely thin potential barriers, it is possible to obtain a solution to the two-level approximation only, in which case only the quantum transitions between two operating levels in the quantum well are considered important [2, 4]. According to this approach, the perturbation theory algorithm [2, 5, 6] is reduced to a simple iterative procedure, in which each subsequent approximation is determined from the previous one by multiplication by a negative parameter $-z$, where

$$z = (0.5q\mathcal{E}\langle 1|x|2\rangle/\Gamma)^2.$$

Here, $\mathcal{E}$ is the amplitude of the alternating component of the electric field; q is the elementary charge; $\langle 1|x|2\rangle$ is the matrix element of perturbation at operating levels $|1\rangle$ and $|2\rangle$; and $\Gamma = (\Gamma_1\Gamma_2)^{1/2}$, where Γ_1 and Γ_2 are the widths of the corresponding levels (the expressions for Γ_1 and Γ_2 in relation to the parameters of a structure with δ-barriers can be found in [7]). As is known, the condition for convergence of such an iterative procedure is expressed by the inequality $|z| < 1$: if the latter is fulfilled, the wave functions at each level of the structure have the form of the wave functions obtained to a first-order approximation and multiplied by the quantity $1/(1 + z)$ (the sum of a geometric progression with a denominator equal to $-z$), which defines the dependence of the electron wave functions in states $|1\rangle$ and $|2\rangle$ on the field amplitude.

The question arises as to whether this limitation has a basic physical origin or is merely a consequence of the fact that a solution is sought in the form of a power series (it should be recalled that, for many functions, in particular for $f = 1/(1 + z)$, the radius of convergence for such a series is limited). It is obvious that, in the first case, the use of the obtained solutions is inadmissible, whereas in the second case, these solutions can be extended far beyond the radius of convergence. To put it differently, it is of interest to determine whether the inequality $|z| < 1$ simultaneously represents the condition for applicability of the two-level approximation or, if this is not the case (as will be shown below), what is this condition and which physical processes should primarily be taken into account beyond the applicability of this approximation.

The class of structures under consideration is distinguished by the following constraints imposed on the widths Γ_1 and Γ_2 of the quasi-levels: on the one hand, the width of each level should be much smaller than the interlevel energy distance equal to the field quantum energy; on the other hand, the mean lifetime of an electron in a quantum well should be shorter than the minimal time between the collisions that disturb the coherence of the passage of electrons through the structure. The first condition ensures that the interaction of electrons with the field is of a resonance nature, whereas the

second condition ensures that the transport is coherent. Elementary estimates show that, in state-of-the-art semiconductor structures exhibiting resonance tunneling and with a distance between the levels corresponding to the terahertz-frequency region and a barrier thickness of several atomic monolayers, both of these conditions can be fulfilled simultaneously.

However, it is clear that, as the amplitude of the perturbing field increases, the nonresonant components of the electron wave function become more and more important. This is primarily true of the components that are close to the resonance components and constitute the so-called side satellites corresponding to the frequencies $\omega_{1,2} \pm \omega$, where $\hbar\omega_{1,2}$ are the energies of the resonance levels and ω is the frequency of the perturbing field. In connection with this, one of the objectives of this work was to estimate the nonresonance components of the wave function of electrons engaged in stimulated transitions in double-barrier structures with current pumping and to determine the boundary of the applicability domain for the two-level approximation, which is widely used beyond this boundary at present (see, e.g., [4]).

The test defining the field amplitude, below which one may ignore the effect of side satellites, makes it possible to develop a two-level model based on a range of admissible amplitudes; this model yields results strictly coinciding (for $|z| < 1$) with those obtained by direct summation of a series in perturbation theory. However, this test has a wider domain of applicability; it can also be used in cases where the field amplitudes are large and the shapes of the barriers and the form of the perturbation are arbitrary. The development of such a model is the second main objective of this work.

In order to avoid cumbersome formulas and designations, we will henceforth (see Sections 2 and 3) consider a symmetric double-barrier structure with a uniform profile of the conduction-band bottom. However, the calculation procedure and the basic result, i.e., the test for applicability of the two-level approximation when the amplitude of the perturbing field is finite, can easily be generalized (by analogy with the transition from the results reported in [5] to those reported in [6]) to an asymmetric structure with dissimilar barrier strengths and piecewise homogeneous height of the conduction-band bottom, where the height takes different values to the left and right of the structure and inside it [6].

2. A PERTURBATION METHOD BASED ON SIMPLE ITERATION

In this section, we introduce the necessary notation and reproduce certain results reported in [5] that are needed to understand the presentation that follows.

Let a monoenergetic beam of electrons with energy ε be incident on a symmetric double-barrier structure of width a that incorporates thin (δ-shaped) barriers with thickness b and height φ_b; we assume that a homogeneous electric field varying with time as

$$\mathscr{E}\cos\omega t = E(e^{i\omega t} + e^{-i\omega t}), \quad \mathscr{E} = 2E$$

is applied to the structure. For definiteness, we also assume that the electrons move from left to right. In this case, in view of the above assumptions, the time-dependent Schrödinger equation has the following form:

$$i\hbar\frac{\partial\psi}{\partial t} = -\frac{\hbar^2}{2m^*}\frac{\partial^2\psi}{\partial x^2} + \alpha\delta(x)\psi + \alpha\delta(x-a)\psi + H(x,t)\psi,$$
$$H(x,t) = -qE\{x[\theta(x) - \theta(x-a)] + a\theta(x-a)\} \quad (1)$$
$$\times(e^{i\omega t} + e^{-i\omega t}).$$

Here, q is the elementary charge, m^* is the electron mass, $\alpha = \varphi_b b$, and $\theta(x)$ is a unit function.

It is known that the transmission factor in double-barrier structures exhibits pronounced resonances; and in symmetric structures with thin barriers, the value of the wave vector $k = (2m^*\varepsilon/\hbar^2)^{1/2}$ defining the resonance levels for which the transmission factor is equal to unity can be determined from the following transcendental equation [7, 8]:

$$\tan ka = -\frac{k\hbar^2}{\alpha m^*} = -\frac{2k}{y}. \quad (2)$$

Here, for convenience, we introduced the designation $y = 2m^*\alpha/\hbar^2$. Let the electrons pass over the Nth resonance level of the structure and let the frequency of the high-frequency (HF) field correspond to transitions to the Lth level. Henceforth, for simplicity, we assume that $N > L$ (the calculations are similar for $L > N$). In [5], for sufficiently small HF field amplitudes and sufficiently strong barriers ($y \gg k$, which is equivalent to the above requirement for a width of operating levels that is small compared to their separation) it is shown that the wave function of electrons inside the structure ($0 < x < a$ and $\omega_0 = \varepsilon/\hbar$) has the form

$$\psi \approx \psi_N(x)e^{-i\omega_0 t} + \psi_L(x)e^{-i(\omega_0-\omega)t}, \quad (3)$$

where

$$\psi_N(x) = \frac{1}{1+z}\begin{cases}(1+z)\exp(ikx) - z\exp(-ikx), & x < 0,\\ A_0\sin kx + B_0\cos kx, & 0 < x < a,\\ C_0\exp[ik(x-a)], & x > a,\end{cases}$$

$$\psi_L(x) = \frac{1}{1+z}\begin{cases}D_-\exp(-ik_-x), & x < 0,\\ A_-\sin(k_-x) + B_-\cos(k_-x), & 0 < x < a,\\ C_-\exp[ik_-(x-a)], & x > a.\end{cases}$$

$$A_0 = \frac{y}{k} + i, \ B_0 = 1, \ C_0 = (-1)^{N+1}, \ D_0 = 0, \quad (4)$$

$$k_- = [2m^*(\varepsilon - \hbar\omega)/\hbar^2]^{1/2},$$

$$B_- \approx D_- \approx (-1)^{L+1} C_- \approx \frac{qEy^2}{im^*\omega^2 k_-}, \quad A_- \approx \frac{qEy^3}{im^*\omega^2 k_-^2}.$$

The solution was obtained in the form of a constant factor and an alternating series (geometric progression)

$$1 - z + z^2 - z^3 + \ldots + (-1)^{n+1} z^n, \qquad (5)$$

where

$$z = \left(\frac{qE}{m^*\omega^2}\right)^2 \frac{y^4}{kk_-}.$$

In its convergence domain of $|z| < 1$, series (5) is equivalent to an expansion of the function $1/(1 + z)$ in powers of z; therefore, the applicability domain of this solution is restricted to the domain of convergence of series (5). In line with the above, this solution is applicable only if the amplitudes of the RF field are very small. In order to gain insight into the origin of restricting the domain of convergence to very small field amplitudes, we should analyze the perturbation method used in [5]. For an initial (zero) approximation, we use the wave function of an electron at the main operating level (through which the pumping current flows), where the second level is completely depleted. The second approximation is equivalent to the first if we retain only the terms with powers no higher than y and multiply the preceding result by $-z$, which leads to the simple iteration method [9]; the latter is, in fact, a first-order method, whose condition for convergence is given exactly by the inequality $|z| < 1$.

3. PERTURBATION THEORY BASED ON EXPANDING THE ANALYTICAL SOLUTION INTO A SERIES

It is reasonable to attempt to base the perturbation theory on a method requiring no iteration; i.e., a direct series expansion of an analytic solution to the Schrödinger equation

$$i\hbar\frac{\partial\psi}{\partial t} = -\frac{\hbar^2}{2m^*}\frac{\partial^2\psi}{\partial x^2} - 2Ex\psi\cos\omega t \qquad (6)$$

for an electron in free space with an electric field that has a constant amplitude $2E$ and varies harmonically with time. The exact time-independent solution to equation (6) is transformed into a monochromatic wave for $E \longrightarrow 0$ and has the form [10]

$$\psi(x, t) = \exp\left[ikx - i\omega_0 t + \frac{2iqEx}{\hbar\omega}\sin\omega t + \frac{2iqEk}{m^*\omega^2}\cos\omega t - \frac{i(qE)^2}{m^*\hbar\omega^3}\left(\omega t - \frac{\sin 2\omega t}{2}\right)\right], \qquad (7)$$

which coincides with a solution to the Schrödinger equation in the quasi-classical case; such a solution was obtained in [11] and was derived, in particular, for the Dirac equation in [12].

In the context of the two-level approximation, the sought-for wave function is represented as a linear combination of the four wave functions given by (7), which correspond to waves traveling over the levels N and L in opposite directions. Linearizing this combination with respect to the field amplitude E and retaining only the terms with $\exp(-i\omega_0 t)$ and $\exp[-i(\omega_0 - \omega)t]$ (the two-level approximation), we can represent the corresponding wave functions as

(inside the structure; i.e., for $0 < x < 0$)

$$\begin{aligned}\psi_N(x, t) = \Big[&A\sin kx + B\cos kx - \frac{qEx}{\hbar\omega}(A_-\sin k_- x + B_-\cos k_- x) \\ &+ \frac{qEk_-}{m^*\omega^2}(A_-\cos k_- x - B_-\sin k_- x)\Big]e^{-i\omega_0 t}, \\ \psi_L(x, t) = \Big[&A_-\sin k_- x + B_-\cos k_- x + \frac{qEx}{\hbar\omega}(A\sin kx + B\cos kx) \\ &+ \frac{qEk}{m^*\omega^2}(A\cos kx - B\sin kx)\Big]e^{-i(\omega_0 - \omega)t};\end{aligned} \qquad (8)$$

(for $x < 0$)

$$\psi(x, t) = [\exp ikx + D\exp(-ikx)]e^{-i\omega_0 t} + D_-\exp(-ik_- x)e^{-i(\omega_0 - \omega)t}; \qquad (9)$$

(for $x > a$, see [9])

$$\begin{aligned}\psi(x, t) = &\left\{C\exp[ik(x-a)] - \frac{qEa}{\hbar\omega}C_-\exp[ik_-(x-a)]\right\} \\ &\times e^{-i\omega_0 t} + \left\{C_-\exp[ik_-(x-a)] + \frac{qEa}{\hbar\omega}C\exp[ik(x-a)]\right\}e^{-i(\omega_0 - \omega)t}.\end{aligned} \qquad (10)$$

Selecting the (so far unknown) coefficients of the wave function given by (8)–(10) such that boundary conditions at the barriers are satisfied, we obtain the linear terms of expansion of the rigorous solution in the parameter

$$\frac{qEa}{\hbar\omega} \ll 1. \qquad (11)$$

It is noteworthy that this condition is fulfilled only for field amplitudes much larger than those following from the condition $|z| < 1$.

Sewing the wave functions at the barriers, we arrive at the following system of equations for the coefficients A, B, C, D, A_-, B_-, C_-, and D_- at any point in time:

$$\begin{pmatrix} M(k) & S \\ W & M(k_-) \end{pmatrix}(a_i) = \begin{pmatrix} f \\ 0 \end{pmatrix}. \quad (12)$$

Here,

$$M(k) = \begin{vmatrix} 1 & 0 & -1 & 0 \\ ik-y & k & 0 & 0 \\ 0 & \sin ka & \cos ka & -1 \\ 0 & -k\cos ka & k\sin ka & ik-y \end{vmatrix},$$

$$f = \begin{vmatrix} -1 \\ ik+y \\ 0 \\ 0 \end{vmatrix}, \quad (13)$$

$$W = \begin{vmatrix} 0 & w_{12} & 0 & 0 \\ 0 & 0 & w_{23} & 0 \\ 0 & w_{32} & w_{33} & w_{34} \\ 0 & w_{42} & w_{43} & w_{44} \end{vmatrix}, \quad (a_i) = \begin{pmatrix} P \\ P_- \end{pmatrix},$$

$$P = \begin{vmatrix} D \\ A \\ B \\ C \end{vmatrix}, \quad y = \frac{2m^*\alpha}{\hbar^2},$$

$$w_{12}(k) = -\frac{qEk}{m^*\omega^2}, \quad w_{23} = -\frac{qE}{\hbar\omega}\left(\frac{2\omega_0-\omega}{\omega}\right),$$

$$w_{34} = -\frac{qEa}{\hbar\omega}, \quad w_{32}(k) = \frac{qEa}{\hbar\omega}\sin ka + \frac{qEk}{m^*\omega^2}\cos ka, \quad (14)$$

$$w_{44}(k) = -\frac{qEa}{\hbar\omega}(ik-y),$$

$$w_{33}(k) = \frac{qEa}{\hbar\omega}\cos ka - \frac{qEk}{m^*\omega^2}\cos ka,$$

$$w_{42}(k) = \frac{qE}{\hbar\omega}\left(\frac{2\omega_0-\omega}{\omega}\right)\sin ka - \frac{qEak}{\hbar\omega}\cos ka,$$

$$w_{43}(k) = \frac{qE}{\hbar\omega}\left(\frac{2\omega_0-\omega}{\omega}\right)\cos ka + \frac{qEak}{\hbar\omega}\sin ka.$$

The matrix S has the same form as the matrix W, with the only difference that

$$s_{12} = w_{12}(k_-), \quad s_{23} = w_{23}, \quad s_{34} = -w_{34},$$

$$s_{44} = -w_{44}(k_-), \quad s_{32} = -\frac{qEa}{\hbar\omega}\sin k_-a + \frac{qEk_-}{m^*\omega^2}\cos k_-a,$$

$$s_{33} = \frac{qEa}{\hbar\omega}\cos k_-a + \frac{qEk_-}{m^*\omega^2}\sin k_-a, \quad (15)$$

$$s_{42} = \frac{qE}{\hbar\omega}\left(\frac{2\omega_0-\omega}{\omega}\right)\sin k_-a + \frac{qEak_-}{\hbar\omega}\cos k_-a,$$

$$s_{43} = \frac{qE}{\hbar\omega}\left(\frac{2\omega_0-\omega}{\omega}\right)\cos k_-a - \frac{qEak_-}{\hbar\omega}\sin k_-a.$$

Analyzing the discriminant Δ of system (12), we can show that, in view of condition (11), this discriminant is equal to

$$\Delta = \Delta[M(k)]\Delta[M(k_-)](1+z+\gamma); \quad (16)$$

since, in this case, $y/k \gg 1$, the inequality $z \gg \gamma$ is valid, and thus we have

$$\Delta = \Delta[M(k)]\Delta[M(k_-)](1+z). \quad (17)$$

It is also worth noting that terms involving the small parameter (11) squared were ignored in expansion (7). Furthermore, we made the substitution

$$k \approx k - \delta k = k - k\frac{(qE)^2}{m^*\hbar\omega^2\omega_0}, \quad (18)$$

which may appear incorrect, because, for the resonance determinant, the following approximate equality is valid [2]:

$$\Delta[M(k+\delta k)] \approx \Delta[M(k)]\left(1 + \frac{iy^2\delta ka}{k^2}\right)$$
$$\approx \Delta[M(k)]\left[1 + \left(\frac{qE}{m^*\omega^2}\right)^2 \frac{\pi y^2\omega^2}{4\omega_0^2}\right], \quad (19)$$

i.e., a small correction is multiplied by a large-valued parameter $(y/k)^2$. However, a comparison of (19) and (5) shows that the correction is invariably smaller than z, and thus the substitution (18) is fully justified.

Further, we can verify that the discriminants for calculating the unknown coefficients of the wave function given by (8)–(10) can be represented in the following form with the use of Cramer's rule ($a_i = \Delta_{a_i}(E)/\Delta$):

$$\Delta_{a_i}(E) = \Delta_{a_i}(E \longrightarrow 0)\left[1 + \rho_i\left(\frac{qE}{m^*\omega^2}\right)^2 y^2\right]. \quad (20)$$

Here, ρ is a numerical coefficient equal to unity in order of magnitude. Thus, for example,

$$\Delta_C = \Delta[C(k)]\Delta[M(k_-)]\left[1+\rho_C\left(\frac{qE}{m^*\omega^2}\right)^2 y^2\right], \quad (21)$$

where the matrix $C(k)$ is obtained from the matrix $M(k)$ by replacing the fourth column with the column f. It automatically follows from (17) and (20) that, if at least the condition

$$\left(\frac{qE}{m^*\omega^2}\right)^2 y^2 \ll 1 \quad (22)$$

is satisfied, the wave function (8)–(10) corresponding to the first approximation of the perturbation theory based on analytic solution (7) coincides exactly with wave function (3)–(4) obtained by summing an infinite series in perturbation theory based on iterative method [5].

Since the condition for applicability of the iteration method [5]

$$z = \left(\frac{qE}{m^*\omega^2}\right)^2 \frac{y^4}{kk_-} \le 1 \quad (23)$$

is more stringent by y^2/kk_- than that given by (22), a solution to (3)–(4) can be extended beyond the domain of convergence of a series defined by (5).

4. A DECAYING QUANTUM-MECHANICAL SYSTEM WITH ELECTRON PUMPING

For sufficiently strong barriers, a double-barrier structure can be regarded as a typical decaying quantum-mechanical system [13], whose decay time τ is governed by tunneling through the barriers as

$$\tau^{-1} = \frac{\Gamma}{\hbar} = \frac{\hbar k}{2am^*}(|T_1|^2 + |T_2|^2), \quad (24)$$

where $|T|$ is the electron transparency (transmission factor) of the first and second barriers. For a δ-shaped barrier, we have $|T| \approx k/y$. To the two-level approximation, the wave function of such a system may be represented as

$$\psi(x,t) = b_N(t)\psi_N(x)e^{-i\omega_N t} + b_L(t)\psi_L(x)e^{-i\omega_L t}, \quad (25)$$

where $\psi(x)$ and $\psi_L(x)$ are the eigenfunctions that are normalized to unity and correspond to energy levels of a structure with completely impermeable barriers $|T_1| \approx |T_2| \approx 0$. By analogy to a closed quantum-mechanical system, the dynamics of a decaying two-level system with pumping can be described by the following equations:

$$\begin{gathered}\hbar\frac{db_N}{dt} + \Gamma_N(b_N - b_0) = -ib_L qE\langle N|x|L\rangle e^{-i(\omega_N-\omega_L+\omega)t},\\ \hbar\frac{db_L}{dt} + \Gamma_L b_L = -ib_N qE\langle L|x|N\rangle e^{-i(\omega_L-\omega_N-\omega)t}.\end{gathered} \quad (26)$$

Here,

$$\langle N|x|L\rangle = \langle L|x|N\rangle = \frac{a}{\pi^2}\frac{NL}{(N^2-L^2)^2} \quad (27)$$

is the matrix element x in the quantum well and b_0 is the parameter characterizing the pumping.

On the other hand, if the pumping electrons arrive at the structure with an energy ω_0 sufficiently close to ω_N and the monochromatic perturbing field has a frequency equal to $\omega \approx \omega_N - \omega_L$, the wave function should have the form

$$\psi(x,t) = c_N\psi_N(x)e^{-i\omega_0 t} + c_L\psi_L(x)e^{-i(\omega_0-\omega)t} \quad (28)$$

in the steady-state mode for $t \longrightarrow \infty$ with

$$\frac{dc_N}{dt} = \frac{dc_L}{dt} = 0.$$

Comparing (25) and (28), we obtain

$$b_N = c_N e^{-i(\omega_0-\omega_N)t}, \quad b_L = c_L e^{-i(\omega_0-\omega-\omega_L)t} \quad (29)$$

and represent the pumping parameter as

$$b_0 = c_0 e^{-i(\omega_0-\omega_N t)}, \quad (30)$$

where

$$\frac{dc_0}{dt} = 0.$$

It is noteworthy that, for a precise resonance, we have $b_N = c_N$, $b_L = c_L$, and $b_0 = c_0$. Substituting the expressions for b_N, b_L, and b_0 into (26), we derive the following relation between the constant coefficients c_N, c_L, and c_0:

$$\begin{gathered}-i\hbar(\omega_0-\omega_N)c_N + \Gamma_N(c_N - c_0) = -ic_L qEa\langle N|x|L\rangle,\\ -i\hbar(\omega_0-\omega-\omega_L)c_L + \Gamma_L c_L = -ic_N qEa\langle L|x|N\rangle.\end{gathered} \quad (31)$$

After simple calculations, we derive the desired relation between the amplitudes of wave function (28) and the parameter c_0 characterizing the pump as

$$\begin{gathered}c_N = c_0(\Delta\omega)\\ \times\left\{1 + \frac{(qE\langle N|x|L\rangle)^2}{[\Gamma_N - i\hbar(\omega_0-\omega_N)][\Gamma_L - i\hbar(\omega_0-\omega-\omega_L)]}\right\}^{-1},\\ c_L = c_N\frac{qE\langle N|x|L\rangle}{[\Gamma_L - i\hbar(\omega_0-\omega-\omega_L)]},\\ c_0(\Delta\omega) = c_0\frac{\Gamma_N}{[\Gamma_N - i\hbar(\omega_0-\omega_N)]}.\end{gathered} \quad (32)$$

For the strictly resonance case (for $\omega_0 = \omega_N$ and $\omega = \omega_N - \omega_L$), it can be shown that the wave function given by (28) with the coefficients defined by (32) coincides with the wave function obtained previously by the per-

turbation method (4); in particular, we have $c_N/c_0 = 1/(1 + z)$, where $z = (qE\langle N|x|L\rangle/\Gamma)^2$, with $\Gamma = (\Gamma_N\Gamma_L)^{1/2}$. It is noteworthy that the above approach to the problem as a resonance interaction of an alternating field with a decaying quantum-mechanical system under electron pumping is valid for any form of the barriers confining the quantum well. In addition, this approach makes it possible to evaluate the structures for an arbitrary form of alternating field $f(x)$ by substituting the matrix element $\langle N|x|L\rangle$ by $\langle N|f(x)|L\rangle$. It is clear that this approach, as distinct from the perturbation methods considered previously, does not impose any internal restrictions on the amplitude of the applied field.

5. APPLICABILITY OF THE TWO-LEVEL APPROXIMATION

However, the question arises as to the amplitudes of the high-frequency field for which the two-level system approximation is valid in general. In order to clarify this issue, we estimate the field amplitude at which the transitions to the region of nonresonance energies become important. To this end, we assume that, by one of the above methods, we obtained the wave function ψ of a resonance two-level system and we estimate the second-order correction ψ_2 arising when the quasi-energy state separated by $\hbar\omega$ from the resonance level is considered. First of all, it is necessary to note that the possibility of considering only the nearest nonresonance levels is ensured by using only the first two orders of perturbation theory with respect to parameter (11). Using the results reported in [5], we can easily demonstrate that the highest power of the large parameter y/k in the correction to the wave function remains the same in transitions to a nonresonance quasi-energy level and increases twofold in transitions to a resonance level. Thus, the second-order correction to the wave function of a two-level system, which arises from transitions of electrons to the nonresonance region and back, is proportional to $(y/k)^2$ and is given by

$$\psi_2 \propto \psi\left(\frac{qE}{m^*\omega^2}\right)^2 y^2. \tag{33}$$

It is noteworthy that, in the case of transitions between resonance levels, we have $\psi_2 \propto (y/k)^4\psi$. Thus, the influence of nonresonance transitions on the wave function of the ground state is unimportant if the following conditions are fulfilled:

$$\left(\frac{qE}{m^*\omega^2}\right)^2 y^2 \ll 1 \quad \text{or} \quad z \ll y^2/kk_- \approx |T|^{-2}. \tag{34}$$

These conditions may serve as tests for the applicability of the two-level approximation in the problem under consideration. It is worth noting that the test coinciding with the applicability condition of the method of expanding into a series (22) described above is, on the one hand, much less stringent (by $|T|^{-2}$ times) than the condition $|z| < 1$ for convergence of a series in perturbation theory and, on the other hand, is more stringent (by approximately $|T|^{-1}$ times) compared to test (11) used in [4] on the basis of other considerations.

In other words, the amplitude of the energy of an alternating electric field $2qEa$ that permits convergence of the iterative method is restricted by the inequality $2qEa \le \Gamma a/\langle N|x|L\rangle$, whereas the applicability of the two-level approximation is restricted by the inequality $2qEa \ll |T||T_-|^{-1/2}\Gamma a/\langle N|x|L\rangle$, where $\langle N|x|L\rangle$ is defined by (27). It is evident that, for $|T| \longrightarrow 0$, $\Gamma \longrightarrow 0$ and the largest admissible energy of the field in both cases tends to zero, so that the narrower the level, the lower the field energies for which the two-level approximation is applicable. However, as shown in [2, 5, 6], the most pronounced redistribution of electrons between the levels under the effect of an alternating field occurs for amplitudes on the order of $\Gamma a/\langle N|x|L\rangle$; therefore, it was very important to show that the two-level approximation is quite applicable under these conditions.

6. CONCLUSION

We analyzed the applicability of different versions of the two-level approximation to calculating electron transitions in a double-barrier structure with current pumping in a resonance electric field of finite amplitude. It was shown that the solution obtained on the basis of a simple iteration procedure in the first-order perturbation method with respect to a field amplitude of the type $1/(1 + z)$ can be substantially extended beyond the convergence domain of the iteration method ($|z| = 1$). On the other hand, it was demonstrated that the two-level approximation itself becomes unacceptable for field amplitudes appreciably smaller than those generally accepted, a restriction that is due to the effect of nonresonance components of the wave function. In this case, a solution based on a series in perturbation theory was found to be valid for any field amplitude where the two-level approximation is valid at all. A model of double-barrier structures with electron pumping, which is valid in the entire range of applicability of the two-level approximation and makes it possible to account for various shapes of barriers and forms of perturbation, is proposed.

ACKNOWLEDGMENTS

This work was supported by the Russian Foundation for Basic Research (project no. 97-02-16652) and the Scientific Council under the Program "The Physics of Solid-State Nanostructures" (project no. 97-1094).

REFERENCES

1. E. I. Golant, A. B. Pashkovskiĭ, and A. S. Tager, Pis'ma Zh. Tekh. Fiz. **20** (21), 74 (1994) [Tech. Phys. Lett. **20**, 886 (1994)].

2. E. I. Golant and A. B. Pashkovskiĭ, Zh. Éksp. Teor. Fiz. **112** (7), 237 (1997) [JETP **85**, 130 (1997)].
3. M. Kira, Phys. Rev. B: Condens. Matter **53** (23), 15789 (1996).
4. V. F. Elesin, Zh. Éksp. Teor. Fiz. **112** (2), 483 (1997) [JETP **85**, 264 (1997)].
5. E. I. Golant and A. B. Pashkovskiĭ, Fiz. Tekh. Poluprovodn. (St. Petersburg) **31** (8), 950 (1997) [Semiconductors **31**, 809 (1997)].
6. E. I. Golant and A. B. Pashkovskiĭ, Pis'ma Zh. Éksp. Teor. Fiz. **63** (7), 559 (1996) [JETP Lett. **63**, 590 (1996)].
7. I. V. Belyaeva, E. I. Golant, and A. B. Pashkovskiĭ, Fiz. Tekh. Poluprovodn. (St. Petersburg) **31** (2), 137 (1997) [Semiconductors **31** (2), 103 (1997)].
8. V. M. Galitskiĭ, B. M. Karnakov, and V. I. Kogan, *Problems in Quantum Mechanics* (Nauka, Moscow, 1981).
9. N. N. Kalitkin, *Numerical Methods* (Nauka, Moscow, 1978).
10. A. B. Pashkovskiĭ, Zh. Éksp. Teor. Fiz. **109**, 1779 (1996) [JETP **82**, 959 (1996)].
11. V. V. V'yurkov and V. I. Ryzhiĭ, Zh. Éksp. Teor. Fiz. **78**, 1159 (1980) [Sov. Phys. JETP **51**, 583 (1980)].
12. V. B. Berestetskiĭ, E. M. Lifshits, and L. P. Pitaevskiĭ, *Quantum Electrodynamics* (Nauka, Moscow, 1980; Pergamon, Oxford, 1982).
13. L. D. Landau and E. M. Lifshits, *Quantum Mechanics* (Nauka, Moscow, 1989, 4th ed.; Pergamon, Oxford, 1977, 3rd ed.).

Translated by A. Spitsyn

Semiconductors, Vol. 34, No. 3, 2000, pp. 334–343. Translated from Fizika i Tekhnika Poluprovodnikov, Vol. 34, No. 3, 2000, pp. 340–348.
Original Russian Text Copyright © 2000 by Pashkovskiĭ.

Alternating Space Charge and Ambiguity of Quantum States in Double-Barrier Structures

A. B. Pashkovskiĭ

GNPO ISTOK, Fryazino, Moscow oblast, 141120 Russia

Submitted September 11, 1999; accepted for publication September 28, 1999

Abstract—Summation of a series of perturbation theory was used to obtain a solution to the time-dependent self-consistent Schrödinger and Poisson equations describing the resonance interaction of electrons that tunnel through asymmetric double-barrier structures with a high-frequency electric field. In the case where electrons are uniformly distributed in energy within the width of the quasi-level, the solution is obtained analytically; if the beam is monoenergetic, solution of the equation is reduced to finding the roots of a fifth-degree algebraic polynomial. It is shown that, in a number of cases, the influence of alternating space charge gives rise to an effect that is quite new for the systems under consideration: several different wave functions may correspond to the same amplitude of the high-frequency voltage applied to the structure; consequently, the values obtained for the high-frequency conductivity and the coefficients of transmission and reflection can differ by several times. As a result, instability of the current flow and hysteresis of the current-voltage characteristics can be observed in these structures. Furthermore, the dependence of the coefficients of transmission and reflection of the electrons and high-frequency conductivity on the voltage amplitude are combinations of the *N*- and *S*-shaped characteristics for uniform distribution of electrons and are looplike in the case of a monoenergetic beam. © *2000 MAIK "Nauka/Interperiodica".*

1. INTRODUCTION

Recently, interest in electron transport through systems of potential wells and barriers in a high-frequency (HF) electric field [1–6] has intensified; this is due to both the development and advancement of a quantum cascade laser operating by intersubband transitions in the infrared region of the spectrum [7, 8] and to prediction of the possibility of observing a number of quantum-mechanical effects that have no analogues in static electron transport in such structures. Thus, for example, new phenomena can be observed if the effects of alternating space charge (plasma oscillations) expressed in the small-signal approximation [9] and the finiteness of the HF-field amplitude [10] are taken into account (even separately) in considering the resonance transitions in a double-well structure. In this case, these phenomena take place even in very weak fields (with infinitely small amplitudes) for low concentrations of electrons and conductivities that are low compared to $\omega\varepsilon$ (here, ω is the HF field frequency and ε is the permittivity of the semiconductor). As will be shown below, the effect of plasma oscillations, even in a weak HF field with finite amplitude, can give rise to another phenomenon that is quite new for the given structures: in the steady-state mode, the same amplitude of HF voltage applied to the structure can correspond to several different electron wave functions; thus, all the observed properties of the structure (electrical conductivity and the transmission and reflection factors) become ambiguous. Therefore, even in an HF field, one can observe a situation (well known in the physics of semiconductors in the case of static fields) where either the same voltage applied to the structure corresponds to several values of current (typically, this is an *S*-shaped characteristic) or where a single value of current corresponds to several values of voltage (typically an *N*-shaped characteristic) [11–13], although in a number of cases, the dependence of current on voltage is more complex. Conceptually, this means that, under certain conditions, the mode of the current flowing through a double-barrier structure can be unstable. It is noteworthy that this effect is fundamentally different (both in the mechanism and the conditions for observation) from the phenomena of optical bistability considered previously [14, 15]. In addition, this problem is also of interest, because it is possible to obtain analytical self-consistent solutions to the time-dependent Schrödinger and Poisson equations for a uniform electron-energy distribution for structures that in principle can be used as components of a new type of unipolar laser operating in the infrared region of the spectrum [16]. The above equations describe the interaction of electrons with an HF electric field of finite amplitude. For a monoenergetic beam, the problem is reduced to finding the roots of an algebraic fifth-degree polynomial.

2. SOLUTION OF THE SELF-CONSISTENT SCHRÖDINGER AND POISSON EQUATIONS

For the sake of definiteness, we consider a flux of electrons that travel from left to right through an asymmetric double-barrier resonance-tunneling structure with thickness a and thin (δ-shaped) barriers [9, 10] in the absence of a constant electric field. It is assumed that a small-amplitude harmonic voltage is applied to the structure, the homogeneous electric field in the structure varies with time as $E(t) = E(e^{i\omega t} + e^{-i\omega t})$, and there is no space charge or electric field outside the structure. Collisions and the effect of static space charge are ignored (for example, it is possible to assume that the space charge is compensated for by the charge of ionized donors). In this case, the time-dependent Schrödinger equation has the following form:

$$i\hbar\frac{\partial\psi}{\partial t} = -\frac{\hbar^2}{2m^*}\frac{\partial^2\psi}{\partial x^2} + H(x)\psi + H(x,t)\psi, \qquad (1)$$

$$H(x) = -U[\theta(x) - \theta(x-a)] - U_1\theta(x-a) + \alpha\delta(x)\psi + \alpha\gamma\delta(x-a),$$

$$H(x,t) = -qE\{x[\theta(x) - \theta(x-a)] + a\theta(x-a)\}(e^{i\omega t} + e^{-i\omega t}) + q\varphi(x,t).$$

Here, q is the elementary charge; m^* is the electron mass; $\alpha = \varphi_b b$; φ_b and b are the height and width of the first potential barrier; $\theta(x)$ is a unit function; γ is a numerical coefficient; U and U_1 are the magnitudes of discontinuity of the conduction-band bottom at the barriers; and $q\varphi(x, t)$ is potential-energy variation related to the space charge, where $\varphi(x, t)$ satisfies the quasi-static Poisson equation

$$\frac{\partial^2\varphi(x,t)}{\partial x^2} = -\frac{Q(x,t)}{\varepsilon}, \qquad (2)$$

where $Q(x, t)$ is the density of alternating space charge in the structure and ε is the permittivity of the semiconductor.

Let the electron flux traverse a resonance level with number K, energy $\mathcal{E}$, and width Γ; and let the electric-field frequency correspond to transitions to a resonance level with number L and width Γ_L. We consider two cases:

(i) The electron-energy distribution in the incident beam is assumed to be uniform, at least if the deviations from the resonance energy are on the order of the ground-level width.

(ii) A monoenergetic electron beam (conceptually, a beam with an energy spread less than the width of the narrowest level of those involved in the transitions) with a concentration n is incident on the midpoint of the resonance-level width of the structure; for example, it may be assumed that the beam is generated by another double-barrier structure.

It is known that, if we deal with resonance transitions in double-barrier structures and if the amplitudes of the high-frequency field are sufficiently small [5, 9, 10], only the transitions between two resonance levels are important, whereas the transitions involving nonresonance levels may be ignored. Therefore, in the calculations below, we consider wave functions related to two levels alone. Furthermore, if $K > L$ (electrons are incident on the upper level), the lower level is assigned the subscript "–" in the formulas; by contrast, if $L > K$ (electrons are incident on the lower level), the subscript "+" in the formulas corresponds to the upper level, whereas the lower level does not have an additional subscript. When the form of the expressions is independent of whether the electrons are incident on the lower or the upper level, the subscript "±" will be used. In the exponent of an exponential function and in formulas defining the quantities, the upper sign in the subscripts "±" and "∓" corresponds to transitions from the lower level to the upper level and the lower sign corresponds to the reverse transition.

We seek a solution to the problem on the assumption that both the signal field and the field of alternating space charge are perturbations with fairly small but finite amplitudes. It is known that, in the case of resonance transitions in double-barrier structures with fairly strong barriers ($y = 2m^*\alpha/\hbar^2 \gg k$, where k is the wave vector of an electron within the structure), corrections of various orders to the unperturbed wave function ψ_0 have the same form (to within a small quantity on the order of k/y) as the form of the wave function for the ground state [10, 17]. Moreover, in this case, the wave function at the resonance level in a field of finite amplitude (without regard for the space charge) can be represented as $\psi_0/(1 + \tilde{z})$, where $\tilde{z}$ is a numerical parameter that depends on the field amplitude and the parameters of the structure. Therefore, it may be assumed that, within the structure, the wave function of the problem under consideration has the following form in case (i):

$$\psi(\mathcal{E} + \delta\mathcal{E}) \approx \frac{1}{1+\tilde{z}}\frac{[f(\mathcal{E})]^{1/2}}{1 + \frac{2i\delta\mathcal{E}}{\Gamma}}$$

$$\times\left\{F\left(\frac{y}{k}\sin kx + \cos kx\right)e^{-i(\omega_0 + \delta\omega)t} + \frac{S_\pm}{1 + \frac{2i\delta\mathcal{E}}{\Gamma_L}}\right. \qquad (3)$$

$$\left.\times\left(\frac{y}{k_\pm}\sin k_\pm x + \cos k_\pm x\right)e^{-i(\omega_0 + \delta\omega \pm \omega)t}\right\}.$$

Here, F and $S_\pm$ are complex numbers remaining to be determined, k and $k_\pm$ are the corresponding wave vec-

tors, $f(\mathscr{E})$ is the electron distribution function, $\delta\mathscr{E}$ is the deviation of the energy from the resonance energy, $\omega_0 = \mathscr{E}/\hbar$, and $\delta\omega = \delta\mathscr{E}/\hbar$. In case (ii), we have

$$\psi(\mathscr{E}) \approx \frac{n^{1/2}}{1+z}\left\{F\left(\frac{y}{k}\sin kx + \cos kx\right)e^{-i\omega_0 t} + S_{\pm}\left(\frac{y}{k_{\pm}}\sin k_{\pm}x + \cos k_{\pm}x\right)e^{-i(\omega_0 \pm \omega)t}\right\}. \quad (4)$$

Here, $\tilde{z}$ and z are the functions to be determined from the equations that will be derived below during the search for a self-consistent solution to the problem. By analogy with [17, 18], it is reasonable to assume that $\tilde{z}$ can be expressed as

$$\tilde{z} = \frac{z}{\left(1 + \frac{2i\delta\mathscr{E}}{\Gamma}\right)\left(1 + \frac{2i\delta\mathscr{E}}{\Gamma_L}\right)}, \quad (5)$$

where z is the value of this function at the midenergy of the level ($\delta\mathscr{E} = 0$).

Wave function (3) in the energy range $d\mathscr{E}$ corresponds to an alternating space charge with density given by

$$dQ_{\pm}(\delta\mathscr{E}) = \frac{qy^2\sin k_{\pm}x\sin kx}{kk_{\pm}|1+\tilde{z}|^2\left|1 + \frac{2i\delta\mathscr{E}}{\Gamma}\right|^2} \times \left(\frac{FS_{\pm}^* e^{\pm i\omega t}}{1 - \frac{2i\delta\mathscr{E}}{\Gamma_L}} + \frac{F^* S_{\pm} e^{\mp i\omega t}}{1 + \frac{2i\delta\mathscr{E}}{\Gamma_L}}\right) f(\mathscr{E})d\mathscr{E}. \quad (6)$$

For small deviations from the midenergy of the level, the wave vectors change only slightly (the strictly resonance values of these wave vectors can be used in calculating the charge). Therefore, the integration of $dQ_{\pm}$ over the energy (formally, between the limits $-\infty$ and $+\infty$, and actually, within distances from the midenergy of the level on the order of its width) yields

$$Q_{\pm}(x, t) = \frac{qy^2\sin k_{\pm}x\sin kx}{kk_{\pm}(1+z)} \times (FS_{\pm}^* e^{\pm i\omega t} + F^* S_{\pm} e^{\mp i\omega t})\frac{\pi f(\mathscr{E})\Gamma\Gamma_L}{2(\Gamma + \Gamma_L)}. \quad (7)$$

For wave function (4) ($\tilde{z} = z$), we have

$$Q_{\pm}(x, t) = \frac{qy^2\sin k_{\pm}x\sin kx}{kk_{\pm}} \times (FS_{\pm}^* e^{\pm i\omega t} + F^* S_{\pm} e^{\mp i\omega t})\frac{n}{(1+z)^2}. \quad (8)$$

For fairly strong barriers ($y/k \gg 1$), the alternating space charge outside the structure is small, it vanishes at the boundary [5, 9], and the boundary conditions for Poisson equation (2) are virtually independent of the properties of the structure beyond the barriers. Therefore, when solving this equation for cases (7) and (8), we represent the perturbation operator inside the structure by

$$\hat{V} = -qEx(e^{i\omega t} + e^{i\omega t}) + \hat{V}_{q+}e^{-i\omega t} + \hat{V}_{q-}e^{-i\omega t}, \quad (9)$$

where

$$\hat{V}_{q+} = \frac{q^2y^2FS_{\pm}^*K^2}{\varepsilon k_k^3}\left[\frac{\cos(K-L)k_1x}{2(K-L)^2} - \frac{\cos(K+L)k_1x}{2(K+L)^2} - \frac{2KL}{(K^2-L^2)^2}\right]\frac{n}{1+z}, \quad (10)$$

$\hat{V}_{q-} = (\hat{V}_{q+})^*$; $k_1 = k/K = k_{\pm}/L$ is the wave vector at the first level;

$$n = \frac{\pi f(\mathscr{E})\Gamma\Gamma_L}{2(\Gamma + \Gamma_L)} \quad (11)$$

is in fact the effective concentration of the electrons involved in transitions in case (i) (in what follows, we will use this quantity in formulas if it does not lead to confusion); and

$$\hat{V}_{q+} = \frac{q^2y^2FS_{\pm}^*K^2}{\varepsilon k_k^3}\left\{\frac{\cos(K-L)k_1x}{2(K-L)^2} - \frac{\cos(K+L)k_1x}{2(K+L)^2} - \frac{2KL}{(K^2-L^2)^2}\right\}\frac{n}{(1+z)^2} \quad (12)$$

for a monoenergetic flux (here, n is the concentration of electrons in the beam).

However, in general, wave functions (3) and (4) are obtained from the wave functions of the unperturbed problem subjected to periodic perturbation (9). Therefore, we will seek a solution in the form of a series of perturbation theory in powers of $\hat{V}$.

Three basic situations are possible:

(I) The transitions are executed between the levels that are located above the conduction-band bottom of both the left-hand-side (at the input) and the right-hand-side (at the output) semiconductor materials (Fig. 1a).

(II) The transitions are executed to the level that is located below the conduction-band bottom of the left-hand-side material and above the conduction-band bottom of the right-hand-side material (Fig. 1b).

(III) The transitions are executed from the level located below the conduction-band bottom of the mate-

rial on the right-hand side to the level located above the conduction-band bottom of this material (Fig. 1c).

We first consider situation I. The wave function of the unperturbed problem has the form

$$\psi_0(x) = [f(\mathscr{E})]^{1/2} \times \begin{cases} \exp ik_0x + D_0\exp(-ik_0x), & x < 0, \\ A_0\sin kx + B_0\cos kx, & 0 < x < a, \\ C_0\exp[ik_1(x-a)], & x > a, \end{cases} \tag{13}$$

where

$$k_0 = [2m^*(\mathscr{E} + \delta\mathscr{E})/\hbar^2]^{1/2},$$

$$k = [2m^*(\mathscr{E} + \delta\mathscr{E} + U)/\hbar^2]^{1/2},$$

$$k_1 = [2m^*(\mathscr{E} + \delta\mathscr{E} + U_1)/\hbar^2]^{1/2}$$

are the wave vectors of the electrons. In the range $0 < x < a$ and for fairly strong barriers ($y \gg k$), the wave function of the ground state can be represented as [17, 18]

$$\psi_0 \approx \beta_0\left(\frac{y}{k}\sin kx + \cos kx\right), \quad \beta_0 = \frac{\beta_0^r}{\left(1 + \frac{2i\delta\mathscr{E}}{\Gamma}\right)}, \tag{14}$$

$$\beta_0^r = \frac{2\gamma^2 k_0}{\gamma^2 k_0 + k_1}[f(\mathscr{E})]^{1/2}, \quad \beta_0 = [f(\varepsilon)]^{1/2}B_0.$$

To the small-signal approximation, the correction ψ_1 to the wave function of the ground state [5, 10] has the following form:

$$\psi_1 = \psi_{1+}(x)e^{-i(\omega_0+\omega)t} + \psi_{1-}(x)e^{-i(\omega_0+\omega)t}$$

$$\omega_0 = \mathscr{E}/\hbar.$$

For $y \gg k_\pm$ and a value of the wave vector corresponding to the resonance level (the latter is true provided that $\tan k_\pm a = -(1+\gamma)k_\pm/\gamma y$ [18, 19]), the first-order correction to the wave function of the ground state (to within small terms on the order of k/y, which do not contribute to the higher-order corrections; for more details, see [10, 17]) has the same form within the structure as that of the wave function itself; i.e., we have

$$\psi_{1\pm} \approx \beta_{1\pm}\left(\frac{y}{k_\pm}\sin k_\pm a + \cos k_\pm a\right), \tag{15}$$

where

$$k_\pm = [2m^*(\mathscr{E} + \delta\mathscr{E} + U + \hbar\omega)/\hbar^2]^{1/2},$$

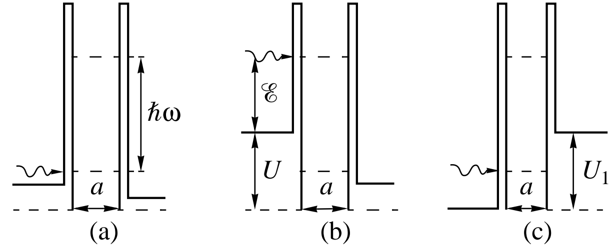

Fig. 1. Schematic representation of energy-band diagram for the double-barrier structure under consideration.

$$\beta_{1\pm} \approx \frac{2}{m^*\omega^2}\frac{k_\pm\beta_0\gamma y^2}{\Delta_\pm}\left[qE + F^*S_\pm\frac{q^2y^2a(K^2+L^2)}{16\varepsilon kk_\pm KL}\frac{n}{1+z}\right](-1)^{L+1}, \tag{16}$$

$$\Delta_\pm(\delta\mathscr{E}) = \frac{ik_\pm}{\gamma}(k_{1\pm} + \gamma^2 k_{0\pm})\left(1 + \frac{2i\delta\mathscr{E}}{\Gamma_L}\right)(-1)^{L+1}.$$

By comparing (15) and (14), we can easily obtain the following expression for the second-order correction:

$$\psi_2 \approx -\beta_0\tilde{\phi}\left(\frac{y}{k}\sin kx + \cos kx\right), \quad 0 < x < a. \tag{17}$$

Here,

$$\phi = z_0\left(1 + \frac{\eta FS_\pm^*}{1+z}\right)\left(1 + \frac{\eta F^*S_\pm}{1+z}\right), \tag{18}$$

$$z_0 = \left(\frac{qE}{m^*\omega^2}\right)^2\frac{4\gamma^4y^4}{(k_1+\gamma^2k_0)(k_{1\pm}+\gamma^2k_{0\pm})}, \quad \eta = \frac{qy^2a(K^2+L^2)n}{16\varepsilon kk_\pm EKL} \tag{19}$$

for a uniform electron-energy distribution and

$$\phi = z_0\left[1 + \frac{\eta FS_\pm^*}{(1+z)^2}\right]\left[1 + \frac{\eta F^*S_\pm}{(1+z)^2}\right] \tag{20}$$

for a monoenergetic electron flux. Furthermore, the relation between ϕ and $\tilde{\phi}$ is identical to that between z and $\tilde{z}$ [see (5)].

If we then continue the procedure for deriving the higher-order corrections and sum them, the coefficients of the wave function for each of the resonance levels can be represented in the form of a constant factor and an alternating series [10, 17]

$$1 - \tilde{\phi} + (\tilde{\phi})^2 - (\tilde{\phi})^3 + \ldots + (-1)^{n+1}(\tilde{\phi})^n + \ldots, \tag{21}$$

which is an expansion of the function $1/(1+\tilde{\phi})$ in powers of $\tilde{\phi}$ in the domain of convergence of this series.

Thus, for the problem under consideration, the wave function is given by

$$\psi \approx \psi_K(x)e^{-i(\omega_0+\delta\omega)t} + \psi_L(x)e^{-i(\omega_0+\delta\omega\pm\omega)t}, \quad (22)$$

where

$$\psi_k(x) \approx [f(\mathcal{E})]^{1/2} \times \begin{cases} \exp ik_0x + D\exp(-ik_0x), & x<0, \\ A\sin kx + B\cos kx, & 0<x<a, \\ C\exp[ik_1(x-a)], & x>a, \end{cases} \quad (23)$$

$$D = D_0 - \frac{\beta_0\tilde{\phi}}{1+\tilde{\phi}}, \quad A = \frac{A_0}{1+\tilde{\phi}},$$

$$B = \frac{B_0}{1+\tilde{\phi}}, \quad C = \frac{C_0}{1+\tilde{\phi}},$$

$$\psi_L(x) \approx \frac{1}{1+\tilde{\phi}} \times \begin{cases} D_{1\pm}\exp(-ik_\pm x), & x<0, \\ A_{1\pm}\sin k_{\pm x} + B_{1\pm}\cos k_\pm x, & 0<x<a, \\ C_{1\pm}\exp[ik_\pm(x-a)], & x>a, \end{cases} \quad (24)$$

$$B_{1\pm} \approx D_{1\pm} \approx (-1)^{L+1}\gamma C_{1\pm} \approx \beta_{1\pm}, \quad A_{1\pm} \approx \frac{y}{k_\pm}D_{1\pm}.$$

Similar expressions can also be obtained for a monoenergetic electron flux by changing $f(\mathcal{E})d\mathcal{E}$ to n and $\tilde{\phi}$ to ϕ for $\delta\omega = 0$.

However, on the other hand, the wave function inside the structure is described by expression (3), whence, by comparing (3) to (23) and (24), we arrive at

$$\tilde{\phi} = \tilde{z}, \quad \phi = z. \quad (25)$$

We next introduce the following designation for the corresponding solution to a small-signal problem without regard for the space charge ($z = 0$) (see [10]):

$$R_\pm = \frac{qE}{im^*\omega^2}\frac{2\gamma^2y^2}{(k_{1\pm}+\gamma^2k_{0\pm})}\beta_0^r. \quad (26)$$

Thus, in view of (18), (20), and (25), we can write the complete system of equations as

$$\begin{cases} F = \beta_0^r \\ S_\pm = R_\pm\left(1+\dfrac{\eta F^* S_\pm}{1+z}\right) \end{cases} \quad (27)$$

for uniform electron distribution and as

$$S_\pm = R_\pm\left(1+\frac{\eta F^* S_\pm}{(1+z)^2}\right) \quad (28)$$

for a monoenergetic electron beam. We find from (27) and (28), respectively, that

$$S_\pm = \frac{R_\pm}{1-\eta R_\pm\dfrac{F^*}{1+z}}, \quad S_\pm = \frac{R_\pm}{1-\eta R_\pm\dfrac{F^*}{(1+z)^2}}. \quad (29)$$

We then substitute (27) and (28) into (18) and (20) and introduce the notation

$$\zeta = \frac{|\sigma_E|}{\omega\varepsilon}, \quad \rho_{KL} = \frac{\pi^2(K^2+L^2)(K^2-L^2)}{64K^2L^2}, \quad X = \frac{1}{1+z}, \quad (30)$$

where σ_E is the small-signal active resonance conductivity calculated without consideration for the space charge [9, 18] and given by

$$\sigma_E \approx \sigma_{\text{sym}}\frac{8\gamma^6k_0^2k_\pm}{(\gamma^2k_0+k_1)^2(\gamma^2k_{0\pm}+k_{1\pm})},$$
$$\sigma_{\text{sym}} \approx \pm\frac{8q^2m^*\alpha^4n}{\pi L\hbar^6\omega^3}[1-(-1)^{K-L}], \quad (31)$$

where σ_{sym} is the resonance conductivity of a symmetric structure with constant height of the conduction-band bottom and barrier strength equal to α (the subscript "+" corresponds to transitions from the lower level to the upper level, and the subscript "–" indicates the reverse transitions). As a result, for the variable $X = 1/(1+z)$, we have

$$X\left(1+\frac{z_0}{1+\rho_{KL}^2\zeta^2X^2}\right) = 1 \quad (32)$$

for a uniform electron distribution and

$$X\left(1+\frac{z_0}{1+\rho_{KL}^2\zeta^2X^4}\right) = 1 \quad (33)$$

for a monoenergetic electron beam.

It is easy to verify that, in cases II and III of the relative position of resonance levels and the conduction-band bottom (Figs. 1b, 1c), for

$$\sigma_E \approx \sigma_{\text{sym}}\frac{8\gamma^6k_0^2k_-}{(\gamma^2k_0+k_1)^2k_{1-}}$$

or

$$\sigma_E \approx \sigma_{\text{sym}}\frac{8\gamma^6k_+}{\gamma^2k_{0+}+k_{1+}}, \quad (34)$$

respectively, we arrive [9, 18] at identical formulas for F, $S_{\pm}$, and X.

We now use (9)–(12) and (27)–(29) to obtain the following formulas for the amplitude of voltage U applied to the structure for a uniform electron distribution and for the amplitude of a monoenergetic flux U_r:

$$|U^2| = (Ea)^2 \frac{1+(1-\rho_{KL})^2\zeta^2X^2}{1+\rho_{KL}^2\zeta^2X^2}, \quad (35)$$

$$|U_r|^2 = (Ea)^2 \frac{1+(1-\rho_{KL})^2\zeta^2X^4}{1+\rho_{KL}^2\zeta^2X^4}. \quad (36)$$

In view of (18) and (29), we can also obtain the following formulas for the structure's conductivity calculated in relation to the applied voltage for a uniform electron distribution (G) and monoenergetic electron beam (G_r):

$$G = \frac{\sigma_E}{a}\frac{X}{1+(1-\rho_{KL})^2\zeta^2X^2},$$
$$G_r = \frac{\sigma_E}{a}\frac{X^2}{1+(1-\rho_{KL})^2\zeta^2X^4} \quad (37)$$

or

$$G = \pm\frac{\omega\varepsilon}{a}\frac{\zeta X}{1+(1-\rho_{KL})^2\zeta^2X^2} = \pm\frac{\omega\varepsilon}{a}\Phi_{KL}, \quad (38)$$

$$G_r = \pm\frac{\omega\varepsilon}{a}\frac{\zeta X^2}{1+(1-\rho_{KL})^2\zeta^2X^4} = \pm\frac{\omega\varepsilon}{a}\Phi_{KL}^r. \quad (39)$$

For a weak field (for $X = 1$), these formulas are transformed into the corresponding expressions reported in [9].

3. ANALYSIS OF SOLUTIONS OBTAINED

Thus, a solution to the original self-consistent problem can be obtained by solving a third-order equation in the case of uniform electron distribution and a fifth-order equation in the case of a monoenergetic electron beam, where the coefficients of the equations are directly related to the electric field strength, the parameters of the structure (z_0), the numbers of the levels involved in the transitions (ρ_{KL}), and the ratio of the small-signal conductivity calculated without considering the space charge to $\omega\varepsilon(\zeta)$. For a uniform electron distribution, the solutions can easily be obtained by the Cardano formula. Moreover, for $\rho_{KL}^2\zeta^2X^2 \gg 1$, two roots can generally be derived by solving a quadratic equation and the third root (this is related to a monoenergetic electron flux) $X = 1/(1 + z_0)$ can be found by solving a linear equation. Thus, in the system under consideration, a completely unique situation (apparently unprecedented so far) is realized; i.e, a solution to the self-consistent time-dependent Schrödinger and Poisson equations describing the interaction between electrons and a high-frequency field with finite amplitude can be derived analytically.

The most interesting special feature of the solutions obtained is the fact that, in general, their dependence on the problem variables is multivalued. It can be shown that, for a uniform electron distribution with $z_0 < 8$ and $\rho_{KL}^2\zeta^2 < 27$, equation (32) has a single root, whereas, for $z_0 = 8$ and $\rho_{KL}^2\zeta^2 = 27$, $X = 1/3$ is an inflection point of the corresponding function. For $z_0 > 8$ and $\rho_{KL}^2\zeta^2 > 27$, equation (32) can have from one to three real roots, depending on the ratio of the above parameters.

In view of (35), the existence of two or three roots automatically signifies that, for $\rho_{KL} \gg 1$, the dependence of the solutions on the applied voltage is multivalued. By way of example, Fig. 2 shows the dependences of X and the amplitude of the applied voltage squared (for the sake of convenience, the function $z_0|U^2|/(Ea)^2$ is used) on the parameter z_0 in the case where electrons pass through the upper levels of a double-barrier structure and the change in the level number is three units ($\rho_{KL} = 9\pi^2/8$ and $\rho_{KL}^2\zeta^2 = 100$). It can be seen that, for certain values of z_0, different values of X (and consequently different electron wave functions defined by this parameter) correspond to the same amplitude of the high-frequency voltage applied. This results in the fact that the dependence of the reflection coefficient T (in the absence of a high-frequency field, we have $T = 1$) of electrons traversing the energy midpoint of the resonance level on the amplitude of the applied voltage also becomes multivalued in a certain voltage range; the same is true of the function Φ_{KL}, which defines the high-frequency conductivity of the structure (for the sake of convenience, the dependences on the parameter $z_0|U^2|/(Ea)^2f$ are shown in Fig. 3). As a result, up to three values of the reflection coefficient (and correspondingly of the transmission coefficient) and the high-frequency conductivity may correspond to a single value of the voltage. In this case, the conductivity values corresponding to the same voltage may differ by several times; moreover, the reflection coefficient may vary from 0 to 0.8. It is also worth noting that the dependences are unconventional: they are represented by combinations of N- and S-shaped curves, one or the other of which is often encountered as a characteristic of semiconductor structures [11–13].

Qualitatively, the mechanism of the appearance of multivalued dependences may be related to the fact that different numbers of electrons at the resonance levels and, consequently, different values of alternating space charge (5) and alternating potential (10) defined by the space charge correspond to different roots of equation (32). Thus, the influence of plasma oscillations in a fairly high HF field can give rise to an effect that is

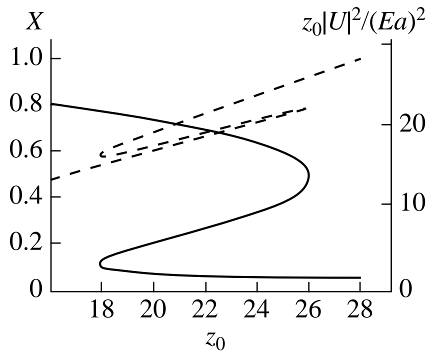

Fig. 2. The values of the roots (X) of equation (32) (solid line) and the function $z_0|U^2|/(Ea)^2$ (dashed line) in relation to the parameter z_0 for $\rho_{KL}^2\zeta^2 = 100$.

completely unknown in the structures under consideration. This effect is manifested in the fact that the dependences of the observed characteristics of the structure (electrical conductivity and the transmission and reflection coefficients) on the amplitude of the applied high-frequency voltage can be multivalued owing to redistribution of electrons between the resonance levels when the electrons pass through these levels in a double-barrier structure.

The existence of multivalued dependences of the current flowing through the structure on the amplitude of high-frequency voltage indicates that, in double-barrier structures with an applied HF field, hysteresis of the current–voltage (I–V) characteristic may be observed and current oscillations may arise under certain conditions. It is also obvious that the characteristic time of redistribution of electrons between the structure's levels can be expected to depend on the amplitude of the high-frequency voltage applied. This makes it possible to assume that the frequency of current oscillations can be controlled by varying the above amplitude.

For a monoenergetic electron beam, the values of the parameters for which the special features appear vary somewhat: for $z_0 < 16/9$ and $\rho_{KL}^2\zeta^2 = (5/3)^5$, equation (33) has a single real root; for $z_0 = 16/9$ and $\rho_{KL}^2\zeta^2 = (5/3)^5$, the point $X = 3/5$ is an inflection point of the corresponding function; and for $z_0 > 16/9$ and $\rho_{KL}^2\zeta^2 > (5/3)^5$, equation (33) may have from one to three real roots. By way of example, Fig. 4 shows the dependences of X and the square of the applied-voltage amplitude (for the sake of convenience, a plot of the function $z_0|U^2|/(Ea)^2$ is shown) on the parameter z_0 when electrons pass through the upper levels of a double-barrier structure and the level number changes by three units ($\rho_{KL} = 9\pi^2/8$ and $\rho_{KL}^2\zeta^2 = 25$). In this case, as in the previous one, different values of X and, consequently, different values of the transmission and reflection coefficients defined by the parameter X correspond to the same amplitude of the applied high-frequency voltage. However, for a monoenergetic electron beam, the plots of the reflection coefficient (and correspondingly the transmission coefficient) for electrons and high-frequency conductivity in relation to the amplitude of the high-frequency voltage acquire a highly unusual looplike shape (Fig. 5). It can be seen that, for given values of ρ_{KL} and ζ, the values of the conductivity and reflection coefficient that correspond to the same voltage differ significantly less than they do in the previous case. However, as the role of plasma oscillations increases (in fact, as the parameter $\rho_{KL}^2\zeta^2$ increases), the difference begins to increase appreciably, as might be expected; at the same time, the dependences of the reflection coefficient and high-frequency conductivity on the amplitude of the applied voltage become even more unusual (see Fig. 6, $\rho_{KL}^2\zeta^2 = 100$).

It is noteworthy that, although Fig. 4 is superficially very similar to Fig. 2, there is a substantial difference between these two cases: for uniform electron distribution, the second root of equation (32) is invariably beyond the radius of convergence of series (21), whereas, for a monoenergetic electron flux, both roots can be found within the radius of convergence.

At first glance, the fact that the roots of equations (32) and (33) can be found beyond the radius of convergence of series (21) makes the use of the obtained solutions in this domain problematic. However, using the method for finding the wave functions of electrons tunneling through systems of rectangular and triangular wells and barriers in a strong homogeneous high-frequency field [5], we can show that, at least for a homogeneous field, the solutions obtained by summing the perturbation-theory series [10] are no different from the exact solutions for a double-barrier structure if the following condition is fulfilled:

$$z\frac{k^2}{y^2} \ll 1. \tag{40}$$

For $y/k \gg 1$, this condition is satisfied for $z > 1$ as well. From this it automatically follows that a limitation of the radius of convergence of series (21) is caused solely by the fact that a solution of type $1/(1 + z)$ was sought for in the form of a power series with positive exponents; in the case under consideration, such a series has a limited radius of convergence. Therefore, we may conclude that the above solutions may be used beyond the radius of convergence of series (21).

It is also of interest that, since $X < 1$, an increase in the signal amplitude significantly suppresses the influence of plasma oscillations on the electrical conductivity of the structure for $\rho_{KL}^2\zeta^2X^2 \gg 1$. Apparently, this can be qualitatively explained by a decrease in the num-

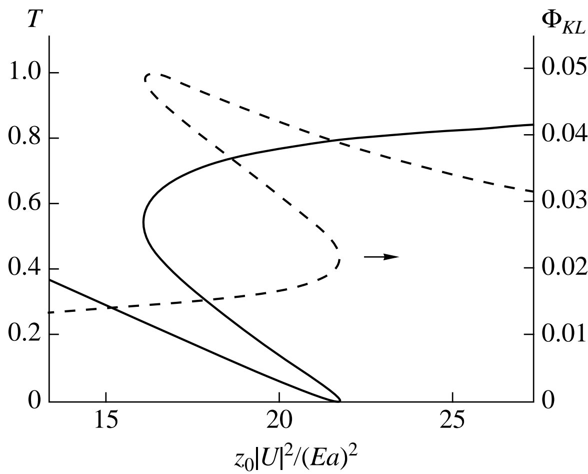

Fig. 3. The coefficient of reflection of electrons (T) passing through the middle of the resonance level in a double-barrier structure (solid line) and the function Φ_{KL} defining the high-frequency conductivity of the structure (dashed line) in relation to the parameter $z_0|U^2|/(Ea)^2$ (proportional to the squared amplitude of the applied high-frequency voltage) for $\rho_{KL}^2 \zeta^2 = 100$.

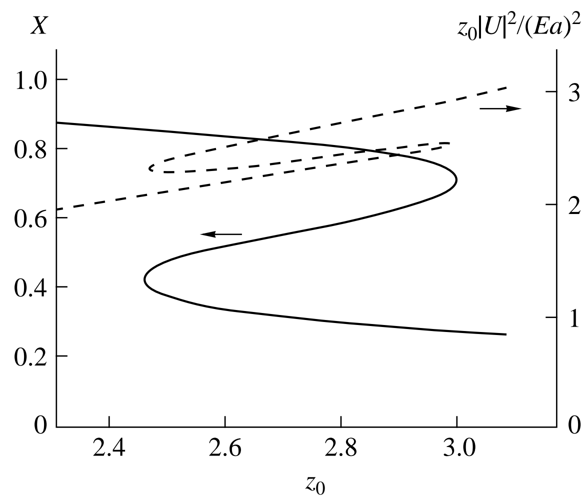

Fig. 4. The values of the roots X of equation (33) (solid line) and the function $z_0|U^2|/(Ea)^2$ (dashed line) in relation to the parameter z_0 for $\rho_{KL}^2 \zeta^2 = 25$.

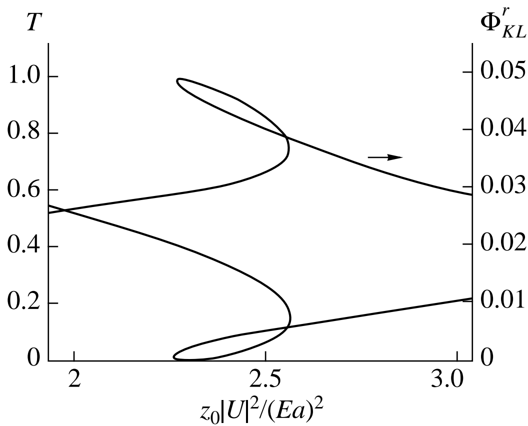

Fig. 5. The coefficient of reflection T of a monoenergetic electron flux from the resonance level of a double-barrier structure (solid line) and the function Φ_{KL}^r defining the high-frequency conductivity of the structure (dashed line) in relation to the parameter $z_0|U^2|/(Ea)^2$ (proportional to the squared amplitude of the applied high-frequency voltage) for $\rho_{KL}^2 \zeta^2 = 25$.

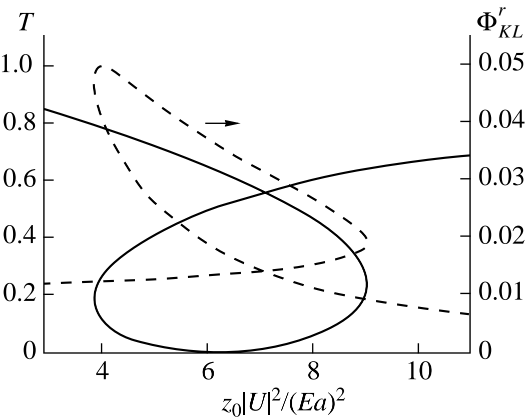

Fig. 6. The coefficient of reflection T of a monoenergetic electron flux from the resonance level of a double-barrier structure (solid line) and the function Φ_{KL}^r defining the high-frequency conductivity of the structure in relation to the parameter $z_0|U^2|/(Ea)^2$ (proportional to the amplitude squared of the applied high-frequency voltage) for $\rho_{KL}^2 \zeta^2 =$ 100.

ber of electrons at the upper level as the signal amplitude increases. However, in this case, the effect of anomalous suppression of resonance transitions persists if the level number changes by more than unity [9].

Generally speaking, the solutions to the self-consistent Schrödinger and Poisson equations were obtained purely formally without considering the exchange interaction and statistical effects. In the limiting case, the two opposite situations can be realized, depending on the parameters of the double-barrier structure and the special features of the region to the left of the structure. In one of these situations, the distribution of electrons is close to that at equilibrium (the current through the structure is small); in this case, the behavior of the electrons is largely controlled by statistical effects.

The second situation occurs if the distribution of electrons is far from that at equilibrium (the current through the structure is large); in this case, statistical effects are insignificant. Previously, it was the second situation that was considered. In order to realize this situation, two conditions must be fulfilled: (i) the lifetime of an electron at the resonance level τ should be much shorter than the characteristic time of electron–electron collisions $\tau \ll \tau_{ee}$ and (ii) the flux of electrons passing through the structure j should be fairly high ($j \gg j_p\tau/\tau_{ee}$, where j_p is the flux of electrons incident on the resonance level from the left). Modern technologies make it possible to form such thin barriers that electron transport through resonance structures can be completely ballistic (the characteristic time of all types of scattering greatly exceeds the lifetime) [16] in a rather wide range of variations in the barrier thickness. In fact, the situation may be realized such that the influence of electron–electron collisions is not yet important but the space charge already significantly affects the resonance transitions (precisely because these level are resonant). For $\tau \ll \tau_{ee}$, fulfillment of the second condition depends on the ratio between the thicknesses of the first and second barriers and also on the magnitude of the discontinuities of the conduction bands at the barriers, which can easily be realized as well.

The results reported above were also obtained without considering the static space charge. Basically, the effect of static space charge can be made less pronounced by selecting an appropriate doping level in the structure. However, this means that, if drastically different values of static space charge correspond to significantly different values of X obtained for the same voltage, we will possibly observe only a single mode of passage of electrons through the structure. However, using (7), (8), and (27)–(29), we can verify that there exist structures and modes in which the same static space charge corresponds to significantly differing values of X; consequently, the current oscillations can in principle be observed experimentally.

4. CONCLUSION

On the basis of summation of a series in perturbation theory, we obtained a solution to the time-dependent self-consistent Schrödinger and Poisson equations describing the resonance interaction of electrons that tunnel through asymmetric double-barrier structures with a high-frequency electric field. For a uniform (within the quasi-level width) electron-energy distribution, the solution is obtained analytically from a third-degree equation, whereas, for a high electron concentration, the quadratic and linear equations must be solved. For a monoenergetic electron beam, the solution is reduced to finding the roots of a fifth-degree algebraic polynomial.

It is shown that, due to redistribution of electrons between the levels, the influence of alternating space charge is manifested in a number of cases by the appearance of an effect so far completely unknown in the systems under consideration: several different electron wave functions (and consequently several different values of the high-frequency conductivity and the transmission and reflection coefficients for the electrons) can correspond to the same amplitude of the high-frequency voltage applied to the structure. Furthermore, the dependences of the transmission and reflection coefficients and also the high-frequency conductivity on the voltage amplitude are represented by a combination of N- and S-shaped curves in the case of a uniform electron distribution and by looplike curves in the case of a monoenergetic electron beam. Thus, in double-barrier structures subjected to a high-frequency field, hysteresis in the current-voltage characteristic can be observed, and current oscillations can emerge under certain conditions. In essence, we have discovered a completely new mechanism underlying the formation of multivalued dependences of the observed characteristics of semiconductor structure on the amplitude of an applied voltage; this mechanism is fundamentally different from the one involved in the previously reported phenomena of optical bistability.

ACKNOWLEDGMENTS

I thank E.I. Golant for his interest in this work and helpful comments.

This work was supported in part by the Russian Foundation for Basic Research (project no. 97-02-16652) and the Scientific Council under the Program "The Physics of Solid-State Nanostructures" (project no. 97-1094).

REFERENCES

1. M. Buttiker and R. Landauer, Phys. Rev. Lett. **49** (23), 1739 (1982).
2. W. R. Frensley, Superlatt. Microstruct. **4** (4/5), 497 (1988).
3. L. Y. Chen and C. S. Ting, Phys. Rev. B: Condens. Matter **43**, 2097 (1991).
4. M. J. Hagmann, J. Appl. Phys. **78** (1), 25 (1995).
5. A. B. Pashkovskiĭ, Zh. Éksp. Teor. Fiz. **109**, 1779 (1996) [JETP **82**, 959 (1996)].
6. V. F. Elesin, Zh. Éksp. Teor. Fiz. **112** (8), 483 (1997) [JETP **85**, 264 (1997)].
7. J. Faist, F. Capasso, C. Sirtori, *et al.*, Appl. Phys. Lett. **64**, 1144 (1994).
8. C. Sirtori, J. Faist, F. Capasso, *et al.*, Appl. Phys. Lett. **68**, 1745 (1996).
9. A. B. Pashkovskiĭ, Pis'ma Zh. Éksp. Teor. Fiz. **64** (12), 829 (1996) [JETP Lett. **64**, 884 (1996)].

10. E. I. Golant and A. B. Pashkovskiĭ, Pis'ma Zh. Éksp. Teor. Fiz. **63** (7), 559 (1996) [JETP Lett. **63**, 590 (1996)].
11. V. L. Bonch-Bruevich, I. P. Zvyagin, and A. G. Mironov, *Domain Electrical Instabilities in Semiconductors* (Nauka, Moscow, 1972; Consultants Bureau, New York, 1975).
12. Yu. K. Pozhela, *Plasma and Current Instabilities in Semiconductors* (Nauka, Moscow, 1977).
13. J. E. Carrol, *Hot Electron Microwave Generators* (Arnold, London, 1970; Mir, Moscow, 1972).
14. R. E. Kunz and E. Schöll, Phys. Rev. B: Condens. Matter **47**, 4337 (1993).
15. Z. Iconić and V. Milanović, IEEE J. Quantum Electron. **31**, 1517 (1995).
16. E. I. Golant, A. B. Pashkovskiĭ, and A. S. Tager, Pis'ma Zh. Tekh. Fiz. **20** (21), 74 (1994).
17. E. I. Golant and A. B. Pashkovskiĭ, Zh. Éksp. Teor. Fiz. **112** (7), 237 (1997).
18. E. I. Golant and A. B. Pashkovskiĭ, Fiz. Tekh. Poluprovodn. (St. Petersburg) **31**, 1077 (1997) [Semiconductors **31**, 921 (1997)].
19. V. M. Galitskiĭ, B. M. Karnakov, and V. I. Kogan, *Problems in Quantum Mechanics* (Nauka, Moscow, 1981).

Translated by A. Spitsyn

Semiconductors, Vol. 34, No. 3, 2000, pp. 344–347. Translated from Fizika i Tekhnika Poluprovodnikov, Vol. 34, No. 3, 2000, pp. 349–353.
Original Russian Text Copyright © 2000 by Khokhlov, Chuchmaĭ, Ershov.

LOW-DIMENSIONAL SYSTEMS

Absorption Features in *a*-Si/ZrO_x Nanostructures

A. F. Khokhlov, I. A. Chuchmaĭ, and A. V. Ershov*

Nizhni Novgorod State University, pr. Gagarina 23, Nizhni Novgorod, 630600 Russia

** e-mail: ershov@phys.unn.runnet.ru*

Submitted October 7, 1999; accepted for publication October 7, 1999

Abstract—Behavior of the absorption coefficient spectra $\alpha(\hbar\omega)$ in the region of the fundamental absorption edge of *a*-Si/ZrO_x multilayer nanostructures obtained by evaporation as the thickness of the amorphous silicon layer decreased from 10 to 3 nm was studied. The number of periods of structures was from 7 to 14. Periodicity was controlled by the methods of small-angle X-ray diffraction and scanning probe microscopy. The regions of linear dependence of $\alpha\hbar\omega = f(\hbar\omega)$ in the absorptivity spectra $\alpha(\hbar\omega)$ and an increase in the effective optical gap for the thickness of *a*-Si layers ≤ 5 nm were observed. The result is interpreted as a manifestation of the quantum-size effect. © *2000 MAIK "Nauka/Interperiodica".*

INTRODUCTION

The development of novel materials and devices based on amorphous silicon has been an important trend in semiconductor physics in recent years. Studies in this field stimulated the development of amorphous multilayer structures with a nanometer period: the analogues of crystalline superlattices. Such structures are often regarded as a new synthesized material with unusual electrical and optical properties that simultaneously combine the features inherent in disordered systems (amorphous semiconductors) while exhibiting carrier quantum-size effects in a system of artificially produced alternating potential wells and barriers. At the present time, most attention is drawn to structures based on hydrogenated amorphous silicon (*a*-Si:H), which is characterized by a low density of states in the mobility gap: this material has found significant applications in the field of development of active film devices [1]. On the other hand, quantum-size effects were observed in *a*-Si/SiO_2 multilayer nanostructures [2], i.e., on the basis of nonhydrogenated amorphous carbon.

This work was devoted to studies of multilayer nanoperiodic structures based on nonhydrogenated amorphous silicon. We obtained the *a*-Si/ZrO_x structures and studied the dependence of optical absorption spectra on the thickness of layers, barriers, and wells.

EXPERIMENTAL

Multilayer structures representing systems of periodically alternating layers of amorphous silicon and zirconium oxide with a period from 45 nm to 6 nm and a number of periods from 7 to 14 were obtained by the method of electron-beam evaporation. The sputtering was carried out in a BU-1A setup with employment of the system of "indirect" photometric thickness measurement. The thickness of amorphous silicon δ_W and zirconium oxide δ_B layers, as well as the number of periods in the structure, are listed in the table.

The period of structures d_{DXR} was measured by the method of small-angle X-ray diffraction using the emission line of CuK_α (the wavelength $\lambda = 1.54$ Å). The calculation was carried out according to the Bragg formula with consideration of X-ray absorption effects and refraction in the samples.

Periodicity was investigated by the method of scanning probe microscopy on a TMX-2100 Accurex atomic-force microscope in the mode of contactless amplitude-frequency modulation (contactless AFM, periodic contact). For this purpose, the etch taper was prepared on the sample, with the surface relief pattern representing the alternation of the layers in the structures.

Spectral dependences of absorption coefficient $\alpha(\lambda)$ for structures was calculated according to experimental dependences of the reflection $R(\lambda)$ and transmission $T(\lambda)$ coefficients in the visible region of the spectrum (0.4–0.75 μm), measured at the incidence angles close

Parameters of *a*-Si/ZrO_x multilayer structures

Sample no.	δ_W, nm	δ_B, nm	Number of periods	d_{DXR}, nm	E_g, eV
1	10	35	9	–	2.1
2	10	17	9	–	–
3	10	12	9	–	2.1
4	10	6	9	17	2.1
5	5	17	9	–	2.36
6	5	12	9	22	2.26
7	5	6	7	15	2.46
8	3	6	14	13	2.3
9	3	3	14	9	2.42

to grazing on a two-beam spectrophotometer. In calculations, the multilayer structure was regarded as an effective medium with the refractive index n_{eff}, extinction coefficient k_{eff}, and the total thickness d. The variances of $n_{eff}(\lambda)$ and $k_{eff}(\lambda)$ were obtained by solving the following set of equations [3]:

$$\begin{cases} T(n_{eff}, k_{eff}, d, n_s, k_s, d_s, \lambda) - T_{exp} = 0, \\ R(n_{eff}, k_{eff}, d, n_s, k_s, d_s, \lambda) - R_{exp} = 0. \end{cases} \quad (1)$$

Here, n_s, k_s, and d_s are the optical constants and thickness of the substrate; T, T_{exp}, and R, R_{exp}, are the calculated and experimental values of transmission and reflection coefficients, respectively. In this case, the substrate influence, as well as the interference of light in the films, was taken in account. As a first approximation, the values of n_{eff}, k_{eff}, and d obtained from ellipsometric measurements at the wavelength $\lambda = 0.63$ μm (an LEF-3M ellipsometer) were used.

Spectral dependences of absorption coefficient $\alpha(\lambda)$ for structures obtained as a result of solution of system (1) were globally approximated for obtaining the analytical dependences $\alpha = f(\lambda)$ and $d\alpha/d\lambda = f(\lambda)$. The approximation was carried out using a cubic spline [4] and minimizing the functional

$$I = \int_{\lambda_1}^{\lambda_2} [\alpha''(\lambda_i)]^2 d\lambda + \xi \sum_{i=1}^{p} [\alpha(\lambda_i) - \alpha_i]^2 W_i, \quad (2)$$

where λ_1 and λ_2 are the boundaries of the λ-range under study; α_i are the experimental points; $\alpha(\lambda_i)$ are the points of the analytical curve; $\alpha''(\lambda_i)$ is the second derivative; p is the number of experimental points; ξ is the coefficient characterizing the ratio of the curve smoothness to the deviation from the experimental points (for $\xi \longrightarrow 0$, the result of approximation is a straight line; for $\xi \longrightarrow \infty$, it is an interpolated curve); and W_i is the individual weight of an experimental point. The first term on the right-hand side of (2) is the condition for the curve smoothness, and the second term describes the least rms deviation of the analytical curve from the experimental one.

RESULTS AND DISCUSSION

Values of the period d_{DXR} for nanostructures a-Si/ZrO_x averaged over the volume are listed in the table; these values are obtained by the method of small-angle X-ray diffraction. A diffraction pattern obtained on sample 7 (see table) is given in Fig. 1 as an example. The diffraction peaks with intensity I/I_0 of orders m = 2, 3, and 4 can be seen in this pattern; these peaks appeared as a result of periodicity of the structure. They are located near the values of angles 2θ = 0.88°, 1.09°, and 1.37°, respectively. The period of the structure was about 15 nm. Similar patterns were obtained for other samples. One should note that the fairly broad diffraction peaks were characteristic of all the samples owing to the period spread in thickness.

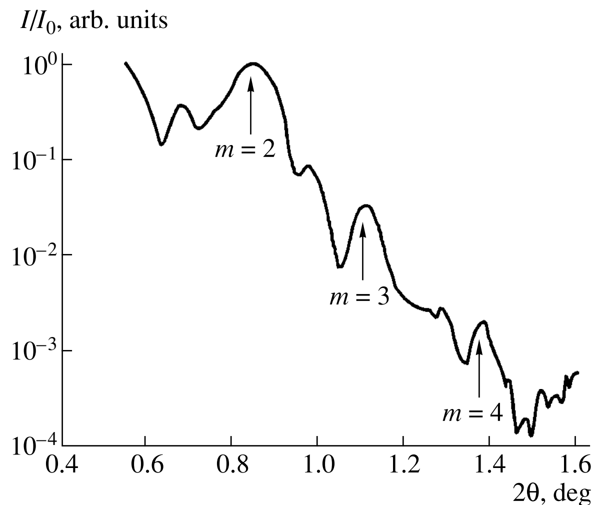

Fig. 1. Diffraction pattern obtained on an a-Si/ZrO_x structure with thicknesses of a-Si and ZrO_x layers of 5 and 6 nm, respectively (sample 7).

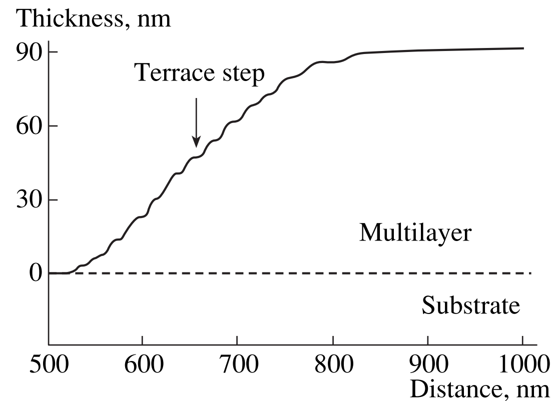

Fig. 2. Profile of the etch taper for an a-Si/ZrO_x structure with thicknesses of a-Si and ZrO_x layers of 3 and 3 nm, respectively, and the number of periods 14 (sample 9), as obtained by the method of scanning probe microscopy.

A profile of the etch taper is shown in Fig. 2 as an example; this profile was obtained by the method of scanning probe microscopy on sample 9. Appearance of steps is caused by the different etching rates of amorphous silicon and zirconium oxide layers. The height of steps corresponds to the period of the structure, and the number of steps corresponds to the number of periods. Unfortunately, the results obtained allow only qualitative assessment of the period of the structure. For exact determination of a period, a more refined selection of the etchant, as well as the obtainment of an ideal sharp etch taper, is necessary. Nonetheless, this result allows us to clearly see the alternation of layers in the structure.

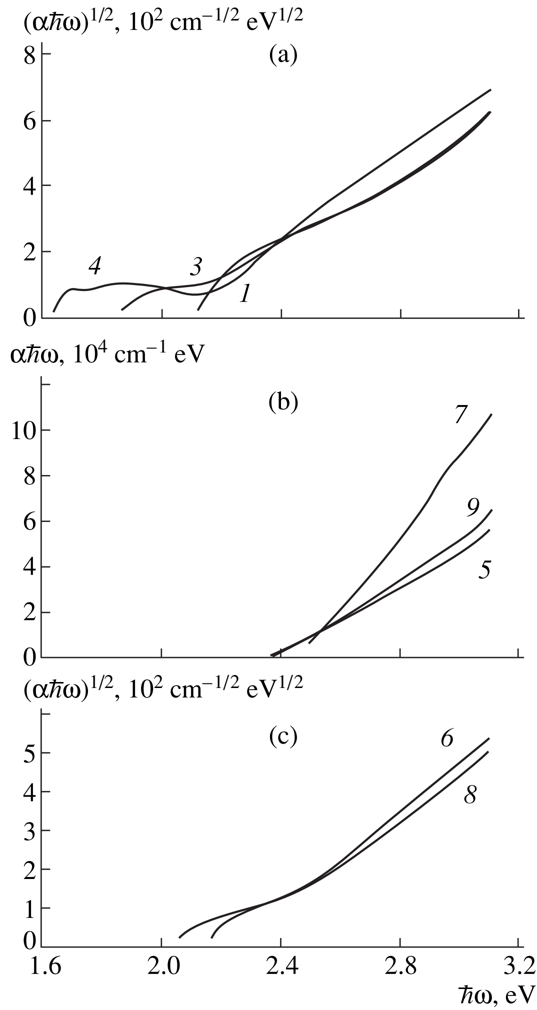

Fig. 3. Spectral characteristics of absorption coefficients for a-Si/ZrO$_x$ structures. Figures by the curves correspond to the numbers of samples in the table. Explanations are in the text.

The spectra of the absorption edge for multilayer a-Si/ZrO$_x$ structures are shown in Fig. 3. These data are indicative of the dissimilar character of α dependence on the photon energy $\hbar\omega$ for the different thickness of silicon layers in the structure.

In structures with a 10-nm-thick a-Si layer (Fig. 3a), dependence $\alpha(\hbar\omega)$ is described by the Tauc law which is characteristic of homogeneous "bulk" amorphous silicon layers [5]:

$$(\alpha\hbar\omega)^{1/2} \sim (\hbar\omega - E_g). \tag{3}$$

Here, E_g is the width of the optical gap according to Tauc's definition. In addition, an absorption tail described by the Urbach law is observed in these structures for $\hbar\omega < E_g$; i.e., we have

$$\alpha \sim \exp(\hbar\omega - E_0)/kT,$$

where E_0 is the band-edge tailing (the Urbach parameter) [5]. Thus, the absorption in structures with a 10-nm-thick a-Si layer is described by the same laws as in amorphous films, and quantum-size effects are not observed.

Anomalous absorption spectra are specific for structures with silicon layers 5 and 3 nm thick (Fig. 3b). The regions of linear dependences for absorption coefficient $\alpha\hbar\omega = f(\hbar\omega)$ and the absence of the Urbach tailing at the absorption edge were observed in these spectra. The character of such dependence suggests a quantized density of states in a-Si layers. This means that the transitions of excited carriers occur between the states of energy subbands of the valence and conduction bands. Therefore, the absorption coefficient obeys the linear dependence [6]

$$\hbar\omega\alpha \sim \sum_n (\hbar\omega - E_n)U(\hbar\omega - E_n), \quad n = 1, 2, 3, \ldots, \tag{4}$$

where E_n is the energy distance between subband edges with the quantum number n in the conduction and valence bands, and $U(E)$ is a step function. According to expression (4), quantization results in a change in the slope for each energy of transition E_n. Several such linear regions can be separated in the curves in Fig. 3b. However, it is difficult to estimate on this basis the values of transition energies with a sufficient accuracy, because the linear regions are weakly pronounced. As a rule, such a linear dependence is not observed experimentally, since the weak features of absorption spectra related to quantization are smeared owing to the broadening caused by the disorder [6].

The spectra shown in Fig. 3c are exactly of such "mixed" character. On the one hand, they obey a quadratic Tauc dependence (3), and, on the other hand, a shift of the absorption edge to higher energies is observed, which is indicative of an increase in the effective optical gap. The latter effect can also be caused by a partial oxidation of a-Si layers.

It is also of interest to note that the thickness of ZrO$_x$ barrier layers affects the shape of the absorption edge for structures with a-Si layers 3 and 5 nm thick. We believe that this is related to the interface properties; however, an unambiguous explanation requires the further studies.

The derivatives $d\alpha/d\lambda$ were plotted for more detailed studies of absorption curve features. As was expected, in absorption spectra of structures with linear regions on the $d\alpha/d\lambda$ dependence, steps appeared that corresponded to the values of transition energies E_n according to expression (4); i.e.,

$$\hbar\omega\frac{d\alpha}{d\lambda} \sim \sum_n U(\hbar\omega - E_n), \quad n = 1, 2, 3, \ldots \tag{5}$$

The derivative of absorption spectra for curve *5* in Fig. 3 is shown in Fig. 4 as an example. The values of

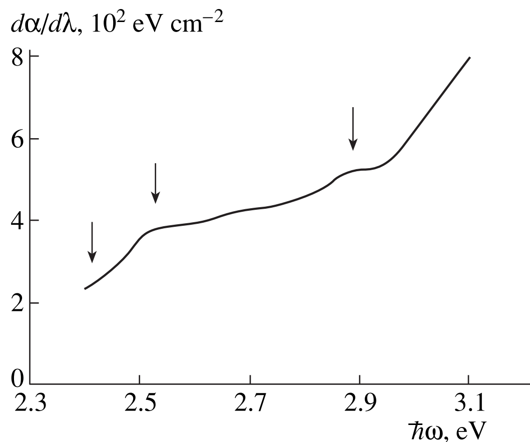

Fig. 4. Derivative of the absorption spectrum $d\alpha/d\lambda$ for sample 5. The energies E_n of transitions are indicated by arrows.

E_n for this derivative were as follows: $E_1 = 2.36$, $E_2 = 2.53$, and $E_3 = 2.89$ eV. According to expression (5), the following relationship is valid in the case of the quantum-size effect [6]:

$$E_n S(E_n)/E_1 S(E_1) = n. \tag{6}$$

Here, $S(E_n) = d\alpha/d\lambda$ are the values of the derivative for each threshold energy of transition $\hbar\omega = E_n$. After substitution, the values of the left-hand side in (6) were 1.87 and 2.92 for $n = 2$ and 3, respectively, which proves the manifestation of the quantum-size effect. We attributed the discrepancy between the results of substitution and integer values n to the following fact: the calculations were carried out on the assumption of a strict periodicity of rectangular potential wells and barriers without considering the layer spread in thickness; obviously, such a spread took place in the experiment.

Minimum values of transition energy E_1 determined for structures with an a-Si layer ≤5 nm thick and values of effective optical gap E_g are given in the table (samples 5, 7, and 9). It can be seen that E_g increases with decreasing thickness of the a-Si layer. This result agrees well with the data of [1, 2, 6] and confirms the relation between the optical absorption features for these structures and quantum-size effects.

The values of the optical gap for structures where the Tauc law is valid (3) are determined by a conventional method [3] for this law and are listed in the table. Thus, for structures with a-Si layer thickness equal to 10 nm, the optical gap is 2.1 eV and is independent of the ZrO_x layer thickness. The value of E_g turns out to be larger (see table) for samples 6 and 8, which reflects the shift of the absorption edge to higher energies in correspondence with Fig. 3c. We note that in the case where the thickness of the a-Si layer is ≤5 nm, a dependence of the value of the optical gap on the thickness of ZrO_x barrier layers is observed. We believe that this effect is caused by the violation of the interface sharpness for these structures, but proof of the latter assumption requires further studies.

CONCLUSION

Thus, the regions of linear dependence of $\alpha\hbar\omega = f(\hbar\omega)$ in absorption spectra and an increase in the effective optical gap are observed for periodic structures a-Si/ZrO_x for a-Si layers ≤5 nm thick; these effects are caused by the quantum-size effects in these structures.

ACKNOWLEDGMENTS

We thank S.S. Andreev for measurements of small-angle X-ray diffraction and Yu.A. Semin for his help with the processing of experimental results.

This work was supported in part by a grant given by the State Committee for Higher Education of RF for Basic and Applied Studies in the Fields of Electronics and Radio Engineering (project no. 97-5-3.1-12) and by the US Civil Research and Development Foundation (CRDF) (grant no. RESC-01-02).

REFERENCES

1. J. P. Conde, V. Chu, D. S. Shen, *et al.*, J. Appl. Phys. **75**, 1638 (1994).
2. E. A. Vinogradov, A. V. Zayats, and F. A. Pudonin, Fiz. Tverd. Tela (Leningrad) **33**, 197 (1991) [Sov. Phys. Solid State **33**, 113 (1991)].
3. A. F. Khokhlov, A. V. Ershov, A. I. Mashin, *et al.*, Fiz. Tekh. Poluprovodn. (Leningrad) **20**, 1288 (1986) [Sov. Phys. Semicond. **20**, 812 (1986)].
4. G. E. Forsythe, M. A. Malcolm, and C. B. Moler, *Computer Methods for Mathematical Computations* (Prentice-Hall, Englewood Cliffs, New York, 1977; Mir, Moscow, 1980).
5. N. F. Mott and E. A. Davis, *Electronic Processes in Non-Crystalline Materials* (Clarendon, Oxford, 1979; Mir, Moscow, 1982).
6. K. Hattori, T. Mori, H. Okamoto, *et al.*, in *Amorphous Silicon and Related Materials*, Ed. by H. Fritzsche (World Scientific, Singapore, 1989; Mir, Moscow, 1991).

Translated by T. Galkina

Semiconductors, Vol. 34, No. 3, 2000, pp. 348–352. Translated from Fizika i Tekhnika Poluprovodnikov, Vol. 34, No. 3, 2000, pp. 354–358.
Original Russian Text Copyright © 2000 by Mezdrogina, Patsekin.

Transformation of an Unordered Structural Network in Amorphous Hydrogenated Silicon Films as a Result of Doping with Boron

M. M. Mezdrogina and A. V. Patsekin

Ioffe Physicotechnical Institute, Russian Academy of Sciences, Politekhnicheskaya ul. 26, St. Petersburg, 194021 Russia

Submitted May 28, 1999; accepted for publication June 3, 1999

Abstract—The influence of the technological parameters of deposition, the purity and relative concentration of diborane, and the substrate temperature on electrical parameters of (a-Si:H):B films obtained by high-frequency decomposition of a gaseous mixture in a multielectrode system was studied. Simultaneous existence of the mechanisms for doping and modification in the case of introduction of boron from diborane in the course of deposition of (a-Si:H):B films is proposed. © *2000 MAIK "Nauka/Interperiodica".*

Boron is typically introduced into the structural network of amorphous hydrogenated silicon (a-Si:H) films in the course of gas deposition using a mixture of diborane or boron–ethylene mixtures with silane [1]. The method of ion implantation for preparation of the p-type (a-Si:H):B layers is used much less frequently, because the concentration of defects in such films is higher than that in films obtained by introducing boron from the gas phase [2]. In a number of works [2, 3], the influence of various types of concentration depth profiles of the films and the types of bonds of boron with silicon and hydrogen on photoelectric properties of (a-Si:H):B films and on the parameters of devices fabricated on the basis of these films was studied.

As shown in [2], for the doping level $C_{\mathrm{B\,vol}} = (B_2H_6/(SiH_4 + B_2H_6)) \times 100\% = 10^{-3}$ vol %, the Fermi level (ε_F) in (a-Si:H):B films is located in the middle of the mobility gap, the charge state of defects corresponds to D^0, the specific drift length of electrons $(\mu\tau)_n$ is equal to that of holes $(\mu\tau)_p$, the activation energy in the temperature dependence of dark conductivity is $\Delta E_\sigma = 0.90$–0.95 eV, and the optical forbidden-band width is $E_g^{\mathrm{opt}} = 1.90$ eV. It was also shown that such films could be used in devices based on a-Si:H as layers with "intrinsic" conduction [4]. At the same time, it is known [1] that less than 0.01 of the total concentration of boron impurity introduced into a-Si:H films is electrically active; in addition, the density of defects in the mobility gap of boron-doped films is much higher than that in undoped films. Doping of amorphous hydrogenated silicon with boron results not only in a shift of the Fermi level ε_F but also in transformation of the density of localized states $g(\varepsilon_F)$ due to the fact that the structural network changes when the impurities are introduced. At the same time, the data about a small fraction of electrically active boron impurity were obtained for the initial films for which the density of states in the mobility gap was $g(\varepsilon_F) \sim 5 \times 10^{16}$–$10^{17}$ eV^{-1} cm^{-3}, the charge state of the defects corresponded to D^-, and the activation energy was $\Delta E_\sigma = 0.70$–0.75 eV. A plausible explanation for a small fraction of electrically active boron impurity in the layers with the aforementioned parameters can be given if we assume that the mechanisms for doping and structural modification exist simultaneously. There are no data available on the charge state of the boron impurity introduced. For the introduced metallic impurity, the charge state was directly determined from the Mössbauer spectra [5, 6]. A correlation between variations in the technological parameters of deposition of a-Si:H films (the substrate temperature T_s during deposition and the impurity concentration) and the existence of the doping and modification processes was reported in [5]. The Fe, Eu, and Dy impurities were introduced into a-Si:H films in which the density of localized states (prior to introduction of impurities) was $g(\varepsilon_F) \sim 5 \times 10^{16}$ eV^{-1} cm^{-3} and the activation energy of σ was $\Delta E_\sigma = 0.65$–0.70 eV; i.e., these parameters were close to those of the films doped with boron.

The objective of this work was to study the influence of technological parameters, namely, the purity of diborane and the substrate temperature, on (i) the doping efficiency, (ii) the photoelectric parameters of a-Si:H films, and (iii) the changes in the type of bonds of silicon with hydrogen and boron. Undoped (starting) a-Si:H films were deposited by the method of high-frequency decomposition of silane (a plasma-enhanced chemical-vapor deposition (PECVD)) in a multielectrode reactor. As reported in [2, 4], the undoped films grown in a multielectrode system have the following parameters: $\Delta E_\sigma = 0.90$–0.95 eV, $g(\varepsilon_F) = 5 \times 10^{15}$ eV^{-1} cm^{-3}, $(\mu\tau)_n =$

$(\mu\tau)_p = 10^{-8}$ cm^2/V, and $E_g^{opt} = 1.90$ eV. According to the infrared (IR) spectroscopy data, the main type of bonding of silicon to hydrogen corresponds to monohydrides [2, 4] in the films doped with boron, with the level of doping (defined by concentration of diborane in a gas mixture) $C_{B\,vol} \le 10^{-3}$ vol %. It is known that the kinetics of the film growth in a multielectrode system is completely defined by the flux of SiH_3^+ radicals and their mobility over the surfaces of substrate and growing film [4]. If diborane is introduced into the gas mixture under conditions of high-frequency discharge, the BH_3 complexes are formed, are attracted by incomplete bonds of silicon–hydrogen radicals, are embedded in the surface of growing film, and finally form a metastable $(BH_5SiH_3)^*$ complex in the excited state. The formation of the metastable complex gives rise to molecular hydrogen, which escapes to the gas phase, and a dangling silicon–silicon bond.

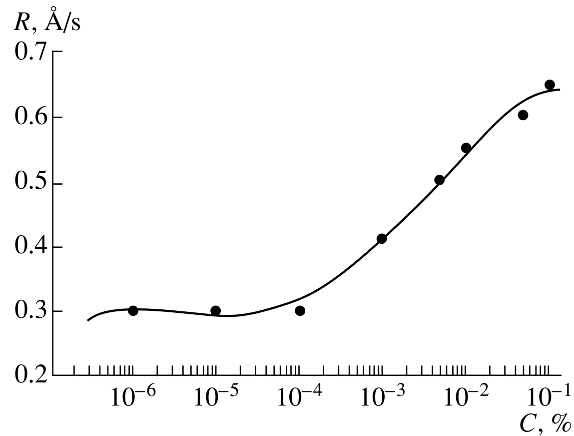

Fig. 1. Growth rate of the film as a function of the concentration of the impurity introduced.

Figure 1 shows the dependence of the film-growth rate on the diborane concentration $C_{B\,vol}$ without considering the diborane purity. For a relative diborane concentration higher than 10^{-3} vol %, a sharp increase in the film-growth rate is observed; i.e., a catalytic effect is observed if a large amount of diborane is added to a gas mixture during deposition of *a*-Si:H films by the method of high-frequency decomposition of a silane mixture.

Introducing boron into an unordered structural network of *a*-Si:H films leads to the formation of various bonds of boron with silicon, such as B–Si (a completing bond for an electrically active fraction of introduced impurity), and boron with hydrogen, such as B–H–B (a bridging bond for an electrically inactive fraction of impurity). Simultaneously, silicon–hydrogen bonds corresponding to SiH and SiH_2 and dangling Si–Si bonds are formed. An increase in the diborane concentration in a gas mixture to $C_{B\,vol} > 10^{-3}$ vol % results in a sharp increase in the deposition rate and is bound to lead to a change in the relation between silicon–hydrogen, boron–silicon, and boron–hydrogen bonds in *a*-Si:H films.

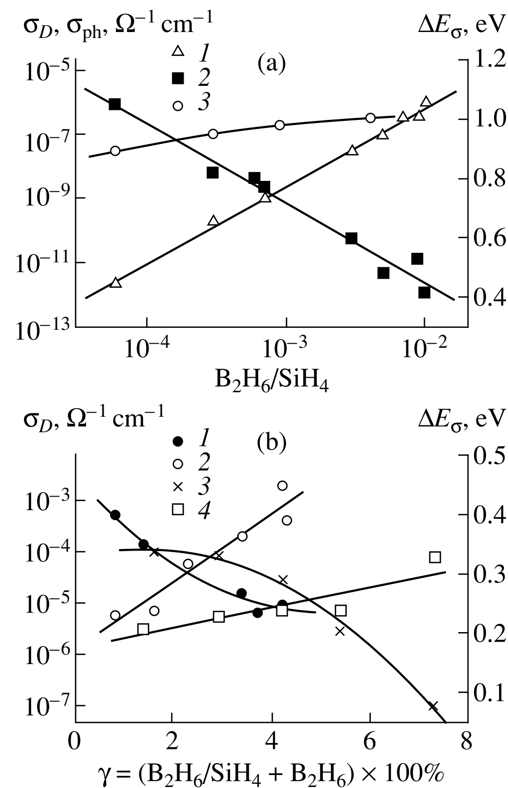

Fig. 2. (a) Dependences of (*1*) activation energy for dark conductivity ΔE_σ, (*2*) photoconductivity σ_{ph}, and (*3*) dark conductivity σ_D on the concentration of diborane of type 1 in the gas phase. (b) Dependences of activation energy for dark conductivity ΔE_σ (curve *1* corresponds to the case where diborane of type 1 is used, and curve *4*, to diborane of type 2) and dark conductivity σ_D (curve *2* corresponds to diborane of type 1, and curve *3*, to diborane of type 2) on the concentration of diborane in gas phase.

Infrared spectra of the films were measured with an IFS-113v Bruker IR Fourier spectrometer in the range of 500–4000 cm^{-1}, with resolution equal to 4 cm^{-1} and averaging performed over 1000 scans.

A variation in the substrate temperature is also bound to change the relative concentration of the aforementioned bonds [7], which would result in changes in photoelectric and optical parameters of deposited films. All photoelectric parameters of the films that were studied and were deposited onto quartz substrates were measured in a planar structure; nichrome contacts were deposited onto the film surface by the method of thermal evaporation, with a distance of 1 mm between the contacts. The film thickness was determined with the use of an MII-4 interference microscope. Optical parameters were measured using a Hitachi system in the range from 500 to 2000 cm^{-1}. Figures 2a and 2b show the dependences of photoelectric parameters (namely, the photoconductivity σ_{ph}, the dark conductiv-

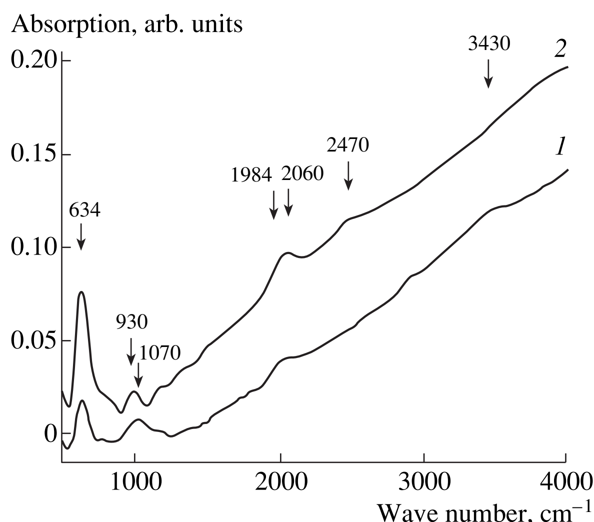

Fig. 3. Infrared absorption spectra of the films of amorphous hydrogenated silicon for two different levels of doping with boron: (*1*) $C_{B\ vol} = 1.25\%$ and (*2*) $C_{B\ vol} = 7\%$.

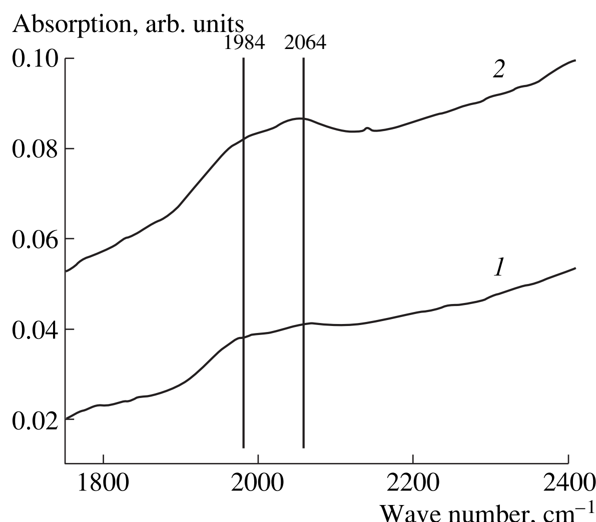

Fig. 4. A relative decrease in the fraction of bridging B–H–B bonds (1984 cm^{-1}) as compared to Si–H bonds (2064 cm^{-1}) with increasing concentration of diborane: curve *1* is for $C_{B\ vol} = 1.25\%$ and curve *2* is for $C_{B\ vol} = 7\%$.

ity σ_D, and the activation energy of conductivity ΔE_σ) on the concentration $C_{B\ vol}$. We used two types of diborane that differed in the degree of removal of oxygen-containing compounds: type 1 corresponded to conventional purification and the diborane of type 2 was subjected to an additional purification procedure. The data on the content of impurities in the diborane of type 2 are listed in the table. It can be seen from Figs. 2a and 2b that, if the level of doping is lower than 10^{-3} vol %, an effect of compensation is observed; i.e., ΔE_σ increases (diborane of type 1 was used) as compared to the value of ΔE_σ for undoped films. If the $C_{B\ vol}$ concentration was further increased to 4.5 vol % (diborane of type 1), the effect of compensation was not observed. If diborane of type 2 was used with a low level of doping, the same dependences were observed as in the case of using the diborane of type 1. An increase in concentration (with diborane of type 2) to 7 vol % does not lead to the appearance of the effect of compensation (Fig. 2b), and ΔE_σ decreases with increasing $C_{B\ vol}$, as distinct from the dependence of ΔE_σ on $C_{B\ vol}$ for type 1 of diborane. Figure 3 shows the IR absorption spectra of the films grown on KDB-10 (*p*-Si:B, $\rho = 10\ \Omega$ cm) single-crystal substrates of ⟨100⟩ orientation for the levels of doping equal to 1.25 and 7 vol % (diborane of type 1) obtained in a multielectrode system. Due to the fact that it was impossible to correctly determine the thickness of such films [4] deposited onto the wafers of silicon single crystals, the spectra were not normalized to the same thickness and represented merely a qualitative pattern of IR absorption by various chemical bonds in the films. In the IR spectra, there exist the absorption bands characteristic of the B–H–B bridging bond (1984 cm^{-1}), the B–H terminal bond (2470 cm^{-1}) [9–11], the silicon–hydrogen bonds (the band at 634 cm^{-1} corresponding to bending vibrations and the features at 2000–2100 cm^{-1} corresponding to stretching vibrations) [12], OH bonds (stretching vibrations correspond to 3200–3600 cm^{-1} and bending vibrations correspond to 930 cm^{-1}) [13], and silicon–oxygen bonds (1000–1200 cm^{-1}) [13]. It can be seen from the spectra shown in Fig. 4 that the fraction of B–H–B bonds increases with an increase in $C_{B\ vol}$ as compared to the fraction of Si–H bonds, which correlates with variations in σ_D and ΔE_σ (Fig. 2). For diborane of type 1, a

Content of impurities in diborane of type 2

Impurities	Content*, %
Organic impurities	1.07×10^{-3}
Methylene chloride	Absent
Fe	5×10^{-6}
Mg	1×10^{-6}
Cr	5×10^{-6}
Ni	1×10^{-6}
Al	1×10^{-6}
Cu	1×10^{-6}
Na	3.9×10^{-6}
Oxygen-containing	5×10^{-5}
Moisture	Absent

Notes: * For organic impurities, the data are expressed in vol %, and, for inorganic impurities, they are expressed in wt %.

gradual decrease of ΔE_σ and an increase in σ_D are observed with increasing $C_{\mathrm{B\,vol}}$. For a small value of $C_{\mathrm{B\,vol}}$ (up to 10^{-2} vol %), the photoconductivity σ_{ph} is independent of the level of doping, which is consistent with the data reported in [8]. It should be emphasized that the absorption bands related to the B–Si bonds (1400 cm^{-1}) are not observed to within the accuracy of measurements. In the films doped with diborane of type 2, the bands related to silicon–oxygen bonds were not observed. On the basis of the data obtained, we may infer the following: to obtain the *a*-Si:H films having $\Delta E_\sigma = 0.20–0.25$ eV, $\sigma_D = 1 \times 10^{-3}–5 \times 10^{-3}\ \Omega^{-1}\ cm^{-1}$, and *p*-type conductivity, it is expedient to use diborane that is preliminarily freed of the oxygen-containing impurities and has a concentration no higher than 1 vol %. In the case of using diborane of type 1, the same parameters of the films could be obtained for $C_{\mathrm{B\,vol}} \le 4.5$ vol %. The absence of B–Si bonds (or their presence with a concentration undetectable in measurements) makes it possible to suggest a plausible assumption about the occurrence of the processes of both doping and modification when the diborane impurity is introduced from the vapor phase into a multielectrode system. It is very likely that, in the course of the introduction of diborane, the B–Si bonds do not play the role of acceptors as could be expected; rather, these acceptors are represented by potential barriers, which are located at the interface between the microcrystalline and amorphous phases and whose existence could be inferred from the data obtained in the studies of the microstructure of *a*-Si:H films doped with boron. In fact, the inhomogeneities in the microstructure of the films doped with boron have a scale of 500–600 nm [7], whereas undoped films have a homogeneous microstructure. Donor levels in the mobility gap are formed by dangling Si–Si bonds. In [15], the possibility of doping the microcrystalline silicon with boron was studied, but the doping effect was not observed. The conclusions concerning the simultaneous existence of the mechanisms of doping and modification were confirmed by the results reported in [14], where the microcrystalline silicon films were obtained by PECVD and were doped with boron. The influence of the substrate temperature on the type of bonds and photoelectric parameters of the film is illustrated in Fig. 5. As can be seen, variation in the parameters with an increase in the substrate temperature is similar to that shown in Fig. 2. The forbidden-band width E_g^{opt} decreases as the substrate temperature increases, which is consistent with data obtained in [6]. On the basis of the results obtained in this work, the following conclusions can be made:

(i) The fraction of bridging B–H–B bonds decreases with increasing diborane concentration.

(ii) An additional freeing of diborane from oxygen-containing impurities makes it possible to obtain the (*a*-Si:H):B films with parameters that satisfy the requirements imposed on the layers to be used in a number of devices based on *a*-Si:H films. Thus, photodetectors with a spectral sensitivity of 0.1–0.15 A/W and photoelectric transducers with short-circuit current densities of $I = 12–15$ mA/cm^2 and an open-circuit voltage equal to $U = 0.75–0.80$ V were fabricated. It is noteworthy that the largest values of the filling factor in the above devices do not exceed 0.40–0.45; this may be due to the existence of the mechanisms of doping and modification in the *p*-type films obtained in a multielectrode system if diborane was added, whereas the available filling factors for *p–i–n* structures amount to 0.50–0.65 [15].

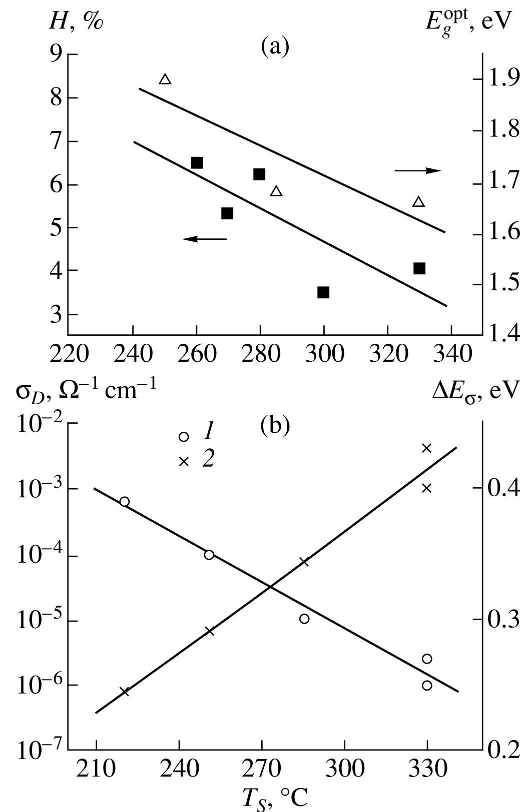

Fig. 5. Hydrogen content in the film [H] and the optical forbidden-band width E_g^{opt} in relation to the substrate temperature T_s during growth. (b) (*1*) Activation energy of dark conductivity ΔE_σ and (*2*) dark conductivity σ_D in relation to the substrate temperature T_s during growth.

ACKNOWLEDGMENTS

We thank M.M. Kazanin for measurements of electrical parameters of the films studied and Yu.V. Zhilyaev for his helpful participation in discussion of the results.

REFERENCES

1. P. G. Le Comber and W. E. Spear, J. Non-Cryst. Solids **35–36**, 327 (1980).

2. O. A. Golikova, U. S. Babakhodzhaev, V. V. Dubro, *et al.*, Fiz. Tekh. Poluprovodn. (St. Petersburg) **26**, 66 (1992) [Sov. Phys. Semicond. **26**, 38 (1992)].
3. M. M. Mezdrogina, O. A. Golikova, M. M. Kazanin, *et al.*, Zh. Tekh. Fiz. **62**, 108 (1992) [Sov. Phys. Tech. Phys. **37**, 55 (1992)].
4. M. M. Mezdrogina, A. V. Abramov, G. N. Mosina, *et al.*, Fiz. Tekh. Poluprovodn. (St. Petersburg) **32**, 555 (1998) [Semicond. **32**, 555 (1998)].
5. A. R. Regel', P. P. Seregin, M. M. Mezdrogina, *et al.*, Fiz. Tekh. Poluprovodn. (Leningrad) **22**, 161 (1988) [Sov. Phys. Semicond. **22**, 100 (1988)].
6. M. M. Mezdrogina, A. F. Bardamid, O. A. Golikova, *et al.*, Neorg. Mater. **26**, 1809 (1990).
7. M. M. Mezdrogina, O. A. Golikova, V. Kh. Kudoyarova, *et al.*, Neorg. Mater. **26**, 455 (1990).
8. A. G. Kazanskiĭ, E. P. Miligovich, and R. A. Urazbaeva, Fiz. Tekh. Poluprovodn. (Leningrad) **24**, 1143 (1990) [Sov. Phys. Semicond. **24**, 724 (1990)].
9. S. C. Shen and M. Cardona, Phys. Rev. B: Condens. Matter **23**, 5322 (1981).
10. W. C. Price, J. Chem. Phys. **16**, 894 (1948).
11. I. Freund and R. S. Halfold, J. Chem. Phys. **43**, 3795 (1965).
12. G. Lukovski, Sol. Energy Mater. Sol. Cells **2**, 431 (1980).
13. W. A. Pliskin and H. S. Lehman, J. Electrochem. Soc. **112**, 1013 (1965).
14. Abstract Mater. Res. Soc. Symp. Proc. (San Francisco, California, April 13–17, 1998), p. 13.
15. Y. Hamakawa, in *Current Topics in Photovoltaics*, Ed. by T. J. Coutts and J. D. Meakin (Academic, London, 1985; Mir, Moscow, 1988).

Translated by A. Spitsyn

Semiconductors, Vol. 34, No. 3, 2000, pp. 353–357. Translated from Fizika i Tekhnika Poluprovodnikov, Vol. 34, No. 3, 2000, pp. 359–363.
Original Russian Text Copyright © 2000 by Zimin.

AMORPHOUS, VITREOUS, AND POROUS SEMICONDUCTORS

Classification of Electrical Properties of Porous Silicon

S. P. Zimin

Demidov Yaroslavl State University, ul. Sovetskaya 14, Yaroslavl, 150000 Russia

e-mail: zimin@univ.uniyar.ac.ru

Submitted July 23, 1999; accepted for publication August 24, 1999

Abstract—The classification of electrical properties of porous silicon is performed on the basis of differences in the structure of this material and in the processes of formation of the regions depleted of charge carriers. It is shown that porous silicon as a class can be subclassified into four groups, each of which has a specific set of characteristic features. For each group, the most probable properties of metal/(porous silicon) and (porous silicon)/(single-crystalline silicon) junctions are described. It is shown that the diversity of electrical properties of porous silicon and its contacts with metallic electrode and silicon substrate brings about the experimentally observed wide set of characteristics of multilayer structures with porous silicon layers. *© 2000 MAIK "Nauka/Interperiodica".*

INTRODUCTION

Porous silicon (*por*-Si) obtained by anodic electrochemical treatment of silicon wafers exhibits a wide set of unique properties and is a promising material for fabrication of various devices of the new generation [1]. The use of *por*-Si layers as active elements of these devices requires that the electrical properties of this material be studied thoroughly. The first works devoted to measurement of electrical parameters of *por*-Si were conducted in the early 1980s [2–4]. In these studies, an anomalously large value of resistivity exceeding 10^5 Ω cm of porous layers was observed in the case of high porosity. Later on, several hypotheses were forwarded to explain the low electrical conductivity of porous Si [5–8]. These hypotheses are based on the existence of depleted layers surrounding the pores [4, 5]; on the existence of quantum-size effects [6, 7]; on the phenomenon of the Coulomb repulsion from the side of charged surface traps [8]; and so on. Starting in 1992, in connection with active studies of electroluminescence [9], a large number of publications devoted to investigations of electrical properties of *por*–Si and contact phenomena at the *por*-Si–metal and *por*-Si–crystalline Si interfaces appeared. In the context of this paper, we do not aim to analyze the entire body of relevant publications in detail; rather, we refer the reader to the reviews [10, 11] and to the most important original publications (for example, [12–17]).

Analysis of published data shows that experimental results obtained by a number of researchers appear contradictory; mutually exclusive properties are assigned to the porous layer; and diverse approaches to describing the phenomena at the boundary of *por*-Si with metals and crystalline silicon substrate are used. However, this superficial inconsistency might be expected. In this paper, the differences in the structure of *por*-Si and in the formation of depleted regions are taken to suggest a classification of *por*-Si that accounts for the diversity of electrical properties of *por*-Si and multilayer structures based on this material.

PROCESSES OF DEPLETION IN POROUS SILICON AND CLASSIFICATION OF ELECTRICAL PROPERTIES

It is known that *por*-Si can exhibit a wide range of porosity (from 2 to 85%) depending on the conditions of electrochemical treatment, the level of doping with donor or acceptor impurities, the electrolyte composition, and so on. It is obvious that *por*-Si with a specific volume of pores of several percent and *por*-Si with the highest porosity differ inevitably from one another not only in structural but also in optical, luminescent, and electrical properties. At present, it can be regarded as conclusively proven that, in the course of the formation of pores, regions depleted of charge carriers can form around each pore [4, 5, 18]. Three reasons are typically regarded as responsible for the formation of depleted regions: the capture of charge carriers by traps at the surface of the pores, the escape of impurity atoms to the electrolyte or the wall of the pores [3, 5], and the passivation of impurity atoms with hydrogen [19–21]. Recently, it has been established (see, e.g., [8]) that the concentration of impurity atoms in a single-crystalline matrix of *por*-Si does not change, and, thus, the second of the above three reasons for the formation of depleted regions should be regarded with a certain reserve. Depletion of charge carriers in the regions under consideration can be significant and can give rise to the state of intrinsic conduction. The depleted regions can extend to fairly large depths in the silicon matrix owing to high hydrogen diffusivity.

Transport of charge carriers in *por*-Si depends to a large extent on porosity, the pore diameter, the sizes of

Electrical properties of porous silicon

Group	Properties of depleted regions	Features of electrical conduction at 300 K	Temperature dependence of electrical conductivity	The most probable properties of contacts
1	Depleted regions are poorly pronounced or are absent	Electrical conduction over the silicon matrix in accordance with the theory of effective medium in the "Si + air" model	The same as in starting silicon	Al–*por*-Si (N), *por*-Si–Si (N)
2	Depleted regions of neighboring pores do not overlap	Conduction over nondepleted regions of the silicon matrix in accordance with the theory of effective medium in the "Si + (air + depleted regions) model"	The same as in starting silicon	Al–*por*-Si (R or N), *por*-Si–Si (N)
3	Depleted regions encompass the entire interpore space	Conduction over the depleted silicon matrix in the model of fluctuating charge pattern	The Arrhenius law for the dependence with various activation energies	Al–*por*-Si (R), *por*-Si–Si (R or N)
4	Silicon nanocrystallites having various fractal dimensionalities are surrounded by the products of electrochemical reactions	Conduction over distributed states in the intercrystallite medium and (or) conduction by way of intercrystallite hops	The Arrhenius law for the dependence with various activation energies	Al–*por*-Si (N), *por*-Si–Si (R)

Note: N stands for a nonrectifying contact, and R stands for a rectifying contact.

depleted regions, the efficiency of charge-carrier capture by traps, and so on. Systematization of the electrical properties of *por*-Si in relation to the distribution of depleted regions in *por*-Si with various morphologies is given in the table and implies the division of the entire class of *por*-Si into four groups. The first group includes the porous material in which the depleted regions are either absent or are poorly pronounced. Such an example was described in [22]. Porous-silicon layers were formed in silicon wafers doped heavily with antimony and had a porosity amounting to 8–27%. Measurements of the Hall effect have shown that the electron concentration in the *por*-Si crystalline matrix is the same as in the starting silicon. The resistivity of *por*-Si increased by 1.2–1.7 times as compared to that of the original silicon wafer, which was consistent with the results of calculations based on the theory of effective medium composed of silicon and air. We observed *por*-Si with the above properties only if the *por*-Si layers were formed on the silicon substrates doped with antimony, which may be explained by the well-known fact that antimony atoms are not passivated with hydrogen. *Por*-Si belonging to the first group, as distinct from porous Si layers of other groups, is insensitive to variations in humidity and to the presence of polar molecules.

The second group corresponds to porous structures in which the large-sized pores are separated by large distances, so that the depleted regions surrounding the pores do not overlap. The *por*-Si layers observed in [18] may serve as examples. A *por*-Si layer with a porosity equal to 5–10% was obtained in silicon wafers that were doped with phosphorus and had a resistivity of 4.5 Ω cm. Studies performed with the use of a scanning electron microscope showed that large cylindrical pores, which have a diameter of about 1 μm and are separated by 3–10 μm, are present in the sample. The Hall measurements indicated that the electron concentration in the region around the pores decreases; an increase in the resistivity of *por*-Si in this case is not consistent with the effective-medium theory for the porosity amounting to 5–10% but is in good agreement with this theory if an additional volume occupied by the depleted regions is taken into account. The resistivity of *por*-Si of the second group exceeds that of the starting silicon by 1.6–15 times and is related to the transport of charge carriers over nondepleted low-resistivity regions of the silicon matrix. *Por*-Si layers with such morphology are effectively formed at the *n*-type substrates, although it is theoretically conceivable that a structure with scarce micropores can be formed on *p*-Si substrates [23].

The third group includes porous structures with a highly developed network of small pores and relatively low porosity (less than 40–50%). Depleted regions of neighboring pores overlap (owing to a small distance between the walls of the pores), and the remaining single-crystalline matrix resembles a coral-like structure that consists, in the general case, of regions with different degrees of depletion and, in the limiting case, of silicon with intrinsic conduction. The resistivity of *por*-Si belonging to the third group is much larger (amounting to ~10^6 Ω cm [24]) as compared to the above cases, and the drift of charge carriers occurs over the high-resistivity silicon matrix and can be accompanied by the Coulomb repulsion from charged walls [8]. Temperature dependences of the *por*-Si electrical conductivity obeys the Arrhenius law, with an activation energy varying from 0.65 to 0.75 eV for the temperature range of 300–500 K [24], which is related to the fluctuations of the

charge pattern. According to the thermal-probe measurements, the *por*-Si layers formed on the *p*-type substrates often exhibit the effective *n*-type conductivity characteristic of intrinsic semiconductors having a mobility of electrons higher than that of holes. Using a short-term thermal annealing, one can increase the concentration of charge carriers in a single-crystalline matrix of *por*-Si as a result of destruction of the (impurity atom)–hydrogen complexes. Description of such experiments through the example of porous boron-doped silicon with porosity amounting to 16–40% is given in [20, 21].

The fourth group of *por*-Si includes structures with high porosity (higher than 40–50%), for which the structural characteristics of the material (and, consequently, the behavior of conduction) undergo a substantial variation. Such a *por*-Si constitutes a combination of silicon nanocrystals having various fractal dimensionality and residing in a porous matrix of complex chemical composition. Silicon nanocrystallites with sizes ranging from several nanometers to several tens of nanometers represent the silicon regions that are not subjected to dissolution and are surrounded by the products of electrochemical reactions. If the crystallite sizes are smaller than 4 nm, quantum-size effects emerge and cause a quantization of the energy spectrum of charge carriers, an increase in the forbidden-band width to 1.8–2.9 eV [25], and a decrease in the permittivity [7]. Charge carriers in a system with high porosity are found to be localized, which gives rise to anomalously high *por*-Si resistivity that may be as great as 10^{11} Ω cm [6]. Temperature dependences of dark conductivity for the *por*-Si samples belonging to the fourth group in the region of room temperature obey the Arrhenius law, with activation energy increasing from 0.30 to 1.01 eV as the porosity increases from 40 to 80% [26, 27]. At present, no significant differences in electrical conductivity of porous material belonging to this group have been revealed in the cases where size quantization is present or absent. It is believed [11, 28] that electrical conduction in such a structure can be accomplished over delocalized states in the matrix (whose properties are close to those of *a*-Si:H) surrounding the crystallites and via the intercrystallite hops. Silicon nanocrystallites are subject to the depletion processes (the concentration of charge carriers in nanocrystallites may vary from 10^{10} cm^{-3} [19] to 10^{13} cm^{-3} [14]); however, the value of electrical conductivity is controlled here by the type of transport rather than by the concentration of charge carriers. The mobility of charge carriers in *por*-Si of the fourth group is very low and varies in the range of 10^{-1}–10^{-4} cm^2/(V s) (see, e.g., [14, 29]).

It is noteworthy that the aforementioned classification is undoubtedly simplified. Here, in a number of cases, we ignored the important issues related to the three-component structure of *por*-Si (silicon + pores + products of electrochemical reactions) [30, 31], the dependence of electrical conductivity of *por*-Si on the presence of ions at the pore surface [32], and the presence of traps in the material; within each group, all the above factors can exert a certain effect on the behavior of the charge-carrier transport. However, the objective of this work was to describe general patterns in the behavior of electrical properties of porous silicon; therefore, we do not discuss here these phenomena in detail. Furthermore, it should be taken into account that, in view of the inhomogeneity of the processes of anodic etching, local regions belonging to neighboring groups and *por*-Si layers with different variation of electrical properties with depth can appear in *por*-Si.

CONTACT PHENOMENA IN THE STRUCTURES WITH POROUS SILICON

On the basis of the above classification, it may be stated that *por*-Si samples belonging to different groups have basically different properties. As a result, the contacts of porous silicon with metals and starting single-crystalline substrates can have either rectifying or nonrectifying properties in the multilayer structures fabricated. It is fairly easy to predict the properties of a metal–*por*-Si contact for porous layers of groups 1–3 as considered below through the example of aluminum metallization. In this case, the theory underlying the formation of nonrectifying or rectifying Al contacts to silicon with various concentrations of charge carriers can be used [33, 34]. It is known that a potential barrier invariably arises at the boundary of aluminum with silicon of various types of electrical conductivity; as a result, the junction is rectifying. However, in the case of a high doping level of silicon (higher than 5×10^{17} cm^{-3}), the barrier becomes thin, and the aluminum/silicon junction becomes nonrectifying owing to the processes of effective tunneling. Due to a high concentration of charge carriers in the single-crystalline matrix of porous silicon, the contacts of aluminum with *por*-Si of the first group are nonrectifying; moreover, due to the large effective surface area of *por*-Si, the contact resistances are found to be much lower than those in the case of aluminum/silicon junctions obtained under similar conditions [35, 36]. The aluminum–*por*-Si junctions for porous silicon belonging to the second group can be either rectifying or nonrectifying, depending on the ratio of the areas of low- and high-resistivity silicon regions at the interface. If the contribution of high-resistivity regions is determining, such contacts are rectifying. The same rectifying properties are also typical of contacts of aluminum with *por*-Si of the third group. As a rule, for *por*-Si belonging to the fourth group, quasi-nonrectifying behavior of the contacts is experimentally observed, which is related by many researchers (see, e.g., [37, 38]) to a high density of surface electron states. At the same time, the absence of significant rectification may be also explained from a different standpoint. In the case of an anomalously high resistivity of a porous layer, almost the entire voltage applied to the structure drops across the *por*-Si layer; as a

result, the voltage drop across the metal–*por*-Si contact is small, and, in this case, even a rectifying contact exhibits an almost linear current–voltage characteristic. Here, an important remark is appropriate. It is known that the processes of pore formation in silicon can be accompanied by the emergence of amorphous silicon film at the surface; therefore, the presence or absence of this amorphous film can significantly affect the properties of the contacts. It should be taken into account that diffusion of hydrogen can give rise to a thin depleted layer at the surface of *por*-Si of the second and third groups. Furthermore, as was mentioned above, a heat treatment of *por*-Si can appreciably affect the concentration of charge carriers in a porous layer, and electrical properties of contacts can depend on temperatures during the fabrication of multilayer structures.

The porous silicon–single-crystalline silicon (*por*-Si–*c*-Si) junction is formed naturally in the course of electrochemical treatment of silicon wafers and is invariably present in multilayer structures with porous layers (see, e.g., [34–44]). Electrical properties of this junction may be different, depending on electrical parameters of *por*-Si. On the basis of theoretical concepts of operation of contacts between semiconductors with different levels of doping and of heterojunctions and diodes, we can predict the presence or absence of rectification at this interface for porous layers belonging to different groups; this method was later verified experimentally. For *por*-Si layers of the first and second groups formed on *n*-type substrates, there is no rectification at the *por*-Si–*c*-Si junction. This is related to invariance of electron concentration in *c*-Si matrix for *por*-Si of the first group and formation of nonrectifying n–n^- junctions in the case of *por*-Si belonging to the second group. In the general case, for *por*-Si of groups 3 and 4, the *por*-Si–Si interface exhibits an appreciable rectification. This is especially evident for *por*-Si of group 3 formed on the *p*-type substrates and for *por*-Si belonging to the fourth group. For *por*-Si of group 4, this is caused by the fact that, if the porosity is high, electronic properties of the material change substantially as a result of large variations in chemical composition; in addition, in the case of small-sized crystallites, the width of the forbidden band increases for *por*-Si nanoparticles owing to quantum-size effects. Furthermore, both isotypic and anisotypic rectifying junctions can be formed. At the same time, situations are possible such that pronounced rectification at the interface can be absent for *por*-Si layers of groups 3 and 4. Such situations can arise for *por*-Si of group 3 formed on *p*-Si substrates, for *por*-Si of group 4 in the case of small bias voltages at the heterojunction, and so on.

CONCLUSION

Thus, differences in structural characteristics of *por*-Si and in the processes of formation of the regions depleted of charge carriers give rise to the observed diversity of electrical properties of porous material itself and the multilayered structures based on this material. A proper selection of the conditions of electrochemical treatment makes it possible to form porous layers with specified electrical properties and to solve problems in the design of devices with various purposes; these applications range from the use of *por*-Si layers as low-resistivity sublayers for aluminum metallization and as buffer layers for the epitaxial growth of various semiconductors on silicon substrates, which involves a large mismatch in crystal lattices, to the use of *por*-Si of group 4 in luminescent and photodetector structures. The diversity of the electrical properties of *por*-Si brings about a wide range of electrical parameters of contacts of the porous layer with metals and single-crystalline silicon. Therefore, in studying the transport of charge carriers in multilayer structures involving *por*-Si, one should take into account all special properties that can have porous material in a given case. In particular, the presence of potential barriers in a structure does not necessarily imply that all these barriers would make themselves evident; the voltage applied to the structure is redistributed among all of its elements, and some of the junctions may be revealed as biased in a linear portion of the current–voltage characteristic (in the vicinity of the origin). As a result, the use of the structures with thick high-resistivity *por*-Si layers makes it possible to completely eliminate the nonlinear phenomena at the contacts [45, 46].

ACKNOWLEDGMENTS

This work was carried out under the Program of the Ministry of Education of Russian Federation (project no. 98-8-4.3-231) and was supported by the International Science Foundation (grant no. d99-633).

REFERENCES

1. *Proceedings of International Conference "Porous Semiconductors—Science and Technology,"* (Mallorca, Spain, 1998).
2. T. Unagami, J. Electrochem. Soc. **127**, 476 (1980).
3. D. I. Bilenko, N. P. Aban'shin, Yu. N. Galishnikova, *et al.*, Fiz. Tekh. Poluprovodn. (Leningrad) **17**, 2090 (1983) [Sov. Phys. Semicond. **17**, 1336 (1983)].
4. M. I. J. Beale, J. D. Benjamin, M. J. Uren, *et al.*, J. Cryst. Growth **73**, 622 (1985).
5. R. C. Anderson, R. S. Muller, and C. W. Tobias, J. Electrochem. Soc. **138**, 3406 (1991).
6. A. J. Read, R. J. Needs, K. J. Nash, *et al.*, Phys. Rev. Lett. **69**, 1232 (1992).
7. R. Tsu and D. Babic, Appl. Phys. Lett. **64**, 1806 (1994).
8. V. Lehmann, F. Hofmann, F. Muller, *et al.*, Thin Solid Films **255**, 20 (1995).
9. A. Richter, P. Steiner, F. Kozlowsky, *et al.*, IEEE Electron Device Lett. **12**, 691 (1991).
10. *Properties of Porous Silicon*, No. 18, Ed. by L. Canham (DERA, Malvern, 1997).

11. L. A. Balagurov, Materialoved. Fiz. Khim. Kondens. Sred., No. 1, 50 (1998); L. A. Balagurov, Materialoved., No. 3, 23 (1998).
12. M. Ben-Chorin, F. Moller, F. Koch, *et al.*, Phys. Rev. B **51**, 2199 (1995).
13. A. J. Simmons, T. I. Cox, M. J. Uren, *et al.*, Thin Solid Films **255**, 12 (1995).
14. C. Peng, K. D. Hirschman, and P. M. Fauchet, J. Appl. Phys. **80**, 295 (1996).
15. N. S. Averkiev and A. Ya. Shik, Fiz. Tekh. Poluprovodn. (St. Petersburg) **30**, 199 (1996) [Semiconductors **30**, 112 (1995)].
16. N. S. Averkiev, L. M. Kapitonova, A. A. Lebedev, *et al.*, Fiz. Tekh. Poluprovodn. (St. Petersburg) **30**, 2178 (1996) [Semiconductors **30**, 1135 (1996)].
17. V. Yu. Timoshenko, E. A. Konstantinova, and E. Dietrich, Fiz. Tekh. Poluprovodn. (St. Petersburg) **32**, 613 (1998) [Semiconductors **32**, 549 (1998)].
18. S. P. Zimin, Pis'ma Zh. Tekh. Fiz. **21** (24), 46 (1995) [Tech. Phys. Lett. **21**, 1015 (1995)].
19. C. Cadet, D. Deresmes, D. Vuillaume, *et al.*, Appl. Phys. Lett. **64**, 2827 (1994).
20. S. P. Zimin and E. P. Komarov, Pis'ma Zh. Tekh. Fiz. **24** (6), 45 (1998) [Tech. Phys. Lett. **24**, 226 (1998)].
21. S. P. Zimin and A. N. Bragin, Fiz. Tekh. Poluprovodn. (St. Petersburg) **33**, 476 (1999) [Semiconductors **33**, 457 (1999)].
22. S. P. Zimin, Pis'ma Zh. Tekh. Fiz. **20** (7), 55 (1994) [Tech. Phys. Lett. **20**, 285 (1994)].
23. E. A. Ponomarev, P. Cowache, and C. Levy-Clement, in *Proceedings of International Conference "Porous Semiconductors—Science and Technology,"* (Mallorca, Spain, 1998), p. 23.
24. A. L. Vinke, S. P. Zimin, and V. H. Palashov, RF Patent No. 2054746 (1996).
25. F. P. Romstad and E. Veje, Phys. Rev. B: Condens. Matter **55**, 5220 (1997).
26. W. H. Lee, C. Lee, and J. Lang, J. Non-Cryst. Solids **198**, 911 (1996).
27. Y. Libianiker, I. Balberg, J. Partee, *et al.*, J. Non-Cryst. Solids **198**, 949 (1996).
28. Y. Libianiker and I. Balberg, Phys. Rev. Lett. **78**, 2433 (1997).
29. S. V. Slobodchikov, Kh. M. Salikhov, E. V. Russu, *et al.*, Fiz. Tekh. Poluprovodn. (St. Petersburg) **31**, 15 (1997) [Semiconductors **31**, 11 (1997)].
30. L. V. Belyakov, T. L. Makarova, V. I. Sakharov, *et al.*, Fiz. Tekh. Poluprovodn. (St. Petersburg) **32**, 1122 (1998) [Semiconductors **32**, 1003 (1998)].
31. S. P. Zimin and E. P. Komarov, Izv. Vyssh. Uchebn. Zaved., Élektron., No. 3, 48 (1998).
32. V. M. Demidovich, G. B. Demidovich, S. N. Kozlov, *et al.*, Pis'ma Zh. Tekh. Fiz. **24** (2), 17 (1998) [Tech. Phys. Lett. **24**, 53 (1998)].
33. E. H. Rhoderick, *Metal–Semiconductor Contacts* (Clarendon, Oxford, 1978; Radio i Svyaz', Moscow, 1982).
34. S. M. Sze, *Physics of Semiconductor Devices* (Wiley, New York, 1981; Mir, Moscow, 1984).
35. S. P. Zimin, V. S. Kuznetsov, and A. V. Prokaznikov, Appl. Surf. Sci. **91**, 355 (1995).
36. V. V. Chistyakov, S. P. Zimin, and A. L. Vinke, RF Patent No. 2065226 (1996).
37. N. J. Pulsford, G. L. J. A. Rikken, Y. A. R. R. Kessener, *et al.*, J. Lumin. **57**, 181 (1993).
38. M. Ben-Chorin, F. Moller, and F. Koch, J. Appl. Phys. **77**, 4482 (1995).
39. D. V. Dimitrov, Phys. Rev. B **51**, 1562 (1995).
40. P. H. Hao, X. Y. Hou, F. L. Zhang, *et al.*, Appl. Phys. Lett. **64**, 3602 (1994).
41. D. Dimova-Malinovska, M. Tzolov, N. Tzenov, *et al.*, Thin Solid Films **297**, 285 (1997).
42. Th. Dittrich, J. Rappich, and V. Yu. Timoshenko, Appl. Phys. Lett. **70**, 2705 (1997).
43. L. A. Balagurov, D. G. Yarkin, G. A. Petrovicheva, *et al.*, J. Appl. Phys. **82**, 4647 (1997).
44. É. B. Kaganovich, É. G. Manoĭlov, and S. V. Svechnikov, Fiz. Tekh. Poluprovodn. (St. Petersburg) **33**, 327 (1999) [Semiconductors **33**, 327 (1999)].
45. M. Ben-Chorin, F. Moller, and F. Koch, Phys. Rev. B: Condens. Matter **49**, 2981 (1994).
46. S. P. Zimin, E. P. Komarov, and Yu. V. Ryabkin, Izv. Vyssh. Uchebn. Zaved., Élektron. (1999) (in press).

Translated by A. Spitsyn

Semiconductors, Vol. 34, No. 3, 2000, pp. 358–362. Translated from Fizika i Tekhnika Poluprovodnikov, Vol. 34, No. 3, 2000, pp. 364–368.
Original Russian Text Copyright © 2000 by Kurova, Larina, Ormont.

AMORPHOUS, VITREOUS, AND POROUS SEMICONDUCTORS

Special Features of Relaxation of Metastable States Induced Thermally and by Photoexcitation in (*a*-Si:H):P Films

I. A. Kurova, É. V. Larina, and N. N. Ormont

Moscow State University, Vorob'evy gory, Moscow, 119899 Russia

Submitted July 23, 1999; accepted for publication September 22, 1999

Abstract—Kinetics of relaxation of metastable states that are induced thermally or by photoexcitation and cause an increase in dark electrical conductivity of (*a*-Si:H):P films is discussed. It is established that the relaxation is described by expanded exponential functions with the parameters τ and β depending differently on temperature in the cases of thermal excitation and photoexcitation. Thus, the relaxation of photo-induced states is characterized by a decrease in β with temperature, whereas the parameter β is almost temperature-independent for thermally induced states. It is shown that these dissimilar temperature dependences of β correlate with temperature variations of the half-width of annealing-energy distribution for these states. The observed features of relaxation of thermally induced and photo-induced metastable states are caused by different mechanisms of their formation. The origin of these states can be the same and related to activation of hydrogen-passivated phosphorus atoms. © *2000 MAIK "Nauka/Interperiodica".*

Photo-induced and thermally induced metastable states bringing about an increase in electrical conductivity are formed in doped *a*-Si:H films under the effects of illumination or quenching (rapid cooling), respectively [1–5]. These states are conventionally related to metastable, electrically active impurity atoms or to complexes containing these atoms. Henceforth, we refer to the aforementioned states simply as metastable states implying that they are related to the above impurity atoms. The mechanism of formation of photo-induced metastable states differs from that of the corresponding thermally induced states. This difference is bound to manifest itself in the relaxation of the corresponding states.

Relaxation of thermally induced metastable states has been studied repeatedly [6, 7]. It was established that relaxation of these metastable states (the variation of the concentration ΔN with time t) in both *n*- and *p*-type films was described by an expanded exponential function; i.e.,

$$\Delta N(t) = \Delta N(0)\exp\{-(t/\tau)^{\beta}\}, \qquad (1)$$

where $\tau = \nu_0^{-1}\exp(E_a/kT)$, with E_a as the annealing-activation energy and ν_0 as the frequency factor for relaxation.

Published data concerning the parameter β are conflicting. Thus, in the case of relaxation of thermally induced metastable states, an increase in β with temperature was observed in boron-doped films, whereas β was temperature-independent in the case of phosphorus-doped films [6]. In [7], it was established that the parameter β decreased with temperature in the case of relaxation of thermally induced metastable states in the films doped with boron.

A decrease in β with temperature was also reported in [3, 4] for the case of relaxation of photo-induced metastable states at elevated temperatures. This observation correlated with the dependence $\Delta E_a(T)$, i.e., with the temperature dependence of the half-width of the initial distribution of photo-induced metastable states in annealing-activation energy; this distribution is determined from the kinetics of the corresponding process and is given [4] by

$$\Delta E_a = AkT/\beta. \qquad (2)$$

A model of the formation of photo-induced metastable states, which is suggested in [4] and is based on a three-level configurational diagram with correlated thermal energies of formation and annealing for the corresponding impurity centers, accounts for an increase in ΔE_a with temperature and, consequently, for a decrease in β.

Obviously, it is necessary to study the relaxation of photo-induced and thermally induced metastable states in *a*-Si:H films doped with the same impurity.

The objective of this work was to perform the aforementioned studies using the *a*-Si:H films doped with phosphorus.

The (*a*-Si:H):P films used in the experiments were grown at the State Research Institute for the Rare-Metals Industry (Moscow) by deposition onto the quartz substrate in the plasma of high-frequency glow discharge, with the substrate temperature $T_s = 250°C$. The phosphorus concentration determined by SIMS was $(1–3) \times 10^{18}$ cm^{-3}.

The procedure used in the studies was based on the assumption that the kinetics of the metastable-state relaxation was similar to the kinetics of variation in the

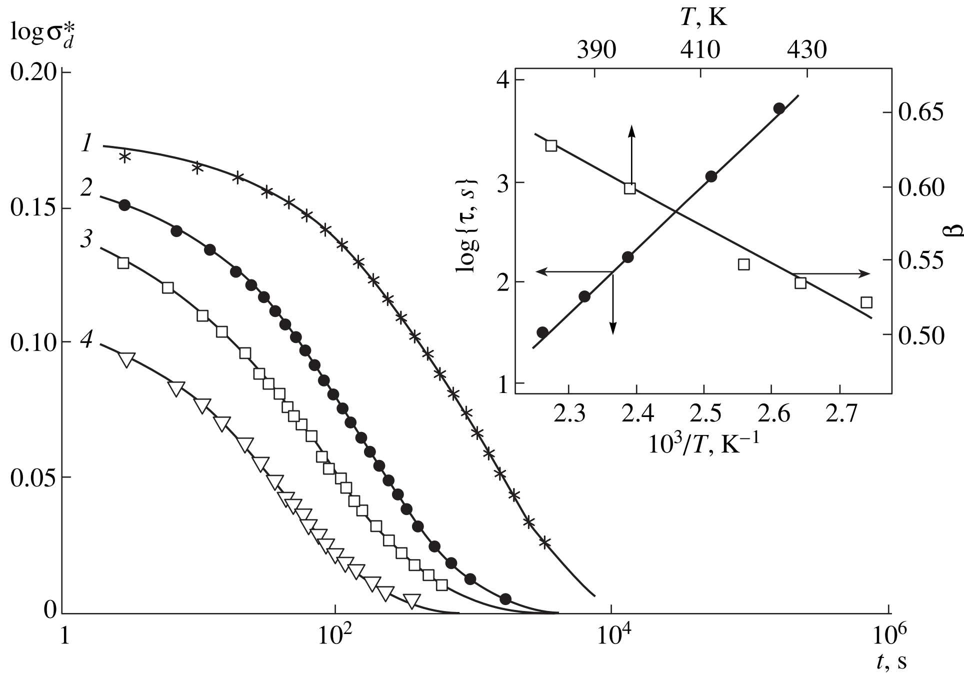

Fig. 1. The kinetics of relaxation of the dark conductivity after illumination of film 1 of (a-Si:H):P for 5 min at T = (*1*) 397, (*2*) 418, (*3*) 429, and (*4*) 441 K. The temperature dependences of the relaxation parameters τ and β for the same film are shown in the insert.

logarithm of the reduced dark conductivity $\sigma_d^* = \sigma_d(t)/\sigma_{d0}$, where σ_{d0} is the dark conductivity that is equilibrium for a given temperature T. In fact, $\ln[\sigma_d(t)/\sigma_{d0}] = [F_0 - F(t)]/kT = \Delta F(t)/kT$. Here, F_0 is the Fermi level at equilibrium. On the other hand, $\Delta F(t) = \Delta N(t)/\rho_0$, where ρ_0 is the constant density of states in the range ΔF of the shifts of the Fermi level. The assumption that ρ_0 is constant is based on the fact that, in the a-Si:H films used in our experiments and doped with phosphorus, the levels of the photo-induced and thermally induced metastable states are located above $F_0 + \Delta F$ in the forbidden band of silicon.

Measurements of relaxation kinetics of the photo-induced metastable states were performed in the following manner: An a-Si:H film was preliminarily annealed for 1 h at a temperature T_a = 460 K and was then slowly cooled to the temperature of measurement. After the required temperature was attained, we checked the establishment of an equilibrium value of dark conductivity, which was indicative of the absence of thermally induced metastable states that could be formed if the film was cooled too rapidly. Later, the film was exposed to 90 mW/cm^2 illumination by a halogen lamp with an infrared filter, and, following the cessation of the illumination, the relaxation kinetics of the dark conductivity of the film was measured.

Figure 1 illustrates the typical kinetics of relaxation of photo-induced metastable states for various temperatures; i.e., we have here $\Delta N(t) \sim \log[\sigma_d(t)/\sigma_{d0}]$. Solid lines represent the plots of the expanded exponential function with the parameters τ and β dependent on temperature. In the insert, the temperature dependences of τ and β are shown. It can be seen that β decreases steadily with temperature. The temperature dependence of τ is described by exponential function (1) with the parameters E_a = 1.3 eV and $\nu_0 = 3.2 \times 10^{12}$ s^{-1}.

Figure 2 shows the distributions of photo-induced metastable states in the annealing-activation energy

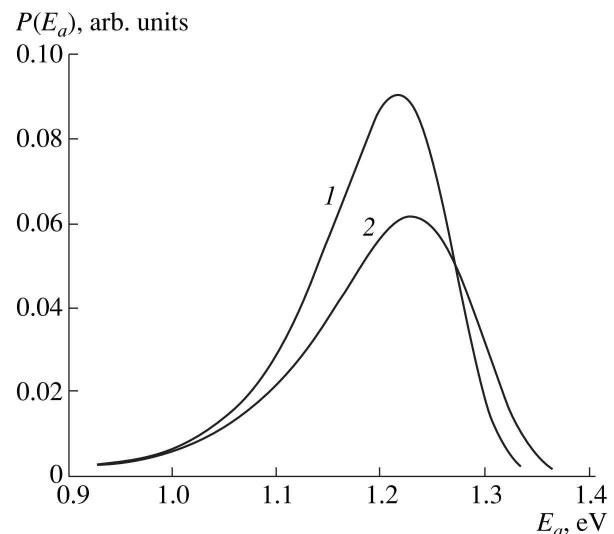

Fig. 2. Initial distribution of photo-induced metastable states in annealing-activation energy after illumination of film 1 for 5 min at T = (*1*) 397 and (*2*) 441 K.

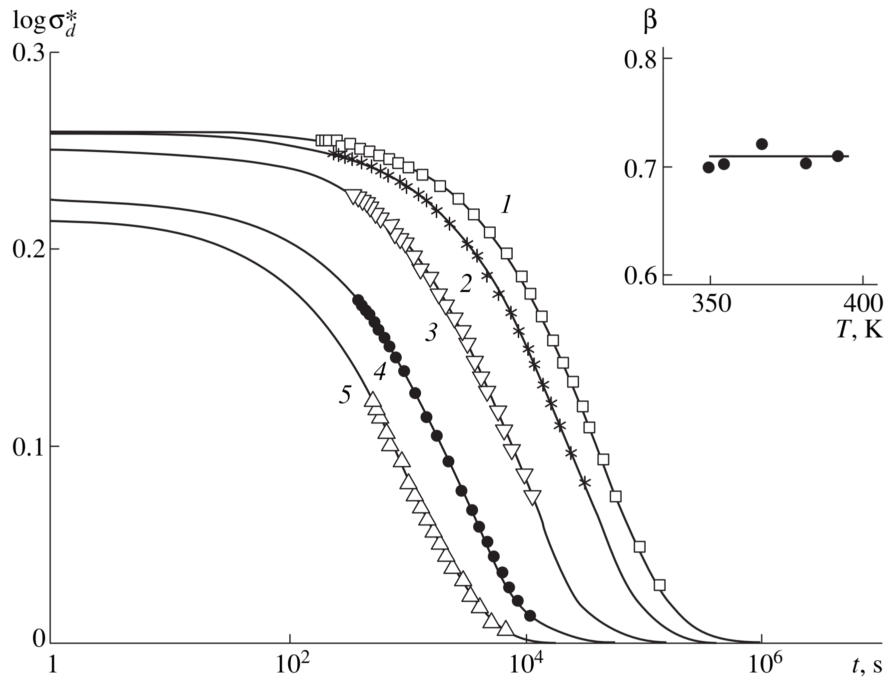

Fig. 3. The kinetics of relaxation of the dark conductivity of film 1 after rapid cooling (with allowance made for the time required to attain the given temperature) for the temperatures T = (*1*) 350, (*2*) 355, (*3*) 368, (*4*) 382, and (*5*) 394 K. Temperature dependence of the parameter β is shown in the insert.

$P(E_a)$ for two temperatures. These distributions are obtained by the method suggested in [8] and involve the differentiation of the calculated dependence $N(E_a)$ with respect to $E_a = kT\ln(\nu_0 t)$, where T is the temperature corresponding to the measurement, t is the time corresponding to a given value of $\log[\sigma_d(t)/\sigma_{d0}]$, and ν_0 is the quantity determined from the experimental dependence $\tau(1/T)$. It is evident that the obtained distribution $P(E_a)$ varies with temperature, and its half-width ΔE_a increases with an increase in temperature more sharply than according to the linear law. This fact explains a decrease in β with temperature in accordance with formula (2).

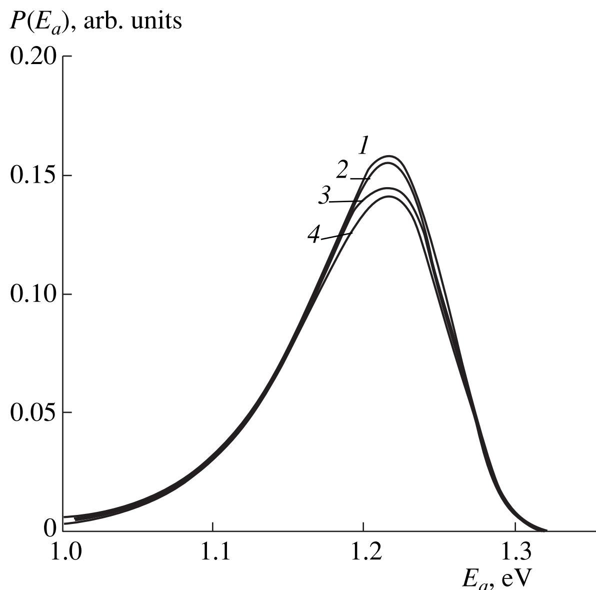

Fig. 4. Initial distribution of thermally induced metastable states in annealing-activation energy after rapid cooling of film 1 for the temperatures T = (*1*) 350, (*2*) 355, (*3*) 382, and (*4*) 394 K.

The kinetics of relaxation of thermally induced metastable states was studied by the following method. Prior to quenching, the sample was annealed at a temperature T_a = 460 K that was higher than the temperature T_E corresponding to the establishment of quasi-equilibrium and equal to 410 K in the films we studied. Liquid nitrogen was then introduced into a hollow holder, on which the sample and the heater were mounted, and the sample was cooled to T = 290 K with a rate of 0.5 K s^{-1}. After this temperature was reached, the sample was rapidly heated to a required temperature, and the temperature dependence of dark conductivity was then measured.

Figure 3 illustrates the kinetics of relaxation of thermally induced metastable states at various temperatures. For each curve, the time was determined with allowance made for the time needed to attain the given temperature after the sample was quenched. Solid curves represent the expanded exponential functions with different parameters τ and β. We found that τ decreases exponentially with temperature, whereas the value of β remains virtually unchanged (see the insert

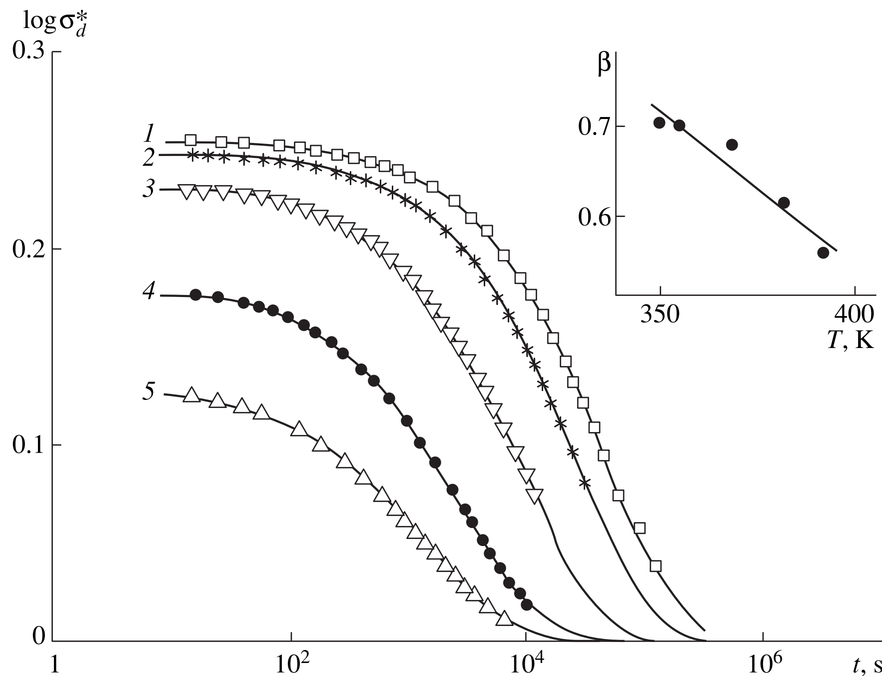

Fig. 5. Kinetics of relaxation of the dark conductivity of film 1 after rapid cooling (without considering the time required to attain the given temperature) for the temperatures T = (*1*) 350, (*2*) 355, (*3*) 368, (*4*) 382, and (*5*) 394 K. Temperature dependence of the parameter β is shown in the insert.

in Fig. 3). This is consistent with the results obtained in [6], where only a short time was needed to attain the desired temperature of measurements after annealing of the sample (~2 s).

Figure 4 shows the initial distributions of thermally induced metastable states in annealing-activation energy $P(E_a)$ obtained from the relaxation curves shown in Fig. 3. It can be seen that the half-width of the distribution increases almost linearly with temperature, which is consistent with the virtually constant value of β.

Figure 5 shows the relaxation curves for thermally induced metastable states for various temperatures without considering the time needed to attain the temperature of measurement. Solid lines represent the expanded exponential functions with different parameters τ and β. It can be seen that both the initial concentration of thermally induced metastable states $\Delta N(0) \sim \log[\sigma_d(0)/\sigma_{d0}]$ and the parameter β decrease significantly with temperature. It is possible that a decrease in β with temperature observed in [7] is related to the neglect of an annealing of metastable states; this annealing occurs in the time needed to attain the given temperature of measuring the relaxation of metastable states.

Thus, we showed that the temperature dependence of β was governed by the temperature dependence of the half-width of the initial distribution of metastable states in annealing-activation energy. This, in turn, is caused by the mechanism of formation of metastable states. In the case of photo-induced metastable states in *a*-Si:H films doped with phosphorus, the formation mechanism is the same as for the metastable states in the films doped with boron and is described in terms of a three-level coordination diagram, in which case the transition from the ground state to the metastable state is accomplished in two stages. The first stage consists in an optical transition from the ground state to an intermediate metastable state, and the second stage involves a thermal transition from the intermediate metastable state to the main metastable state. The thermally induced metastable states are formed thermally at the same temperature as the photo-induced metastable states are formed and are "frozen" in the course of rapid cooling. It is noteworthy that the origin of photo-induced metastable states formed at elevated temperatures and the origin of thermally induced metastable states are apparently the same and are related to the activation of phosphorus atoms passivated (i.e., rendered electrically inactive) by hydrogen.

ACKNOWLEDGMENTS

We thank I.P. Zvyagin for his participation in discussion of the results.

This work was supported by the Program "Universities of Russia: Basic Research."

REFERENCES

1. X. M. Deng and H. Fritzsche, Phys. Rev. B: Condens. Matter **36**, 9378 (1987).
2. J. Jang, S. C. Park, S. C. Kim, *et al.*, Appl. Phys. Lett. **51**, 1804 (1987).
3. I. A. Kurova, É. V. Larina, N. N. Ormont, *et al.*, Fiz. Tekh. Poluprovodn. (St. Petersburg) **31**, 1455 (1997) [Semiconductors **31**, 1257 (1997)].
4. A. G. Kazanskiĭ, I. A. Kurova, N. N. Ormont, *et al.*, J. Non-Cryst. Solids **227–230**, 306 (1998).
5. R. A. Street, J. Kakalios, C. C. Tsai, *et al.*, Phys. Rev. B: Condens. Matter **35**, 1316 (1987).
6. C. E. Nebel, R. A. Street, W. B. Jackson, *et al.*, J. Non-Cryst. Solids **164–166**, 203 (1993).
7. R. Meaudre, M. Meaudre, and P. Roca i Cabarrocas, Appl. Phys. Lett. **62**, 594 (1993).
8. M. Stutzmann, W. B. Jackson, and C. C. Tsai, Phys. Rev. B: Condens. Matter **32**, 23 (1985).

Translated by A. Spitsyn

Semiconductors, Vol. 34, No. 3, 2000, pp. 363–366. Translated from Fizika i Tekhnika Poluprovodnikov, Vol. 34, No. 3, 2000, pp. 369–372.
Original Russian Text Copyright © 2000 by Golikova.

Amorphous Boron Films with Enhanced Electrical Conductivity

O. A. Golikova

Ioffe Physicotechnical Institute, Russian Academy of Sciences, Politekhnicheskaya ul. 26, St. Petersburg, 194021 Russia

Submitted September 20, 1999; accepted for publication September 23, 1999

Abstract—The results of studying the electrical properties of nanostructured films of amorphous boron *a*-B are compared with the results obtained for bulk samples of the same material and also for the crystals of certain quasi-amorphous borides with complex icosahedral structure. Models accounting for the enhanced electrical conductivity of amorphous boron films are suggested. © *2000 MAIK "Nauka/Interperiodica".*

1. INTRODUCTION

At present, the so-called nanostructured thin films of amorphous semiconductors are attracting considerable attention; such films contain inclusions of nanocrystals or nanoclusters ~1 nm in size and are distributed over the amorphous matrix. As was shown, for example, for *a*-Si:H [1, 2], electrical conductivity σ of such inhomogeneous films

$$\sigma \sim \exp(-\Delta E_\sigma/kT)$$

is higher by approximately an order of magnitude as compared to σ in conventional homogeneous films for ΔE_σ = const and T = const. It is noteworthy that the nanoinclusions in these films appear under special conditions of the film deposition [1].

The amorphous boron (*a*-B) films are distinct in that they invariably contain nanoinclusions, i.e., icosahedral clusters (B_{12} icosahedrons with sizes $d = 0.51$ nm or their conglomerates). Therefore, these films are of special interest for the physics of nanostructured films. It is worth noting that icosahedral clusters were identified not only in the films but also in powders and bulk *a*-B samples with the use of various structure-analysis methods (the diffraction of electrons [3], neutrons [4], and X-rays [5], and the IR [6, 7] and Raman [7, 8] spectroscopies).

The objective of this paper is to report the results of studying the electrical properties of *a*-B films and compare these results with the data obtained for bulk samples and also for crystals of certain quasi-amorphous borides [9].

2. THE SAMPLES

The *a*-B films were deposited onto quartz substrates in the course of evaporation of crystalline B with the use of electron-beam heating and also as a result of sputtering the crystalline-boron target by Ar ions. The films were doped with carbon by cosputtering a graphite target. The substrate temperature during deposition was $T_s = 300$–350°C, and the thickness of the films was $d \lesssim 1$ μm.

Recently, other methods have also been used to produce such films [5]; among these, the method of remote EPR plasma based on $B_2H_6 + H_2$ gaseous mixtures is the most promising. Using this method and varying T_s and the quantity

$$c(B_2H_6) = Q(B_2H_6)/[Q(B_2H_6) + Q(H_2)],$$

where Q is the rate of gas flowing, one can obtain either *a*-B films or *a*-B:H films. In relation to uncontrolled impurities, this method is regarded as ensuring the highest purity of the material [10]. Therefore, it is especially important to compare the properties of the films produced in this work with those of the films obtained in [10].

The bulk *a*-B samples were obtained by thermal decomposition of boron hydrides [11]. The samples with dimensions of 0.2 cm × 0.4 cm × 1.5 cm were used for electrical measurements. The crystals of REB_{66} (RE stands for a rare-earth element) quasi-amorphous borides with the dimensions l = 7.5 cm and d = 0.4–0.6 cm were obtained by vertical floating-zone melting in an inert atmosphere [9].

3. RESULTS AND DISCUSSION

Let us consider the properties of *a*-B films. Irrespective of the method of deposition, all these films have an unusually high electrical conductivity at room temperature: $\sigma \simeq 10^{-3}$ S/cm. On this basis, these films were assumed to be "metallic" [5]. However, a number of facts contradict this assumption.

First of all, studies of these films made it possible to determine both the thermal and optical bandgaps (1.3 and 1.1 eV, respectively); furthermore, the temperature dependence of electrical conductivity for $T < 700$ K was found to be typical of a nonhydrogenated amorphous semiconductor (Fig. 1). Moreover, the phenomenon of switching, which is also characteristic of amor-

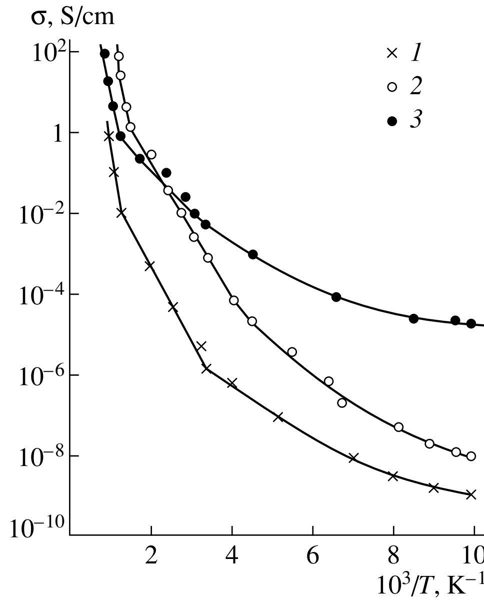

Fig. 1. Temperature dependences of electrical conductivity in (*1*) a bulk sample of *a*-B, (*2*) an *a*-B film, and (*3*) a YB_{66} crystal; all the REB_{66} compounds are similar in electrical parameters to the samples studied in [9].

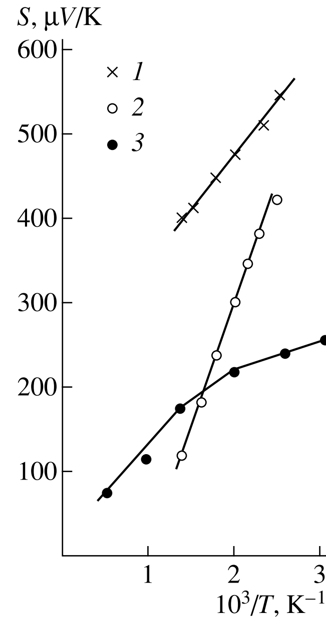

Fig. 2. Temperature dependences of thermal emf. The same symbols for curves *1*–*3* are used as in Fig. 1.

phous semiconductors, is observed in strong electric fields.

In addition, other published data, which we will now outline, contradict this assumption.

First, absorption by free charge carriers was not observed in studies of the absorption coefficient. Second, in the range of long wavelengths (2–4 μm), the refractive index $n(\omega)$ = const, whereas, in the case of metals, a sharp increase in n should be observed as ω decreases [10]. Finally, the coordination number for B atoms in the films is $Z = 6$, whereas $Z = 12$ is typical of amorphous metals [5].

We now compare the electrical conductivity of *a*-B films with that of bulk samples of *a*-B (Fig. 1). It can be seen that, in the temperature range before the onset of intrinsic conduction (i.e., at $T < 700$ K), the values of activation energies ΔE_σ are almost identical in both cases, but the value of σ in the bulk sample is approximately 200 times lower than that in the film. This difference can be apparently related to the aforementioned effect that consists in an increase in electrical conductivity and is inherent in nanostructured films.

Thermal emf of *a*-B is invariably positive (Fig. 2), which indicates that holes are dominant in charge transport. In the temperature range where electrical conductivity exponentially increases and thermal emf decreases with increasing temperature ($T = 400$–700 K), we have

$$S = (k/e)(\text{const} + \Delta E_s/kT).$$

In this case, $\Delta E_\sigma > \Delta E_s$; i.e., $\Delta E_\sigma - \Delta E_s = \Delta E_\mu$, where ΔE_μ is the activation energy for the mobility of holes in the case of charge transport via delocalized states of the valence band.

The quantity ΔE_μ is regarded as a measure of fluctuations of electrostatic potential in the matrix of amorphous film and, consequently, as a measure of fluctuations of the band edge, through the states of which the charge transport proceeds. It is important that ΔE_μ depends on the density of defects (dangling bonds) N_D. For example, $\Delta E_\mu = 50$ meV for undoped *a*-Si:H films having $N_D < 10^{16}$ cm^{-3}, whereas ΔE_μ becomes as high as 250 meV after the films are subjected to prolonged intense illumination, in which case the value of N_D increases to 10^{17} cm^{-3} (the Staebler–Wronski effect) [12]. Typically, for bulk *a*-B samples, $\Delta E_\mu = 190$ meV, whereas $\Delta E_\mu = 100$ meV for *a*-B films. Thus, the values of ΔE_μ indicate, first, that the valence-band edge has a more "perfect" structure in the case of the films. Second, these values account for the fact that electrical conductivity of the films is higher as compared to the bulk samples in the aforementioned temperature range.

We now consider the results of studying the drift mobility of holes (μ_D) in *a*-B films [13] (Fig. 3). The mobility is given by

$$\mu_D \sim \exp(-\Delta E_{\mu_D}/kT),$$

where the activation energy $\Delta E_{\mu_D} = 85$ meV is considerably lower than that in other amorphous semiconductors; i.e., the charge transport involves capture of carriers at a shallow level of traps. Obviously, this indicates that the density of localized states decreases rapidly with distance from the valence-band edge; i.e., the

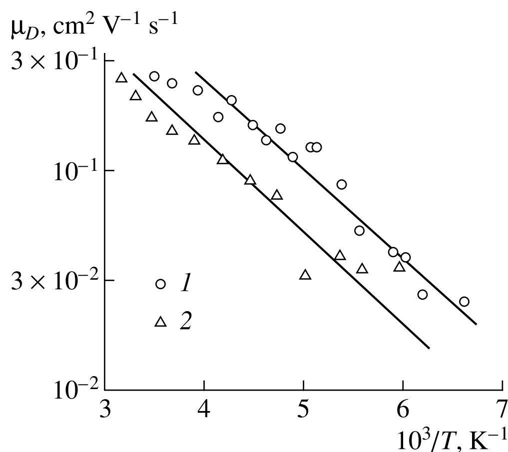

Fig. 3. Temperature dependences of drift mobility of holes μ_D in *a*-B films deposited on the substrate at T_s = (*1*) 300 and (*2*) 350°C.

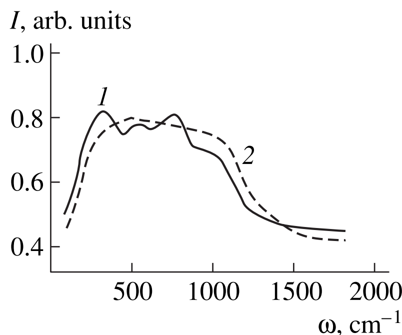

Fig. 4. The Raman spectra for (*1*) undoped *a*-B films and (*2*) the films doped with carbon.

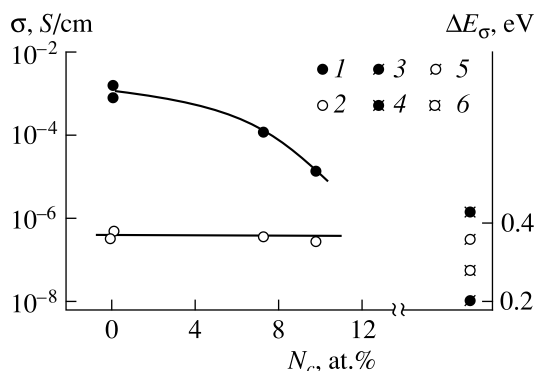

Fig. 5. (*1*) Electrical conductivity measured at room temperature and (*2*) the activation energy of electrical conductivity in relation to the concentration of carbon in *a*-B films. The data reported in [14] for (*3*, *4*) electrical conductivity and (*5*, *6*) activation energy of electrical conductivity in (*3*, *5*) undoped *a*-B:H films and (*4*, *6*) films doped with carbon are also shown; the ratio of concentrations B : C in the plasma of glow discharge was 125 : 1.

degree of structural ordering increases. In our opinion, a decrease in the value of ΔE_μ is bound to be accompanied by a decrease in the value of ΔE_{μ_D}, which has been observed.

It is of interest to consider the influence of impurities on the structure and electrical conductivity of *a*-B films. Figure 4 shows the Raman spectra of undoped films and films doped with carbon [8]. In spite of "diffuseness" of the spectra characteristic of an amorphous semiconductor, the peaks at 270, 580, 760, and 1220 cm^{-1} can be clearly recognized in the spectrum of an undoped film. It is noteworthy that the frequencies corresponding to the peaks at 760 and 1220 cm^{-1} are close to the frequencies (related to vibrations of atoms inside the B_{12} icosahedron and in neighboring icosahedrons) that are characteristic of crystals (800 and 1160 cm^{-1}, respectively). After introduction of 9 at. % of carbon, the spectrum becomes appreciably smoothed (Fig. 4). This signifies that carbon "decomposes" the icosahedral inclusions in the films. In line with this, as the content of carbon increases, electrical conductivity σ of *a*-B films decreases, with ΔE_σ remaining unchanged (Fig. 5). It may be inferred from the above that carbon modifies the structure of *a*-B films rather than acting as an electrically active impurity, as in the case of *a*-B:H [14].

4. CONCLUSION

We now dwell on the models that have been suggested to explain the high electrical conductivity of nanostructured *a*-B films.

If the nanoinclusions of clusters distributed in the amorphous matrix of the film bring about a decrease in local stresses and, as a consequence, a decrease in the density of defects in this matrix, the magnitudes of fluctuations of electrostatic potential and, correspondingly, the fluctuations of the valence-band edge decrease. As a result, the activation energy ΔE_μ decreases, and the mobility of holes in delocalized states increases. Thus, electrical conductivity σ of *a*-B films increases; this effect is inherent in the films alone and is not observed in the bulk samples, although the latter also contain icosahedral inclusions. This model is supported by the results of studies of the *a*-B films doped with carbon, which changes the structure of the films. As a result of such doping, the values of σ in *a*-B films decrease significantly. In the context of this model, the boron nanoclusters act as modifiers of the film structure, and the charge transport proceeds over the amorphous matrix.

According to a possible alternative model, an *a*-B film is mainly composed of icosahedral nanoclusters separated by thin amorphous interlayers. In fact, in certain *a*-B films, clusters of various sizes were observed, up to and including the B_{156} cluster, i.e., the $B_{12}(B_{12})B_{12}$ supericosahedron [5] that, as is known, represents a basic unit of crystalline REB_{66} compounds (it should be remembered that the latter have the most complex

structure among all boron compounds) [15]. These compounds were named quasi-amorphous borides [9], because their optical, thermal, and electrical properties are no different from those of bulk *a*-B samples, except for the fact that, at room temperature, the electrical conductivity in these compounds is appreciably higher and the thermal emf is lower (Figs. 1, 2) than those in bulk *a*-B samples. In fact, the value of σ in YB_{66} is closer to that of *a*-B films.[1]

The composition of a unit cell of REB_{66} crystal is represented as $RE_{24}[B_{12}(B_{12})_{12}][B_{36}]_4[B_{48}]_4$, with the crystal being structured in such a way that the B_{156} clusters are surrounded by "interlayers" composed of REB_{36} and REB_{48} conglomerates [15]. It is important that the degree of disordering in the structure of the cluster is much smaller than that of the interlayers. Thus, the B–B bond length in a cluster increases consistently (from 0.173 to 0.184 nm) if we pass from the central icosahedron to the outer icosahedron, whereas, in a YB_{36} conglomerate, this length increases from 0.172 to 0.217 nm. It is evident that such a structure resembles that of *a*-B films if they are largely composed of nanoclusters separated by thin amorphous interlayers. In this case, the main contribution to charge transport at sufficiently high temperatures comes from clusters with a comparatively ordered structure, which accounts for the high electrical conductivity of both the REB_{66} compounds and the *a*-B films.

The results of studies of *a*-B films reported here are interpreted in the context of the first of the aforementioned models (charge transport over the matrix); the same applies to the results for nanostructured films of other amorphous semiconductors. The second model based on charge transport via nanoclusters is apparently applicable only to *a*-B films having a specific structure consisting largely of large-sized nanoclusters. Such films are undoubtedly of interest in their own right.

[1] Nevertheless, the discrepancy between the thermoelectric coefficient *S* of REB_{66} and that of *a*-B films is appreciable both in magnitude and in the temperature dependence (Fig. 2). Furthermore, the values of σ at low temperatures are larger for REB_{66} than for *a*-B films (Fig. 1).

REFERENCES

1. P. Roca i Cabarrocas, S. Hamma, P. St'ahel, *et al.*, in *Proceedings of Conference EPSEC-14, Barcelona, Spain, 1997*, p. 5A20.
2. O. A. Golikova and M. M. Kazanin, Fiz. Tekh. Poluprovodn. (St. Petersburg) **33**, 97 (1999) [Semiconductors **33**, 97 (1999)].
3. K. Katada, Jpn. J. Appl. Phys. **5**, 582 (1966).
4. R. G. Delaphane, T. Lundström, U. Dahlberg, *et al.*, in *Boron-Rich Solids (AIP Conference 231)*, Ed. by D. Emin, T. L. Aselage, A. C. Switendick, B. Morosin, and C. L. Beckel (Albuquerque, New Mexico, 1990), p. 241.
5. M. Kabayashi, I. Higashi, T. Oyama, *et al.*, Jpn. J. Appl. Phys. **10**, 25 (1993).
6. A. A. Berezin, O. A. Golikova, M. M. Kazanin, *et al.*, J. Non-Cryst. Solids **16**, 237 (1974).
7. U. Kuhlmann, H. Werheit, T. Lundström, *et al.*, Jpn. J. Appl. Phys. **10**, 88 (1993).
8. J. S. Lannin, Solid-State Commun. **25**, 363 (1978).
9. O. A. Golikova, Fiz. Tekh. Poluprovodn. (St. Petersburg) **26**, 1604 (1992) [Sov. Phys. Semicond. **26**, 900 (1992)].
10. K. Shurai and S. Gonda, J. Phys. Chem. Solids **53**, 1081 (1992).
11. A. F. Zhigach and D. C. Stasinevich, in *Boron and Refractory Borides*, Ed. by V. I. Matkovich (Springer, 1997), p. 214.
12. D. Ruff, H. Mell, L. Tolt, *et al.*, in *Abstracts of Papers Presented at the Conference ICAMS-17, Budapest, Hungary, 1997*, abstract No. ThP113/4.
13. M. Takeda, K. Kimura, and K. Murayama, in *Abstracts of the Papers Presented at the Conference ICAS-16, Kobe, Japan, 1995*, p. 244.
14. B. L. Zalph, L. J. Dimmey, H. Park, *et al.*, Phys. Status Solidi A **62**, K186 (1980).
15. K. E. Spear, in *Phase Diagrams. Materials Science and Technology* (Academic, New York, 1976), Vol. 4, p. 92.

Translated by A. Spitsyn

Semiconductors, Vol. 34, No. 3, 2000, pp. 367–369. Translated from Fizika i Tekhnika Poluprovodnikov, Vol. 34, No. 3, 2000, pp. 373–375.
Original Russian Text Copyright © 2000 by Kazanskiĭ, Mell, Terukov, Forsh.

AMORPHOUS, VITREOUS, AND POROUS SEMICONDUCTORS

Absorption and Photoconductivity of Boron-Compensated μ*c*-Si:H

A. G. Kazanskiĭ*, H. Mell, E. I. Terukov***, and P. A. Forsh***

** Moscow State University, Vorob'evy gory, Moscow, 119899 Russia*
e-mail: Kazanski@scon279.phys.msu.su
*** Philipps-Universität Marburg, Fachbereich Physik, D-35032, Marburg, Germany*
**** Ioffe Physicotechnical Institute, Russian Academy of Sciences, Politekhnicheskaya ul. 26, St. Petersburg, 194021 Russia*

Submitted July 12, 1999; accepted for publication October 4, 1999

Abstract—A study is reported of absorption, conductivity, and photoconductivity of photosensitive μ*c*-Si:H weakly doped with boron. The dependences of photoconductivity on the temperature and the intensity of light were measured in a temperature range of 100–400 K for photon energies of 0.9, 1.3, and 1.8 eV. The results obtained are explained by the dominant contribution of the microcrystalline phase and the states at the interfaces of microcrystals to the transport and recombination of nonequilibrium carriers in μ*c*-Si:H. Possible recombination mechanisms and the change of their role with temperature are analyzed. *© 2000 MAIK "Nauka/Interperiodica".*

In recent years, microcrystalline hydrogenated silicon (μ*c*-Si:H) has attracted the attention of scientists because of its potential in the development of thin-film solar cells, photosensors, and thin-film transistors. It has a rather high conductivity in comparison with amorphous silicon (*a*-Si:H) and, according to the data of [1], retains these properties under long-term illumination. In contrast to polycrystalline materials, in which crystal size is several hundreds of nanometers, in the general case, μ*c*-Si:H consists of amorphous and crystalline phases, and their proportion and crystal sizes in a range from units to tens of nanometers depend on production conditions.

The effect of production conditions on the structure [2], the conductivity (σ_d) [3–7], and the edge of optical absorption [8–10] of μ*c*-Si:H has been studied in much detail. However, the photoconductivity ($\Delta\sigma_{ph}$) and the processes governing this characteristic have been studied to a smaller extent [1, 5, 11]. This is likely to be associated with the fact that undoped μ*c*-Si:H films have a rather high *n*-type conductivity (10^{-4}–10^{-3} Om^{-1} cm^{-1}) and a low photosensitivity ($\Delta\sigma_{ph}/\sigma_d$) [5]. According to [12], a high conductivity of undoped μ*c*-Si:H is associated with oxygen, which penetrates uncontrollably into films during their production.

The introduction of boron with relatively low concentrations (10^{17}–10^{18} cm^{-3}) into μ*c*-Si:H considerably (by 4–5 orders of magnitude) reduces the conductivity of the film [1, 5, 6]. Such "uncompensated" films have a rather high photosensitivity, which makes it possible to use them in the study of processes determining the photoconductivity of μ*c*-Si:H.

In this work, we studied the absorption, conductivity, and photoconductivity of μ*c*-Si:H lightly doped with boron. Films 0.6–0.7 μm thick (produced at Marburg University) were deposited on quartz in the course of glow-discharge decomposition of silane (SiH_4) strongly diluted with hydrogen (the silane content in the gas mixture was 1.5%). Doping with boron was carried out by introducing diborane (B_2H_6) in the proportion $[B_2H_6]/[SiH_4] = 4 \times 10^{-6}$ into the reaction chamber. The substrate temperature in the course of film deposition was 220°C. Prior to the measurements, the samples were annealed at 180°C for 30 min. The annealing and the measurements were carried out in vacuum with a residual pressure of 10^{-3} Pa.

According to the data of scanning and transmission electron microscopy, the films have a columnar structure directed perpendicular to the substrate surface, with columns 30–100 nm in diameter, and contain crystals from 3 to 30 nm in size. The analysis of Raman spectra showed that the contribution crystalline component to the spectrum of the films under study had an area of 85% of the total area under the peak. According to the data on thermoelectric power, the films had *p*-type conduction.

The spectral dependence of the relative absorption coefficient $\alpha_{cpm}/\alpha_{cpm}(1.8\text{ eV})$, which was measured by the direct-photocurrent method, is shown in Fig. 1 (curve *1*). In the insert of Fig. 1, this spectral dependence is given in the coordinates $\alpha_{cpm}^{1/2}(h\nu)$. One can see from the figure that the change of $\alpha_{cpm}(h\nu)$ in the region of photon energies $h\nu > 1.2$ eV is well described, within the limits of the accuracy determined by the

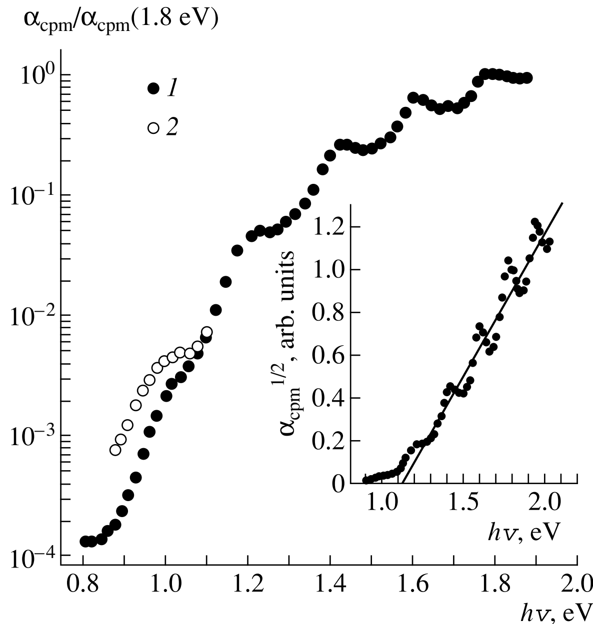

Fig. 1. Spectral dependence of the absorption coefficient of μc-Si:H, expressed in relative units $\alpha_{cpm}/\alpha_{cpm}(1.8\text{ eV})$, measured by the direct-photocurrent method (*1*) without background illumination and (*2*) under conditions of background illumination by photons with energies $h\nu = 1.8$ eV and intensity $I = 5 \times 10^{14}$ cm^{-2} s^{-1}. The insert presents the spectral dependences in the coordinates $\alpha_{cpm}^{1/2}(h\nu)$.

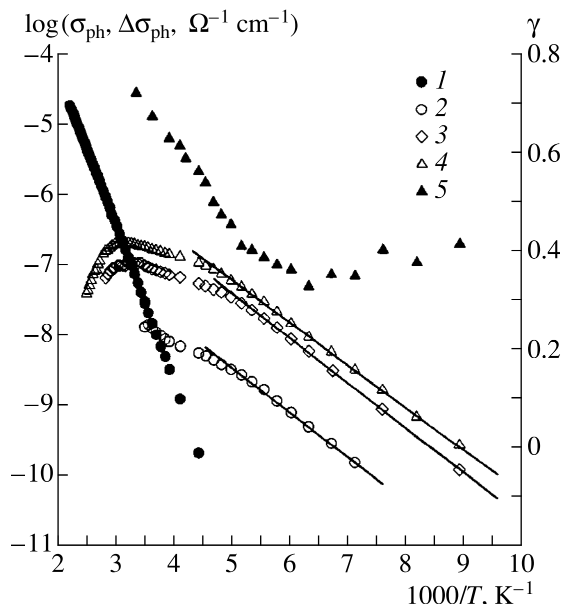

Fig. 2. Temperature dependences of (*1*) the conductivity and (*2–4*) the photoconductivity for the excitation with photons of energy (*2*) 0.9, (*3*) 1.3, and (*4*) 1.8 eV and (*5*) the parameter γ of the current–illumination characteristic for $h\nu$ = 1.8 eV.

effect of interference on the spectra under study, by the quadratic dependence, which is typical of indirect optical transitions involving phonons in c-Si. The extrapolation of the dependence obtained in the region $h\nu >$ 1.2 eV to zero gives the value $E_0 = 1.12$ eV, which is close to the band gap of c-Si. The result obtained suggests that the dominant contribution to absorption measured by the direct-photocurrent method was made by the crystalline phase of μc-Si:H.

One can see from Fig. 1 that the region $h\nu < 1.1$ eV contains a "tail" of optical absorption. The measurements made by us for the spectra of α_{cpm} under conditions of background illumination with 1.8-eV photons showed that the background illumination caused an increase of absorption in the region of this tail (curve *2*). This may be associated with an increase in the population of localized states determining absorption for $h\nu < 1.1$ eV. In the opinion of the authors of [9], these states may represent the states of defects at the microcrystal interfaces.

Figure 2 presents the temperature dependence of the background conductivity of the μc-Si:H under study. In the temperature region T = 220–450 K, the dependence $\sigma_d(T)$ is of the activation nature with activation energy $E_a = 0.43$ eV. The same figure presents the temperature dependences of photoconductivity measured for the photon energies $h\nu$ = 1.8, 1.3, and 0.9 eV. One can see that the temperature changes of $\Delta\sigma_{ph}$ were similar for all the values of $h\nu$ used by us. In the temperature region $T < 200$ K, $\Delta\sigma_{ph}$ increases with temperature, and this increase is well described by the exponential law with an activation energy of 0.12–0.13 eV. As the temperature is further increased, an increase of $\Delta\sigma_{ph}$ slows down, and, in the temperature region where $\Delta\sigma_{ph} \leq \sigma_d$, the quantity $\Delta\sigma_{ph}$ decreases with increasing temperature. Changes of intensity of incident radiation caused no substantial changes in the character of the temperature dependence of $\Delta\sigma_{ph}$, especially in the activation energy.

The study of conductivity–illumination characteristics of photoconductivity showed that the character of variation of $\Delta\sigma_{ph}$ with the light intensity I ($\Delta\sigma_{ph} \sim I^{\gamma}$) was determined by the value of photoconductivity and was independent of the energy of an incident photon. Figure 2 presents the effect of temperature on the parameter γ. The film under study was excited with 1.8-eV photons in the intensity range $I = 6 \times 10^{13} \times 6 \times 10^{14}$ cm^{-2} s^{-1}. We note that $\gamma < 0.5$ for $T < 200$ K.

Let us discuss the results obtained. The interpretation of the phenomena observed for charge transport in μc-Si:H depends on its structure, in particular, the proportion of amorphous and crystalline phases in its composition. If microcrystals in μc-Si:H are separated by a-Si:H, then, in the opinion of the authors of [1], the activation energy for σ_d in boron-compensated μc-Si:H films will be determined by the height of the barrier in the valence band at the boundary of the c-Si/a-Si:H

junction. The data of Raman spectroscopy and the absorption spectra obtained by the direct-current method suggest that the carriers in μ*c*-Si:H under study are transported mainly through microcrystals. It is likely that, in this case, one may use the barrier model [3], according to which the trapping of carriers by the states at the interfaces is bound to cause the formation of potential barriers at the interfaces. Because the concentration of carriers required for the formation of barriers in the μ*c*-Si:H under study is considerably lower than the concentration of microcrystals (10^{18} cm^{-3} for a crystal size of 10 nm), it is reasonable to assume that barriers are formed, for example, at the boundaries of columns [7]. At the same time, the states at the boundaries of microcrystals can form localized states in the forbidden band of microcrystals inside the columns, and the latter states determine the absorption observed in the region $h\nu < 1.1$ eV. Thus, the value $E_a = 0.43$ eV in μ*c*-Si:H under study may be determined by the position of the Fermi level with respect to the valence band edge in a microcrystal and the barrier height, which determines the activation of carrier mobility and whose value in undoped μ*c*-Si:H is 0.05–0.1 eV [3, 7].

One can see from Fig. 2 that the form of the temperature dependence of $\Delta\sigma_{ph}$ remains unchanged upon changing $h\nu$ from 0.9 to 1.8 eV. This is likely to be associated with the fact that the generation, transport, and recombination of nonequilibrium charge carriers in the μ*c*-Si:H under study are determined by the microcrystalline phase. In our opinion, the change in the nature of $\Delta\sigma_{ph}(T)$ for $T = 200$–220 K suggests that the processes governing the recombination of nonequilibrium carriers are changed at these temperatures. This statement is supported by the temperature dependence of the parameter γ in Fig. 2. For $T < 200$ K, $\gamma = 0.3$–0.4 and insignificantly changes with temperature. On the other hand, the parameter γ increases with temperature for $T > 200$ K. The absence of data on recombination processes in μ*c*-Si:H allows no unambiguous interpretation. It is reasonable to assume that the range $T = 200$–220 K is characterized by the change of the contribution of different regions of the material and, therefore, of different states to the recombination of nonequilibrium charge carriers. In particular, such regions may represent microcrystalline regions inside columns and the region of potential barriers at the boundary of columns. In the second case, the lifetime will show an activation decrease with temperature. If the recombination of nonequilibrium charge carriers in the low-temperature region ($T < 200$ K) is related to tunneling and is therefore independent of temperature, the activation energy observed for the dependence $\Delta\sigma_{ph}(T)$ may be determined by the activation dependence of the mobility of nonequilibrium carriers, which is associated with the presence of potential barriers. The hypothetical increase of the contribution of the states in the region of potential barriers to recombination with increasing temperature can weaken the temperature dependence of $\Delta\sigma_{ph}$ in the high-temperature region. Finally, we note that the potential relief inside μ*c*-Si:H columns, if present, and its change under the action of temperature and illumination are also capable of producing an effect on the transport and the recombination of nonequilibrium carriers in the μ*c*-Si:H under study.

ACKNOWLEDGMENTS

This work was supported by INTAS, project no. 97-1910.

REFERENCES

1. M. J. Williams, C. Wang, and G. Lucovsky, Mater. Res. Soc. Symp. Proc. **219**, 389 (1991).
2. I. Beckers, N. H. Nickel, W. Pilz, *et al.*, J. Non-Cryst. Solids **227–230**, 847 (1998).
3. P. G. LeComber, G. Willeke, and W. E. Spear, J. Non-Cryst. Solids **59–60**, 795 (1983).
4. G. Lucovsky and C. Wang, Mater. Res. Soc. Symp. Proc. **219**, 377 (1991).
5. R. Flückiger, J. Meier, M. Goetz, *et al.*, J. Appl. Phys. **77**, 712 (1995).
6. M. Bruggemann, A. Hierzenberger, P. Reining, *et al.*, J. Non-Cryst. Solids **227–230**, 982 (1998).
7. D. Ruff, H. Mell, L. Toth, *et al.*, J. Non-Cryst. Solids **227–230**, 1011 (1998).
8. F. Seibke, S. Yata, Y. Hishikawa, *et al.*, J. Non-Cryst. Solids **227–230**, 977 (1998).
9. N. Beck, J. Meier, J. Fric, *et al.*, J. Non-Cryst. Solids **198–200**, 903 (1996).
10. M. Vanecek, A. Poruba, Z. Remes, *et al.*, J. Non-Cryst. Solids **227–230**, 967 (1998).
11. H. N. Liu, Y. L. He, F. Wang, *et al.*, J. Non-Cryst. Solids **164–166**, 1005 (1993).
12. P. Torres, J. Meier, R. Flückiger, *et al.*, Appl. Phys. Lett. **69**, 1373 (1996).

Translated by A. Kirkin